Light Induced Processes in Near-Orthogonal Bichromophores Separated Through a Single Bond

A thesis submitted for the degree of

Doctor of Philosophy

in the

School of Chemistry

Rijo T. C.

School of Chemistry
Indian Institute of Science Education and Research
Thiruvananthapuram-695016, India

June 2014

Declaration

I hereby declare that the work reported in this thesis is original and was carried out by me during my tenure as a PhD student at the School of Chemistry, Indian Institute of Science Education and Research Thiruvananthapuram. Such material as has been obtained from other sources has been duly acknowledged in the thesis.

Place : IISER Thiruvananthapuram **Rijo T. C.**
Date : June 2014

Certified that the work incorporated in this thesis "**Light Induced Processes in Near-Orthogonal Bichromophores Separated Through a Single Bond"** submitted by **Rijo T. C.** was carried out by the candidate under my supervision. This thesis has not formed the basis for the award of any degree, of any university or institution.

Place : IISER Thiruvananthapuram **Dr. Mahesh Hariharan**
Date : June 2014 (Thesis supervisor)

To My Late Beloved Mother and Family

Acknowledgements

First and foremost, I would like to thank God Almighty for giving me the courage and patience to complete my research work.

Next, I would like to express my deepest gratitude to my thesis supervisor, Dr. Mahesh Hariharan, for his constant guidance and support and for providing excellent research environment during the five years of my doctoral study. He has been the greatest source of motivation during the difficult times in research and I have acquired immense scientific knowledge under his expert guidance.

I would like to express my sincere thanks to Professor E. D. Jemmis, Former Director, IISER-TVM for providing excellent research facilities to carry out my research work. I would also like to thank Professor V. Ramakrishnan, Director, IISER-TVM for his motivation and support and Professor M. S. Gopinathan, Former Dean, IISER-TVM for his valuable suggestions and inspiration. I would like to express my deep sense of gratitude to Professor K. George Thomas, Dean, IISER-TVM for all the help and extensive support during my doctoral program. I thank my doctoral committee members, Dr. Ramesh Chandra Nath and Dr. Kana M. Sureshan for their advice and suggestions on my research work and dissertation. I sincerely express my gratitude towards Dr. Anil Shaji, IISER-TVM for TDC calculation. I express my sincere thanks to Dr. Suresh Das, Director, NIIST Trivandrum for allowing me to conduct various microscopic and spectroscopic measurements. I also thank Mr. O. Thomas for his valuable support during my doctoral program. I gratefully acknowledge all the faculty members and students of School of Chemistry as well as IISER-TVM for their valuable support and help throughout my life at IISER-TVM. I express my sincere thanks to Mr. Jayaram, Mr. Mohanan, Mr. Kurup, Mr. Hariharan and Mr. Ramesh for their care and support during my life at IISER-TVM.

My heartfelt thanks goes to Mr. Alex for single crystal XRD measurements and helping in various computational calculations as well as formatting various documents related to my thesis. I express my sincere gratitude to Mr. Robert, Mr. Kiran and Mr. Chandran, NIIST Trivandrum for TEM and SEM microscopic imaging. I also thank Mr. Adarsh, Mr. Shiju, Mr. Manoj, Mr. Nibith, Dr. Suneesh, Dr. Ratheesh, Dr. Ramesh, Dr.

Pratheesh, Mr. Aneesh, Mr. Akhil, Mr. Charles and Mr. Aneesh for helping in various spectroscopic and microscopic measurements. I also thank Dr. Sainul Abideen, Mrs. Divya, Mrs. Suja, Mrs. Mini, Mrs. Nimi, Mr. Ajith, Mr. Praveen, Mr. Vijesh, Mr. Shebin, Mr. Shameer, Mr. Sreekumar, Mr. Vivek, Mr. Deepu and all administrative and academic staff members of IISER-TVM for various helps during my PhD program.

I am deeply indebted to all my group members: Shinaj, Sharon, Jimmy, Ajith, Kalivanan, Abbey, Somadrita, Dr. Salini, Vishnu, Athira, Shareefa, Hitesh, Arun, Sumayya, Haritha, Murugan and Ranjith. I also remember the first batch PhD students of IISER-TVM, Gireesh, Manil, Anoop, Atchuth Rao, Vidyasgar, Prtatp Zalake, Priya, Saritha, Subila, Sreerekha, Deepthi, Salini and Vidya for the harmony and support. Thanks to all my colleagues especially Baiju, Reshmi, Jissy, Nijamudheen, Vinayak, Libin, Geethu, Balu, Amol, Soumik, Mohan Rao, Shine K Albert, Jiji, Sabnam, Jyothish, Rohini, Shine A, Sandeep, Shyama, Santhosh, Sankaran, Harris, Joshya, Abyson, Krishnaprasad, Dijo, Renjith, Asish, Vijith, Pola, Damodhar, Noufal, Saleem, Pradeep, Jose, Anu, Asa and Mahroof for the support and care. I remember all 2009 BS-MS batch students especially Sujeesh, Ajay, Ajeesh and Sarang for their support and love. I thank all my friends in Techiespark hostel especially 2011 BS-MS batch boys for their support, love and care. Special thanks to Gireesh who was always with me as a roommate and friend to face all kind of situations.

I express my immense gratitude towards Dr. E. A. Jose, St. Thomas College, Thrissur for the continuous support and care that he has provided me since my M.Sc. days. I also thank all my teachers for their care and support. Thanks to all my M.Sc. colleagues for their support and care in the last five years of my doctoral program.

I am so grateful to my parents for the support and freedom they have given me and for my education. I greatly thank my mother, who passed away last year, for showering her endless support and love on my life. My father has always been a motivation for me throughout my life for being a hard worker. I also remember my elder sisters, elder brother, sister-in-law, brother-in-laws, nephews and all family members for their support, care and love during my lifetime.

Finally, I would like to thank all the people who supported and helped me during my PhD study.

Preface

This thesis is focused on the light induced processes in near-orthogonally arranged bichromophores separated through a single bond. Developing efficient donor-acceptor dyads which shows high fluorescent quantum yield in solution, crystalline as well as self-assembled state is crucial for designing photonic and opto-electronic devices. The energy transfer followed by electron transfer in a self-assembled state can have potential use in the area of artificial photosynthesis. In this regard, we have designed an near-orthogonal energy-transfer dyad based on naphthalenimide, energy donor and perylenimide, energy acceptor units. The present thesis is divided into four chapters.

The first chapter of the thesis is a review of the donor-acceptor systems explored for studying photoinduced energy as well as electron transfer processes. A brief introduction about the various mechanisms of photoinduced energy as well as electron transfer processes will be discussed. It will cover important donor-acceptor dyads used for photoinduced electron and energy transfer processes in single molecule as well as in supramolecular assemblies that are reported in the literature. It also provides the merits of orthogonal donor-acceptor dyads over existing donor-acceptor dyads in photoinduced electron and energy transfer processes.

The second chapter discusses the synthesis and photophysical properties of a near-orthogonal donor-acceptor dyad in which naphthalenimide (energy donor) and perylenimide (energy acceptor) units are connected through a carbon-carbon single bond. The napthalenimide-perylenimide dyad **NP** was synthesized through Stille coupling reaction between the tributyltin derivative of N-hydroxypropyl naphthalenimide and bromoperylenimide. A significant barrier (ca. 100 kJ/mol) to rotation through the interchromophoric carbon-carbon single covalent (1.49 Å) bond between the naphthalenimide and perylenimide units prevents coplanarization of the two units in the dyad **NP** thereby acting as independent chromophores/redox centers. Upon photoexcitation, highly efficient energy transfer is observed from naphthalenimide (energy donor) to perylenimide (energy acceptor) moiety predominantly through Coulombic coupling completely isolating the orbital overlap (Dexter type) interaction between the chromophoric units at such short separation, by virtue of their orthogonal arrangement. Because Förster's ideal-dipole approximation ignores the contribution from significant higher-order Coulombic interactions at such short distances between donor and acceptor moieties, the complete coupling was computed from the transition densities, giving an estimate of the energy-transfer rate from the naphthalenimide donor to the perylenimide acceptor of $k_{\mathrm{ET}} = 2.2 \times 10^{10}\ \mathrm{s}^{-1}$, in agreement with experimental observations. Ultrafast excitation energy (ca. 40 ps, 90%) and electron (<0.5 ps, 10%) transfer from the singlet excited state of naphthalenimide to the perylenimide moiety competes with further delayed processes in the conjugate **NP**. Upon excitation at 345 nm, conjugate **NP** exhibits near-quantitative energy transfer in combination with the solvent polarity dependent (solvatochromic) perylenimide fluorescence resulting in a remarkable Stoke's shift of ca. 175-240 nm.

In the third chapter, the crystal packing and solid state photoluminescence properties of the dyad **NP** in crystalline state in comparison to solution and thin film states will be discussed. Highly efficient photoinduced energy transfer is observed in an orthogonal bichromophore naphthalenimide-perylenimide (**NP**), leading to strong solid-state luminescence ($\Phi = 0.5 \pm 0.04$) in the red region ($\lambda_{\mathrm{em}} = 631$ nm). Steric hindrance imparted by orthogonal naphthalenimide and diisopropyl phenyl units prevents the association of perylenimide moieties, thereby retaining a high quantum yield of fluorescence emission even in the crystalline state. Upon photoexcitation at 340 nm, the intramolecular parallel orientation of the transition dipoles permits efficient Coulombic coupling between naphthalenimide and perylenimide units in combination with weak H-type excitonic interactions between the intermolecular perylenimide units that results in intense red fluorescence in the crystalline state of dyad **NP**. We also tune the photophysical properties of dyad **NP** by successfully attaching different alkyl chain units of various lengths to the **NI** unit.

The fourth chapter discusses the synthesis and vesicular self-assembly formation of a near-orthogonal perylenimide-naphthalenimide bichromophoric array **(*R*/*S*)-NP(OH)$_2$** having a α,β–dihydroxypropyl side-chain which exhibits efficient photoinduced energy transfer followed by electron transfer in the presence of an electron donor, indole. Energy as well as electron transfer processes in self-assembled systems are crucial in the development of artificial light harvesting and solar cell based functional materials. Existing non–covalent donor–acceptor containing self-assembled light harvesting systems lack control on i) stoichiometry, ii) orientation and iii) distance between the constituent donor and acceptor units that can limit the efficiency of excitation energy transfer. In order to overcome these limitations we have utilized near-orthogonal perylenimide-naphthalenimide bichromophoric array **(*R*/*S*)-NP(OH)$_2$** for the present study. This light harvesting donor-acceptor dyad **(*R*/*S*)-NP(OH)$_2$** containing a α,β–dihydroxypropyl side-chain can undergo molecule-bilayer-vesicle-gel-crystal transition. The vesicular nature of the self-assembly is characterized by using various microscopic techniques including atomic force microscopy (AFM), scanning electron microscopy (SEM), transmission electron microscopy (TEM) and fluorescence optical microscopy (OM) imaging. By virtue of steric hindrance offered by orthogonal naphthalenimide and 2,6-diisopropylphenyl substituents, a very weak H-type excitonic interactions between the perylenimide units resulted in high fluorescence quantum yield in the dyad based metastable vesicular gel having a near-quantitative excitation energy transfer from naphthalenimide to perylenimide. Femtosecond transient absorption measurements of the dyad **(*R*/*S*)-NP(OH)$_2$**:indole co-gel exhibit the vesicular scaffold promoted extension of the survival time of charge separated states (~1.4 ns) when compared to ultrafast charge recombination (~6 ps) in dyad **(*R*/*S*)-NP(OH)$_2$**:indole solution.

Contents

List of Figures

List of Tables

List of Schemes

Chapter 1

Introduction

Photoinduced energy transfer (ET) cassettes have important applications in the area of DNA sequencing[1,2], cellular imaging[3], artificial photosynthesis[4-8], photonic devices[9-13] and biomolecular sensing[14-18]. Understanding the various mechanisms underlying excitation energy transfer (EET) processes are very important for designing optoelectronic devices based on energy transfer processes. The Förster[19] and Dexter[20] theory provides mechanistic insights into the basic EET processes. The Förster theory is based on ideal dipole approximation of point charges and it is no longer valid at places where the distance between the donor (D) and acceptor (A) is comparable to the size of the individual chromophore. In such systems approaches based on quantum mechanics provide more accurate descriptions and it can be useful in designing efficient optoelectronic and photonic devices for future applications.

Organic solid-state materials having intense solid state fluorescence exhibit wide applications in the area of optoelectronic devices such as organic light-emitting diodes (OLED)[21], solid-state lasers[22,23], organic light-emitting field effect transisitors[24,25] and organic luminescent sensors[26,27]. Generally most of the organic chromophores having strong luminescence in solution shows very low fluorescence quantum yield in the solid-state due to concentration quenching[28-31]. Especially the red emitting dye molecules including perylenimides with extended aromatic conjugated systems show various types of aggregation properties in the solid state which diminishes the fluorescence emission[32-34]. There are some exception to this behaviour which have been observed in molecules containing spirobifluorene core[35] which are either weakly emissive or non-fluorescent in solution shows enhanced fluorescence in the solid state due to the restricted internal rotation in the solid state. One of the peculiarities of spiro type compounds is the perpendicular arrangement of the two molecular halves leading to a high steric demand of the resulting rigid structure, efficiently suppressing molecular interactions between the π-systems. The donor-acceptor (D-A) dyads which show efficient solid-state luminescence in the crystalline state were less explored in the literature[36].

Photoinduced energy as well as electron transfer processes in self-assembled systems are crucial in the development of functional materials for artificial light harvesting and solar cell applications [37,38]. Existing non–covalent donor–acceptor containing self-assembled light harvesting systems lack control on i) stoichiometry, ii) orientation and iii) distance between the constituent donor and acceptor units that can limit the efficiency of excitation energy transfer. The vesicular nature of the natural light harvesting unit provides efficient energy as well as electron transfer in the photosynthetic unit of purple bacteria[39,40] which motivated us to exploit self-assembled vesicular scaffold for photoinduced energy and electron transfer processes. For this purpose we have chosen a covalently linked near-orthogonal perylenimide-naphthalenimide chromophoric array for the present study, expected to be a potential material in photonic devices. Perylenimides are well known for its excellent light fastness, high chemical stability, high photoluminescence quantum yield, and a wide range of colours that can be tunable by various substituents at the bay position[41].

1.1 Energy Transfer Mechanisms

The photoinduced energy transfer processes take place by two distinct types of electronic interaction between the donor (D) and acceptor (A) units. First one is the electron exchange interaction also known as orbital overlap mechanism and second is the dipole-dipole interaction known as Coulombic or resonance mechanism for energy transfer. Dexter[20] and Förster[19] established the theory of energy transfer based on electron exchange and dipole-dipole interactions respectively. In honour of the developers the theories for energy transfer are known as Dexter and Förster mechanisms in the literature.

1.1.1 Dexter Energy Transfer

The Dexter excitation transfer mechanism is based on electron exchange; this means that it requires an overlap between the wave functions of the donor and acceptor units. Dexter excitation transfer is possible when the donor is in the excited state and the acceptor can have a compatible lowest unoccupied molecular orbital (LUMO) with either equal or lower in energy. In that case the electron from the singly occupied molecular orbital (SOMO) of the donor can be transferred to the LUMO of the acceptor and simultaneously an electron is transferred from the highest occupied molecular orbital (HOMO) of the acceptor to the HOMO of the donor (which must be equal or higher in energy than the HOMO of the donor, Figure 1.1). In this way the net result is the transfer of the excited state from the donor to the acceptor unit.

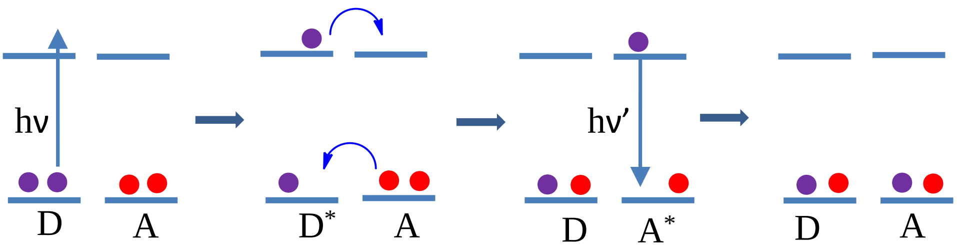

Figure 1.1 *Schematic representation of the Dexter energy transfer mechanism.*

The rate of energy transfer for the Dexter mechanism is dependent primarily on the distance between the donor and acceptor (R_{DA}) and on the overlap between the respective orbitals (Eq.1.1).

$$k_{ET}\ (\text{Dexter}) = KJe^{\left(\frac{-2R_{DA}}{L}\right)} \tag{1.1}$$

where K is a collection of constants related to specific orbital interactions, L is the sum of the Van der Waals radii of the donor and the acceptor and J is the spectral overlap integral (Eq. 1.2).

$$J = \int_0^{\infty} f_D\,(\sigma)\epsilon_A(\sigma)d\sigma \tag{1.2}$$

For the Dexter electron exchange mechanism the spectral overlap integral J (Eq. 1.2) is dependent on the integrated overlap of the donor fluorescence spectrum (f_D) and the acceptor absorption spectrum (ϵ_A), over wavenumbers σ. Both the absorption and emission spectra are normalized to unity (i.e. complete overlap would give J = 1). As a result J does not depend on the magnitude of ϵ_A, and therefore k_{ET} (Dexter) is independent of the oscillator strength of the $D^* \rightarrow D$ and $A \rightarrow A^*$ transitions; in contrast to Förster resonance energy transfer. Both singlet-singlet and triplet-triplet energy transfer can occurs through Dexter mechanism.

1.1.2 Förster Resonance Energy Transfer

Förster resonance energy transfer (FRET)[19], is often referred to as fluorescence resonance energy transfer in the literature even though fluorescence is not actually involved. However, the overlap between the donor fluorescence spectrum and the acceptor absorption spectrum plays an important role in the mechanism of FRET. Overlap between wave functions is not a requirement for FRET and exchange of electrons does not occur as with the Dexter mechanism. The FRET mechanism is based on the resonance between two oscillating dipoles (i.e. the electric fields associated with electrons). When the excited state has an energetically matching oscillating electric field to that of a nearby molecule in its ground state $[\Delta E(D^* \rightarrow D) = \Delta E(A \rightarrow A^*)]$ it is possible for the two dipoles to couple Coulombically and the excited state energy can be transferred from the donor to the acceptor without exchange of electrons, bringing the donor to the ground state and the acceptor to the excited state (Figure1.2).

The Förster mechanism depends largely on three factors, 1) the overlap between the donor fluorescence spectrum and the acceptor absorption spectrum (J), 2) the orientation between the dipoles of the chromophores (κ), better orientation gives better coupling and therefore better k_{ET} and 3) inverse sixth power of the

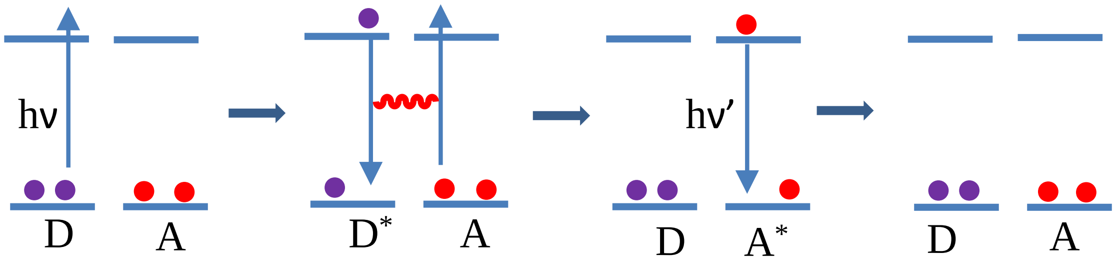

Figure 1.2 *Schematic representation of the Förster resonance energy transfer mechanism.*

distance between the donor and acceptor units ($\frac{1}{R_{DA}^6}$), where R_{DA} is the distance between donor and acceptor (Eq. 1.3).

$$k_{ET}(\text{Förster}) = \frac{\kappa^2\ J\phi_D\ 8.8 \times 10^{-28}\ mol}{n^4\tau_D\ R_{DA}^6} \qquad (1.3)$$

Where κ^2 being the orientation factor, n is the refractive index of the medium, ϕ_D is the fluorescence quantum yield of the donor in the absence of acceptor and τ_D is the radiative lifetime of the donor in the absence of acceptor. In the case of FRET the overlap integral J is the overlap integral between the donor emission spectrum and acceptor absorption spectrum (Figure 1.3). The orientation factor κ^2 between the donor and acceptor dipole moments is given by (Eq. 1.4, 1.5)

$$\kappa^2 = (cos\theta_T - 3cos\theta_D \cos\theta_A)^2 \qquad (1.4)$$

$$\kappa^2 = (\sin\theta_D \sin\theta_A cos\phi - 2cos\theta_D \cos\theta_A)^2 \qquad (1.5)$$

where θ_T being the angle between the emission transition dipole of the donor and the absorption transition dipole of the acceptor, θ_D and θ_A being the angles between these dipoles and the vector joining the donor-acceptor pair and ϕ being the angle between the planes (Figure 1.4). Depending on the relative orientation of donor and acceptor transition dipoles the values for κ^2 range from zero to four. Accordingly, for collinear orientation of the transition dipoles κ^2 equals to 4, and for parallel orientation, κ^2 equals to 1, whereas for a perpendicular arrangement of the transition dipoles κ^2 vanishes to zero (Figure 1.4). For a randomized arrangement of donors and acceptors due to rotational diffusion prior to energy transfer, κ^2 is generally assumed to be 2/3, given that a variety of static donor-acceptor orientations are present.

1.1.2 Förster Resonance Energy Transfer

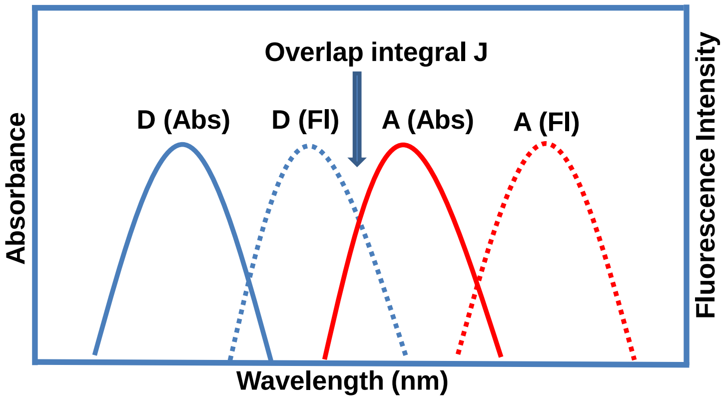

Figure 1.3 Schematic representation of the overlap integral J.

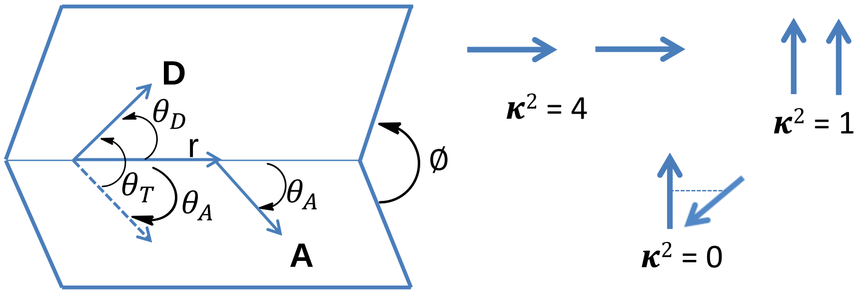

Figure 1.4 *Dependence of the orientation factor* κ^2 *on the directions of the emission transition dipole of the donor and the absorption transition dipole of the acceptor.*

The distance between the donor and the acceptor can be determined by the following equation (Eq. 1.6)

$$E = \frac{1}{\left[1 + \left(\frac{R_{DA}}{R_0}\right)^6\right]} \qquad (1.6)$$

where E is the energy transfer efficiency and R_0 is the Förster radius, which is the distance at which energy transfer is 50% efficient and which is a property of an individual donor and acceptor pair. The energy transfer efficiency can be determined by either measuring the fluorescence lifetime of the donor in the presence (τ) and absence of acceptor (τ') or the donor fluorescence intensity in the presence (F') and absence of acceptor (F), (Eq. 1.7).

$$E = 1 - \frac{\tau'}{\tau} = 1 - \frac{F'}{F} \qquad (1.7)$$

If the Förster radius is known then the distance between the chromophores can be determined. The Förster radius can be determined using the following equation (Eq. 1.8)

$$R_0 = 8.8 \times 10^{-28} \phi_D . \kappa^2 . J \tag{1.8}$$

where ϕ_D is the donor fluorescence quantum yield.

Förster theory is based on the ideal dipole approximation which states that the two dipoles are considered as point charges and it is valid when the separation of the two charges is larger than the size of individual donor-acceptor units. According to Förster theory the Coulombic coupling ($V^{d\text{-}d}$) between the donor and acceptor transition dipoles is obtained by dipole-dipole interaction as

$$V^{d-d} = \frac{1}{4\pi\epsilon_0} \kappa \frac{|\mu_D||\mu_A|}{R^3} \tag{1.9}$$

where $|\mu_D|$ and $|\mu_A|$ are the transition dipoles of the donor and acceptor units respectively, κ is the orientation factor and R is the centre-to-centre separation between the dipoles. But at shorter distance (<20 Å) the ideal dipole approximation breaks and the two dipoles will no longer act as a point charges. In such cases the full Columbic coupling will not follow the R^{-3} relationship and it can be calculated either by energy-gap-based scheme or by direct coupling method[42]. The direct coupling methods are using multipolar expression (includes dipole-dipole, dipole-quadrupole, quadrupole-quadrupole, dipole-octopole, and octopole–octopole coupling contributions to the exact coupling, V^{Coul})[43] or transition density cube method (TDC)[44] for calculating the coupling constant. In the present thesis we have used TDC method to calculate the Coulombic coupling between the donor–acceptor units[44-49]. In TDC method the quantum mechanical wavefunctions of initial and final states of electronic transitions are used to calculate the coupling between the donor-acceptor units. The inverse product of these two wavefunctions or the off diagonal elements of the quantum density matrix connecting the two electronic states of a molecule gives the transition density (Eq. 1.10).

$$M_k\ (\vec{r}) = \int \psi_{kg}\ (\vec{r})\psi^*_{ke}(\vec{r})ds \tag{1.10}$$

where g and e describe the ground and excited state of the molecule k. The Coulombic coupling is obtained by the Eq. 1.11

$$V_{DA}^{Coul} = \frac{1}{4\pi\epsilon_0}\int \frac{M_D(\vec{r})M_A(\vec{r})}{|\ \vec{r_i}-\vec{r_j}\ |}\,\mathrm{d}\vec{r_i}\ \mathrm{d}\vec{r_j} \tag{1.11}$$

where $M_D(\vec{r})$ and $M_A(\vec{r})$ are the donor and acceptor transition density respectively. The short range coupling can also be occurring due to orbital overlap effects and exchange interactions other than columbic coupling. This can be calculated by using fragment charge difference (FCD)[50] scheme by using an additional operator to describe the extent of excitation localisation.

1.2 Förster Resonance Energy Transfer in Orthogonally Arranged Chromophores

The donor-acceptor dyads (**D-A**) in which the donor and acceptor units are connected by a flexible linker is associated with lower efficiency in energy transfer[51]. This can be attributed to the larger spatial separation and various dipolar orientations of individual donor-acceptor units. Interestingly donor and acceptor units connected through a rigid spacer with steric blocks to prevent the conjugation become increasingly important for various applications like cellular imaging[52,53], biomolecular sensing and photonic devices[2,16,54-58]. The rigid **D-A** pairs also shows better energy transfer efficiency as well as faster rate of energy transfer.

1.2.1 Photoinduced Energy Transfer in Single Molecular Donor-Acceptor Dyads

According to Förster resonance energy transfer theory the energy transfer between the donor-acceptor pairs with perpendicular transition dipoles are forbidden.

Contrary to this, Langhals and co-workers clearly demonstrated that efficient Förster type energy transfer is possible in the case of benzoperylene hexacarboxylic trisimide as the donor unit and perylene bisimide as the acceptor unit which are connected through a 2,3,5,6-tetramethyl phenyl spacer with perpendicular dipole arrangements (Figure 1.5)[59,60].

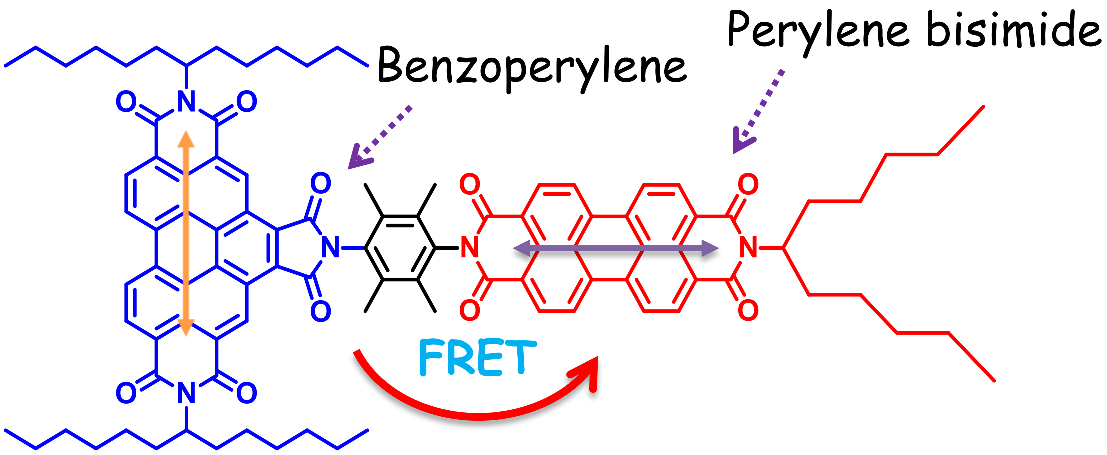

Figure 1.5 *Perylene bisimide dyad with orthogonal transition dipole moments between the energy donor (benzoperylene) and the energy acceptor (perylene bisimide). Reprinted with permission from ref. [59]. Copyright 2010, American Chemical Society.*

Even though the two dipoles are orthogonal to each other, the dyad shows quantitative energy transfer efficiency with a rate of energy transfer, 1.06 x 10^{-11} s^{-1}. The observed rate of energy transfer is not in good agreement with the Förster theory. Recent literature shows that ideal dipole approximation fails to predict the rate of energy transfer when the distance between the donor-acceptor units compared to the size of the individual chromophoric units. In such cases transition density cube (TDC) method[44] gives actual Coulombic coupling which retains all terms in multipole expansion. However in this system TDC method shows negligible Coulombic coupling between the donor-acceptor units. Taking all these in consideration, authors claim that the efficient energy transfer in this system could be due to the involvement of low-wavenumber ground state **–C-N** bond bending vibrations which break the orthogonal arrangement of the transition dipole moments. This work clearly shows that the fluctuations in the molecular geometry is a decisive factor that has to receive more attention in future physical and chemical applications involving energy transfer processes.

1.2.2 Photoinduced Energy Transfer in Supramolecular Assembly

Solar light harvesting in natural photosynthetic unit is achieved by unique arrangement of the various chlorophyll pigment molecules in the protein matrix[45,61,62]. Inspired by natural photosynthesis various energy transfer systems in self-assembled media are reported in the literature[63-66]. Meijer *et al.* reported energy transfer in the self-assembled vesicles of oligo(p-phenylenevinylene) (**OPV**) derivatives in which **OPV5** act as an energy donor and **CN-OPV5** act as an energy acceptor (Figure 1.6)[67]. Each of the donor and acceptor units form vesicles in THF/water mixture (Figure 1.6 B) and it still retains the vesicle nature even after mixing both the donor and the acceptor units in the same solvent mixture, confirmed by confocal microscopic imaging (Figure 1.6 C, D).

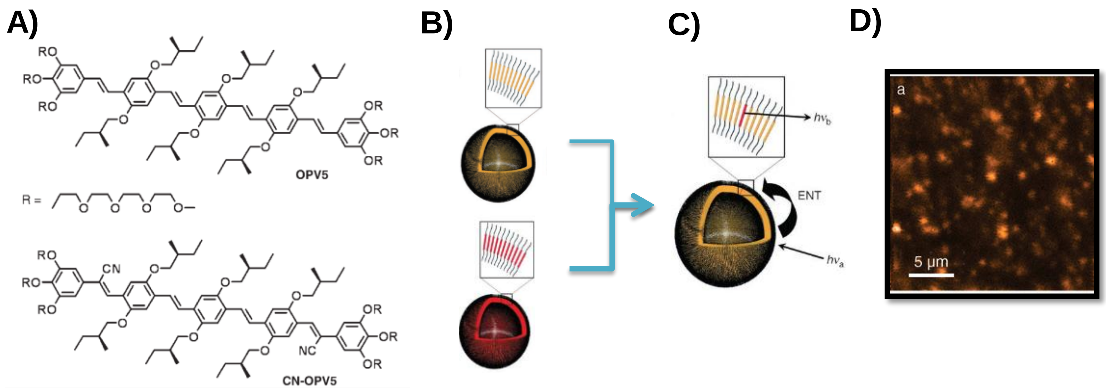

Figure 1.6 A) *Chemical Structures of* ***OPV5*** *and* ***CN-OPV5****; Schematic representation of the formation of B) individual vesicles formed from* ***OPV5*** *and* ***CN-OPV5****; C) vesicles formed from mixture of* ***OPV5*** *and* ***CN-OPV5*** *and D) confocal microscopic image of vesicles formed from mixture of chromophores* ***OPV5*** *and* ***CN-OPV5*** *in THF/water mixture.* Reprinted with permission from ref. *[67]. Copyright 2006, Wiley-VCH.*

Ajayaghosh *et al.* reported photoinduced energy transfer from oligo(p-phenylenevinylene) (**OPV**) to rhodamine B in the xerogel phase with an efficiency of 90% in comparison to 60% efficiency in the solution state[68] indicating the role of hydrogen-bonding and π-stacking in OPV self-assembly in facilitating energy transfer and light harvesting processes. The same group reported efficient energy transfer from **OPV** based self-assembled gel state to acceptor **PYPV** with extremely low concentration (2M%) (Figure 1.7)[69]. **OPV1** forms a strong gel in cyclohexane solvent while **OPV2** forms a weak gel and **OPV3** do not form the gel at similar conditions. This was one of the first example which demonstrated the use of semiconducting molecular wire as an energy trap in the design of a light-harvesting gel. Energy transfer occurs exclusively from the self-assembled donor (**OPV**) structure to the molecular wires as a result of fast and efficient exciton migration (Figure 1.8). The serious drawbacks of non-covalent donor-acceptor systems in energy transfer dyads are the inability to control the distance and orientation of the two moieties in the self- assembled media.

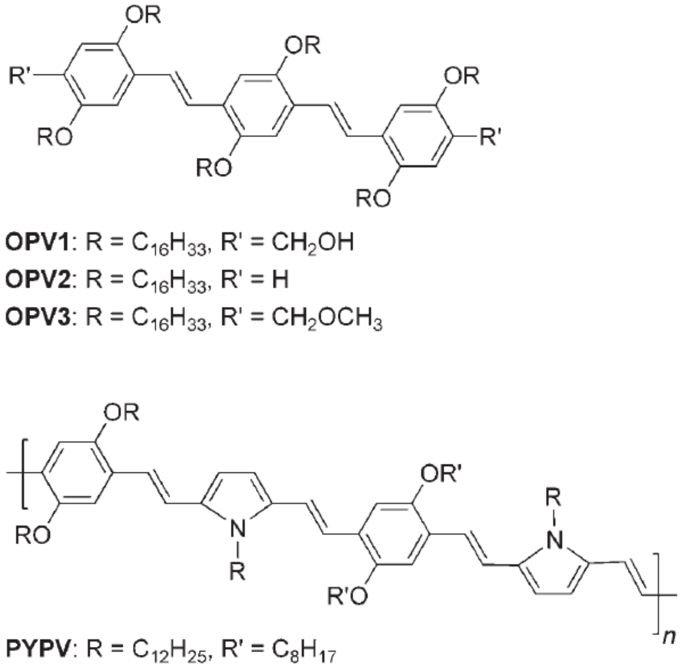

Figure 1.7 *Molecular structures of the **OPV** donors (**OPV1–3**) and the **PYPV** acceptor. Reprinted with permission from ref. [69]. Copyright 2003, Wiley-VCH.*

1.2.2 Photoinduced Energy Transfer in Supramolecular Assembly

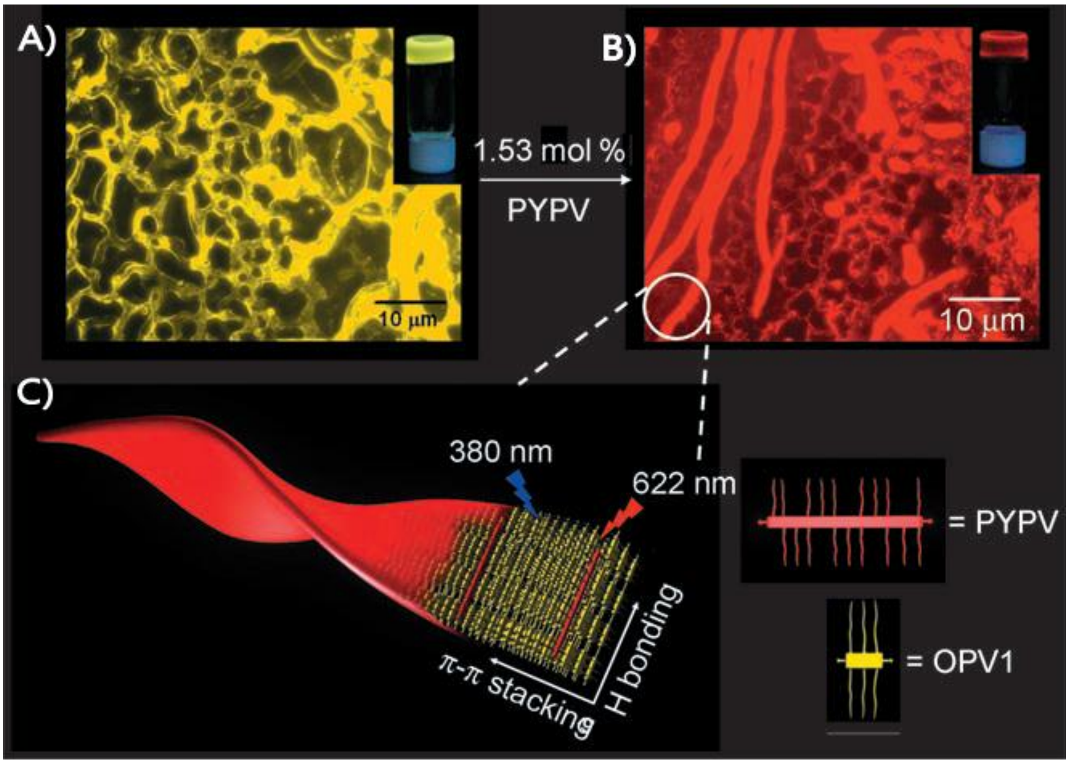

Figure 1.8 *Fluorescence microscopic images of the drop-casted* ***OPV1****-cyclohexane gel (1.12 mm); A) in the absence and B) in the presence of* ***PYPV*** *(1.53 mol%), the insets show photographs of the gels under the respective conditions when illuminated at 365 nm; C) A schematic representation of a* ***PYPV****-encapsulated* ***OPV1*** *tape. Reprinted with permission from ref. [69]. Copyright 2003, Wiley-VCH.*

Würthner *et al.* reported self-assembled covalently linked donor-acceptor dyad containing naphthalene bisimide (**NBI**) as the energy donor and zinc chlorin (**ZnChl**) as the energy acceptor (Figure 1.9)[65]. The **ZnChl-NBI** dyad self-assembles into rod like structure (Figure 1.10) in cyclohexane/tetrachlorethane (1%) exhibiting efficient energy transfer occuring from peripheral blue naphthalene bisimide (**NBI**) dyes to the core **ZnChl** rod. The peculiar feature of these aggregates are the **ZnChl** units form the ordered stacks of rod like structure and the **NBI** units hang around the periphery without forming the aggregates. This will allow efficient energy transfer from **NBI to ZnChl** and also shows increased light harvesting ability in the aggregate structure compared to monomeric state. However in this system also different orientation of donor-acceptor moieties are possible due to the flexibility of

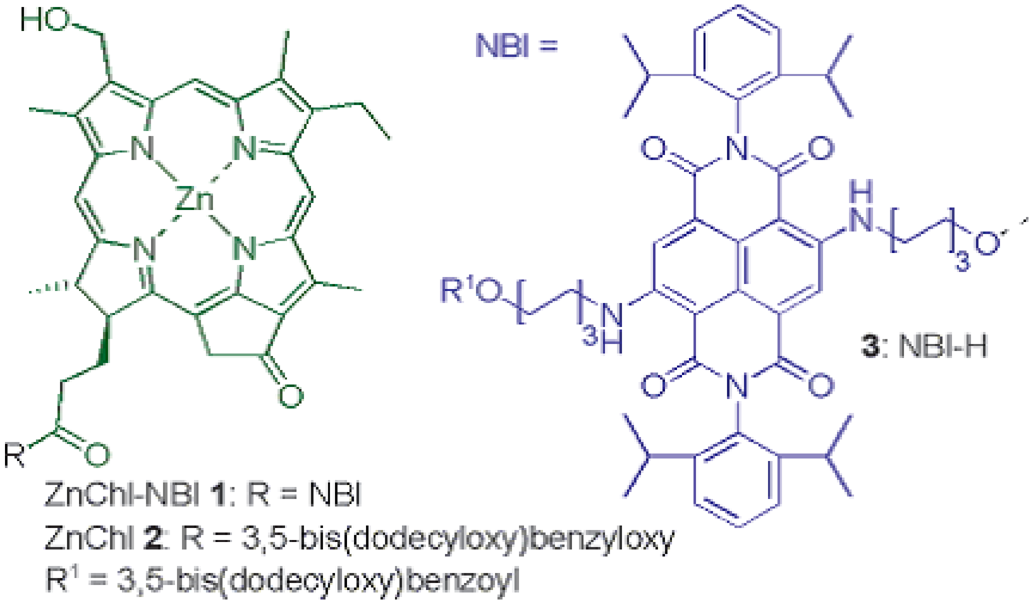

Figure 1.9 *Chemical Structures of* ***ZnChl-NBI 1*** *and isolated chromophores* ***2*** *and* ***3****. Reprinted with permission from ref. [65]. Copyright 2006, American Chemical Society.*

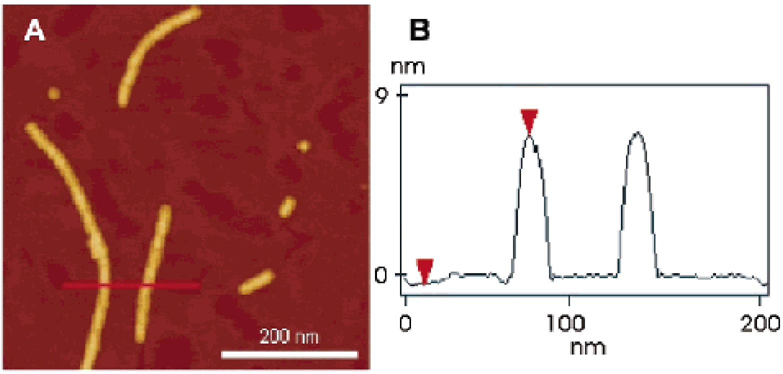

Figure 1.10 *A) Tapping mode AFM image of a* ***ZnChl-NBI 1*** *sample, which was prepared by spin-coating a solution of* ***1*** *in cyclohexane/THF (1%) onto highly ordered pyrolytic graphite (HOPG) and measured under ambient conditions. B) Profile of the red line in A); the vertical distance between the red triangles provides the height of the rod aggregate. Reprinted with permission from ref. [65]. Copyright 2006, American Chemical Society.*

the linker which connects the donor and acceptor moieties. In comparison to the conventional energy transfer dyads, orthogonal donor-acceptor dyads possess control on orientation and the distance between donor and the acceptor moieties which will be beneficial in designing efficient self-assembled energy transfer cassettes.

1.3 Photoinduced Electron Transfer

The photoinduced electron transfer process plays vital role in natural[70] and artificial photosynthesis[4,5,71-74], bio-molecular sensing[75] and photo-voltaic devices[10,76-78]. Electron transfer processes can operate through two possible mechanisms namely oxidative and reductive electron transfer both of which require a compatible acceptor in close proximity to the donor moiety. In oxidative electron transfer an electron is transferred from the donor excited state (LUMO) to the empty, lower energetic LUMO of the nearby acceptor unit creating a charge separated state with a positively charged donor and negatively charged acceptor (Figure 1.11). In the reductive electron transfer HOMO of the acceptor in the excited state abstract an electron from the HOMO of the donor thereby creating similar charge separated state as in the case of oxidative electron transfer. Both the electron transfer mechanisms can be followed by back electron transfer, after which both donor and acceptor will be returned to the ground state. The high energy charge separated state lead to various types of photochemistry, which can be useful for various photochemical reactions and also the long-lived charge separated intermediates are useful for n- and p-type based dye-sensitized semiconducting solar cells in which the reduced rate of back electron transfer is desired. The Rhem-Weller analysis[79,80] provides an estimate of the free energy of electron transfer by the following equation (Eq. 1.12)

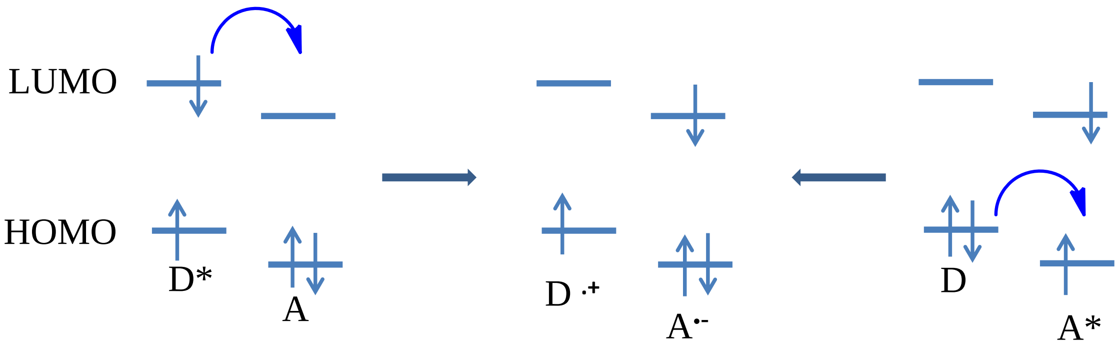

Figure 1.11 *Schematic depiction of oxidative (left) and reductive (right) electron transfer.*

$$\Delta G_{et} = E_{1/2}^{ox}(D) - E_{1/2}^{red}(A) - E_{(00)}(A) + \Delta E_{Coulombic} \quad (1.12)$$

where $E_{1/2}^{ox}(D)$ and $E_{1/2}^{red}(A)$ are the half-wave oxidation and reduction potential of the donor and acceptor respectively, $E_{(00)}(A)$ is the excited state energy of singlet or triplet state involved and $\Delta E_{Coulombic}$ is the Coulombic energy of the separated charges in the solvent in which the electron transfer reaction is carried out. The quantitative picture of electron transfer kinetics can be obtained by Marcus theory which is not studied in the current thesis.

Fluorescence Quenching by Electron Transfer Reactions

Photoinduced electron transfer may lead to fluorescence quenching of the sample. There are two types of quenching mechanisms by which electron transfer can occur namely which are collisional or dynamic quenching and static quenching[29,81]. Both static and dynamic quenching need molecular contact between the fluorophore and the quencher. In collisional quenching the quencher will diffuse to the fluorophore in the lifetime of the excited state. After molecular contact the fluorophore return to the ground state without the emission of light. In static quenching a nonfluorescent encounter complex is formed between the fluorophore and the quencher. Various substances can act as quenchers which include molecular oxygen, different amines, halogenated compounds, metallic ions, indole, carbazole etc.[29].

Collisional or Dynamic Quenching

The collisional quenching can be clearly described by Stern-Volmer equation (Eq. 1.13),

$$\frac{F_0}{F} = 1 - k_q \tau_0 [Q] = 1 - K_D [Q] \quad (1.13)$$

where F_0 and F are the fluorescence intensities in the absence and presence of quencher; k_q is the bimolecular quenching constant; τ_0 is the lifetime of the fluorophore in the absence of quencher, $[Q]$ is concentration of the quencher and K_D is the Stern–Volmer[82] quenching constant that can be expressed as $K_D = k_q\tau_0$. On plotting F_0/F versus $[Q]$, a straight line with intercept on the y-axis and a slope equals to K_D is obtained. The dynamic quenching process can also depopulate the excited state, the Stern-Volmer equation could be represented as (Eq. 1.14)

$$\frac{\tau_0}{\tau} = 1 - k_q\tau_0[Q] \; = 1 - K_D[Q] \tag{1.14}$$

Hence comparing Eq. 1.13 and 1.14 we got an expression as (Eq. 1.15)

$$\frac{F_0}{F} = \frac{\tau_0}{\tau} \tag{1.15}$$

One of the basic criteria for dynamic quenching is one should get the same slope for fluorescence and time-resolved based Stern-Volmer plots (Figure 1.12). Also, in the case of dynamic quenching process the high temperature produce faster diffusion of charged intermediates which results in, an increase in the rate of bimolecular quenching. The diffusion controlled quenching frequently results k_q value of $1 \times 10^{10}\ \mathrm{M^{-1}s^{-1}}$. A smaller value of k_q can result from steric shielding of the fluorophore or a low quenching efficiency and higher value may indicates some type of binding interaction[29].

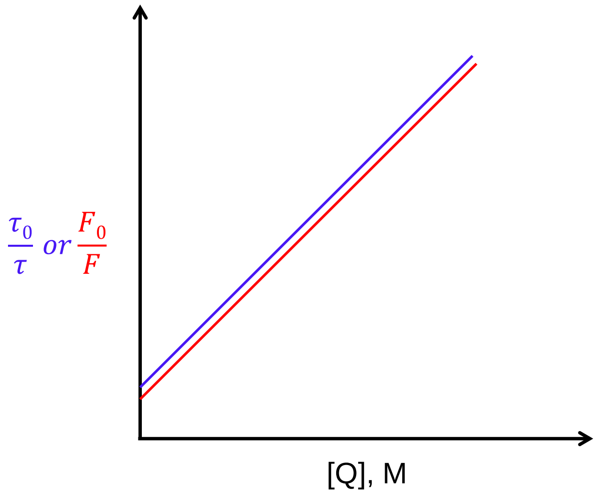

Figure 1.12 *Stern–Volmer plot for time-resolved (blue) and steady-state (red) dynamic fluorescence quenching process.*

Static Quenching

In static quenching a non-fluorescent ground state complex is formed between the quencher and fluorophore[83]. After absorbing light, this complex returns to the ground state without emitting light energy. The Stern- Volmer constant can be easily derived by considering the association constant for the complex formation as (Eq. 1.16)

$$\frac{F_0}{F} = 1 + K_S[Q] \tag{1.16}$$

where K_S is the association constant and similar to dynamic quenching it also shows linear relationship of F_0/F versus $[Q]$ (Figure 1.13). In static quenching there will not be any change in fluorescence lifetime since the complexed fluorophores are nonfluorescent and the lifetime of uncomplexed fluorophore will remain the same. Hence for static quenching $\tau_0/\tau = 1$ instead for dynamic quenching $\tau_0/\tau = F_0/F$. The increase temperature results dissociation of weakly bound complexes and reduce the rate of static quenching process.

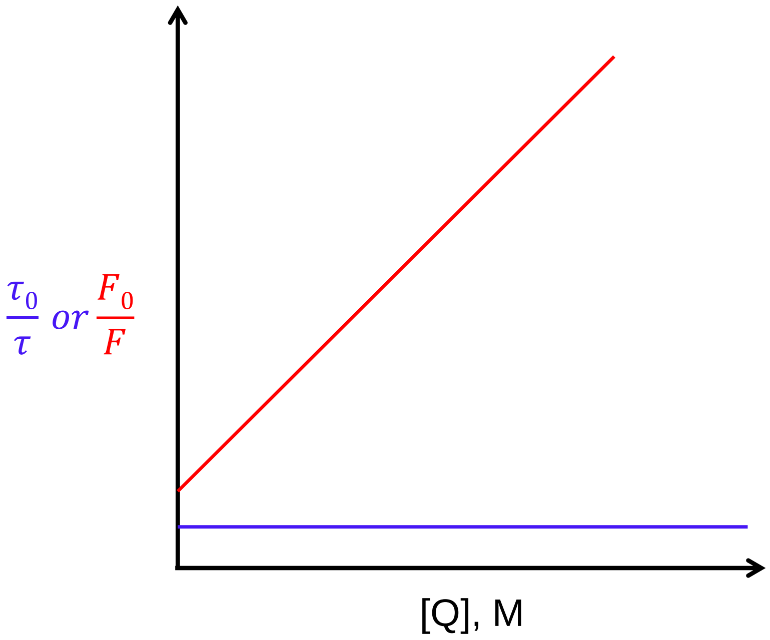

Figure 1.13 *Stern–Volmer plot for time-resolved (blue) and steady-state (red) static fluorescence quenching process.*

1.3.1 Photoinduced Electron Transfer in Single Molecular Donor-Acceptor Dyads

The intermolecular photoinduced electron transfer (PET) reactions are greatly supressed due to fast charge recombination by the backward electron transfer (BET) between the charged intermediates[71,84]. Also the intermolecular electron transfer has no control over the distance and orientation between the donor and acceptor molecules. To overcome this problem donor and acceptor moieties are covalently linked by a flexible or rigid linker (Scheme 1.1)[85]. The porphyrin (donor) and quinone (acceptor) is one of the most studied covalently linked systems for photo-induced electron transfer processes because of its resemblance with natural light harvesting assembly (Figure 1.14)[71].

$$\begin{aligned} \mathrm{D-A} &\xrightarrow{h\nu} {}^{1}\mathrm{D^{*}-A} \\ {}^{1}\mathrm{D^{*}-A} &\xrightarrow{k_{ET}} \mathrm{D^{\cdot+}-A^{\cdot-}} \\ \mathrm{D^{\cdot+}-A^{\cdot-}} &\xrightarrow{k_{BET}} \mathrm{D-A} \end{aligned}$$

Scheme 1.1 *Shows the forward and backward electron transfer processes in a donor-acceptor dyad upon photoexcitation.*

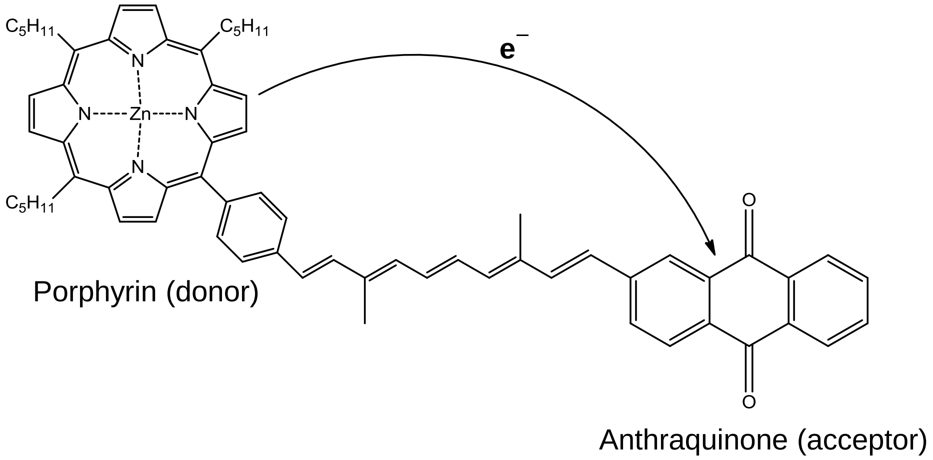

Figure 1.14 *Structure of covalently linked porphyrin-anthraquinone donor-acceptor pair. Reprinted with permission from ref. [71]. Copyright 1997, Royal Society of Chemistry.*

1.3.1 Photoinduced Electron Transfer in Single Molecular Donor-Acceptor Dyads

Fukuzumi *et al.* reported longer lifetime (2 h at 203 K) for charge separated intermediate upon photoexcitation in an orthogonal dyad consisting of 9-mesityl-10-methylacridinium ion (Acr^+-Mes) in which mesityl group act as electron donor and methylacridinium group act as an electron acceptor[86]. The X-ray crystal structure clearly indictes the perpendicular arrangement of donor-acceptor units in the dyad (Figure 1.15A). The HOMO and LUMO orbitals of Acr^+Mes calculated by DFT method with Gaussian 98 (B3LYP/6-31G* basis set) were found to be localized on individual mesitylene and acridinium units, respectively (Figure 1.15B, C).

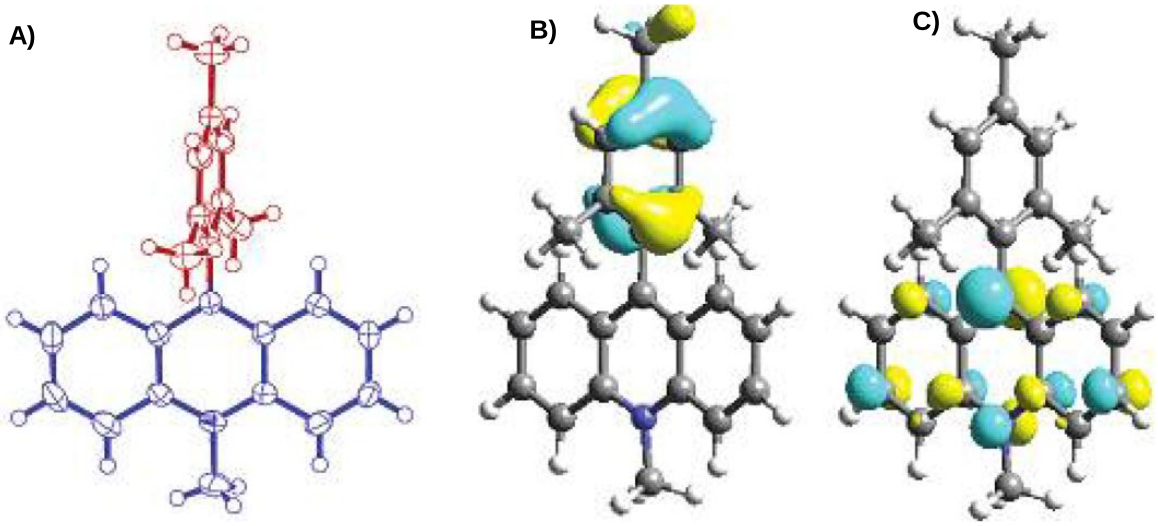

Figure 1.15 *A) Crystal structure of Acr^+-Mes; B) HOMO and C) LUMO orbitals of Acr^+-Mes calculated by a DFT method with Gaussian 98 (B3LYP/6-31G* basis set). Reprinted with permission from ref. [86]. Copyright 2004, American Chemical Society.*

The natural photosynthetic reaction center exploits sequential multistep electron transfer from the excited chromophore to the terminal electron acceptor mediated by multiple donor-acceptor units, which are well-organized in a protein matrix in order to attain a longer lifetime for the final charge-separated (CS) state. Learning from the natural photosynthesis, various systems were developed by covalently linking multiple donor-acceptor units for maximising the charge separation efficiency as well as lifetime[84,87]. Wasielewski *et al.* reported efficient photoinduced electron transfer in donor-acceptor-acceptor triad consisiting 9-(N-pyrrolidinyl)- and 9-(N-piperidinyl)perylene-3,4-dicarboximides, 5PMI and 6PMI respectively as two different donors and pyromellitimide as the primary acceptors and naphthalene monoimide and naphthalene diimide as two different secondary acceptors respectively (PMI-PI and PMI-PI-NI, Figure 1.16)[8]. One of the important facts about this system is that the donor PMI moiety shows 70% charge transfer character in the singlet excited state allowing further charge shift reactions to produce the charged intermediates. The authors found that depending on the nature of polarity of the solvent the triad shows different mechanisms of energy transfer as changing from sequential electron transfer in tetrahydrofuran (THF) to single step superexchange mechanism in toluene which produce final charged intermediates as $\mathrm{PMI}^{\cdot+} - \mathrm{PI} - \mathrm{NI}^{\cdot-}$. But in the sequential electron transfer initially $\mathrm{PMI}^{\cdot+} - \mathrm{PI}^{\cdot-} - \mathrm{NI}$ is formed which undergo charge shift reaction to produce the final charged intermediate.

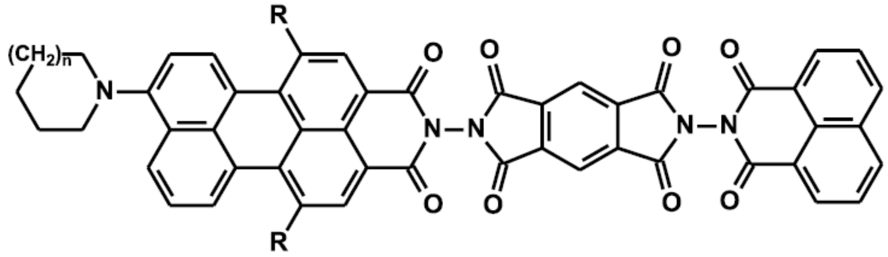

5PMI-PI (n=0), 6PMI-PI (n=1)

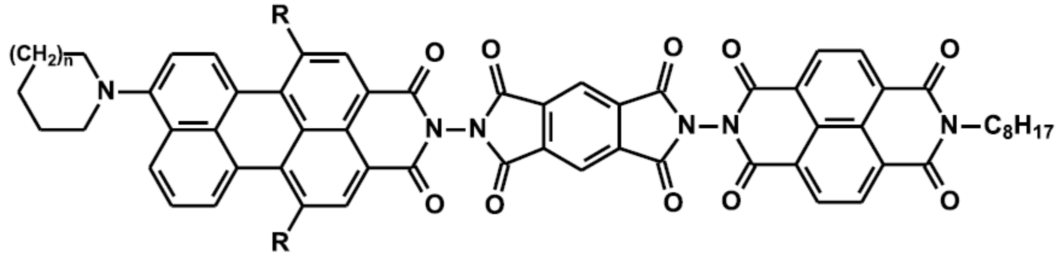

5PMI-PI-NI (n=0), 6PMI-PI-NI (n=1)

Figure 1.16 *Structure of covalently linked perylenimide-pyromellitimide-napthalenimide triad. Reprinted with permission from ref. [8]. Copyright 2009, American Chemical Society.*

1.3.2 Photoinduced Electron Transfer in Self-Assembled State

Self-assembled donor-acceptor molecules play important role in photoinduced electron transfer processes as evident from natural photosynthesis. The self-assembled systems use non-covalent interactions like hydrogen bonding[88], metal–ligand coordinate bond[89,90], aromatic π-stacking[37] and hydrophobic interactions[91] that will arrange the donor-acceptor moieties in well-defined three dimensional arrays for facilitating efficient photoinduced electron transfer processes. Meijer *et al.* reported photoinduced electron transfer in hydrogen bonded self-assembly of oligo(*p*-phenylenevinylene) (**OPV**) and perylene bisimide (**PBI**) which forms chiral fibers in cyclohexane medium (Figure 1.17)[92]. Femtosecond transient absorption measurements indicate the formation of **OPV** radical cation upon photoexcitaion of **OPV** at 450 nm in the self-assembled fibres which confirms the photoinduced electron transfer occuring from **OPV** to **PBI.**

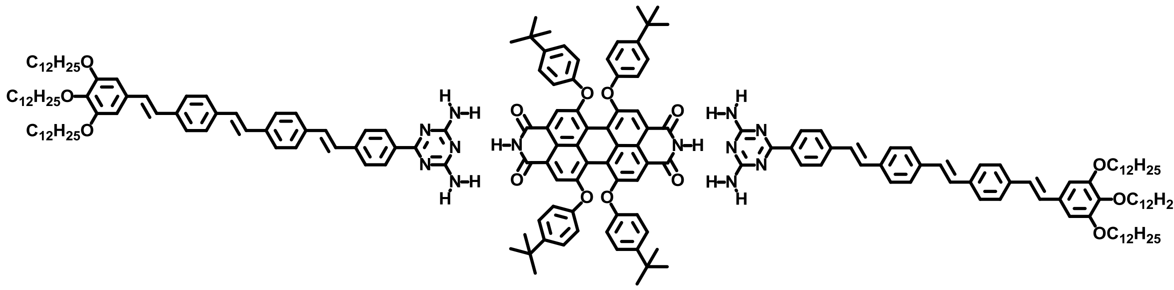

OPV **Perylenen bisimide (PBI)** **OPV**

Figure 1.17 Shows the 2 : 1 assembly of **OPV** and **PBI.** *Reprinted with permission from ref. [92]. Copyright 2002, American Chemical Society.*

Recently Wasielewski and co-workers reported the synthesis, self-assembled properties, and ultrafast electron transfer dynamics in perylene-3,4-dicarboximide (**PMI**) covalently linked to an N,N′-bis(3,4,5-tridodecyloxyphenyl)melamine (elelctron donor, **D**) via a biphenyl spacer (**PMI-Ph$_2$-D**). Synchrotron-based small- and wide-angle X-ray scattering (SAXS/WAXS) measurements in methylcyclohexane solution concluded that **PMI-Ph$_2$-D** forms self-assembled π−π stacked hydrogen-bonded foldamers consisting of two or three hexameric rings or helices (Figure 1.18)[93]. Femtosecond transient absorption spectroscopic measurements revealed that photoinduced charge separation within these nanostructures occurs by an exclusive pathway evolved in the self-assembly, whereas electron transfer does not occur in the **PMI-Ph$_2$-D** monomers in tetrahydrofuran solution. Upon photoexcitation at 532 nm, the hydrogen bonded self-assembly exhibits singlet excited state absorption of **PMI** at 690 nm immediately followed by the formation of $\pi-\pi$ stacked radical anion of **PMI** at 630 nm. Singular value decomposition (SVD) of the three-dimensional ΔA versus time and wavelength data set followed by global fitting yields three principal components with a charge separation lifetime, τ_{CS} = 3.4 ns and two charge recombination times of τ_{CR1} = 25 $\mp$ 2 ps (60 %) and τ_{CR2} = 260 $\mp$ 30 ps (40 %) (Figure 1.19).

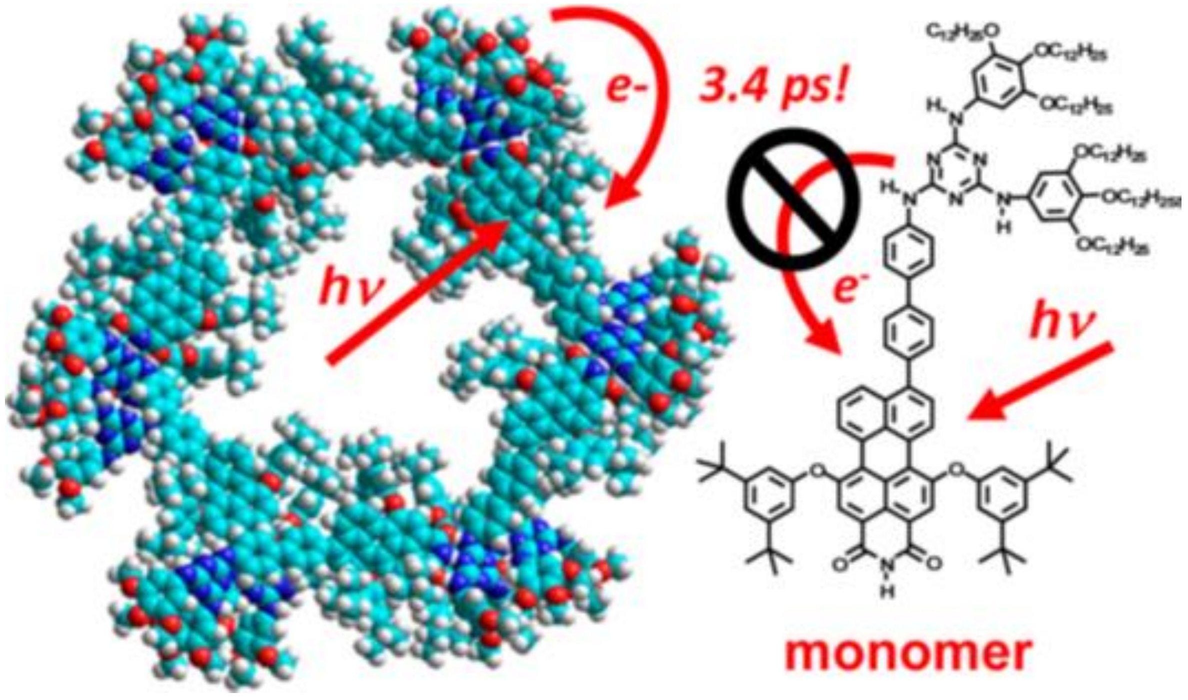

Figure 1.18 *Shows that intramolecular electron transfer is not happening in the monomeric (**PMI-Ph$_2$-D**) state (right) and intermolecular electron transfer is occurring in the hydrogen -bonded assembly (left). Reprinted with permission from ref. [93]. Copyright 2012, American Chemical Society.*

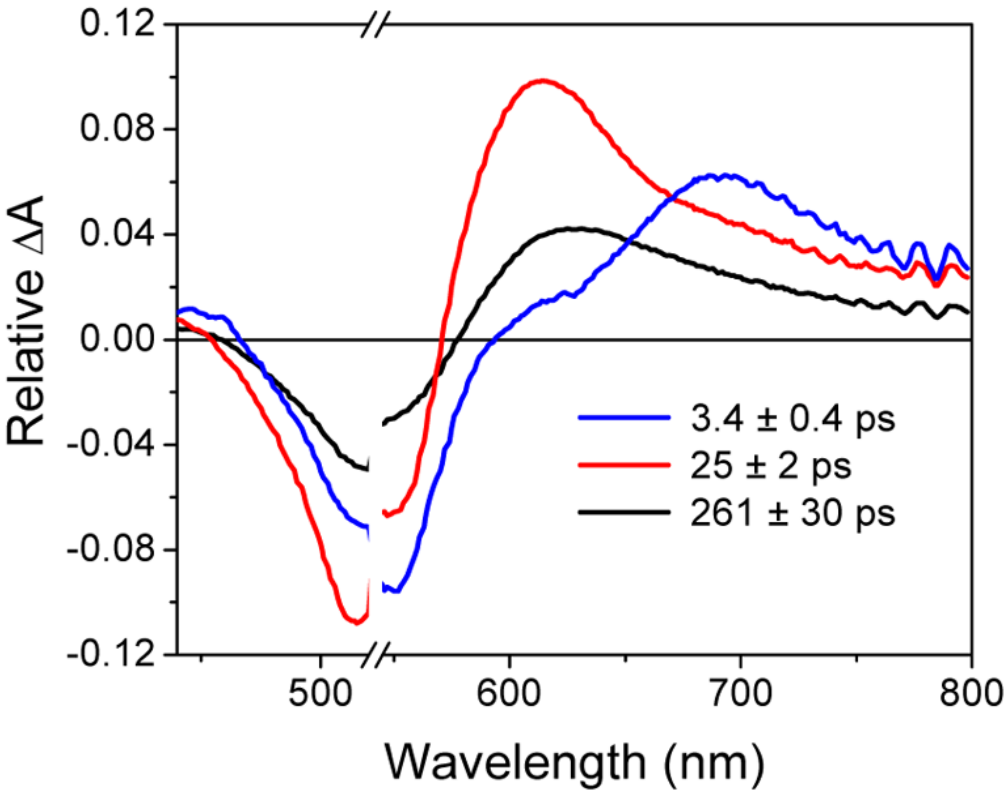

Figure 1.19 *Principal components of the femtosecond transient spectra obtained by SVD analysis. Scattered laser light at 520‒540 nm is removed from the spectra. Reprinted with permission from ref. [93]. Copyright 2012, American Chemical Society.*

Previously the same group reported efficient photoinduced electron transfer in self-assembled π-stacked helical hexameric triad consisting of aminopyrene primary donor (**APy**) and p-diaminobenzene secondary donor (**DAB**) attached to a both imide nitrogen atoms of a perylene-3,4,9,10-bis(dicarboximide) (**PDI**) electron acceptor (**DAB-APy-PDI-APy-DAB**, Figure 1.20)[8]. The small and wide angle X-ray diffraction studies and the time-resolved electron paramagnetic resonance (TREPR) spectra showed rapid formation of $\boldsymbol{DAB}^{\cdot+} - \boldsymbol{PDI}^{\cdot-}$ radical ion pairs with an average distance of 31 Å between the two radical ions, which is much larger in the assembly than in their monomeric building blocks (23 Å). This work emphasises the importance of π-π stacking to facilitate rapid charge separation to compete with charge recombination in self-assembled state which will have potential applications in the area of artificial photosynthesis and organic photovoltaics.

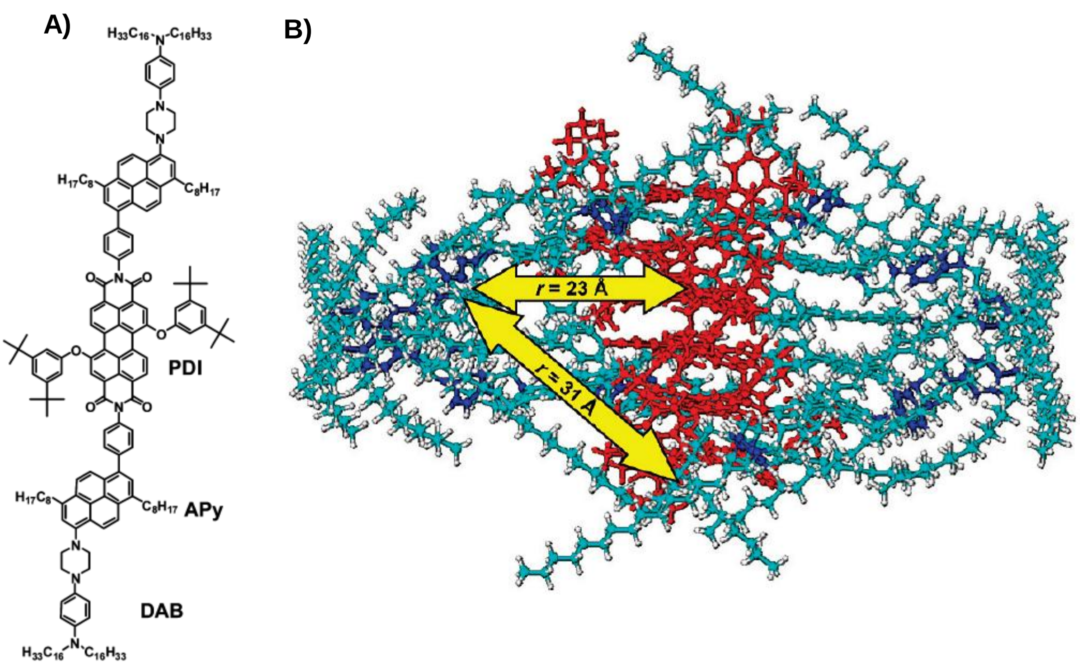

Figure 1.20 A) *Structure of the triad* **DAB-APy-PDI-APy-DAB**; *B) intra vs inter-molecular charge separation distance of hexameric* **DAB-APy-PDI-APy-DAB** *in methyl cyclohexane. Reprinted with permission from ref. [8]. Copyright 2009, American Chemical Society.*

1.4 Artificial Light Harvesting Systems

Photosynthesis is a natural process in which sunlight is collected efficiently by vast array of light-harvesting chromophores and absorbed energy is fed into the single reaction centre (RC). Nature uses antennae systems to enhance the problem of light-harvesting efficiency (Figure 1.21A). Collecting light by means of antenna systems provides the absorption of sunlight over a wide range of wavelength and which will eventually produce much more concentrated energy at the RC by the successive energy transfer processes.

The most widely studied natural antennae are the light-harvesting complexes of photosynthetic purple bacteria. Figure 1.21B is the schematic representation of overall photoinduced energy and electron transfer processes occurring in purple bacteria[94]. The crystal structure of light-harvesting antennae complex LH2 was

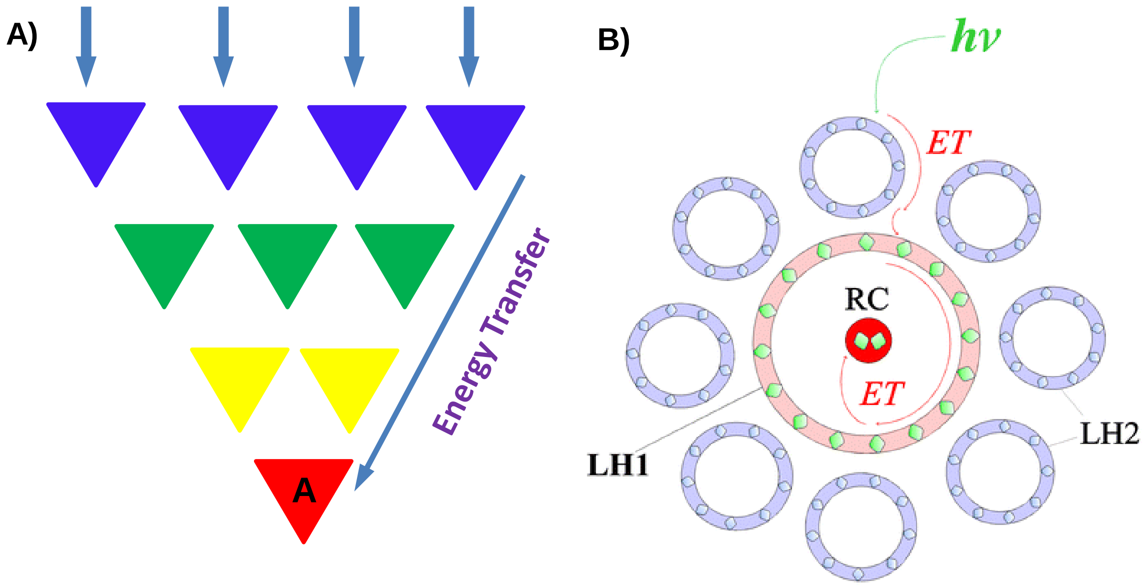

Figure 1.21 *A) Schematic representation of a light-harvesting antenna system where A indicates the final acceptor unit; B) schematic representation of the overall light-harvesting process by LH2 and LH1. Reprinted with permission from ref. [94]. Copyright 2000, Royal Society of Chemistry.*

determined by high resolution X-ray[95]. It is composed of ring shaped assembly of chlorophyll molecules and carotenoids molecules embedded in a protein matrix. Chlorophyll molecules function as light harvesting antennae. The energy collected by LH2 is transferred to LH1 antennae complex, which surrounds the RC. The reaction centre is the final destination of the collected energy, undergo further electron transfer following which splitting of the water molecule takes place. Schulten *et al.* simulated the structure of chromatophore vesicle of the photosynthetic unit of the purple bacteria with the help of atomic force microscopy (AFM), electron microscopy and X-ray crystal structure (Figure 1.22)[96]. The detailed analysis of the crystal structure indicates that the curvature properties of chromatophoric vesicular nature of the purple bacteria provides close packing between the chlorophyll molecules required for effective coupling which helps for efficient energy transfer. The natural photosynthetic unit not only harvest the light energy but also facilitate efficient photoinduced electron transfer followed by rapid charge migration by using multiple donor-acceptor units which separate the charge far apart preventing the fast charge recombination by back electron transfer mechanism.

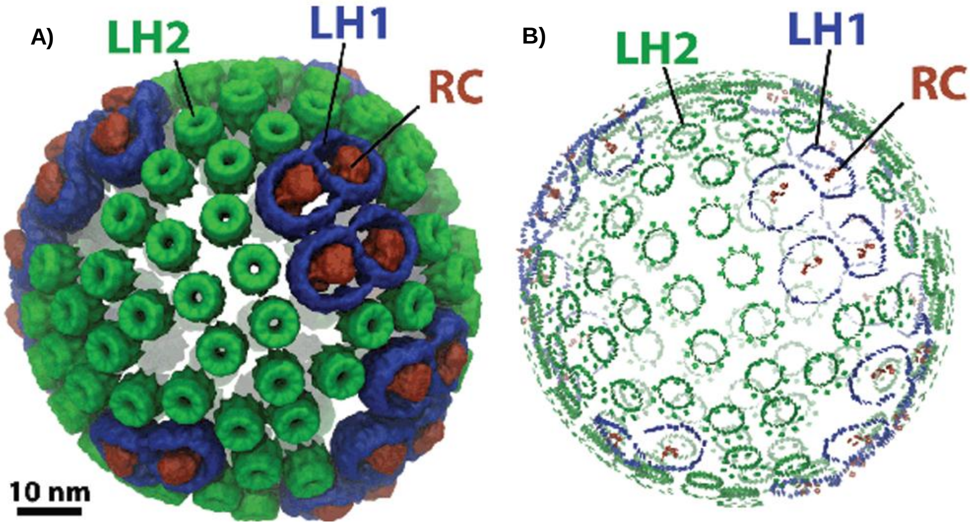

Figure 1.22 *Spherical chromatophore from Rhodobacter sphaeroides showing A) proteins and B) bacteriochlorophylls. The RC is shown in red, LH1 is in blue, and LH2 is in green. LH1–RC complexes form figure-eight-shaped dimers in Rhodobacter sphaeroides. Reprinted with permission from ref. [96]. Copyright 2012, American Chemical Society.*

1.4.1 Photoinduced Energy and Electron Transfer in Single Molecular Donor-Acceptor Dyads

As a mimic to natural photosynthesis both energy and electron transfer processes in single molecular donor-acceptor systems had been studied in the literature[73,74]. Moore *et al.* reported photoinduced energy transfer followed by electron transfer in a molecular pentad (**C-P$_{Zn}$-P-Q$_{N}$-Q$_{B}$**) containing carotenoid species (**C**), zinc porphyrin (**P$_{Zn}$**), free base porphyrin (**P**), napthoquinone (**Q$_{N}$**) and benzoquinone (**Q$_{B}$**) which are linked covalently (Figure 1.23)[74]. Upon photoexcitation of **P$_{Zn}$** energy transfer will occur from **P$_{Zn}$** to **P** followed by electron transfer to **Q$_{N}$** to produce **C-P$_{Zn}$-P$^{\cdot+}$-Q$_{N}^{\cdot-}$-Q$_{B}$** which can further undergo electron migration to **Q$_{B}$** and donation of an electron from **P$_{Zn}$** to **P$^{\cdot+}$** followed by charge shift from carotenoid species produce final charge transfer intermediate $\mathbf{C^{\cdot+}\text{-}P_{Zn}\text{-}P\text{-}Q_{N}\text{-}Q_{B}^{\cdot-}}$. The final charge separated state exhibits a lifetime of 200 μs with a quantum yield of 0.6 in dichloromethane solvent.

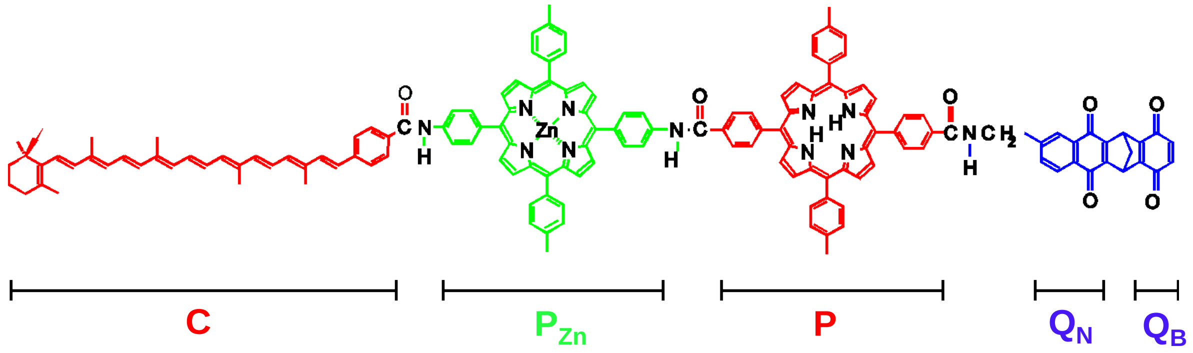

Figure 1.23 *Structure of molecular pentad* $\mathbf{C\text{-}P_{Zn}\text{-}P\text{-}Q_{N}\text{-}Q_{B}}$*. Reprinted with permission from ref. [74]. Copyright 1993, American Chemical Society.*

1.4.2 Photoinduced Energy and Electron Transfer in Self-Assembled Systems

Numerous classes of functional dyes have been employed to design multichromophoric architectures among which perylenimides (**PIs**) exhibit strong tunable absorption in the visible region, bright photoluminescence with quantum yields close to unity, chemical inertness, low triplet yield and excellent photostability[32,97-99]. Perylenimides have been utilized in various electronic and optical applications such as photovoltaic devices, dye lasers, light-emitting diodes, field-effect transistors, electrophotographic devices and solar collectors[13,21,100]. Furthermore, their ability to form supramolecular light-harvesting architectures by π-π stacking, hydrogen-bonding or metal-ion-coordination justifies their wide use as building blocks for the design and synthesis of artificial antenna model systems[93,101-103].

Wasielewski *et al.* reported the antenna reaction-centre array as shown in Figure 1.24A. These molecules can be prepared by functionalization of a 1,7-dipyrrolidino-perylene bisimide chromophore with four 1,7-(3′,5′-di-tert

-butylphenoxy)-perylene bisimide moieties which self-assembles to form stacked dimers in toluene[37]. Self-assembly is used here to produce an artificial light-harvesting antenna structure containing a functional special pair unit of two stacked 1,7-pyrrolidino-substituted **PBIs** (Figure 1.24B). Upon photoexcitation, energy transfer from the 1,7-(3′,5′-di-tert-butylphenoxy)-perylene bisimide moiety to the 1,7-dipyrrolidino-perylene bisimide unit occurs with a lifetime of τ = 21 ps. The energy transfer followed by ultrafast charge separation occurs due to excited-state symmetry breaking that produces a charge separated state with a lifetime of, τ = 7 ps which could be attributed to 1,7- dipyrrolidino-perylene bisimide monoanion and -cation. The ion pair recombines with a lifetime of τ = 420 ps. Notably, the electron transfer occurs only in the dimeric system and is not observed in the disassembled monomer, thus mimicking both antenna and special pair function in photosynthesis.

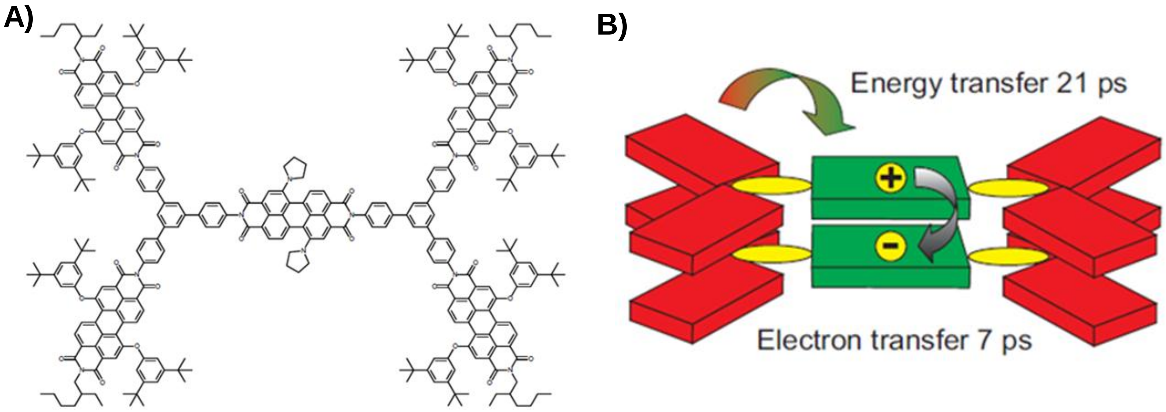

Figure 1.24 A) *Chemical structure of the antenna reaction-center array obtained by functionalization of a 1,7- dipyrrolidino-perylene bisimide chromophore with four 1,7-(3′,5′-di-tert-butylphenoxy)-perylene bisimide moieties; B) schematic representation of the processes occurring in the excited state after photoexcitation. Reprinted with permission from ref. [37]. Copyright 2004, American Chemical Society.*

Guldi *et al.* reported energy transfer followed by electron transfer in a hydrogen-bonded self-assembly of perylene diimide **1a** with zinc tetraphenylporphyrin (**ZnP**) **2** complexed with 4-pyridinylfulleropyrrolidine **3[89]** (Figure 1.25). Steady-state fluorescence and femtosecond time-resolved transient absorption measurements support that in the triad **1a.2.3**, an initially energy transfer occurs (53 ± 3 ps) from **1a** to **2** is followed by an electron transfer (12 ± 1 ps) from **2** to **3**. Multiwavelength analyses indicate that the correspondingly formed radical ion-pair states are longer lived in **1a.2.3** (3.8 ± 0.2 ns) than in **2.3** (1.0 ± 0.1 ns).

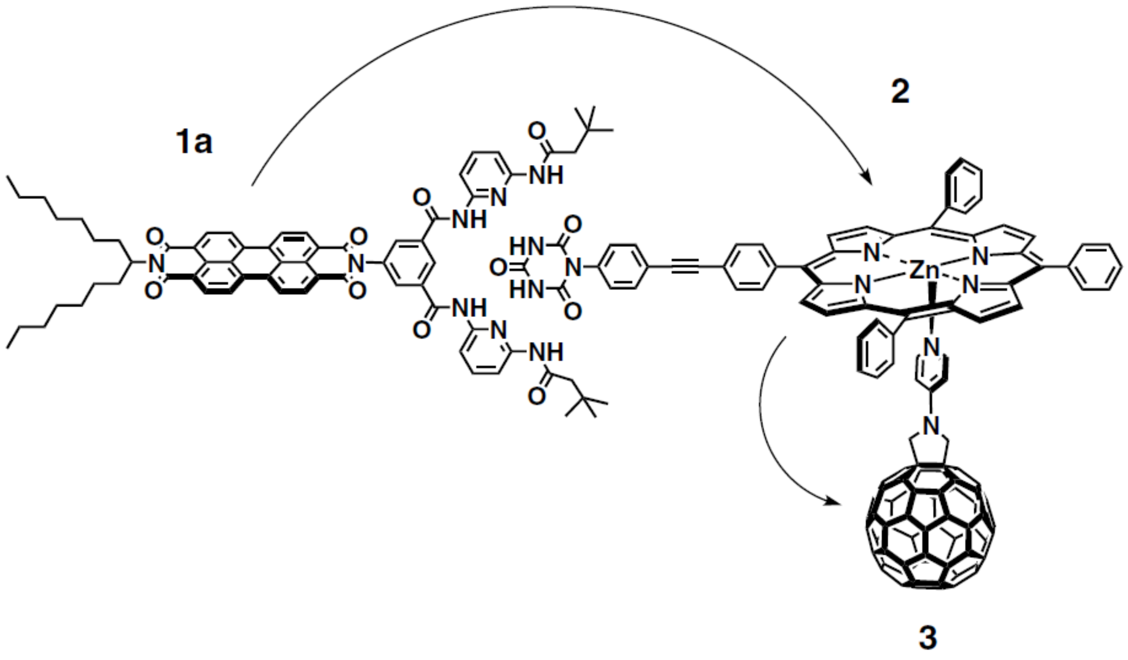

Figure 1.25 *Structure of the triad **1a.2.3**. Reprinted with permission from ref. [89]. Copyright 2012, Proceedings of the National Academy of Sciences of the United States of America.*

Meijer *et al.* reported energy transfer followed by electron transfer in a mixed assembly of $(OPV4)_4$ porphyrins (Zn porphyrin **1** and free base porphyrin **2,** Figure 1.26A) and C_{60} in the presence of water[38]. The self-assembled fibres $(OPV4)_4$ porphyrins (Figure 1.26B) exhibit energy transfer from OPV via Zn porphyrin **1** to free base porphyrin **2.** The addition of C_{60} to aggregated **1** or **2** results in photoluminescence quenching of porphyrin emission indicating the possibility of photoinduced electron transfer to C_{60}. But the detailed analysis of electron transfer kinetics are not discussed in the present literature even though it claim the first report of sequential energy and electron transfer in a self-assembled system.

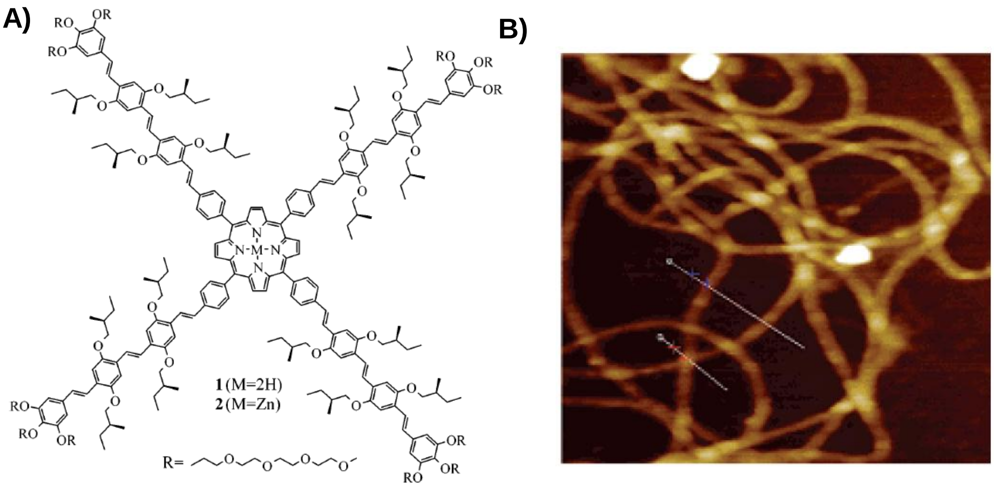

Figure 1.26 *A) Structure of (OPV4)$_4$-H$_2$ porphyrin (**1**) and (OPV4)$_4$-Zn porphyrin (**2**); B) Tapping mode AFM image showing fibers of **1**, dropcast from water (10-5 M) onto a mica surface (420 × 420 nm). Reprinted with permission from ref. [38]. Copyright 2005, American Chemical Society.*

1.5 Thesis Outline

From the discussions on the photoinduced energy and electron transfer process we can understand that near-orthogonal dyads are less explored in the literature. The energy or electron transfer in single molecule or self-assembled systems is well studied in the literature. It is well understood from the literature that the π-π stacked self-assembly promotes efficient photoinduced electon transfer by reducing the charge recombination pathway. Also both energy and electron transfer in single molecules and dimeric assemblies are well explored in the literature. The existing challenge is to develop a self-assembled system of a covalently linked donor-acceptor dyad which undergoes efficient photoinduced energy transfer followed by electron transfer in the presence of a suitable external electron donor or acceptor (Figure 1.27). In this scenario we have designed a near-orthogonal donor-acceptor dyad consisting of naphthalenimide (energy donor) and perylenimide (energy acceptor) having parallel dipole orientations with effective spectral overlap between donor emission and acceptor absorption.

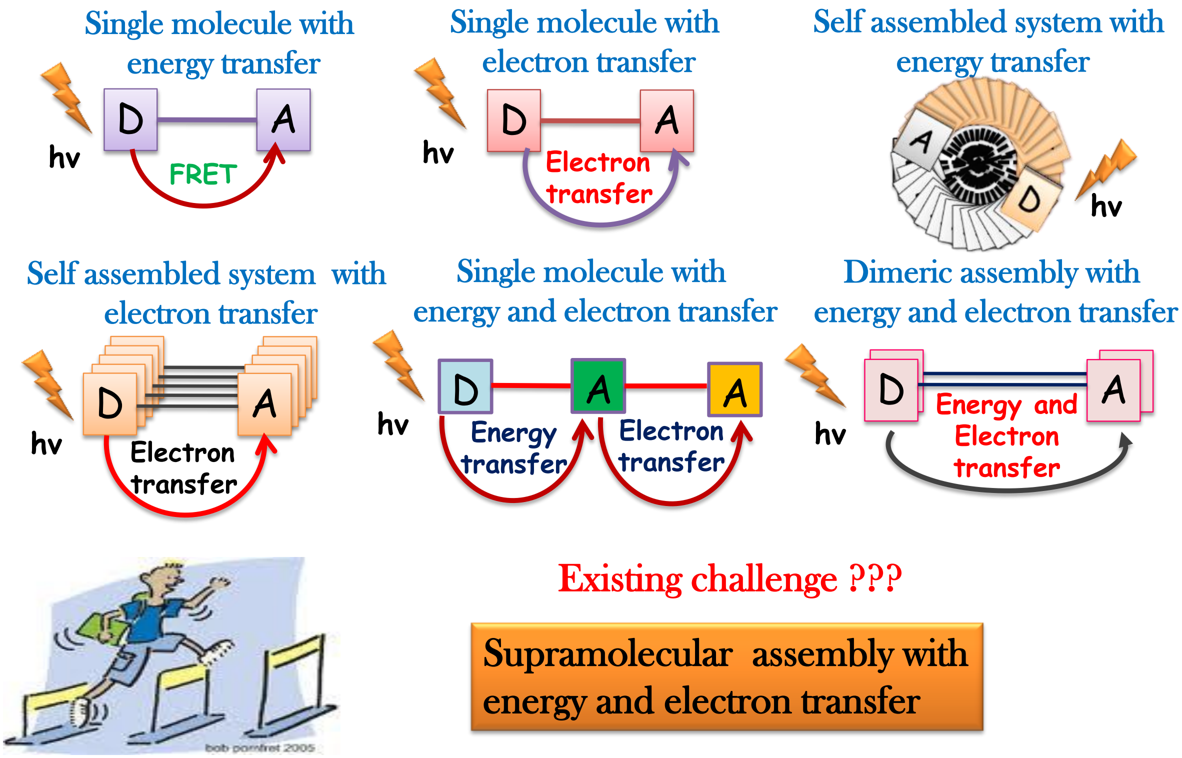

Figure 1.27 *Schematic representation of strategy of the thesis.*

The current thesis is divided into three major chapters excluding the introduction (chapter 1). Chapter 2 describes the design, synthesis and energy transfer properties of near-orthogonal donor-acceptor dyad in the solution state. Chapter 3 highlightes the prominence of crystal ordering in modulating the photophysical properties of the donor-acceptor dyad in the crystalline state. The final part of the thesis (chapter 4) focuses on the energy transfer followed by electron transfer in a π-π stacked vesicular scaffold in the presence of an external electron donor. We were successful in enhancing the survival time of the charge-separated state with the proposed design which will find applications in designing various types of photo-functional materials.

Chapter 2

Photoinduced Energy Transfer in Near-Orthogonally Arranged Chromophores Separated through a Single Bond

2.1 Introduction

Energy transfer (ET) cassettes have gained immense importance during the last decade in the areas of DNA sequencing[1,2], microscopic imaging[3], artificial light-harvesting[7,60,66,98,104-124] and biomolecular sensing[14-18,48,49,55,59,125-130] among others. Electronic excitation energy transfer (EET) is the ubiquitous mechanism for energy transfer in multi-chromophoric systems[131]. EET mechanisms, characterized by their different distance dependences, include the Förster type 'Coulombic' interactions, Dexter type exchange interactions[20] and other contributions to short range coupling due to orbital overlap effects[42,44,50,132-134]. Recently, coherent effects including interference between the different EET mechanisms have also been of interest[45,47]. When orbital overlap between the chromophores is minimal, then the Dexter type, through bond interactions including exchange effects due to the indistinguishability of electrons are highly (exponentially) suppressed. Typically when the chromophores are separated by more than $2-5$ Å, orbital overlap effects can be ignored. At large separations, the dominant through space Coulombic interaction is described by Förster theory wherein the electrostatic coupling is approximated by the dipole-dipole interaction between the chromophores. However the ideal-dipole approximation (IDA) proposed by Förster to predict the rate of energy transfer in such cassettes breaks down at distances that are short compared to the size of the

Publication based on this work has been reported in *J. Phys. Chem. C* **116**, 12489-12498 (2012) chromophores[135] due to higher order interactions such as quadrupole - quadrupole, octupole - octupole interactions.

At relatively short separations between the chromophores, efficient energy transfer through the Dexter mechanism has been isolated and studied[2,53] in orthogonally aligned chromophoric dipoles (orientation factor; $\kappa^2 \cong 0$) for which Coulombic coupling is suppressed due to perpendicular orientation. However, the electronic coupling for excitation energy transfer through predominant Coulombic interactions at short separations compared to the size of the chromophores excluding the possibility of energy transfer through orbital overlap has received less attention. Understanding mutually exclusive energy transfer pathways at short separation is demanding to yield better insight on coherence in quantum energy transfer[45]. Detailed analysis of such short distance energy transfer conjugates having negligible orbital overlap and the design of novel probes that combine solvatochromism[136] offering large Stoke's shift for biological applications[3,137,138] is of significant interest.

Herein, we report the synthesis and photophysical properties of a new candidate (extended 1,1′-bithahthyl derivative) to act as an energy transfer conjugate (Figure 2.1) that can be conveniently incorporated into oligo-nucleotides or peptides. The present molecular system integrates naphthalenimide (energy donor) and perylenimide moieties (energy acceptor; dipolar) at the distance of a single covalent bond and enforces a sterically driven orthogonality between the two chromophores[139]. The perpendicular arrangement of the incorporated chromophores results in negligible orbital overlap thereby isolating efficient energy transfer that effects through Coulombic interactions at short separations. By virtue of the dipolar nature of the perylenimide moiety and the possibility of exciting the naphthalenimide moiety (energy donor), this conjugate exhibits remarkable pseudo Stoke's shift of ca. 175-240 nm that is promising for biological applications.

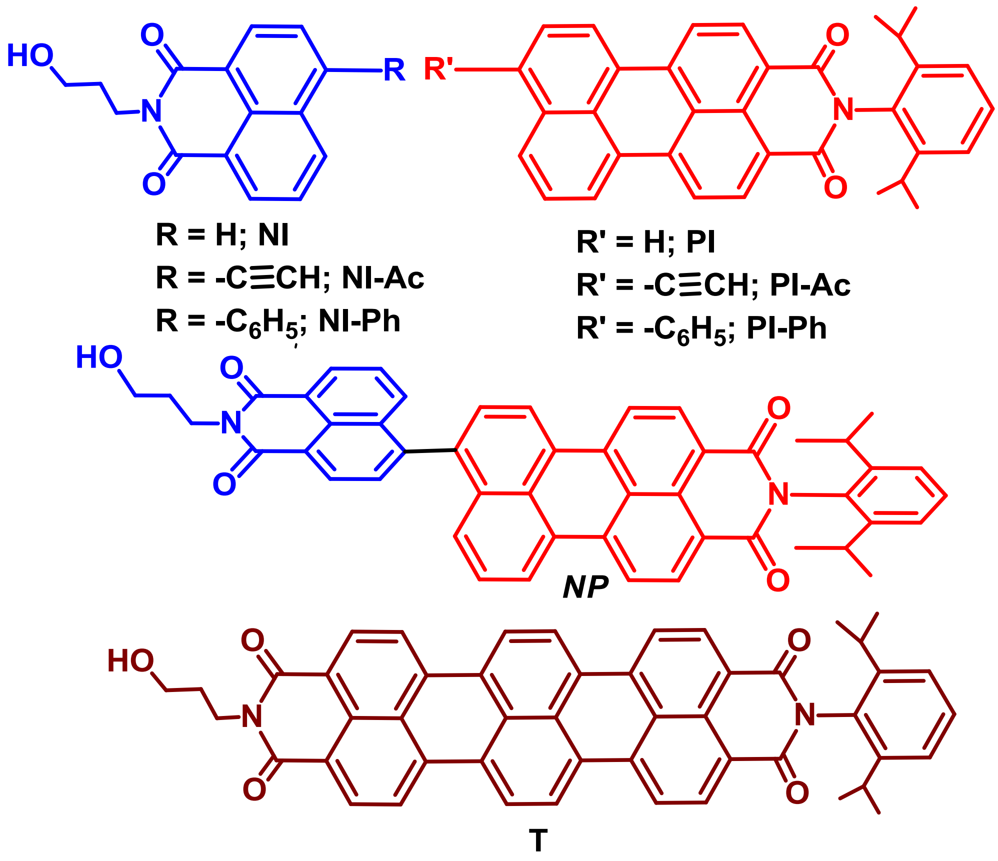

Figure 2.1 *The structures of* ***NI, NI-Ac, NI-Ph, PI, PI-Ac, PI-Ph, NP*** *and* ***T****.*

2.2 Results and Discussions

2.2.1 Electron Transfer Rate and Energy Transfer Rate

From the relative fluorescence quantum yields of the model derivative **PI** (Φ_{ref}) and conjugate **NP** (Φ) and the fluorescence lifetime of the model derivative **PI** (τ_{ref}) in toluene, an estimate of the rate constant of the electron-transfer process can be made using Eq. 2.1,

$$k_{electron-transfer} = \frac{(\Phi_{ref}/\Phi)-1}{\tau_{ref}} \tag{2.1}$$

The changes in free energy for the electron transfer from the singlet excited state of naphthalenimide moiety to perylenimide and from the singlet excited state of perylenimide moiety[140] to naphthalenimide moiety was calculated using the Rehm-Weller equation[79,80], Eq. 2.2,

2.2.1 Electron Transfer Rate and Energy Transfer Rate

$$\Delta G^0 = E_{ox}\,(D^{+\cdot}/D) - E_{red}\,(A/A^{-\cdot}) - E_{0,0} \tag{2.2}$$

where ΔG^0 is change in free energy for photo-induced electron transfer, E_{ox} is the oxidation potential of the donor, E_{red} is the reduction potential of the acceptor and $E_{0,0}$ is the singlet excited state energy of the donor.

The electronic excitation energy transfer rate according to the Förster theory is

$$k_{ET} = \frac{4\pi^2}{h^2 c}|V_{DA}|^2 J \tag{2.3}$$

where V_{DA} is the Coulombic coupling between the donor and acceptor expressed in wave numbers. The spectral overlap J is given by the integral,

$$J = \int G'_D\,(\nu) G_A(\nu) d\nu \tag{2.4}$$

where,

$$G'_D(\nu) = A\frac{g_D(\nu)}{\nu^3},\; G_A(\nu) = B\frac{g_A(\nu)}{\nu} \tag{2.5}$$

in which $g_D(\nu)$ and $g_A(\nu)$ are the donor emission and acceptor absorption spectra respectively. A and B are constants that normalize the line shape functions G'_D and G'_A to unit area in the wave number (ν) scale[134].

In order to compute the EET rate, the coupling V_{DA} must be estimated along with the overlap integral. Let a denote the highest occupied molecular orbital (HOMO) of the donor and a′ the corresponding lowest unoccupied orbital (LUMO) and let b and b'denote the same for the acceptor. The transition of interest that transfers the excitation from one chromophore to the other is between the state given by the Slater determinant, $\left(|a\bar{a}'b\bar{b}| + |a'\bar{a}b\bar{b}|\right)/\sqrt{2}$ to the state $\left(|a\bar{a}b\bar{b}'| + |a\bar{a}b'\bar{b}|\right)/\sqrt{2}$ where the bar over a and b means that the corresponding orbital contains an electron with β spin, otherwise it is occupied by an α spin electron. The interaction that transfers the excitation may therefore be formally written down in its entirety as[131]

$$H_{full} = \left\langle |a\bar{a}'b\bar{b}|\left|\hat{H}\right||a\bar{a}b'\bar{b}|\right\rangle \tag{2.6}$$

In the absence of significant orbital overlap between the donor and acceptor, the leading contribution to the interaction is

$$H_{full} \cong 2(aa'|bb') = 2\iint a'(r_1)\, b(r_2) \frac{1}{|r_1 - r_2|}\, a(r_1) b'(r_2) d^3 r_1 d^3 r_2 \equiv V_{ed} \qquad (2.7)$$

where the integrals are over all space. The Coulomb interaction in Eq. 2.7 is between two transition densities $P_{aa'}^{donor}(r_1)$ and $P_{bb'}^{acceptor}(r_2)$ and not between the electron clouds corresponding to each molecular orbital because a and b orbitals do not overlap due to the orthogonality between the chromophores while a and a' (b and b') orbitals have no overlap with each other since they represent mutually orthogonal states. The transition density is the off-diagonal element of the quantum density matrix connecting the two electronic states of a molecule. One can think of the transition density as describing the deformation to the electronic cloud of a molecule when a transition occurs between two levels induced by either a real or a virtual photon. The interaction in Eq. 2.7 is the long-range Coulombic coupling between the transition densities by means of which the de-excitation of the energy donor resonates with the excitation of the acceptor. In terms of the transition densities, this electrodynamic interaction can be written as

$$A = \frac{e^2}{4\pi\varepsilon_0} \iint \frac{P_{aa'}^{donor}(r_1) P_{bb'}^{acceptor}}{|r_1 - r_2|} d^3 r_1 d^3 r_2 \qquad (2.8)$$

When the separation between the donor and acceptor chromophores is large compared to their size, the resonant interaction between the transition densities is mediated by a real photon and in this case, the interaction can be approximated well by the dipole-dipole coupling between two ideal dipoles kept at the charge centers of the respective chromophores. However, when the separation is small compared to the size of the chromophores, the possibility of interaction mediated by virtual photons makes the ideal dipole approximation inadequate. In the case of the conjugate **NP**, the orthogonal arrangement of the two chromophores minimize orbital overlaps making the EET mechanism dominantly Coulombic. However the separation between the chromophores is only one covalent bond (1.49 Å) and the separation between their respective centers (<7Å) is comparable to the size of both **NI** and **PI**.

2.2.2 Synthesis and Structure of the Conjugate NP

Since the ideal dipole approximation cannot be used in the case of conjugate **NP**, the relevant transition densities for both **NI** and **PI** are computed using Qchem and they are, in turn, used to compute V_{ed}. Numerically computed transition density cubes (TDC) are not functions over space but rather values defined on a grid. The transition density values on the grid points are treated as integrals of the continuous transition density in Eq. 2.8 over cubes of volume $V_\delta = \delta_x\delta_y\delta_z$, where δ_x, δ_y and δ_z are the lattice constants defining the computational grid. Spin dependencies, if any, of the continuous transition density are also assumed to be summed over while computing the TDC elements. In terms of the TDC elements M_D (i) and M_A (j) of the donor and acceptor respectively, we can write the electrodynamic component of EET as[141]

$$V_{ed} = \sum_{ij} \frac{M_D(i) M_A(j)}{4\pi\varepsilon_0 r_{ij}} \tag{2.9}$$

where r_{ij} is the separation between the i^{th} lattice point of the donor's TDC and the j^{th} lattice point of the acceptor's TDC.

2.2.2 Synthesis and Structure of the Conjugate NP

N-subtituted 9-bromoperylenimide (**PI-Br**) was synthesized from perylene-3,4,9,10-tetracarboxylic anhydride through monoprotection using 2,6-diisopropylaniline and decarboxylation followed by bromination (Schemes 2.1-2.3) as per the reported procedure[97,98]. N-(hydroxypropyl)bromonaphthalenimide derivative was converted to corresponding tributyltin derivative and further subjected to Stille coupling[142] with **PI-Br** to yield 50% of naphthalenimide-perylenimide conjugate **NP** (Schemes 2.3). Model derivatives such as **NI-Ac**[143], **NI-Ph**, **PI-Ac**[144], **PI-Ph** and **T**[145] were synthesized as per reported procedures (Scheme 2.1-2.3).

As shown in Figure 2.2, the conjugate **NP** crystallizes in the triclinic space group $P\bar{1}$ with two molecules in the asymmetric unit (Table 2.1). The conjugated nature of the individual chromophores was confirmed from the analysis of the

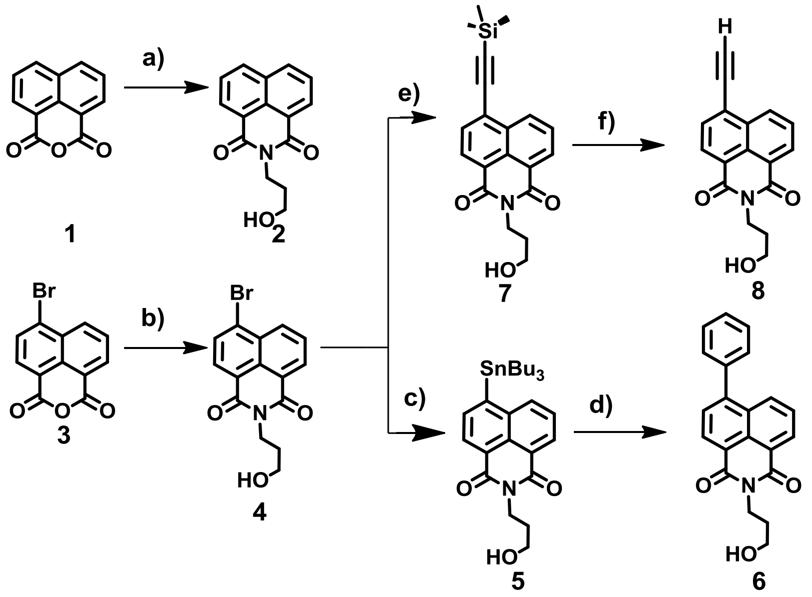

a, b) 3-Aminopropanol/H_2O;70 °C; c) Hexabutylditin/$Pd(PPh_3)_4$/toluene /reflux; d) Bromobenzene/$Pd(PPh_3)_4$/toluene/reflux; e) Trimethylsilylacetylene/CuI/ $PdCl_2(PPh_3)_2$/diisopropylamine/reflux; f) K_2CO_3/dry CH_3OH

Scheme 2.1 *Synthesis of the model derivatives of naphthalenimide (**NI**).*

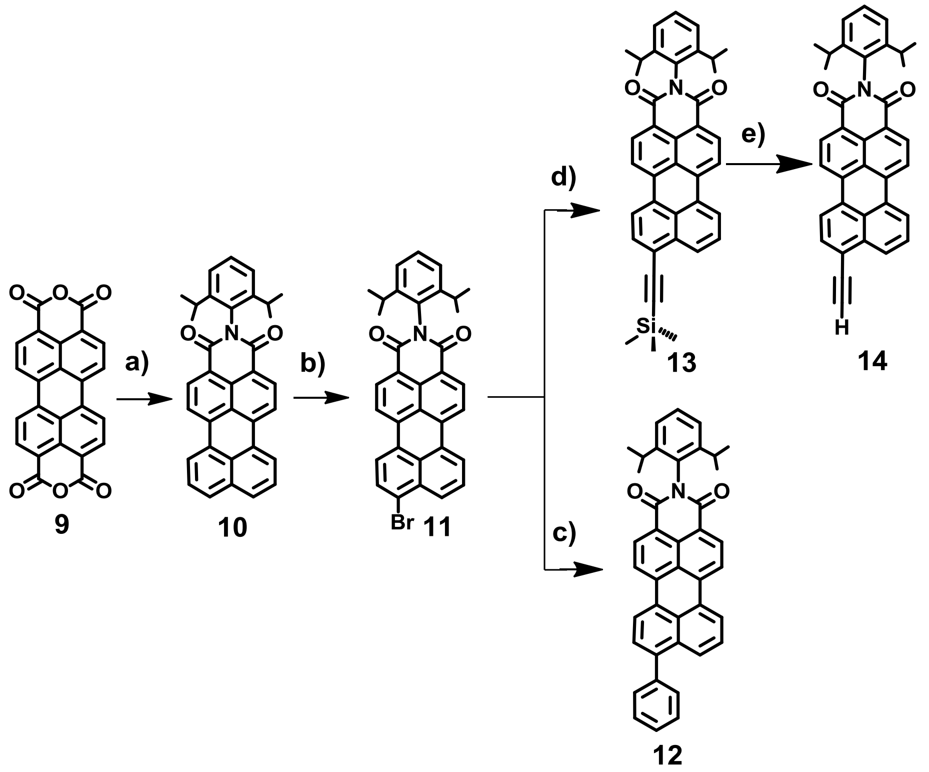

a) 2,6-Diisopropylaniline/imidazole/zinc acetate/H_2O/190 °C; b) Br_2/chlorobenzene /50 °C; c) Phenylboronic acid, $Pd(PPh_3)_4$/toluene/aq. K_2CO_3 solution(1M)/100°C; d) Trimethylsilyl- acetylene/CuI/$PdCl_2(PPh_3)_2$/triethylamine/toluene/reflux; e) K_2CO_3/ dryCH_3OH/dry CH_2Cl_2

Scheme 2.2 *Synthesis of the model derivatives of perylenimide (**PI**).*

2.2.2 Synthesis and Structure of the Conjugate NP

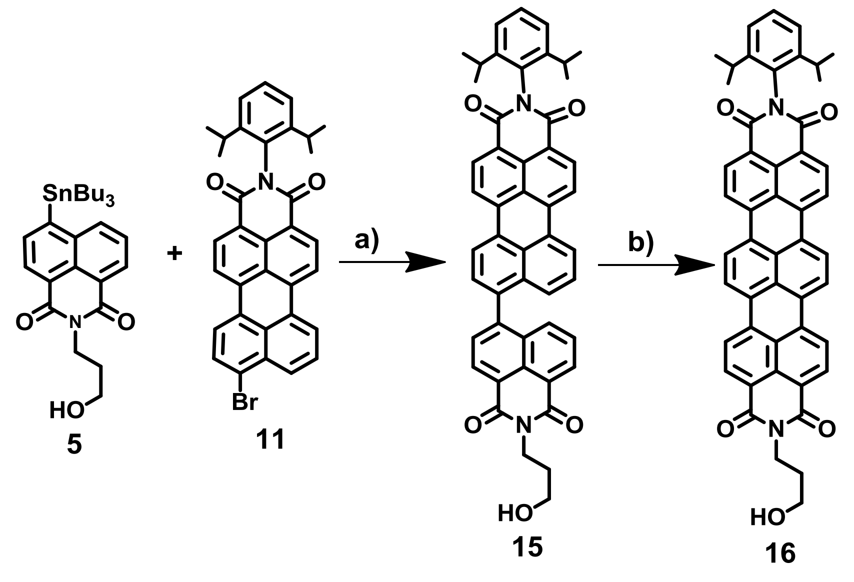

a) Pd(PPh$_3$)$_4$/DMF/ 90 °C; b) K$_2$CO$_3$/Ethanolamine/160 °C.

Scheme 2.3 *Synthesis of naphthalenimide-perylenimide conjugate* **15** *(***NP***) and terrylenimide* **16** *(***T***).*

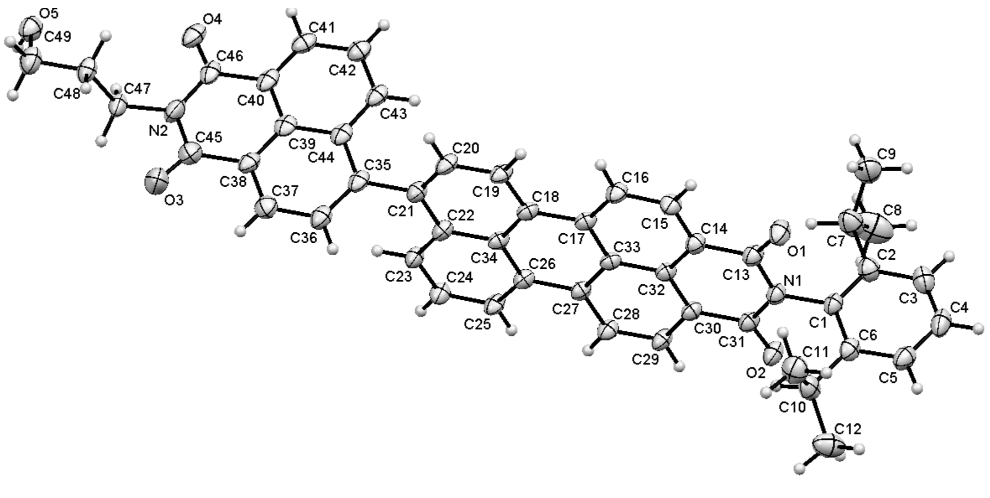

Figure 2.2 *Crystal structure of the conjugate* **NP***.*

crystal structure with comparable bond lengths corresponding to conjugated carbon-carbon single and double bonds. However, the interchromophoric C–C bond length is found to be 1.49 Å comparable to that of C–C single bond length. Confirmation of this behaviour arises from the crystal structure of conjugate **NP** that shows the naphthalenimide donor moiety to be twisted out of planarity by 75 °. Consequently, the naphthalene imide and perylenimide units act as independent chromophores and not as a conjugated system. In order to understand the structure of dyad **NP** in

Table 2.1 *Crystal data and structure refinement for conjugate* ***NP****.*

	Conjugate **NP**
Empirical formula:	$C_{49}H_{38}N_2O_5$
a:	10.482 Å
b:	12.374 Å
c:	16.356 Å
α (alpha):	83.74 °
β (beta):	86.77 °
γ (gamma):	68.52 °
Volume:	1962.16 $Å^3$
Space group:	$P\bar{1}$
Calculated density:	1.242 g/cm^3
Z:	2
Temperature:	-173.0 °C
Formula weight:	734.843 g/mole
R(F):	5.32
$R_w(F^2)$:	0.1556

solution, we carried out NMR experiments in $CDCl_3$. 2D ^1H NMR studies of conjugate **NP** in solution clearly revealed through-space interaction between the protons attached to a) C36 and C23; b) C43 and C20 (Figure 2.3-2.7). No NOE coupling was observed between the protons attached to a) C43 and C23; b) C43 and C24 (Figure 2.6, 2.7). This further confirms the non-planarization of the two constituent chromophoric units in conjugate **NP** in solution.

Furthermore, the extent of electronic interactions between the constituents **NI** and **PI** was understood through the examination of the electron density distributions in the frontier molecular orbitals (FMO) of the constituents of the conjugate. The calculated electron density distributions in the frontier molecular orbitals (FMO) of the constituents of the conjugate are shown in the Figure 2.8. Inclusion of all the four orbitals in each case is essential as the transitions HOMO → LUMO and HOMO -1 → LUMO + 1 are possible. Careful analysis of the FMOs clearly indicates that, for substituents that can be coplanar to **NI** and **PI** (eg. acetylene substituted **NI-Ac** and **PI-Ac**), the electron density is distributed in the substituent (acetylenyl) moiety in the LUMO (Figure 2.9). Such delocalization results in a decrease in the energy difference between the HOMO and LUMO levels as seen in the case of **PI-Ac** (4.12 eV), compared to **PI** (4.21 eV). In contrast, substituents such as phenyl (**PI-Ph**; 4.31 eV) and naphthalenimide (**NP**; 4.37 eV) moieties exhibit (Figure 2.10, 2.11) increase in the HOMO-LUMO gap. This could be attributed to large steric repulsion between hydrogen atoms preventing the rotation about the internuclear bond leading to non-coplanar arrangement of the phenyl/perylenimide and naphthalenimide/perylenimide moieties.

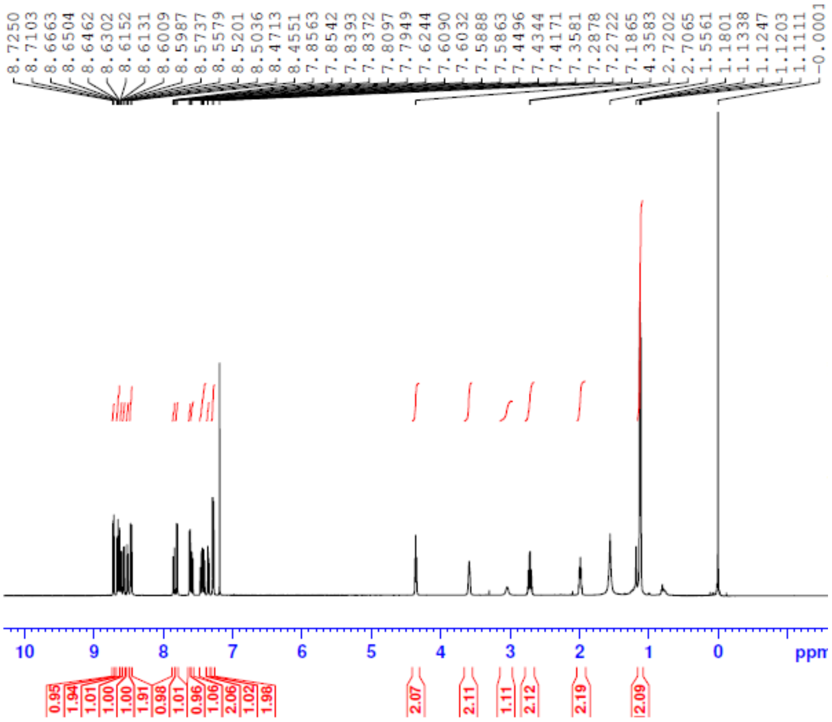

Figure 2.3 *Shows 1D ^{1}H NMR spectrum of conjugate* ***NP*** *in CDCl$_3$.*

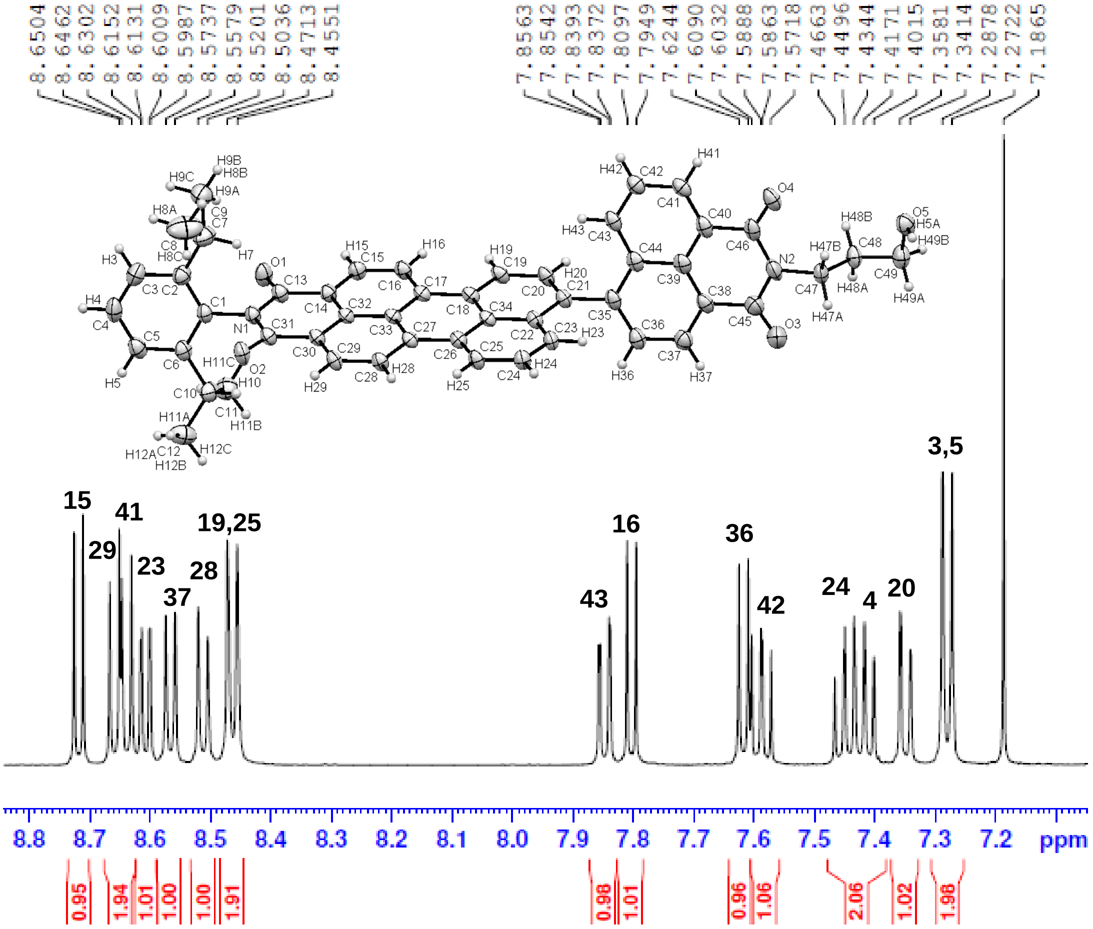

Figure 2.4 *Shows 1D ^1H NMR spectrum of conjugate* ***NP*** *in $CDCl_3$ including assignment of protons.*

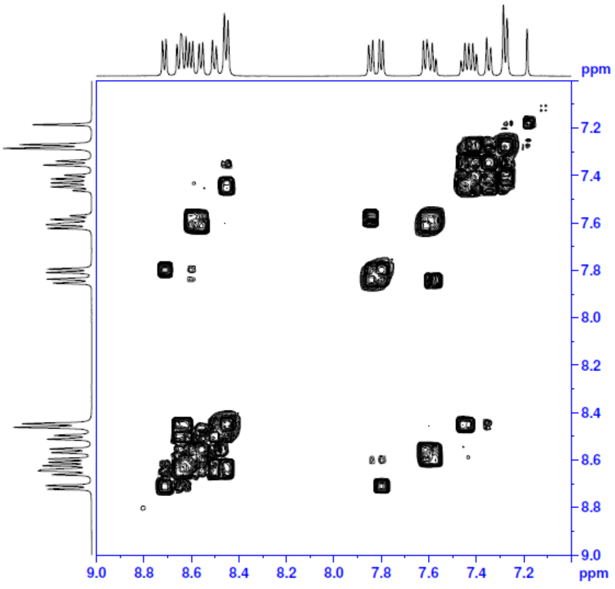

Figure 2.5 *Shows 2D ^1H COSY NMR spectrum of conjugate* ***NP*** *in $CDCl_3$.*

2.2.2 Synthesis and Structure of the Conjugate NP

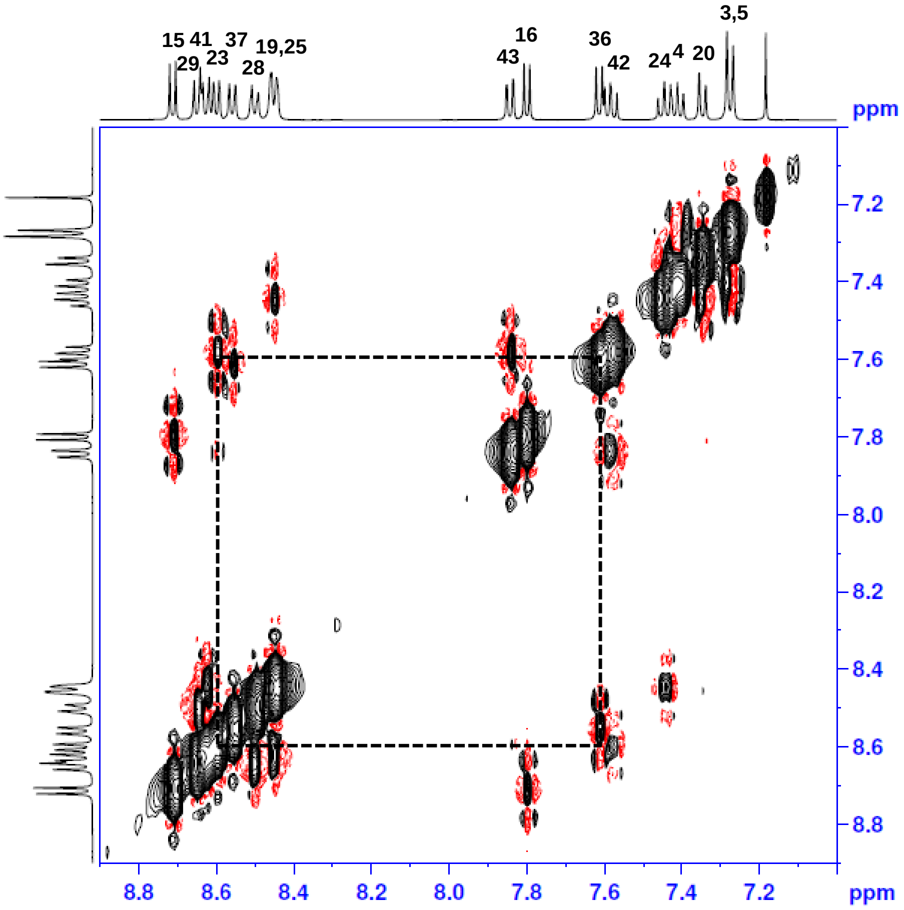

Figure 2.6 *Shows expanded 2D* ^1H *NOESY NMR spectrum of conjugate* ***NP*** *in* $CDCl_3$ *indicating through space coupling between H-36 and H-23.*

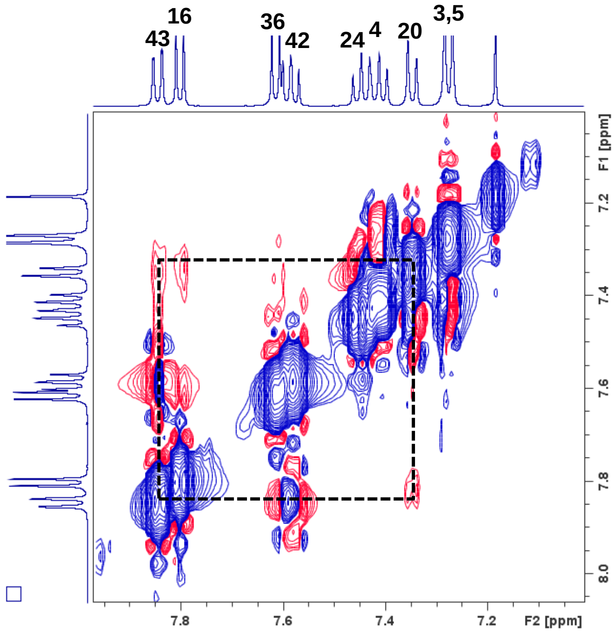

Figure 2.7 *Shows expanded 2D* ^1H *NOESY NMR spectrum of conjugate* ***NP*** *in* $CDCl_3$ *indicating through space coupling between H-43 and H-20.*

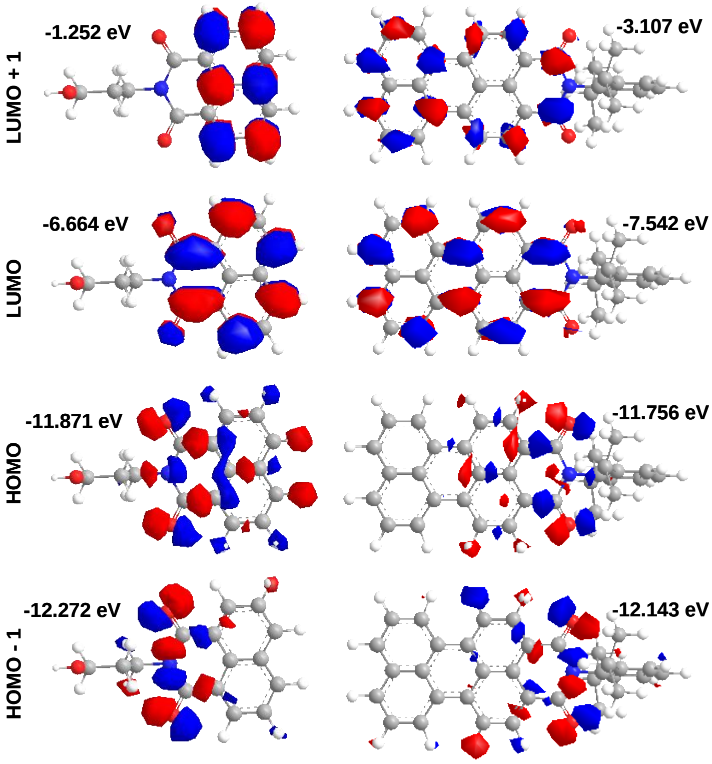

Figure 2.8 *Electron density distributions and energies of the frontier molecular orbitals of the derivatives* ***NI*** *and* ***PI****.*

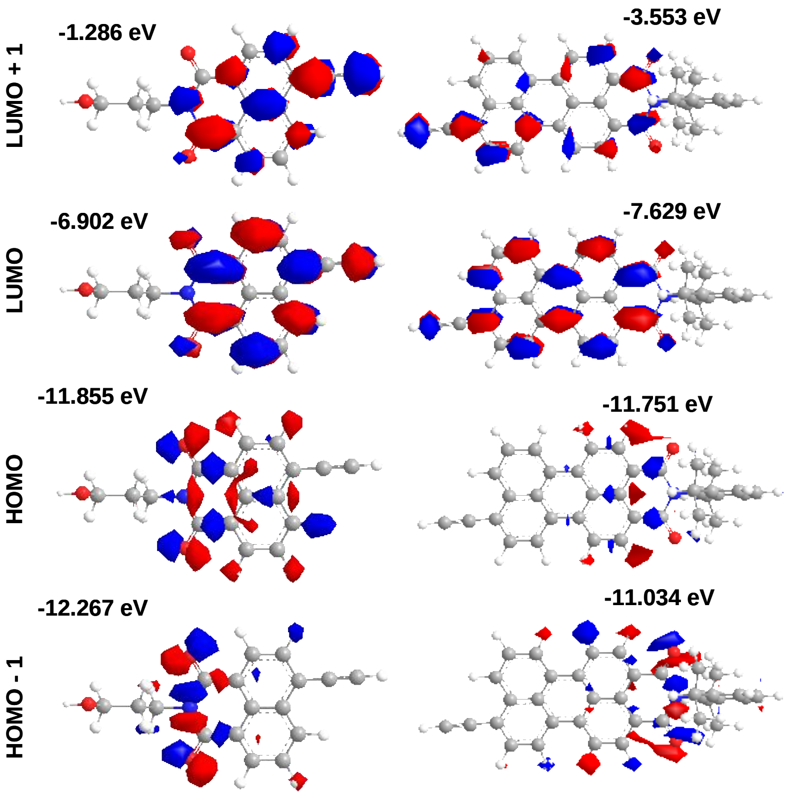

Figure 2.9 *Electron density distributions and energies of the frontier molecular orbitals of the derivatives* ***NI-Ac*** *and* ***PI-Ac****.*

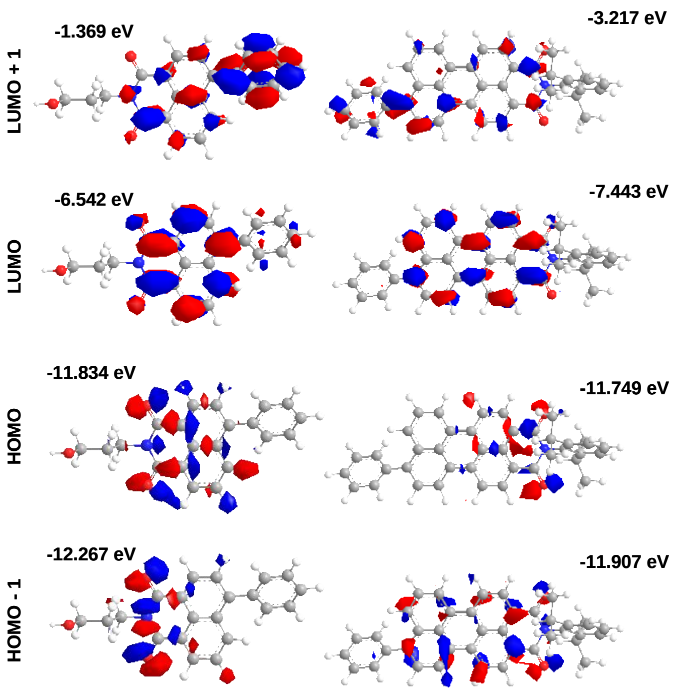

Figure 2.10 *Electron density distributions and energies of the frontier molecular orbitals of the derivatives* ***NI-Ph*** *and* ***PI-Ph****.*

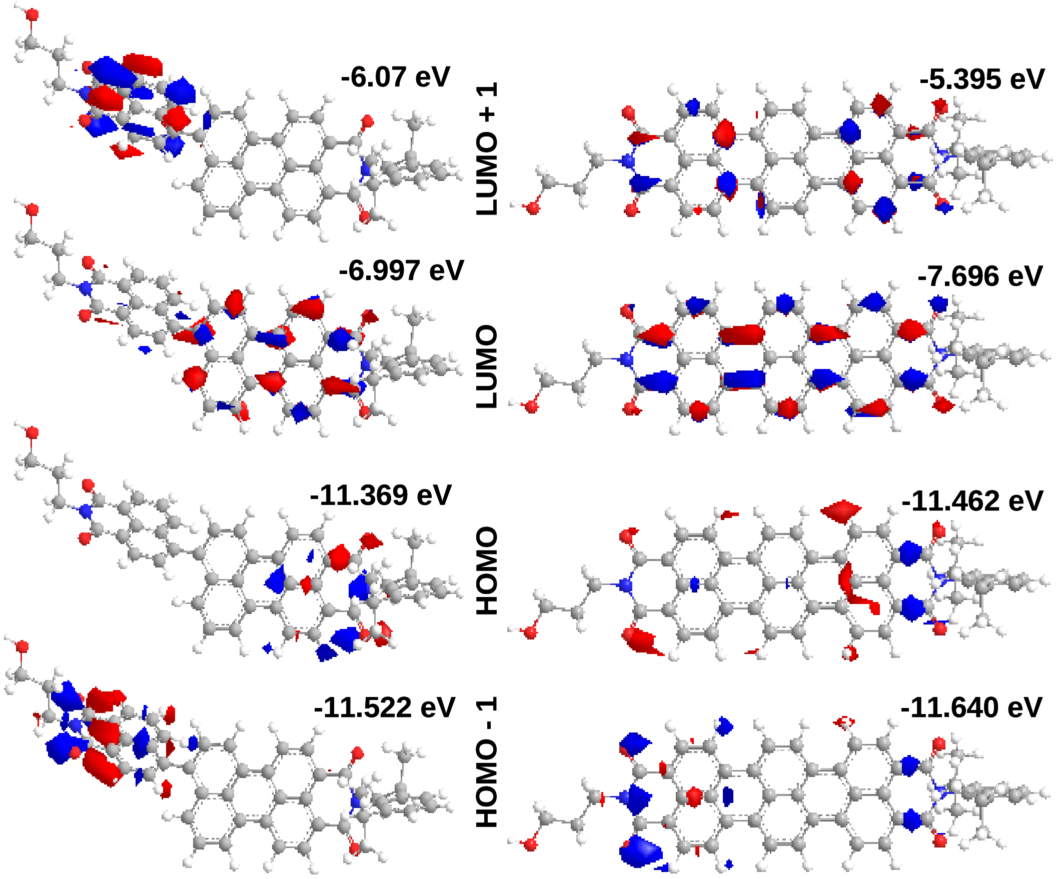

Figure 2.11 *Electron density distributions and energies of the frontier molecular orbitals of the derivatives* **NP** *and its planar analogue* **T***.*

2.2.3 Photophysical and Redox Properties of the Conjugate NP

Figure 2.12A shows the absorption spectra of the conjugate **NP** and the corresponding model chromophores **NI** and **PI** in acetonitrile. Absorption spectrum of conjugate **NP** is the summation of the absorption spectra of **NI** centered around 340 nm and **PI** centered around 480 nm indicating that **NP** behaves as two separately conjugated chromophores though connected through a single covalent bond. The ratio of molar extinction coefficients $\varepsilon_{\boldsymbol{PI}}$(507 nm) / $\varepsilon_{\boldsymbol{NI}}$(334 nm) is found to be ca. 2.85 in the individual model chromophores, identical to that in the conjugate **NP** (Table 2.2). A slight red shift (5-6 nm) in the band corresponding to perylenimide moiety of the conjugate **NP** indicates a very weak electronic coupling between the constituents. Similar results are obtained for **NP** in nonpolar solvents like cyclohexane and toluene and in polar solvents like chloroform and methanol.

The UV-Vis spectra of the conjugate **NP** and the model derivatives **NI** and **PI** in acetonitrile solution were calculated using time-dependent density functional theory (TD-DFT)[146] at the B3LYP[147,148]/6-311G++(2d,2p) level associated with the polarized continuum model (PCM)[149]. This method provides an accurate description of UV-Vis spectra of chromophoric systems[150]. Figure 2.12C shows the calculated UV-Vis spectra of the derivatives **NI** and **PI** and the conjugate **NP** in acetonitrile. Absorption spectrum of **NI** in acetonitrile shows a broad band centred around 365 nm, nearly consistent with experimental maximum of 340 nm. Absorption spectrum of **PI** in acetonitrile followed a similar discrepancy of 13 nm in the calculated maximum at 520 nm from the experimental data (507 nm). While conjugate **NP** in acetonitrile exhibited two bands which is the summation of the absorption spectra of model derivatives **NI** and **PI** in acetonitrile with the ratio $\varepsilon_{\boldsymbol{PI}}$(520 nm) / $\varepsilon_{\boldsymbol{NI}}$(365 nm) as 2.7, in good agreement with the experimental data.

Thus a localized description of the individual components **NI** and **PI** is valid for the conjugate **NP**.

Table 2.2 *Photophysical properties of model derivatives* ***NI****,* ***PI*** *and conjugate* ***NP*** *in toluene.*[a]

	Absorption λ_{max}, nm (ε, M^{-1} cm^{-1})	ε_{PI}@507 nm / ε_{NI}@334 nm	Emission λ_{max}, nm	Φ_F[b]	Φ_T[c]
NI	334 (1.27×10^4)	2.85	390	0.09 ± 0.001	0.49 ± 0.03[d]
PI	356 (0.05×10^4) 507 (3.7×10^4)		531	0.86 ± 0.002	0.08 ± 0.005
NP	338 (1.63×10^4) 511 (4.6×10^4)	2.83	541	0.81 ± 0.002	0.11 ± 0.004

[a] Photophysical properties are measured in toluene due to solubility reasons. [b] Fluorescence Quantum yield; [c] Triplet quantum yield; [d] taken from the reference [151]

Figure 2.12 B shows the fluorescence spectra of conjugate **NP** and the derivatives **NI** and **PI**. **NI**, the energy donor, has no emission at the wavelength range (500-700 nm) where the perylenimide moiety in **NP** and **PI** exhibits fluorescence. **PI**, the energy acceptor, excited at 345 nm shows a very weak fluorescence, while conjugate **NP** strongly emits at long wavelength region (500-700 nm) corresponding to the perylenimide moiety when excited at 345 nm. At 345 nm, naphthalenimide can be excited with a good selectivity (> 95%), whereas above 420 nm perylenimide moiety absorbs exclusively (Table 2.2). While the energy acceptor **PI** absorbs feebly at 345 nm and gives a correspondingly weak fluorescence, conjugate **NP** exhibits energy transfer. Negligible fluorescence from naphthalenimide (energy donor) moiety in **NP** is consistent with energy transfer to the acceptor perylenimide moiety. The fluorescence intensity of perylenimide moiety through energy transfer (λ_{ex} = 345 nm) is less compared to the direct excitation (475 nm) of conjugate **NP**. Consistent with absorption spectra, a red shift (9-10 nm) in the perylenimide emission band of the conjugate **NP** indicates a weak electronic coupling between the constituents.

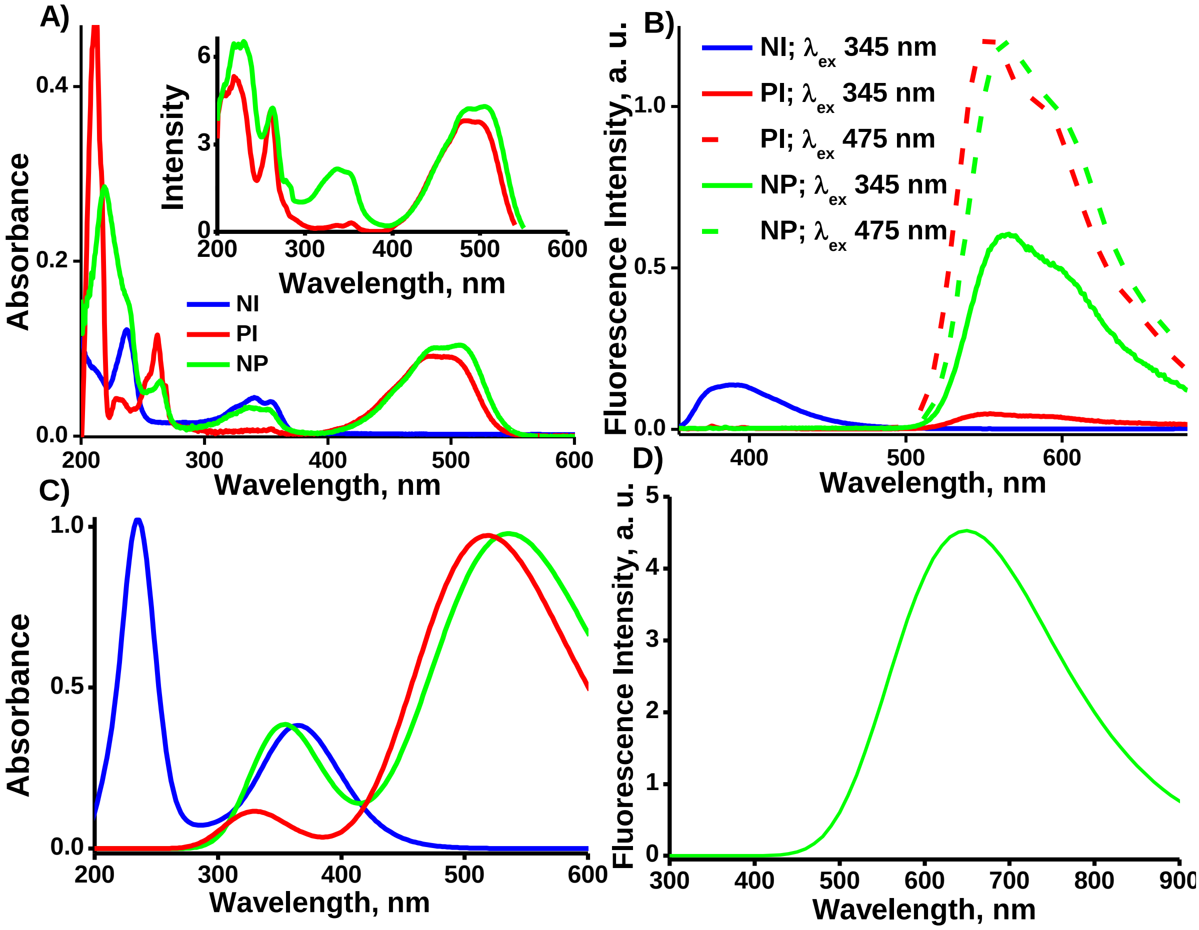

Figure 2.12 *Shows the experimental A) absorption and B) fluorescence emission of* ***NI****,* ***PI*** *and* ***NP*** *in acetonitrile; calculated C) absorption spectra of* ***NI****,* ***PI*** *and* ***NP*** *and D) fluorescence emission spectrum of* ***NP*** *in acetonitrile. Inset of A) shows the excitation spectra of* ***PI*** *(red) and* ***NP*** *(green) in acetonitrile monitored at 553 nm.*

Quantum yield of **NP** is found to be ca. 0.81 ± 0.002, marginally lower compared to that of **PI** (Φ_F = 0.86 ± 0.002). TD-DFT calculation of the emission spectra of **NP** conjugate (Figure 2.12D) resulted in the fluorescence emission only at the wavelength region corresponding to the perylenimide moiety, consistent with the experiment data. Upon excitation at both 345 and 475 nm, conjugate **NP** in ethanol at 77 K exhibited negligible phosphorescence[124], similar to the model derivative **PI** under similar conditions (Figure 2.13). While the model derivative **NI** in ethanol at 77 K showed significant phosphorescence intensity centred around 540 nm, upon excitation at 345 nm[152].

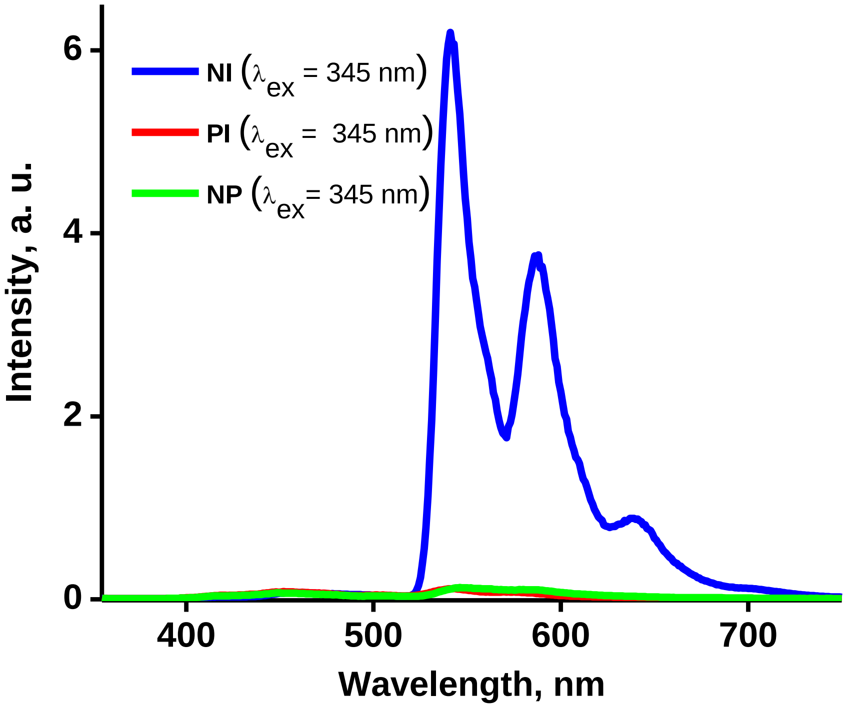

Figure 2.13 *Phosphorescence spectra of model derivatives **NI**, **PI** and conjugate **NP** in ethanol recorded at 77 K; excited at 345 nm.*

The excitation spectra of **NP** (inset of Figure 2.12A) monitored at 553 nm is clearly superimposable upon the absorption spectrum, confirming an efficient energy transfer from naphthalenimide to perylenimide moiety. Similar extent of energy transfer is observed for **NP** in nonpolar solvents like cyclohexane and toluene and in polar solvents like chloroform and methanol. Furthermore, conjugate **NP** exhibits strong solvent polarity dependent perylenimide emission upon excitation at 345 nm (Figure 2.14A). Pseudo Stoke's shift range of 165-240 nm is observed in varying solvent medium from cyclohexane (non-polar) through methanol (polar). Solvatochromic behaviour of conjugate **NP** could be attributed to the dipolar nature of the perylenimide moiety, in contrast to quadrupolar terrylene derivative **T** (Figure 2.14B) that exhibited negligible Stoke's shift.

Moreover, the synthesis and photophysical studies of naphthalenimide (**NI-Ac**, **NI-Ph)** and perylenimide (**PI-Ac**, **PI-Ph**) based model derivatives containing extended conjugation such as acetylenyl and phenyl moieties were carried out.

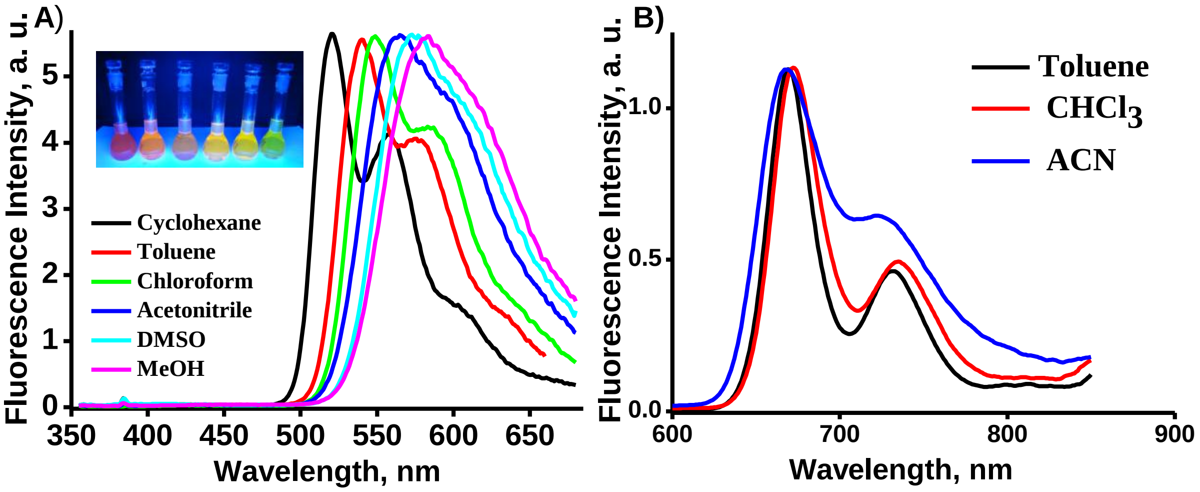

Figure 2.14 *Solvent-polarity-dependent emission spectra of A) conjugate* ***NP*** *excited at 345 nm ; B) emission spectra of terrylene derivative,* ***T*** *when excited at 550 nm.*

Acetylenyl and phenyl substituents were chosen due to their ability to i) extend the conjugation and ii) lower the barrier to rotation about the carbon-carbon bond at the junction, unlike naphthalenimide moiety in conjugate **NP**. Both the acetylenyl and phenyl derivatives exhibited red shift in the absorption and emission spectra when compared to **NI** and **PI** respectively (Figure 2.15), consistent with the extent of conjugation and in good agreement with TD-DFT calculations (Figure 2.16).

TD-DFT calculations clearly showed that the UV-Vis spectrum of **PI-Ph** is significantly red shifted compared to **PI** in acetonitrile, consistent with the experimental observation but in contrast to FMO analysis, whereas accurate description of **NP** in acetonitrile is provided by both FMO analysis and TD-DFT calculations. Such consistency in the FMO and TD-DFT analyses of the conjugate **NP** could be attributed to near orthogonalization of the chromophoric units that results in the negligible perturbation of HOMO-LUMO levels. On the other hand, inconsistent FMO analysis of **PI-Ph** could be attributed to the static orthogonal geometry of the phenyl and perylenimide moieties resulting from DFT method. Similar trends in FMO analysis and TD-DFT calculations are observed in the case of naphthalenimide derivatives. Interestingly, minimum energy conformer of conjugate

2.2.3 Photophysical and Redox Properties of the Conjugate NP

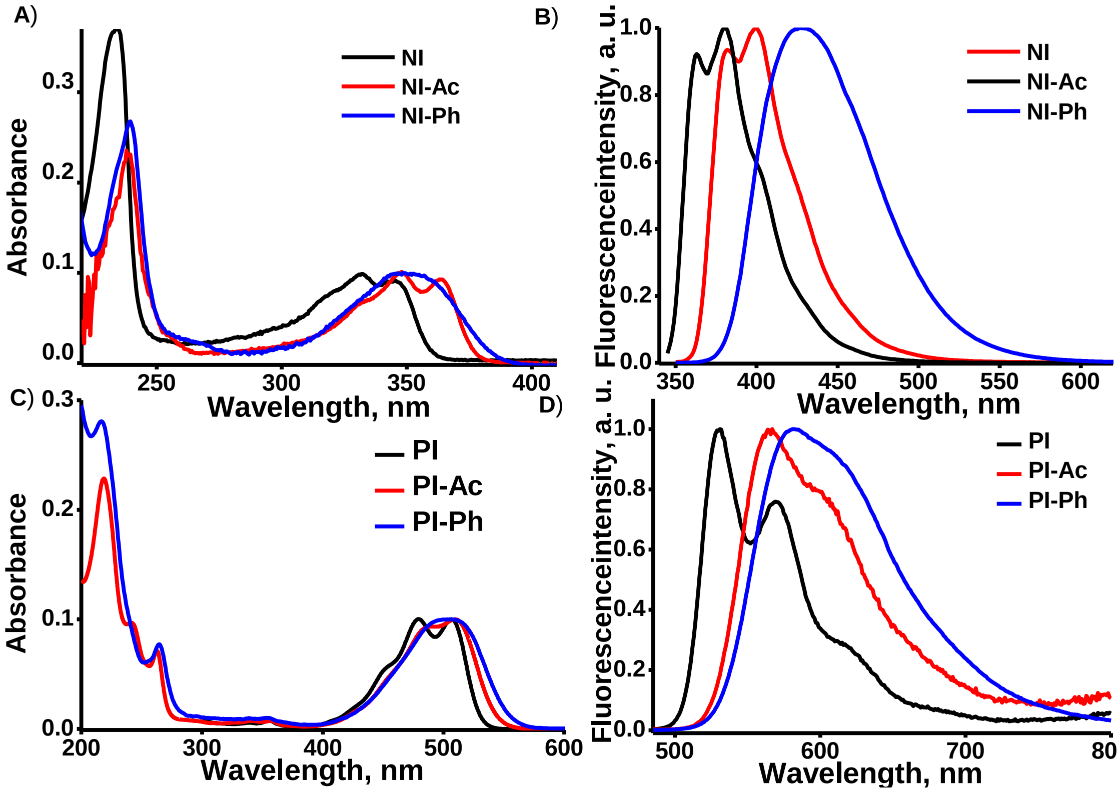

Figure 2.15 *Shows A) absorption and B) fluorescence spectra of* ***NI, NI-Ac*** *and* ***NI-Ph*** *in acetonitrile and C) absorption and D) fluorescence spectra of* ***PI, PI-Ac*** *and* ***PI-Ph*** *in acetonitrile.*

NP is found to have dihedral angle of 75° and large barrier (ΔG≅100 kJ/mol)[139] to rotation through internuclear bond between naphthalenimide and perylenimide units that prevents coplanarization, consistent with the crystal structure of the conjugate **NP**.The model derivative terrylene **T** having overall planar and conjugated structure exhibited significantly lower HOMO-LUMO energy difference (3.766 eV). This is consistent with the observed emission maximum centered on 651 nm, significantly red-shifted (ca. 100 nm) compared to conjugate **NP** in acetonitrile (Figure 2.14B).

Figure 2.17 shows the fluorescence decay profiles of **NP** in various solvents monitored at 563, 549 and 521 nm in acetonitrile, chloroform and cyclohexane respectively and excited at 340 and 439 nm. The singlet excited state lifetime of conjugate **NP** in acetonitrile is found to be 4.2 ns when excited at 340 and 439 nm

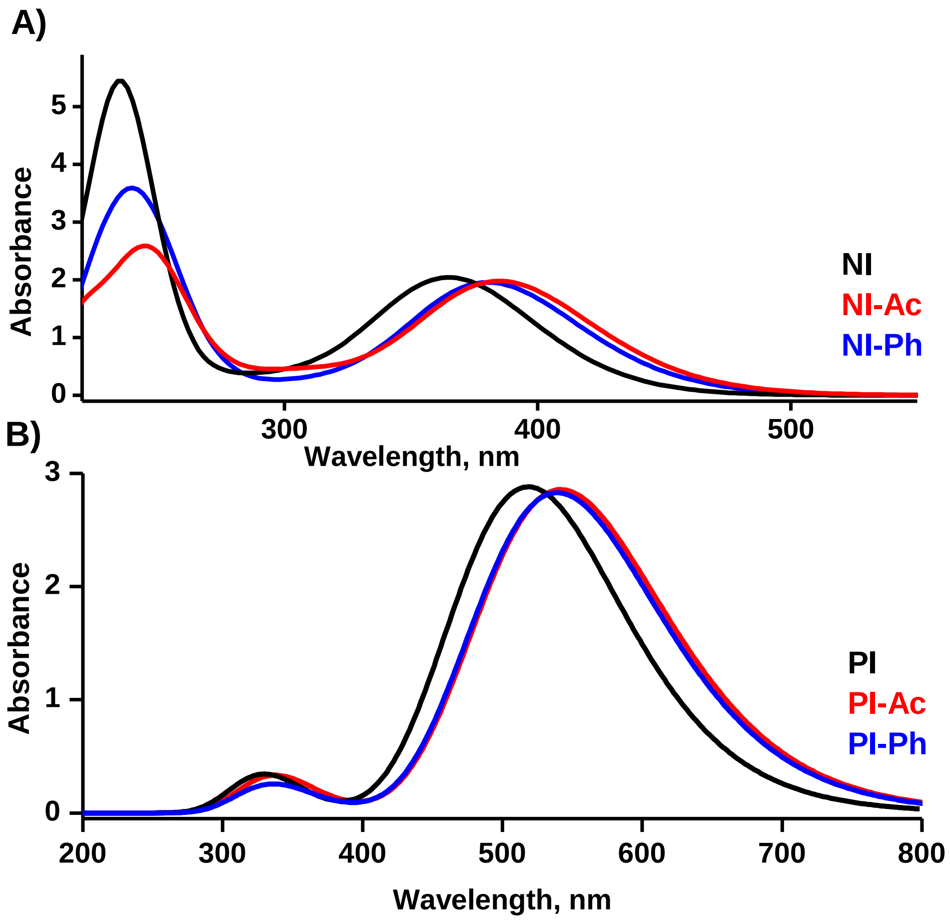

Figure 2.16 *Shows calculated absorption spectra of A)* ***NI, NI-Ac*** *and* ***NI-Ph*** *and B)* ***PI, PI-Ac*** *and* ***PI-Ph*** *in acetonitrile.*

and monitored at 563 nm that corresponds to singlet excited state of perylenimide moiety (Table 2.3). Whereas the lifetime of the model derivative **PI** under similar conditions exhibit a marginally longer lifetime of 5.1 ns, fluorescence lifetime of the **NI** is < 0.005 ns[121]. A shorter singlet excited state lifetime of the perylenimide chromophore excited at both 340 and 439 nm in conjugate **NP** compared to model derivative **PI** further confirms a weak electronic perturbation in the perylenimide moiety in agreement with steady state absorption and emission spectra.

The efficiency of energy transfer from naphthalenimide to perylenimide moiety in conjugate **NP** is evaluated using the equation,

$$\%\text{Efficiency} = \left(1 - \frac{\Phi_{\text{NP}}}{\Phi_{\text{PI}}}\right) \times 100 \tag{2.10}$$

and is found to be 90%, where the quantum yield of **NP**, Φ_{NP} was corrected for competitive absorption by perylenimide moiety (ca. 5%) when excited at 345 nm. A similar high efficiency of energy transfer was achieved in an analogous donor-acceptor system only through the incorporation of four units of donor and one acceptor unit separated via lengthy flexible spacer[124]. In order to understand the marginal loss in efficiency of energy transfer, we calculated the change in free energy for the electron transfer reaction[79,80], using redox potentials and the singlet excited state energies of the **NI** and **PI**[121] (Table 2.4, Refer Eq. 2.2). The change in free energy was found to be ΔG_{ET} = −0.17 eV for electron transfer from singlet excited state of **NI** to **PI** and ΔG_{ET} = 0.44 eV from singlet excited state of **PI** to **NI** in acetonitrile. As expected from the calculated change in free energy values for the electron transfer from **NI** to **PI**, we observed non-negligible loss of photons when conjugate **NP** is excited at 345 nm.

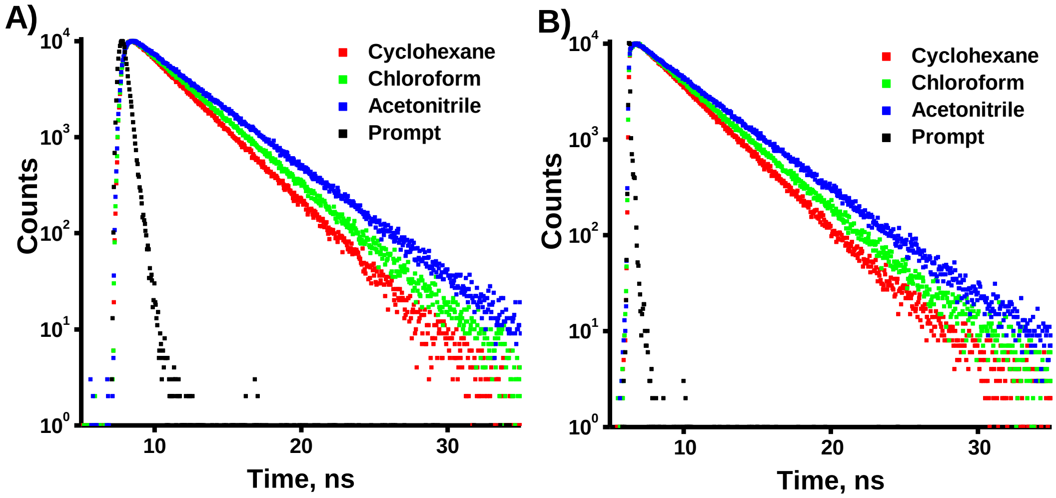

Figure 2.17 *Shows the fluorescence lifetime of* **NP** *excited at A) 340 nm and B) 439 nm; emission collected at 563, 549 and 521 nm for acetonitrile, chloroform and cyclohexane respectively.*

This clearly demonstrates that the naphthalenimide moiety upon excitation can undergo electron transfer to reduce perylenimide moiety[116] leading to the formation of radical ion pair $\mathbf{N^{\cdot+}P^{\cdot-}}$ and consequently decreasing the efficiency of

Table 2.3 *Shows the fluorescence lifetime of* ***NP*** *and model derivative* ***PI*** *under different conditions in ns.*

	Cyclohexane	Chloroform	Acetonitrile
PIτ^b	4.42	4.85	5.06
NPτ^a	3.29	3.68	4.21
NPτ^b	3.29	3.69	4.22

^{a}Excited at 340 nm ^{b}Excited at 439 nm

energy transfer[124]. This marginal free energy change for favourable electron transfer from **NI** to **PI** is consistent with decrease in the quantum yield of **NP** compared tothat of **PI** in toluene. Radical anions of **NI**[152] and **PI**[121] are centred around 413 and 581 nm respectively whereas radical cations of **NI** and **PI** exhibit very low molar extinction coefficient, as observed by using spectroelectrochemical methods (Figure 2.18 and 2.19). We observed no charge separated species generated through the electron transfer from singlet excited state of naphthalenimide to perylenimide moiety, $k_{\text{electron - transfer}} = 2.29 \times 10^{12}$ s^{-1} (Figure 2.20) in nanosecond flash photolysis studies which could be attributed to fast charge recombination on the sub-nanosecond timescale.

We observed the decay (τ = 440 ns) of the triplet excited state corresponding to the perylenimide moiety[116,119,144] in conjugate **NP** in toluene (Φ_T = 0.11) upon photoexcitation at 355 nm when monitored at 550 nm using nanosecond time resolved absorption spectrometer (Figure 2.20C). While the photoexcitation of the model derivative **PI** in toluene at 355 nm showed significantly lower triplet quantum yield (Φ_T = 0.08; τ = 960 ns) when compared to that of conjugate **NP** in toluene. Lower triplet quantum yield of **PI** in toluene could be attributed to reduced intersystem crossing to the triplet state similar to that of perylenediimide derivatives ($\Phi_T \cong 0.001$)[153,154]. In addition, photoexcitation of model derivative **NI** in toluene under similar conditions exhibited the decay (τ = 650 ns) of triplet-excited state of

2.2.3 Photophysical and Redox Properties of the Conjugate NP

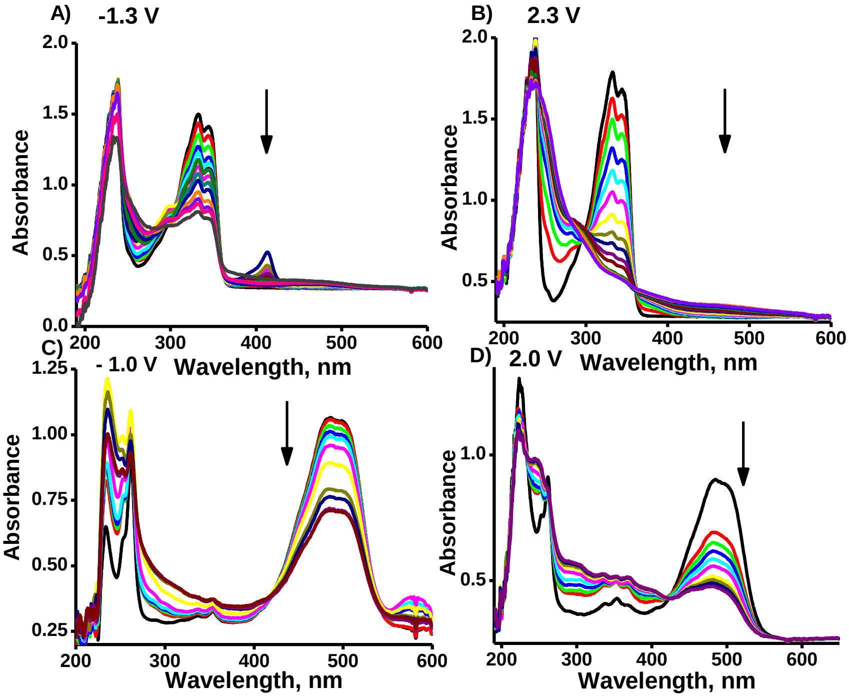

Figure 2.18 *Sshows spectroelectrochemical spectra of A)* ***NI*** *at -1.3 V; B)* ***NI*** *at 2.3 V; C)* ***PI*** *at -1.0 V; and D)* ***PI*** *at 2.0 V in acetonitrile under ambient conditions at intervals of 10 s.*

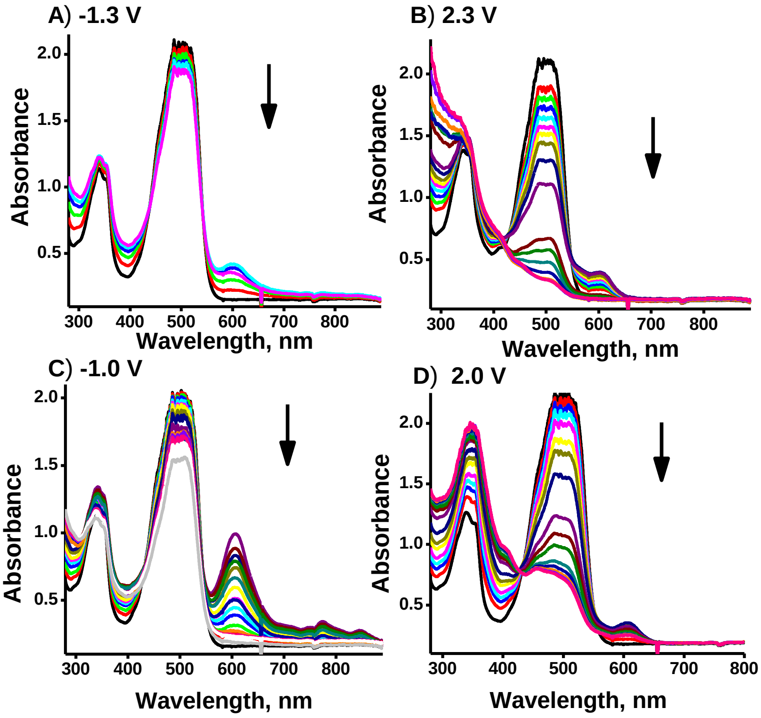

Figure 2.19 *Shows spectroelectrochemical spectra of A)* ***NP*** *at -1.3 V; B)* ***NP*** *at 2.3 V; C)* ***NP*** *at -1.0 V and D)* ***NP*** *at 2.0 V in acetonitrile/chloroform mixture under ambient conditions at intervals of 10 s.*

naphthalenimide moiety when monitored at 470 nm (Φ_T = 0.49)[151], as reported earlier.

In Figure 2.21, the cyclic voltammogram of **NP** in $CH_3CN/CHCl_3$ is shown together with those of the model derivatives **NI** and **PI.** A comparison with the model derivatives reveals that the three reversible reduction waves of **NP** correspond to two reversible reductions of the **PI** moiety followed by one reduction of the **NI** moiety (Table 2.4). The oxidation of **NP** reveals three reversible peaks, which results from two reversible oxidation waves of the perylenimide unit and one reversible oxidation wave from the naphthalenimide unit (Table 2.4). From these measurements, it is evident that for **NP** the first reduction peak involves the formation of the perylenimide anion [E_0(**NP**/**NP**$^-$) = 0.97 V vs. Ag/AgCl], whereas the first oxidation results in the perylenimide cation [E_0(**NP**/**NP**$^+$) = +1.48 V vs. Ag/AgCl].

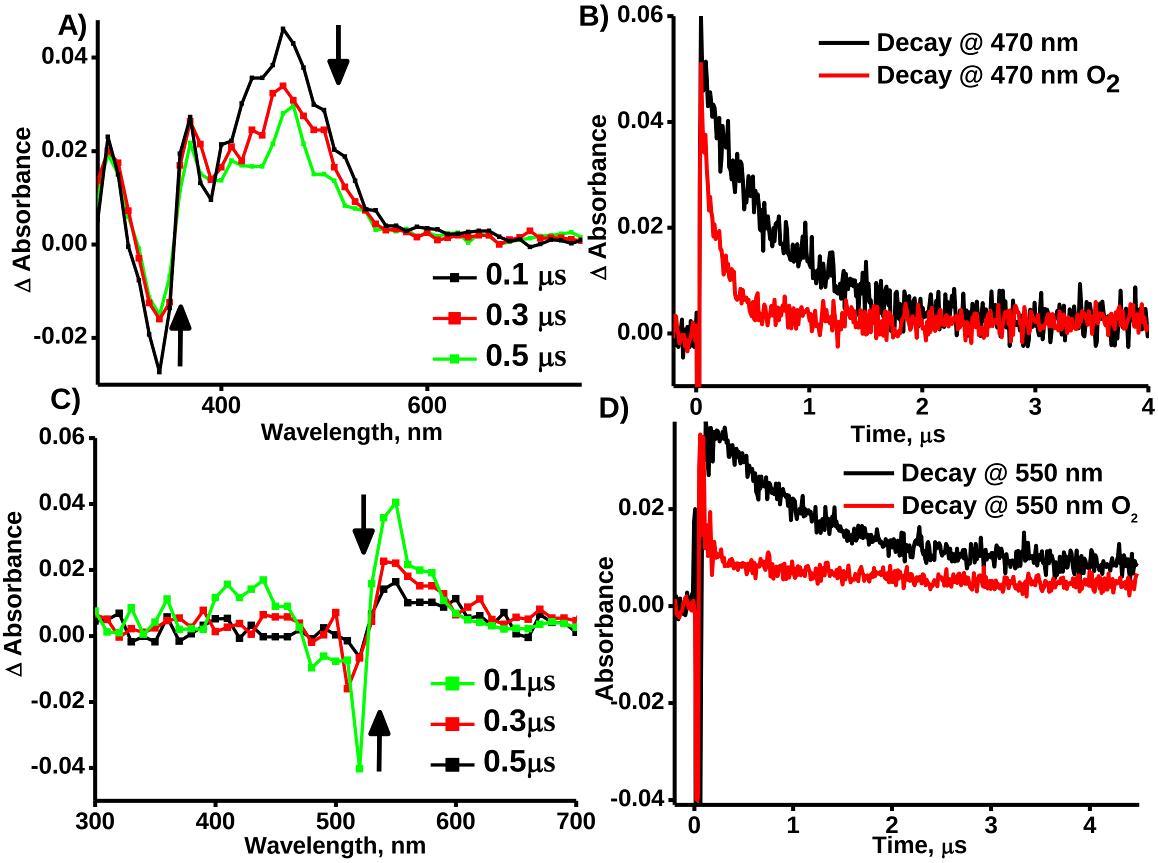

Figure 2.20 *Shows transient absorption spectra of A)* ***NI****; C)* ***NP*** *in toluene; B); D) corresponding decay profiles; excited at 355 nm.*

2.2.3 Photophysical and Redox Properties of the Conjugate NP

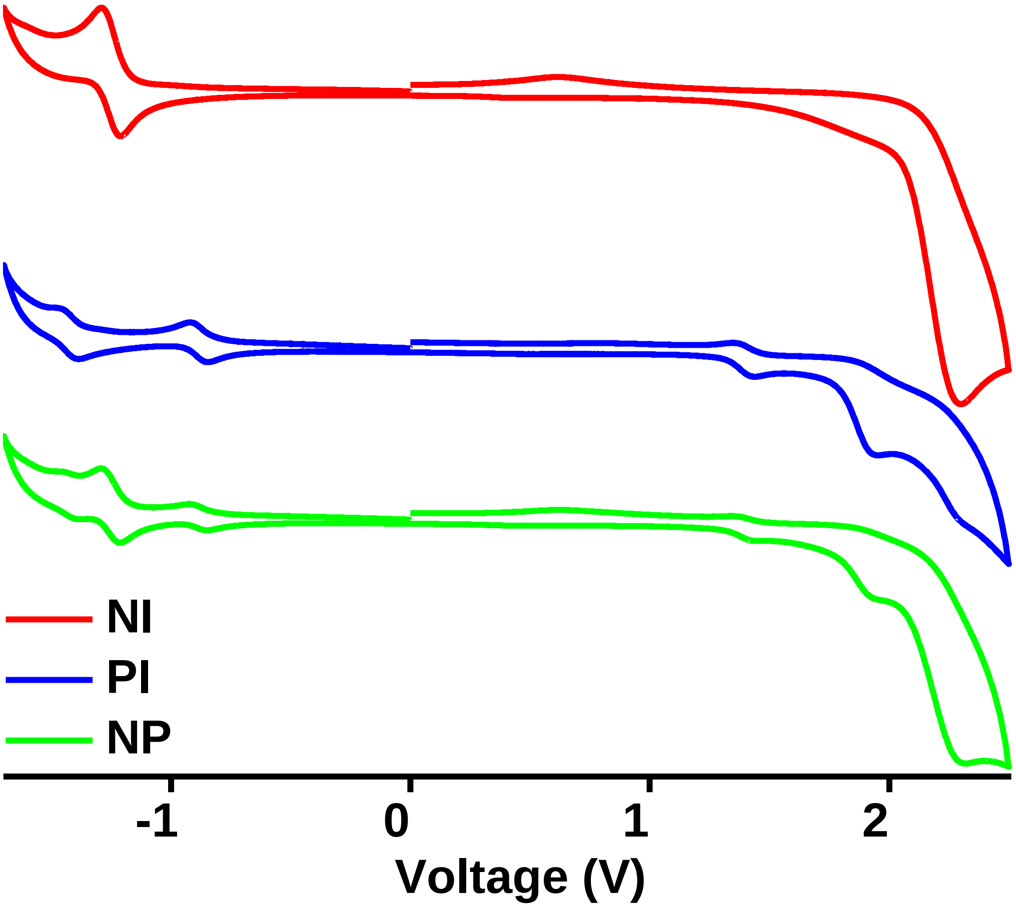

Figure 2.21 *Cyclic voltammogram of* **NI**, **PI** *and* **NP** *in* $CH_3CN/CHCl_3$ *(3:2) mixture.*

Table 2.4 *The redox potentials (V vs. Ag/AgCl) of conjugate* **NP** *and derivatives* **NI** *and* **PI** *in* $CH_3CN/CHCl_3$ *mixture.*

	E_{ox}	E_{red}	$E_{0,0}$
NI	2.26	-1.33	3.38
PI	1.49, 2.01	-0.95, -1.49	2.38
NP	1.48, 2.08, 2.27	-0.97, -1.33, -1.49	2.40

The energy difference between oxidation and reduction of **NP** hence amounts to 2.45 eV, consistent to difference in value for **PI** (2.44 eV). This clearly confirms that theidentity of two redox centers[155] is unperturbed in the conjugate **NP**, though connected through a single covalent bond.

2.2.4 Energy and Electron Transfer from Naphthalenimide to Perylenimide Unit

In Figures 2.22 and 2.23 the strength of the electrodynamic coupling V_{ed} between **NI** and **PI** computed using their transition density cubes (TDCs) is shown. Figure 2.22 shows the dependence of the coupling on the torsional angle between the energy donor and acceptor while keeping the distance between them equal to 1.49 Å. Figure 2.23 shows the dependence on the distance between the two chromophoric units while the torsional angle is kept equal to that of the conjugate **NP** (78°). The dipole-dipole interaction is also shown in Figure 2.22 (green solid line) to illustrate the extent to which ideal dipole approximation fails to estimate the coupling between the two chromophores accurately. A deviation from R^{-6} in distance and angular dependence of Coulombic coupling is clearly indicative of the existence of higher order interactions between the naphthalenimide (donor) and the perylenimide (acceptor) moeity. The results obtained from the TDC calculations indicate a strong coupling of 3.5 cm^{-1} and the rate of energy transfer k_{ET} = 2.2×10^{10} s^{-1} from naphthalenimide to perylenimide moiety at a dihedral angle of 75 ° and separartion

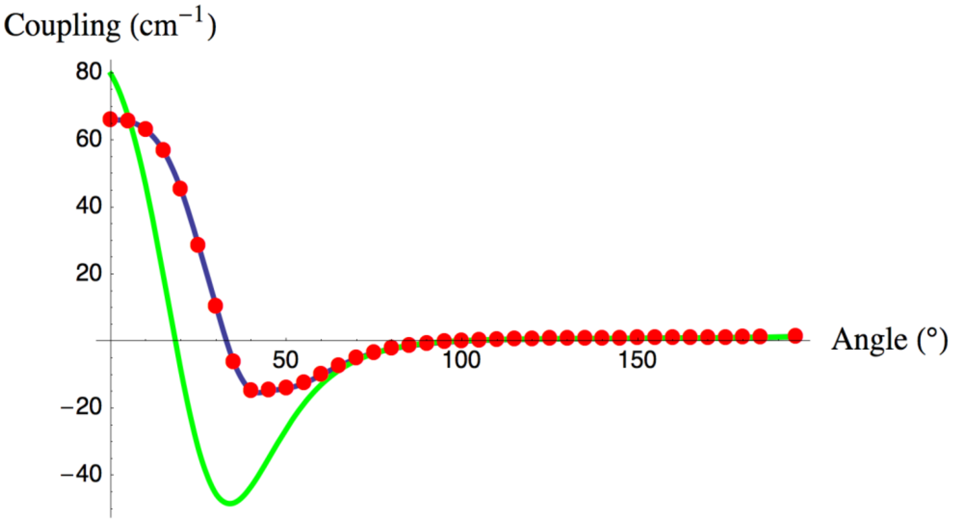

Figure 2.22 *Torsional angle dependence on Coulombic coupling between naphthalenimide (energy donor) and perylenimide (energy acceptor). The green line shows the coupling computed using the ideal dipole approximation.*

2.2.4 Energy and Electron Transfer from Naphthalenimide to Perylenimide Unit

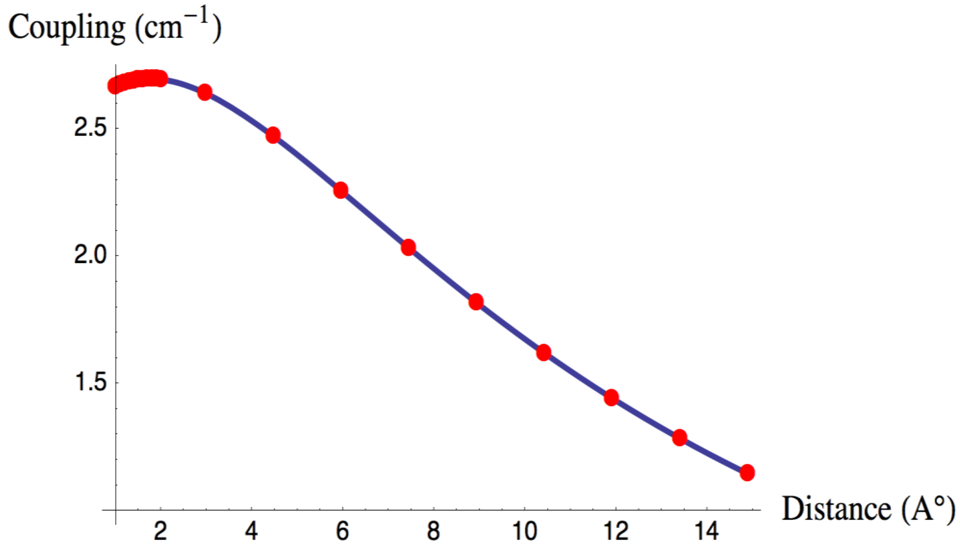

Figure 2.23 *Distance dependence on Coulombic coupling between naphthalenimide (energy donor) and perylenimide (acceptor).*

distance of 1.49 Å. The shallow nature of the twist-potential (75 ± 15 °) between the two chromophoric units can allow the dyad to adopt various conformers in solution thereby resulting in different coupling strengths.

FMO analysis further supports the possibility of photoinduced electron and excitation ET. The fact that HOMO - 1 and LUMO + 1 of the **NP** (electron density located on donor naphthalenimide moiety) is bracketed outside the HOMO - LUMO gap of the conjugate **NP** (electron density located on acceptor perylenimide moiety) accounts for the possibility of minimal radiative photoinduced electron transfer followed by nonradiative relaxation, i.e. excitation energy transfer (Figure 2.24)[156-159]. It is also apparent from the FMO calculations, that the orbitals involved in the electronic transitions are localized in respective chromophores and hence the efficiency of energy transfer via orbital overlap is negligible.

The absence of the triplet state corresponding to naphthalenimide moiety in conjugate **NP** is indicative of the fact that the ultrafast energy and electron transfer processes are competing to prevent the population of alternate delayed processes such as phosphorescence. Significantly higher triplet quantum yield of conjugate **NP** corresponding to perylenimide moiety compared to the model derivative **PI** suggests the possibility of recombination of charge separated state leading to the formation of triplet excited state as the possible pathway, as shown in Figure 2.20[144]. The absence of the triplet state and the phosphorescence corresponding to naphthalenimide unit in conjugate **NP** rules out the possibility of the formation of **PI** triplet state through Dexter type energy transfer from naphthalenimide (donor) to perylenimide (acceptor) moiety in conjugate **NP**. Thus overall efficiency in energy transfer (ca. 90%) can be attributed to predominant Coulombic interactions, with the remaining 10% efficiency dissipated via photo-induced electron transfer resulting in the formation of triplet state of perylenimide moiety. In view of the negligible orbital overlap between the electronic systems, the present work allows the accurate quantification of the contributions from higher order interactions to the overall Coulombic coupling for excitation energy transfer excluding other energy transfer mechanisms.

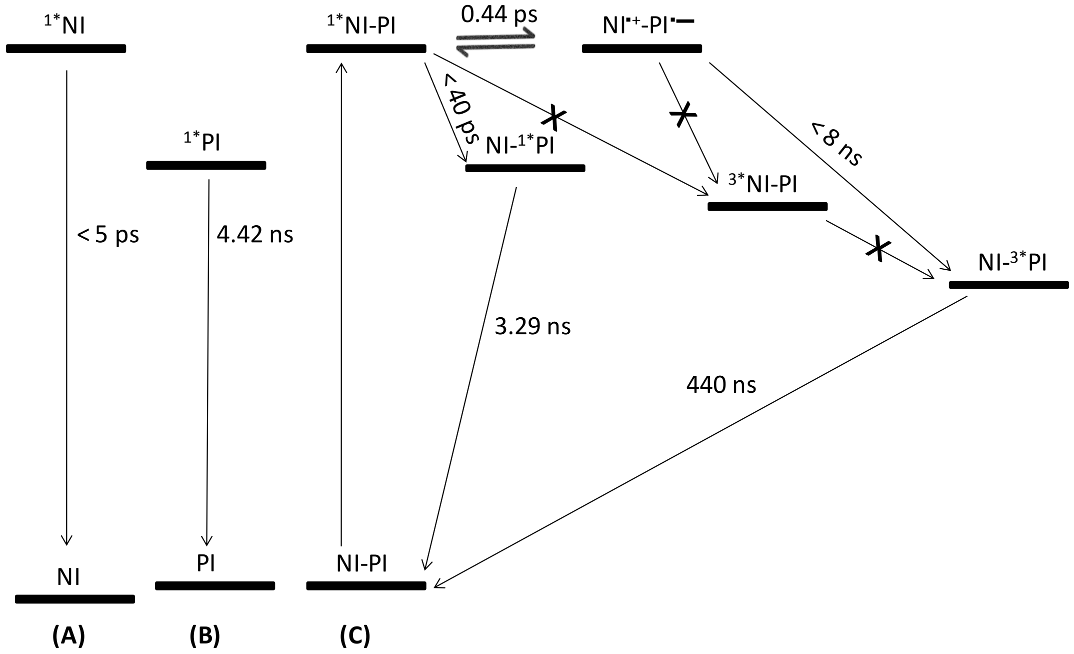

Figure 2.24 *The energy level diagram for (A)* ***NI****; (B)* ***PI*** *and* ***NP*** *(indicated for clarity as* ***NI-PI*** *in this scheme) in toluene excited at 355 nm.*

By virtue of steric repulsion between interchromophoric hydrogens present in the conjugate **NP** (similar to that of 1,1′-binaphthyl system), the conjugate assumes near-orthogonal arrangement of the chromophoric subunits as confirmed from the crystal structure and 2D NMR measurements. Despite being at the proximity of a carbon-carbon single covalent bond (1.49 Å), the orthogonal arrangement of chromophoric units makes the conjugate **NP** a combination of two independent chromophores/redox centers. Such behaviour could be attributed to the poor orbital overlap of the two chromophoric units in the orthogonal arrangement. The identity of the two units is confirmed using UV-Visible, fluorescence and electrochemical studies. Excitation of naphthalenimide (donor) moiety results in highly efficient energy transfer (90%) leading to fluorescence of perylenimide moiety (acceptor). Excitation energy transfer (k_{ET} = 2.2 × 10^{10} s^{-1}) observed could be due to efficient spectral overlap and favorable dipole-dipole orientation (Figure 2.25). Moreover, a minor pathway (<10%) of photoinduced electron transfer from singlet excited state of naphthalenimide to perylenimide moiety (Figure 2.24) leads to a charge separated state.

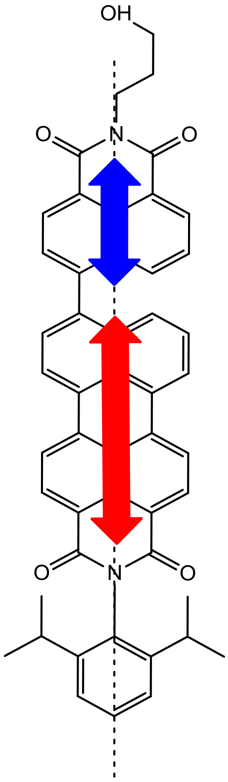

Figure 2.25 *Shows the orientation of transition dipole moment of napthalenimide (blue) and perylenimide (red) units for their respective S_0 - S_1 transitions in the dyad* ***NP****.*

2.3 Conclusions

In conclusion, we have designed and synthesized a donor-acceptor conjugate at a separation distance of a single bond (1.49 Å). Sterically driven orthogonality retains the individuality of the two chromophores/redox centers as confirmed through crystal structure, cyclic voltammetry and photophysical studies. Upon photoexcitation at 345 nm, we observed efficient energy transfer from naphthalenimide (donor) to perylenimide (acceptor) moiety leading to solvatochromic perylenimide fluorescence emission. Orthogonalization of the chromophores enforced by the steric barrier allows the donor and the acceptor moieties to be held at a distance of a single bond maximizing Coulombic coupling and simultaneously nullifying any orbital overlap contribution to energy transfer. Transition density cube (TDC) analysis showed strong Coulombic coupling between the transition densities of napthalenimide and perylenimide moieties. Transient absorption studies and FMO analysis unequivocally suggests that energy transfer predominantly occurs via through space interactions. Marginal radiative electron transfer; high fluorescence quantum yield (Φ_F = 0.81), wide excitation range and large solvatochromic shift (240 nm) makes the energy transfer conjugate **NP** attractive for biological applications[29]. Further progress is underway in our laboratory to incorporate this conjugate in oligonucleotides.

2.4 Experimental section

2.4.1 Materials and Methods

All chemicals were obtained from commercial suppliers and used as received without further purification. All reactions were carried out in glassware oven-dried prior to use and wherever necessary, were performed under dry nitrogen in dried, anhydrous solvents using standard gastight syringes, cannulae, and septa. Solvents were dried and distilled by standard procedures. TLC analyses were performed on precoated aluminum plates of silica gel 60 F254 plates (0.25 mm, Merck) and developed TLC plates were visualized under short and long wavelength UV lamps. Flash column chromatography was performed using silica gel of 200-400 mesh employing a solvent polarity correlated with the TLC mobility observed for the substance of interest. Yields refer to chromatographically and spectroscopically homogenous substances.

Melting points were obtained using a capillary melting point apparatus and are uncorrected. IR spectra were recorded on a Shimadzu IRPrestige-21 FT-IR spectrometer as neat thin films between NaCl plates in case of liquids and as KBr pellets in the case of solids. ^{1}H and ^{13}C NMR spectra were measured on a 500 MHz Bruker advanced DPX spectrometer. Internal standard used for ^{1}H and ^{13}C NMR is 1,1,1,1-tetramethyl silane (TMS). All CHN analyses were carried out on an Elementar vario MICRO cube Elemental Analyzer. All values recorded in elemental analyses are given in percentages. Absorption and emission spectra were recorded on Shimadzu UV-3600 UV-VIS-NIR and Horiba Jobin Yvon Fluorolog spectrometers respectively. The fluorescence quantum yields were determined by using optically matched solutions. Nile red in dioxane ($\Phi_F = 0.7$)[160] and anthracene in cyclohexane ($\Phi_F = 0.36$)[140] were used as the standards for perylenimide and naphthalenimide derivatives, respectively. Fluorescence measurements of perylene moiety were carried out at [**NI**]/[**PI**] $\approx$ 1000 and excited indirectly at 345 nm to rule out the possibility of radiative energy transfer mechanism between the two chromophoric units[29]. Fluorescence lifetime measurements were carried out in an IBH picosecond single photon counting system. The fluorescence decay profiles were de-convoluted using IBH data station software version 2.1, and fitted with a mono-exponential decay, minimizing the χ^2 values of the fit to 1 ± 0.05. Laser flash photolysis experiments of the argon purged solutions were carried out in an Applied Photophysics Model LKS-60 laser kinetic spectrometer using the third harmonic (355 nm) of a Quanta Ray INDI-40-10 series pulsed Nd:YAG laser. Triplet states of the **NI**,

PI and **NP** in toluene were confirmed using the measurement of oxygen purged solutions through nanosecond flash photolysis studies, as per the reported procedure[161,162]. Extent of triplet energy transfer from the sample (**NI**, **PI** or **NP**) to β-carotene in comparison with a reference compound, $Ru(bpy)^{3+}$ ($\Phi_T = 1$) to β-carotene provided the triplet yield of the compounds. Cyclic voltammetry was performed on a BASi E2 cyclic voltammeter with tetrabutylammoniumhexafluorophosphate as supporting electrolyte in acetonitrile/chloroform mixture. A standard three-electrode configuration was used with a platinum disc (diameter: 1.6 mm) working electrode, a platinum wire auxiliary electrode and Ag/AgCl (3M NaCl) reference electrode. A scan rate of 100 mV/s was used throughout the measurements. The scans were performed using a Ag/AgCl reference electrode with a ferrocene-ferrocenium couple (Fc/Fc^+) as an external standard (+0.47 V vs Ag/AgCl in CH_3CN). Electrochemical measurements were performed at room temperature with nitrogen-purged solutions. UV-Vis spectroelectrochemical studies were carried out using Ocean Optics DT-Mini-2 UV-Vis spectrometer coupled with the BASi E2 cyclic voltammeter. All spectroscopic experiments were performed using standard quartz cuvettes of path length 1 cm and using dried and distilled solvents.

2.4.2 X-ray Crystallography

Red, single crystals of conjugate **NP**, which exhibited needle morphology, was grown from an ethanol/chloroform diffusion. A high quality specimen of approximately 0.25 × 0.05 × 0.05 mm^3 was selected for the X-ray diffraction experiment. Single crystals were mounted using oil (Infineum V8512) on a glass fiber. All measurements were made on a CCD area detector with graphite monochromated CuKα radiation. The data was collected using Bruker APEXII detector and processed using APEX2 from Bruker. All structures were solved by direct methods and expanded using Fourier techniques. The non-hydrogen atoms were refined anisotropically. Hydrogen atoms were included in idealized positions, but not refined. Their positions were constrained relative to their parent atom using the appropriate HFIX command in SHELXL-97.

2.4.3 Computational Methods

DFT geometry optimization[163] using nonlocal hybrid three-parameter Lee-Yang-Parr (B3LYP)[147,148] level of theory with the (6-31G+(d,p)) basis set as implemented in the Gaussian 09W program suite was performed to optimize all the structures[146] and energy of the frontier molecular orbitals (FMO) was obtained using simple extended Hückel approximation using ChemBioOffice Ultra 2010. Electronic spectra were calculated using optimized structures subjected to unrestricted open shell time dependent DFT calculations (B3LYP/6-311G++(2d,2p)). The polarisable continuum model (PCM)[149] was used for the solvent calculations which were performed at B3LYP/6311G++(2d,2p) level. Number of excitations used was 45. Output of the calculations was viewed and analysed using GaussView 5.0. The transition densities corresponding to the HOMO to LUMO transitions for both **NI** and **PI** fragments were computed[44,132] using Qchem 3.2.0.2. For **NI** the transition density cube was computed on a grid of 83 × 66 × 50 = 273900 points while for **PI** the grid had 107 × 66 × 75 = 529650 points. The independently computed TDC cubes were read into Matlab R2009 for implementing the coordinate transformation that fixes the relative orientation of the two fragments. This gives the freedom to change the distance between the chromophore as well as the torsional angle between them at will. Modified TDCs with shifted and rotated coordinates is the output of a custom made Matlab program. These TDCs were used as input to the Coupling6 program for which the source code was kindly provided by Prof. Brent P. Krueger. The electrodynamic coupling given in Eq. 2.9, that is the dominant contribution to EET, is computed for various separations between the chromophores and for various torsional angles between them using Coupling6. The program also offers the dipole-dipole coupling allowing a comparison of the full interaction with the ideal dipole approximation for conjugate **NP**.

2.4.4 Synthesis Details

2.4.4.1 Synthesis of N-(3-hydroxypropyl)-naphthalene-1,8-dicarboximide 2 (NI)

To a solution of 1,8-naphthalic anhydride (**1**) (1.00 g, 5.05 mmol) in 100 ml of water 3-aminopropanol (3.79 g, 50.50 mmol) was added and heated at 70 °C for 5 h. The reaction mixture was then cooled and filtered; the precipitate was washed with water and dried. Purification by column chromatography (silica gel, EtOAc : petroleum ether 1 : 1) afforded compound **2** (1.16 g, 90%) as a white solid. mp 76 °C;^{1}H NMR (500 MHz, $CDCl_3$): δ = 8.53 (d, J = 7.5 Hz, 2H), 8.16 (d, J = 8.5 Hz, 2H), 7.69 – 7.68 (m, 2H), 4 .27 (t, J = 6.5 Hz, 2H), 3.52 – 3.51(m, 2H), 3.16 (s, 1H), 1.94 – 1.90 (m, 2H); ^{13}C NMR (125 MHz, $CDCl_3$): δ = 164.90, 134.31, 131.60, 131.58, 128.16, 127.04, 122.28, 58.90, 36.81, 30.98;IR (KBr): 3460, 3192, 2953, 2860, 2401, 1693, 1653,1622, 1587, 1444, 1392, 1361, 1350, 1242, 1274, 1170, 1074, 1058, 923, 850, 783, 734 cm^{-1}; Anal. Calcd. for $C_{15}H_{13}NO_3$: C, 70.58; H, 5.13; N, 5.49. Found: C, 70.34; H, 5.58; N, 5.20.

2.4.4.2 Synthesis of 4-Bromo-N-(3-hydroxypropyl)-naphthalene-1,8-dicarboximide 4 (NI-Br)

To a solution of 4-bromo-1,8-naphthalic anhydride (**3**) (1.00 g, 3.60 mmol) in 100 ml water 3-aminopropanol (2.70 g, 36.00 mmol) was added. This reaction mixture was heated at 70 °C for 5 h following which it was filtered and the precipitate was washed with water and dried. The crude product was then purified by column chromatography (silica gel, EtOAc : petroleum ether 1 : 1) to afford compound **4** (1.08 g, 90%) as a white solid. mp 125 °C; ^{1}H NMR (500 MHz, $CDCl_3$): δ = 8.60 (d, J = 7 Hz, 1H), 8.52 (d, J = 8.5 Hz, 1H), 8.35 (d, J = 7.5 Hz, 1H), 7.99 (d, J = 8 Hz, 1H), 7.79 (t, J = 8 Hz, 1H), 4.27 (t, J = 6 Hz, 2H), 3.53 (t, J = 5.5 Hz, 2H), 2.13 (s, 1H), 1.92 - 1.90 (m, 2H); ^{13}C NMR (125 MHz, $CDCl_3$): δ = 164.23, 164.22, 133.58, 132.35, 131.52, 131.19, 130.67, 130.64, 128.98, 128.16, 122.74, 121.85, 59.00, 37.01, 30.98; IR (KBr): 3473, 2972, 2939, 2862, 2358, 1695, 1647, 1589, 1570, 1438, 1340, 1332, 1232, 1180, 1126, 1074, 1039, 954, 846, 779, 767, 750, 734 cm^{-1}; Anal. Calcd. for $C_{15}H_{12}BrNO_3$: C, 53.91; H, 3.62; N, 4.19. Found: C, 54.04; H, 3.69; N, 4.20.

2.4.4.3 Synthesis of 4-tributylstannyl-N-(3-hydroxypropyl)-naphthalene-1,8-dicarboximide 5

A solution of 4-Bromo-N-(3-hydroxypropyl)-naphthalene-1,8-dicarboximide (**4**) (0.50 g, 1.49 mmol), hexabutylditin (1.74 g, 2.99 mmol) and $Pd(PPh_3)_4$ (5.16 mg, 4.46 μmol) in 40 ml toluene was refluxed for 4 days. The solvent was then removed under reduced pressure and the residue was purified by column chromatography (silica gel, EtOAc : petroleum ether 1 : 9) to give the product **5** (0.45 g, 52.9%) as a viscous yellow liquid. ^1H NMR (500 MHz, $CDCl_3$): δ = 8.56 (d, J = 7.3 Hz, 1H), 8.43 (d, J = 7 Hz, 1H), 8.08 (d, J = 8.25 Hz, 1H), 7.86 (d, J = 7 Hz, 1H), 7.72 – 7.69 (m, 1H), 4.28 (t, J = 6 Hz, 2H), 3.53 – 3.50 (m, 2H), 3.17 – 3.15 (m, 1H), 1.93 – 1.91 (m, 2H), 1.51 – 1.45 (m, 6H), 1.30 – 1.18 (m, 12H), 0.80 (t, J = 7.3 Hz, 9H) ; ^{13}C NMR (125 MHz, $CDCl_3$): δ = 165.41, 164.88, 155.27, 137.51, 136.55, 136.01, 131.17, 129.88, 128.14, 126.61, 123.08, 122.14, 58.86, 36.70, 31.03, 29.07, 27.24, 13.58, 10.88; IR (KBr): 3606, 3506, 3018, 2958, 2927, 2852, 2358, 1708, 1695, 1651, 1585, 1508, 1444, 1365, 1344, 1232, 1224, 1176, 1126, 1045, 999, 950, 862, 788, 769, 756, 725 cm^{-1}; Anal. Calcd. for $C_{27}H_{39}NO_3Sn$: C, 59.58; H, 7.22; N, 2.57. Found: C, 59.52; H, 6.80; N, 2.51.

2.4.4.4 Synthesis of 4-Phenyl-N-(3-hydroxypropyl)-naphthalene-1,8-dicarboximide 6 (NI-Ph)

A solution of 4-tributylstannyl-N-(3-hydroxypropyl)-naphthalene-1,8-dicarboximide (**5**) (0.35 g, 0.64 mmol), bromobenzene (0.15 g, 0.96 mmol) and $Pd(PPh_3)_4$ (11.37 mg, 9.83 μmol) in 35 ml toluene was refluxed for 4 days. The solvent was evaporated and purification of the residue by column chromatography (silica gel, EtOAc : petroleum ether 1 : 4) afforded the compound **6** (0.16 g, 77%) as a yellow solid. mp 165 °C;^1H NMR (500 MHz, $CDCl_3$): δ = 8.61 – 8.58(m, 2H), 8.24 – 8.22 (m, 1H), 7.67 – 7.64 (m, 2H), 7.50 – 7.43 (m, 5H), 4.32 (t, J = 6.25 Hz, 2H),3.56 – 3.52 (m, 2H), 3.11 – 3.08 (m, 1H), 1.98 – 1.93 (m, 2H); ^{13}C NMR (125 MHz, $CDCl_3$): δ = 165.08, 164.90, 147.41, 138.68, 133.13, 131.62, 131.27, 130.11, 129.88, 128.75, 128.72, 128.60, 127.97, 126.96, 122.49, 121.33, 58.84, 36.79, 31.01; IR (KBr):3547, 3055, 2960, 2924, 2879, 2808, 1961, 1695, 1651, 1614, 1587, 1514, 1492, 1465, 1442, 1388, 1363, 1346, 1307, 1267, 1230, 1176, 1138, 1085, 1068, 1058, 1012, 943, 920, 873, 785, 767, 756, 738, 704 cm^{-1}; Anal. Calcd. for $C_{21}H_{17}NO_3$: C, 76.12; H, 5.17; N, 4.23. Found: C, 76.60; H, 5.38; N, 4.12.

2.4.4.5 Synthesis of 4-(Trimethylsilylethynyl)-N-(3-hydroxypropyl)-naphthalene-1,8-dicarboximide 7

4-Bromo-N-(3-hydroxypropyl)-naphthalene-1,8-dicarboximide (**4**) (0.40 g, 1.20 mmol) and trimethylsilylacetylene (0.11 g, 1.20 mmol) were dissolved in 25 ml diisopropylamine along with CuI (4.64 mg, 24.3 μmol) and $PdCl_2(PPh_3)_2$ (16.84 mg, 24.02 μmol). The resulting yellow solution was stirred for 1 h at room temperature and then refluxed for 30 min. The solvent was then removed under reduced pressure and column chromatography (silica gel, EtOAc : petroleum ether 1 : 9) of the residue yielded the product **7** (0.25 g, 60%) as a pale yellow solid. mp 152 °C;^{1}H NMR (500 MHz, $CDCl_3$): δ = 8.59 – 8.56 (m, 2H), 8.45 (d, J = 7.6 Hz, 1H), 7.83 (d, J = 7.6 Hz, 1H), 7.78 – 7.75 (m, 1H), 4.27 (t, J = 6.25 Hz, 2H), 3.54 – 3.51 (m, 2H), 3.05 – 3.02 (m, 1H), 1.94 – 1.90 (m, 2H), 0.30 (s, 9H) ; ^{13}C NMR (125 MHz, $CDCl_3$): δ = 164.85, 164.55, 132.98, 132.11, 131.97, 131.41, 130.79, 128.14, 127.91, 127.76, 122.69, 122.05, 105.93, 101.30, 59.11, 37.06, 31.16, 1.18; IR (KBr): 3404, 2954, 2154, 1701, 1662, 1589, 1508, 1438, 1357, 1234, 1176, 1055, 864, 844, 781, 752 cm^{-1}; Anal. Calcd for $C_{20}H_{21}NO_3Si$: C, 68.35; H, 6.02; N, 3.99. Found: C, 68.34; H, 6.04; N, 4.10.

2.4.4.6 Synthesis of 4-Ethynyl-N-(3-hydroxypropyl)-naphthalene-1,8-dicarboximide 8 (NI-Ac)

4-(Trimethylsilylethynyl)-N-(3-hydroxypropyl)-naphthalene-1,8-dicarboximide (**7**) (0.24 g, 0.70 mmol) and K_2CO_3 (0.99 g, 7.16 mmol) were stirred in 12.5 ml dry methanol at room temperature for 1 h. The solvent was removed under reduced pressure and purification by column chromatography (silica gel, EtOAc : petroleum ether 1 : 2) afforded the compound **8** (0.14 g, 74%) in the form of a yellow solid. mp 155 °C;^{1}H NMR (500 MHz, $CDCl_3$): δ = 8.60 (d, J = 8.35 Hz, 2H), 8.56 (d, J = 7.20, 1H), 8.46 (d, J = 7.5 Hz, 1H), 7.86 (d, J = 7.5 Hz, 1H), 7.78 – 7.75 (m, 1H), 4.27 (t, J = 7.0 Hz, 2H), 3.69 (s, 1H), 3.54 – 3.52 (m, 2H), 3.01 (s, 1H), 1.93 – 1.91 (m, 2H); ^{13}C NMR (125 MHz, $CDCl_3$): δ = 164.58, 164.29, 132.57, 132.04, 131.95, 131.69, 130.51, 127.93, 127.77, 126.65, 122.58, 122.38, 86.84, 80.21, 58.96, 36.95, 30.99;IR (KBr): 3469, 3213, 3072, 2951, 2926, 2856, 2362, 2094, 1751, 1697, 1639, 1612, 1589, 1512, 1442, 1386, 1367, 1325, 1278, 1234, 1182, 1083, 1056, 1029, 999, 972, 931, 879, 858, 781, 734, 704, cm^{-1}; Anal. Calcd. for $C_{17}H_{13}NO_3$: C, 73.11;H, 4.69; N, 5.02. Found: C, 73.48; H, 4.447; N, 5.29.

2.4.4.7 Synthesis of N-(2,6-diisopropylphenyl)-perylene-3,4-dicarboximide 10 (PI)

A solution of perylene-3,4,9,10-tetracarboxylic dianhydride (**9**) (3.66 g, 9.34 mmol), 2,6-diisopropylaniline (0.91 g, 5.12 mmol), zinc acetate (1.32 g, 7.19 mmol) and imidazole (18.70 g, 274.70 mmol) in 8 ml water was heated at 190 °C in a pressure tube for 23 h. The reaction mixture was extracted by chloroform and filtered through celite. The filtrate was then washed with dilute HCl and water and concentrated under reduced pressure to give a brown-red residue which was then purified by column chromatography (silica gel, chloroform : petroleum ether 3 : 2) to produce compound **10 (**1.291 g, 30%) as a red solid. mp> 300 °C;^{1}H NMR (500 MHz, $CDCl_3$): δ = 8.58 (d, J = 8 Hz, 2H), 8.39 – 8.36 (m, 4H), 7.84 (d, J = 8 Hz, 2H), 7.57 (t, J = 8 Hz, 2H), 7.41 (t, J = 8 Hz, 1H), 7.27 (d, J = 8 Hz, 2H), 2.70 – 2.68 (m, 2H), 1.11(d, J = 7 Hz,12H); ^{13}C NMR (125 MHz, CDCl3): δ = 163.99, 145.73, 137.46, 134.25, 131.94, 131.10, 130.50, 129.44, 129.15, 127.93, 127.00, 126.97, 124.02, 123.78. 120.97, 120.13, 29.19, 24.03; IR (KBr): 3061, 2962, 2926, 2868, 1693, 1654, 1589, 1568, 1500, 1467, 1408, 1357, 1294, 1246, 1197, 1178, 1136, 1029, 920, 889, 858, 831, 810, 754 cm^{-1};Anal. Calcd. for $C_{34}H_{27}NO_2$: C, 84.80; H, 5.65; N, 2.91. Found: C, 84.89; H, 5.62; N, 2.96.

2.4.4.8 Synthesis of 9-Bromo-N-(2,6-diisopropylphenyl)-perylene-3,4-dicarboximide 11 (PI-Br)

N-(2,6-diisopropylphenyl)-perylene-3,4-dicarboximide (**10**) (1.0 g, 2.07 mmol) was dissolved in 100 ml chlorobenzene with moderate heating. To this solution bromine (1.50 g, 9.50 mmol) was added and the reaction mixture heated at 50 °C for 4.5 h. Chlorobenzene and unreacted bromine were removed under vacuum and the residue was purified by column chromatography (silica gel, chloroform : petroleum ether 2 : 3) to yield compound **11** (0.93 g, 80%) as a bright red solid. mp > 300 °C; ^{1}H NMR (500 MHz, $CDCl_3$): δ = 8.60 – 8.57 (m, 2H), 8.41 – 8.37 (m, 2H), 8.32 (d, J = 8 Hz, 1H), 8.23(d, J = 8.5 Hz, 1H), 8.15 (d, J = 8.5 Hz, 1H), 7.83 (d, J = 8 Hz, 1H), 7.64 (t, J = 7.5 Hz, 1H), 7.42 (t, J = 8 Hz, 1H), 7.28 (d, J = 8 Hz, 2H), 2.72 – 2.10 (m, 2H), 1.12(d, J = 7 Hz, 12H);^{13}C NMR (125 MHz, $CDCl_3$): δ = 163.88, 145.72, 136.86, 136.73, 132.97, 132.10, 132.03, 131.28, 130.96, 130.41, 130.05, 129.61, 129.48, 129.14, 129.06, 128.16, 126.64, 126.21, 124.45, 124.03, 123.78, 121.42, 120.72, 120.45, 29.18, 24.00; IR (KBr): 3061, 2962, 2926, 2868, 1693, 1654, 1589, 1568, 1500, 1467, 1408, 1357, 1294, 1246, 1197, 1178, 1136, 1029, 920, 889, 858, 831, 810, 754 cm^{-1}; Anal. Calcd. for $C_{34}H_{26}BrNO_2$: C, 72.86; H, 4.68; Br, 14.26; N, 2.50. Found: C, 72.39; H, 4.97; N, 2.39.

2.4.4.9 Synthesis of 9-Phenyl-N-(2,6-diisopropylphenyl)-perylene-3,4-dicarboximide 12 (PI-Ph)

9-Bromo-N-(2,6-diisopropylphenyl)-perylene-3,4-dicarboximide (**11**) (0.1 g, 0.18 mmol), phenyl boronic acid (18 mg, 0.15 mmol) and $Pd(PPh_3)_4$ (17 mg, 14.7 μmol) were dissolved in 9 ml toluene and 1.37 ml of 1M aqueous K_2CO_3. This reaction mixture was heated at 100 °C for 24 h, after which it was extracted using chloroform. The solvent was removed under reduced pressure and the residue purified by column chromatography (silica gel, EtOAc : petroleum ether 1 : 1) to yield the product **12** (10 mg, 10%)as a red solid. mp> 300 °C; ^{1}H NMR (500 MHz, $CDCl_3$): δ = 8.67 (d, J = 7.95 Hz, 2H), 8.54 – 8.47 (m, 4H), 8.02 (d, J = 8.4 Hz, 1H), 7.62 – 7.46 (m, 8H), 7.35 – 7.33 (m, 2H), 2.79 – 2.75 (m, 2H), 1.18 (d, J = 6.75 Hz, 12H); ^{13}C NMR (125 MHz, $CDCl_3$): δ = 164.03, 145.75, 143.46, 139.85, 137.81, 137.62, 132.70, 132.13, 132.09, 131.09, 130.60, 130.00, 129.48, 129.39, 128.59, 128.53, 128.30, 128.01, 127.05, 124.01, 123.98, 123.60, 120.97, 120.88, 120.33, 120.09, 29.15, 24.03; IR (KBr): 3450, 2964, 2868, 2391, 2349, 2310, 1759, 1697, 1658, 1571, 1535, 1408, 1357, 1294, 1246, 1178, 1026, 898, 839, 812, 756, 702 cm^{-1}; Anal. Calcd. for $C_{40}H_{31}NO_2$: C, 86.15; H, 5.60; N, 2.51. Found: C, 86.31; H, 5.43; N, 2.66.

2.4.4.10 Synthesis of 9-(Trimethylsilylethynyl)-N-(2,6-diisopropylphenyl)-perylene-3,4-dicarboximide 13

9-Bromo-N-(2,6-diisopropylphenyl)-perylene-3,4-dicarboximide (**11**) (0.1 g, 0.18 mmol) and trimethylsilylacetylene (24 mg, 0.243 mmol) were dissolved in 30 ml toluene and 6 ml triethylamine along with CuI (2 mg, 10.5 μmol) and $PdCl_2(PPh_3)_2$ (12 mg, 17.11 μmol). The resulting dark red solution was refluxed for 24 h. The reaction mixture was then filtered and column chromatography (silica gel, EtOAc : petroleum ether 1 : 9) of the filtrate yielded the product **13** (73 mg, 74.5%) as a dark red solid. mp> 300 °C;^{1}H NMR (500 MHz, $CDCl_3$,): δ = 8.61 - 8.58 (m, 2H), 8.46 (d, J = 7.4 Hz, 1H), 8.43 – 8.36 (m, 3H), 8.33 (d, J = 8 Hz, 1H), 7.76 (d, J = 7.8 Hz, 1H), 7.68 (t, J = 7.9 Hz, 1H), 7.41 (t, J = 7.9 Hz, 1H), 7.27 (d, J = 7.8 Hz, 2H), 2.71 – 2.66 (m, 2H), 1.10 (d, J = 6.85, 12H), 0.3091 (s, 9H); ^{13}C NMR (125 MHz, $CDCl_3$): δ = 163.92, 163.90, 145.68, 137.20, 136.75, 134.31, 132.00, 131.89, 131.52, 130.98, 130.38, 129.46, 129.44, 129.25, 129.18, 127.62, 127.58, 126.68, 124.11, 124.01, 123.59, 122.92, 121.19, 121.02, 120.71, 120.41, 103.39, 102.45, 30.91, 29.15, 23.98; IR (KBr): 3446, 2358, 2330, 1942, 1869, 1843, 1791, 1701, 1653, 1558, 1456, 1417, 1361, 1247, 1128, 1056, 862, 771, 669, 580 cm^{-1}; Anal. Calcd. for $C_{39}H_{35}NO_2Si$: C, 81.07; H, 6.11; N, 2.42. Found: C, 81.89; H, 6.28 ; N, 2.44.

2.4.4.11 Synthesis of 9-Ethynyl-N-(2,6-diisopropylphenyl)-perylene-3,4-dicarboximide 14 (PI-Ac)

9-(Trimethylsilylethynyl)-N-(2,6-diisopropylphenyl)-perylene-3,4-dicarboximide (**13**) (0.1 g, 0.17 mmol) and K_2CO_3 (24 mg, 0.17 mmol) were stirred in 7 ml dry methanol and 3.5 ml dry dichloromethane at room temperature for 1 h. The solvent was removed under reduced pressure and purification by column chromatography (silica gel, EtOAc : petroleum ether 1 : 9) afforded the compound **14** (84 mg, 96%) in the form of a bright red solid. mp> 300 °C;^{1}H NMR (500 MHz, $CDCl_3$): δ = 8.67 – 8.64 (m, 2H), 8.47 – 8.40 (m, 4H), 8.35 (d, J = 7.9 Hz, 1H), 7.82 (d, J = 7.7 Hz, 1H), 7.70 (t, J = 7.7 Hz, 1H), 7.48 (t, J = 7.8 Hz, 1H), 7.35 (d, J = 7.9 Hz, 2H), 3.67 (s, 1H), 2.80 – 2.74 (m, 2H), 1.18 (d, J = 6.8 Hz, 12H); ^{13}C NMR (125 MHz, $CDCl_3$): δ = 163.90, 145.70, 137.15, 136.68, 134.54, 132.10, 132.04, 131.97, 130.96, 130.43, 129.95, 129.49, 129.46, 129.02, 127.82, 127.73, 126.80, 124.22, 124.04, 122.85, 122.54, 121.47, 121.22, 120.89, 120.59, 85.01, 81.36, 29.16, 24.02; IR (KBr): 3423, 3251, 2962, 1764, 1701, 1658, 1591, 1552, 1512, 1444, 1408, 1359, 1292, 1246, 1178, 1141, 1056, 991, 906, 839, 808, 771, 754 cm^{-1}; Anal. Calcd. for $C_{36}H_{27}NO_2$: C, 85.52; H, 5.38; N, 2.77. Found: C, 85.88; H, 5.59; N, 2.89.

2.4.4.12 Synthesis of 9-(4-(N-(3-hydroxypropyl)naphthalene-1,8-dicarboximide)yl)-N-(2,6-diisopropylphenyl)-perylene-3,4-dicarboximide 15 (NP)

A solution of9-Bromo-N-(2,6-diisopropylphenyl)-perylene-3,4-dicarboximide (**11**) (0.50 g, 0.89 mmol), 4-tributylstannyl-N-(3-hydroxypropyl)-naphthalene-1,8-dicarboximide (**5**) (0.61 g, 1.12 mmol) and $Pd(PPh_3)_4$ (10.28 mg, 8.89 µmol) in 50 ml DMFwas heated at 90 °C for 2 days. The solvent was removed under reduced pressure and the residue was purified by column chromatography (silica gel, EtOAc : petroleum ether 1 : 1) to afford compound **15** (0.33 g, 50%) as a yellow-orange solid. mp> 300 °C; ^{1}H NMR (500 MHz, $CDCl_3$): δ = 8.72 (d, J = 7.35 Hz, 1H), 8.67 – 8.60 (m, 3H), 8.56 (d, J = 7.9 Hz, 1H), 8.51 (d, J = 8.25 Hz, 1H), 8.46 (d, J = 8.1 Hz, 2H), 7.86 – 7.84 (m, 1H), 7.80 (d, J = 7.5 Hz, 1H), 7.62 – 7.57 (m, 2H), 7.47 – 7.40 (m, 2H), 7.35 (d, J = 8.5 Hz, 1H), 7.28 (d, J = 8 Hz, 2H), 4.37 (t, J = 6.2 Hz, 2H), 3.60 – 3.58 (m, 2H), 3.04 (s, 1H), 2.75 – 2.68 (m, 2H), 2.01 – 1.96 (m, 2H), 1.13 – 1.11 (m, 12H); ^{13}C NMR (125 MHz, $CHCl_3$): δ = 164.82, 164.67, 163.94, 145.75, 145.72, 144.72, 139.01, 137.27, 133.41, 132.91, 132.17, 132.14, 131.91, 131.15, 130.95, 130.10, 129.75, 129.53, 129.16, 129.06, 128.86, 128.56, 128.29, 127.70, 127.41, 126.99, 124.14, 124.07, 123.15, 122.71, 122.41, 121.41, 120.80, 120.68, 59.00, 36.98, 31.07, 29.19, 24.05, 24.03; IR (KBr): 3466, 2960, 2927, 2866, 2358, 1699, 1658, 1591, 1577, 1467, 1444, 1359, 1244, 1178, 1132, 1056, 1039, 844, 812, 786, 758, 748 cm^{-1}; Anal. Calcd. for $C_{49}H_{38}N_2O_5$: C, 80.09; H, 5.21; N, 3.81. Found: C, 80.59; H, 5.21; N, 3.85.

2.4.4.13 Synthesis of N-(2,6-diisopropylphenyl)-N′-(3-hydroxypropyl)-terrylene-3,4,11,12-tetracarboxdiimide 16 (T)

9-(4-(N-(3-hydroxypropyl)naphthalene-1,8-dicarboximide)yl)-N-(2,6-diisopropyl phenyl)-perylene-3,4-dicarboximide (**15**) (200 mg, 0.27 mmol) and K_2CO_3 (37 mg, 0.27 mmol) were stirred in ethanolamine (2.48 g, 40.6 mmol) under argon for 3 h at 160°C. After cooling down to room temperature, the solution was poured into methanol and then centrifuged. The supernatant was discarded and the pellet was dried under vacuum and purified by column chromatography (silica gel, $CHCl_3$: Methanol 19 : 1) to yield the blue colored product **16** (148 mg, 75%). mp> 300 °C;^{1}H NMR (500 MHz, $C_2D_2Cl_4$, 100 °C): δ = 8.61 (d, J = 7.55 Hz, 2H), 8.57 – 8.45 (m, 10H), 7.37 (t, J = 7.82 Hz, 1H), 7.23 (d, J = 7.75 Hz, 2H), 4.38 - 4.37 (m, 2H), 3.92 – 3.90 (m, 2H), 3.03 (s, 1H), 2.75 – 2.66 (m, 2H), 2.26 – 2.23 (m, 2H), 1.11(d, J = 6.75 Hz 12H); IR (KBr): 3421, 3165, 2918, 2848, 2677,2492, 2380, 1697, 1691, 1654, 1651, 1585, 1573,1471, 1398, 1379, 1251, 1035, 840, 810, 752 cm^{-1}.

Chapter 3

Single-Component Organic Light-Harvesting Red Luminescent Crystal of a Near-Orthogonal Dyad

3.1 Introduction

Organic solid-state luminescent materials[164] have immense importance in the area of optoelectronic and photonic devices[100,165,166]. Aggregation of π-conjugated molecules can either increase or decrease the luminescence quantum yield considerably going from dilute solutions to ordered phase. Aggregation can restrict certain bond rotations that can reduce the non-radiative loss resulting in aggregation induced enhanced emission (AIEE)[167-169]. On the other hand, intermolecular vibronic interactions such as excimer/exciplex formation and exciton coupling in the aggregate can quench the fluorescence through enhanced non-radiative deactivation of the excited state[29]. Recently, attention has been focussed towards the theoretical analysis[170,171] and crystal engineering[172,173] to orthogonally orient the long axes in the ordered phase to prevent non-radiative deactivation. Alternatively, we propose to incorporate orthogonal π-surface that promotes self-aggregation leading to crystallisation but prevents the association of the fluorescent chromophoric units. Though the constituent chromophores are arranged in orthogonal planes, the parallel orientation of transition dipoles of the donor and the acceptor moieties can efficiently transfer energy upon photoexcitation thereby making the dyad a light harvesting organic luminescent crystal. Moreover, light harvesting single molecule organic crystals have received very less attention[20,21]. Efficiency of energy and/or electron transfer in similar orthogonal chromophoric dyads are well-documented in solution[22-24], thin films[25], nickel oxide films[26] and liquid crystalline medium[27].

Publication based on this work has been reported in *J. Phys. Chem. C* **117**, 3240-3248 (2013)

3.1 Introduction

The first experimental observation for orthogonally oriented long axes in the crystalline state is reported by Xie, Z. *et al.*. Their work clearly demonstrates that cross dipole stacking in the crystal of distyrylbenzene derivative (trans-**DPDSB**) that exhibits high fluorescence quantum yield in the solid state (Figure 3.1A, B)[172]. The crystal

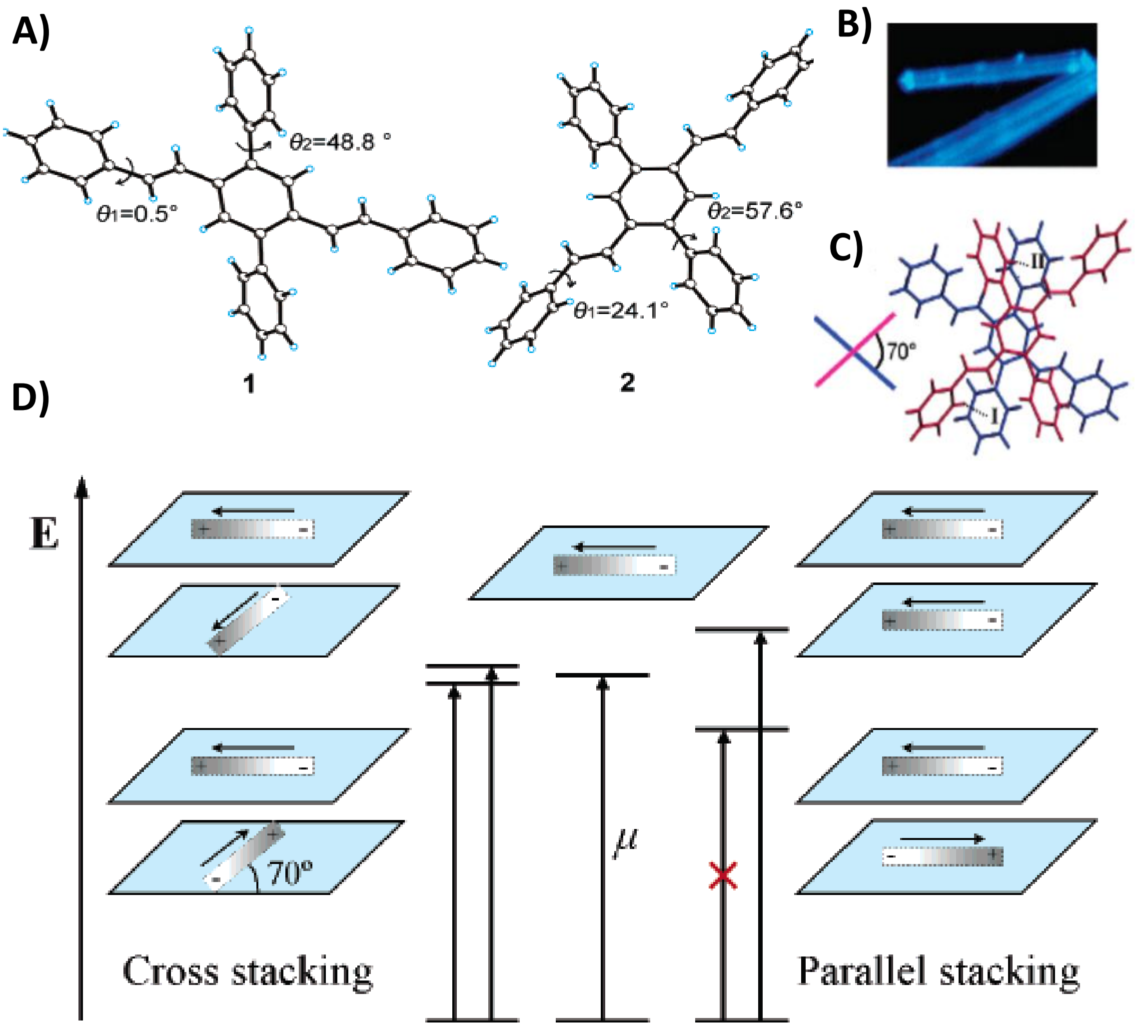

Figure 3.1 *A) Different conformational structures of trans-**DPDSB** in crystal; B) Crystals of trans-**DPDSB** under UV light (365 nm); C) Schematic of the aromatic CH/π hydrogen bonds between two adjacent molecules. Interaction distances for I and II are 3.08 and 2.67 Å respectively. Conformation **1** is drawn in blue and **2** in red and D) Splitting of the optically allowed transitions of a single chain (sketched in the middle) in a cross-stacking configuration (trans-DPDSB) and a parallel-stacking configuration (H-aggregate). Reprinted with permission from ref. [172]. Copyright 2005, American Chemical Society.*

data indicates that there are two crystallographically independent conformations of trans-**DPDSB** (Figure 3.1 A) in which two molecules are arranged in such a fashion that the long axes are inclined at an angle of 70° through aromatic CH/π interactions (Figure 3.1C). In the parallel stack of the dimer, the lowest excited state corresponds to the destructive combination of the transition dipole moment of the individual chains, and it is optically forbidden (Figure 3.1D). But in the cross-stacking dimer of trans-DPDSB , the energy splitting between the lowest two excited states of the dimer is reduced, and a progressive transfer of energy from the second excited state to the lowest excited state occurs (Figure 3.1D). This facilitates a finite transition dipole moment between the ground state and the lowest excited state of the clusters, which is highly favourable for the light-emission properties in the solid state.

Red luminescent organic molecules in the condensed media possess a strong tendency to aggregate that can result in quenching of fluorescence, due to (i) π-π interactions from the large planar π-surface[32] or (ii) the electrostatic interaction induced by substituents that can act as donors or acceptors[28,33]. Therefore the design and synthesis of red emissive non-doped fluorescent crystals that operate without a hole-blocking layer is still a challenging task for high hole injection efficiency and mobility that can have potential light emitting device applications. We herein report the solid state packing and light harvesting properties of a thermally stable organic single crystal based on naphthalenimide and perylenimide units with strong red luminescence that can have potential photonic applications and further tuning of photophysical properties of the dyad by incorporating alkyl-side units of different length.

3.1.1 Luminescence Properties of Aggregates

The π-conjugated molecules in solution or amorphous or crystalline solid state exhibit two distinct types of aggregate namely J- and H-aggregates. The J-aggregates (J for Jelly who discovered the phenomenon of J-aggregates) show bathochromic shift (red shift) and H-aggregate show hypochromic shift (blue shift) in absorption spectra in comparison to the monomer spectra. The exciton theory[174] is developed by Micheal Kasha, describes the correlation between structure of aggregates and their absorption spectra. According to exciton theory, dye molecules are considered as point dipoles and upon aggregation the excited state split into two levels one being higher in energy and the other being lower in energy compared to the monomeric excited state (Figure 3.2). The allowed and forbidden transitions of the electron are governed by the tilt or slip angle (α) which is the angle between the transition dipole moments and the line joining the centres of the molecule. In the case of J-aggregates having head to tail arrangement of molecules ($\alpha < 54°$), the allowed transition is to the lowest excited state which results narrow red shifted emission (Figure 3.2). But in the case of H-aggregate having face to face or sandwich type of molecular arrangement ($\alpha > 54°$), the allowed transition is to the upper excited state level which results blue shifted emission (Figure 3.2).

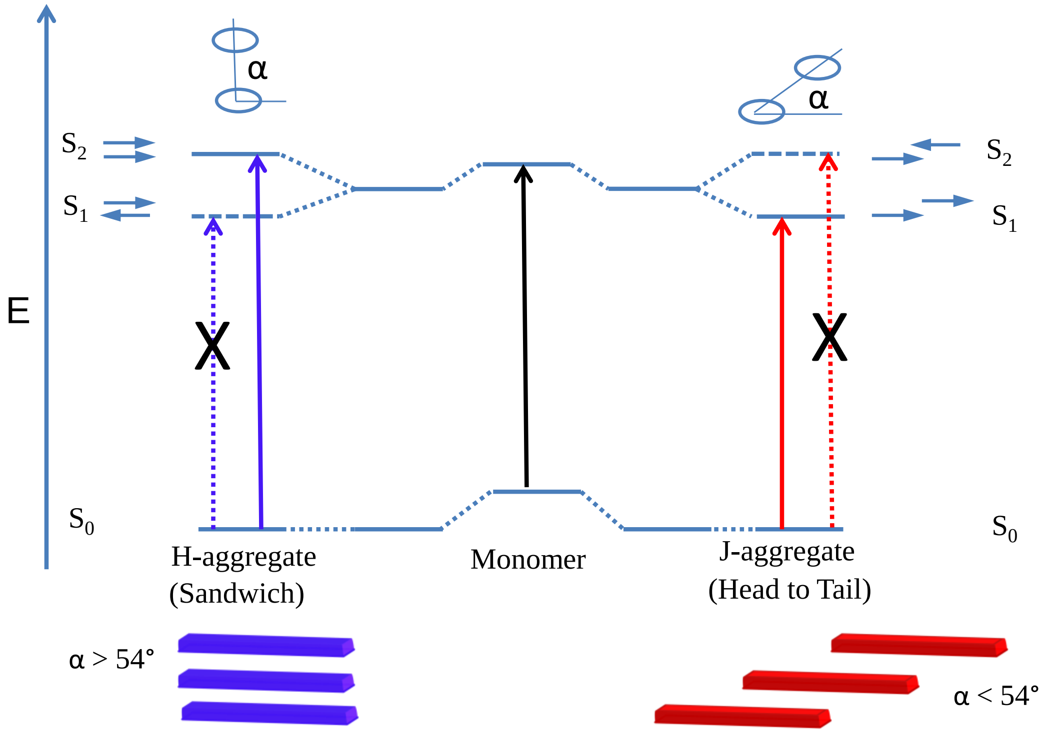

Figure 3.2 *Schematic diagram showing the formation of H- and J-aggregates with their possible electronic transitions.*

3.1.2 Relation between Solid State Luminescence of Perylenimides and their Molecular Packing

The colour of a dye is not only determined by the electronic properties of the individual molecular chromophores, but also is influenced by the electronic interactions with the vicinal molecules in the crystal. The solid state packing of perylenimide dyes have been extensively studied for optimising the colour as well as the solid state luminescence quantum yield. The important work carried out by Graser, Hädicke and Klebe of BASF company, Germany has revealed the crystal structures of 18 perylene bismide (**PBI**) derivatives [175-179]. Recently Zugenmaier *et al*. reported crystal structure of 6 more **PBI** pigments[180]. All these crystal structure shows planar geometry of **PBI** molecules with a parallel orientation at a stacking distance between 3.35 and 3.55 Å (for comparison, a distance of 3.35 Å is found in graphite, Figure 3.3)[41]. However the perylene planes are not fully overlapping with each other in the crystal structure. The transverse (t) and longitudinal (l) offsets (slips) differentiate one perylene plane from another where t and l describes the coordinates of a given atom in the next perylene down the stack relative to previous one along the short and long axes of PBI respectively (Figure 3.3).

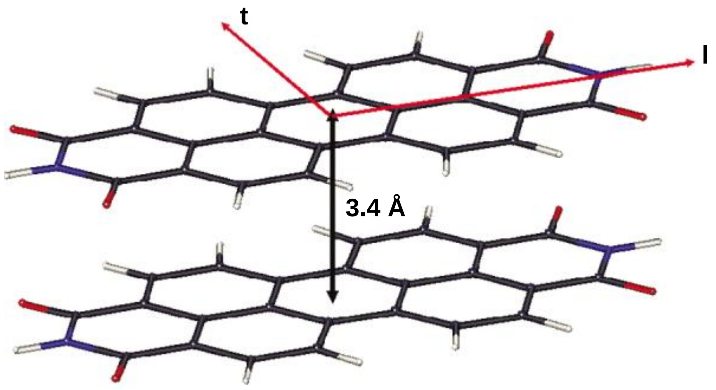

Figure 3.3 *The most common π–π stacking of perylene bisimides (**PBI**) in the solid state involving longitudinal and transverse offsets. Reprinted with permission from ref. [41]. Copyright 2004, Royal Society of Chemistry.*

3.1.2 Relation between Solid State Luminescence of Perylenimides and their Molecular Packing

Although the basic chromophore in **PBI** is identical, different substituents can change the colour of bisimides due to the difference in transverse and longitudinal offset. Thus, **PBI** may exhibit different colours in the solid state depending on the packing eventhough they have almost identical absorption spectra in solution. In comparison to longitudinal offset, the transverse offset produce dramatic change in the absorption maxima of **PBI**. Thus pigments like azobenzene substituted **PBI** (pigment red **PR 178**) with larger transverse slip shows similar colour in solution (red colour) due to minimum π-π interaction between the nearby **PBI** molecules (Figure 3.4A). But the methyl substituted **PBI** (**PR 179**) exhibits more perturbation in the electronic spectra due to smaller transverse ofset which will produce maroon colour in the solid state (Figure 3.4B). But in the case of para methoxy benzyl substituted **PBI** (**PBI 32**) shows black clour attributes to stronger electronic interaction between neighbouring **PBI** molecules (Figure 3.4C).

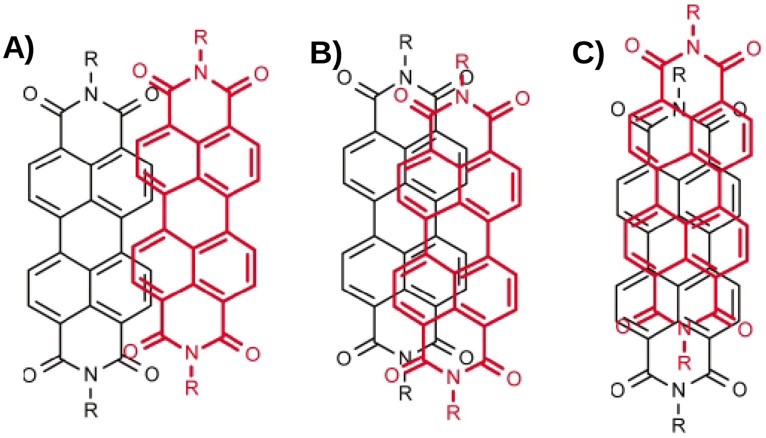

R = Azobenzene
(PR 179)

R = CH_3
(PR 179)

R = -p-CH_3OPhCH_2-
(PR 179)

Figure 3.4 *Transverse and longitudinal displacements of the stacked π-systems in the crystals of A) red (**PR 178**); B) maroon (**PR 179**) and C) black (**PBI 32**) perylene bisimide pigments. Reprinted with permission from ref. [41]. Copyright 2004, Royal Society of Chemistry.*

The substitution of hydrogen atoms at bay positions of **PBI** reduces intermolecular close packing but it also destroys the planarity of the perylene scaffold. Wurthner *et al.* reported nearly flat 1,7-di-(2,6-terphenyl) substituted (**PBI 1**) and 1,7-diphenoxy-substituted (**PBI 2**) **PBI**s (Figure 3.5)[181]. In comparison to the unsubstituted parent derivative **PBI 3** (Φ_F = 0.03) both **PBI 1** (Φ_F = 0.37) and **PBI 2** (Φ_F = 0.13) shows enhanced solid state fluorescence. The bulky terphenyl group efficiently shield the perylene core from nearby perylene unit there by completely eliminate the intermolecular **PBI** contacts in the solid state. Unlike **PBI**s the solid state fluorescence propertis of perylene monoimides (**PMI**) are not well studied in the literature.

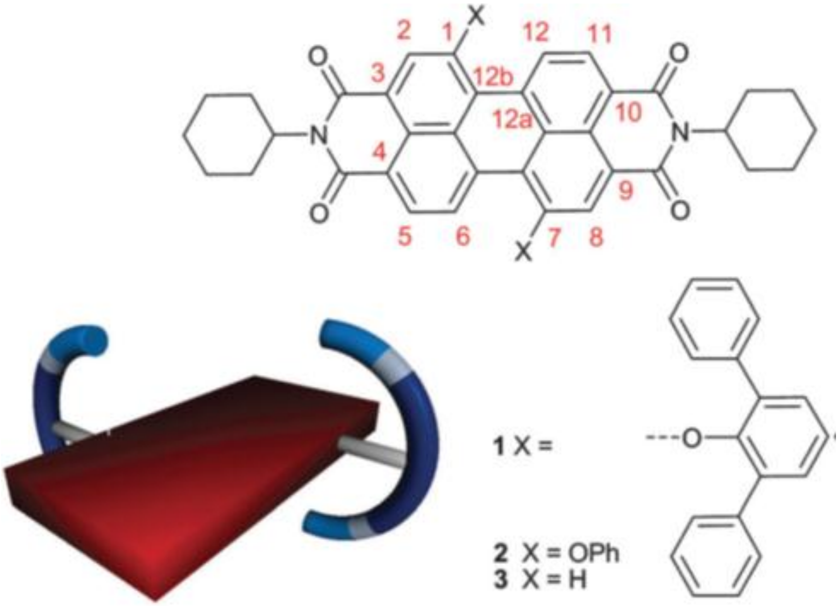

Figure 3.5 *Concept of inhibiting the formation of* ***PBI*** *aggregates by bulky groups at 1,7-bay positions (left) and chemical structure of* ***PBI 1*** *as well as reference* ***PBI*** *dyes* ***2*** *and* ***3****. Reprinted with permission from ref. [181]. Copyright 2012, Royal Society of Chemistry.*

3.2 Results and Discussions

3.2.1 Crystal Structure of the Dyad NP and the Model Derivative PI

We have synthesised the napthalenimide-perylenimide dyad **NP** (Figure 3.6A) through Stille coupling between the tributyltin derivative of N-hydroxypropyl naphthalenimide and bromoperylenimide which is described in chapter 2[182]. The dyad **NP** exhibits exceptional thermal stability upto 425 °C (Figure 3.7) which is consistent with the polyarenimide based systems reported earlier[183]. The corresponding model perylenimide (**PI**) derivative (Figure 3.6B) is also synthesized for comparison[97].

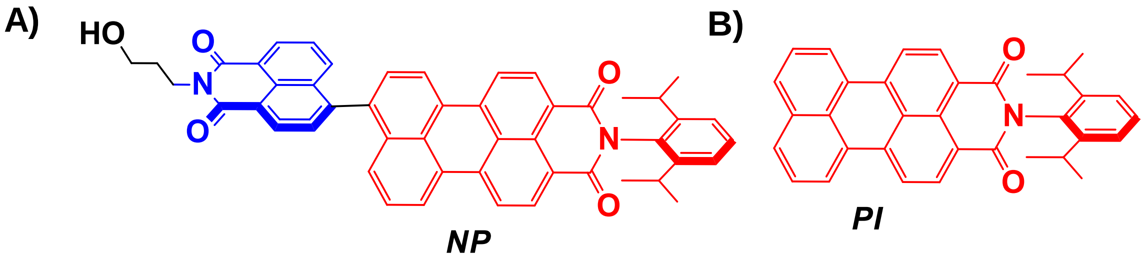

Figure 3.6 *Shows A) and B) the molecular structure of the dyad* ***NP*** *and the model derivative* ***PI*** *respectively.*

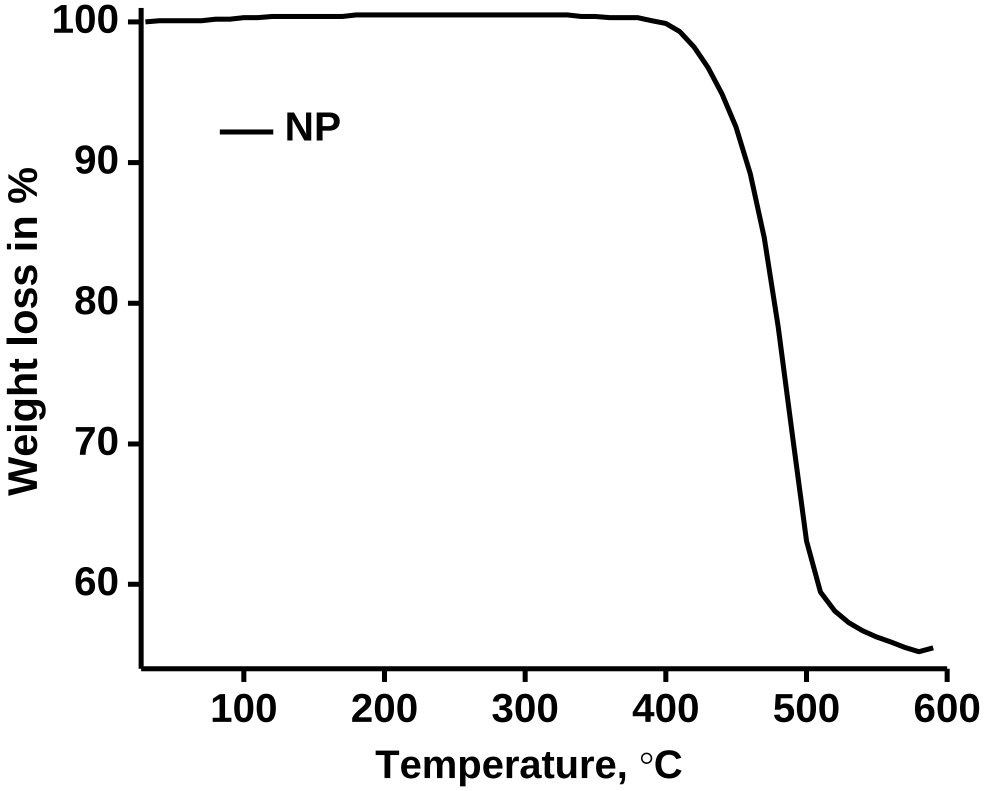

Figure 3.7 *Shows the thermogravimetric analysis of the dyad NP.*

3.2.1 Crystal Structure of the Dyad NP and the Model Derivative PI

Single crystal X-ray analysis of the dyad **NP** indicates near-orthogonal arrangement of the napthalenimide and peryelenimide planes (θ = 75°). The dyad **NP** crystallizes in the triclinic space group $P\bar{1}$ having two molecules in the asymmetric unit (Refer Table 2.1, Chapter 2). Detailed analysis of the crystal structure of the dyad **NP** revealed conjugated nature of the individual chromophoric units as observed from the comparable bond lengths corresponding to conjugated carbon-carbon single and double bonds in the crystal structure. The interchromophoric C–C bond length is found to be 1.49 Å comparable to that of a freely rotating C–C single bond length. By virtue of the near-orthogonal arrangement (twisted out of planarity by 75°) between the two chromophoric units, the naphthalenimide and perylenimide units act as independent chromophores and not as a conjugated system. The remarkable structural feature of the crystal packing is that the non-planar arrangement of the two chromophoric units prevents the possibility of close-packing of the fluorescent perylenimide units in the solid state. Interplanar distance between the two nearest perylenimide units is found to be 7 Å having a transverse slip (along the molecular short axis of the perylenimide unit) of 0.95 Å and longitudinal slip (along the molecular long axis of the perylenimide unit) of 8.05 Å (Figure 3.8A). Partially slipped-stack perylenimide dimers are also observed at short stacking distance of 3.4 Å having a transverse slip of 2.82 Å and longitudinal slip of 3.28 Å (Figure 3.8B). While nearest naphthalenimide-naphthalenimide units are found to be at van der Waals distance (3.1 Å) (Figure 3.8C). The close packing of the perylenimide unit is strongly hindered due to the presence of the sterically bulky ortho-substituents at the phenyl ring on the imide end and orthogonally oriented naphthalenimide unit on the other end. Strong CH···π interactions between the π–surface of the perylenimide unit and (i) the naphthalenimide (CH···π; 3.2 Å) and (ii) methyl protons of the isopropyl substituent (CH···π; 2.8 Å) forces this molecule to have such distinct arrangement (Figure 3.8C)[184]. An efficient π-π interaction between the adjacent naphthalenimide units (Figure 3.8C) drives the formation of the ordered crystalline structure of the dyad

3.2.1 Crystal Structure of the Dyad NP and the Model Derivative PI

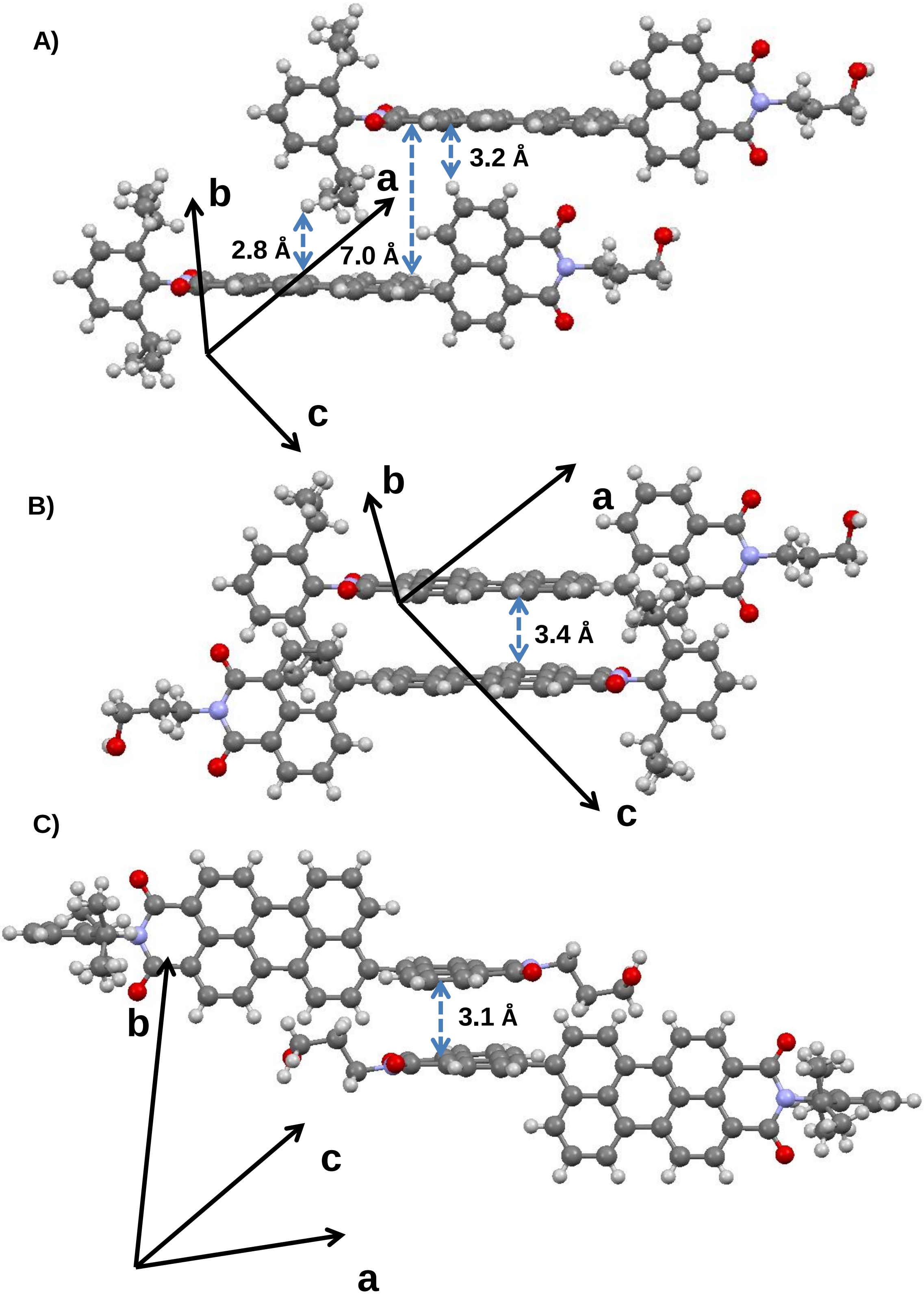

Figure 3.8 Shows *A) and B) two different types of perylenimide-perylenimide geometry available in the crystal lattice of the dyad* ***NP****; C) naphthalenimide-naphthalenimide close packing observed in the dyad* ***NP****.*

NP despite the inefficient π-π overlap in perylenimide units. The antiparallel packing of two **NP** molecules in the unit cell reveals the fact that the dipoles of the **NI** and **PI** have favourable orientation for energy transfer in the crystalline state minimizing the aggregation effects of the emissive perylenimide units (Figure 3.8B). The crystal structure of the model derivative **PI** having orthogonal sterically bulky subsituent only at one end, i.e. diisopropyl phenyl unit, exhibited two types of aggregate between the perylenimide units (Figure 3.9). Perylenimide-perylenimide dimer in the model derivative **PI** is found at a stacking distance of 3.5 Å having an average transverse slip of 1.5 Å and longitudinal slip of 2.4 Å. While an alternate perylenimide-perylenimide arrangement in the model derivative **PI** is also observed at a stacking distance of 3.5 Å having an average transverse and longitudinal slip of 1.2 and 7.08 Å respectively.

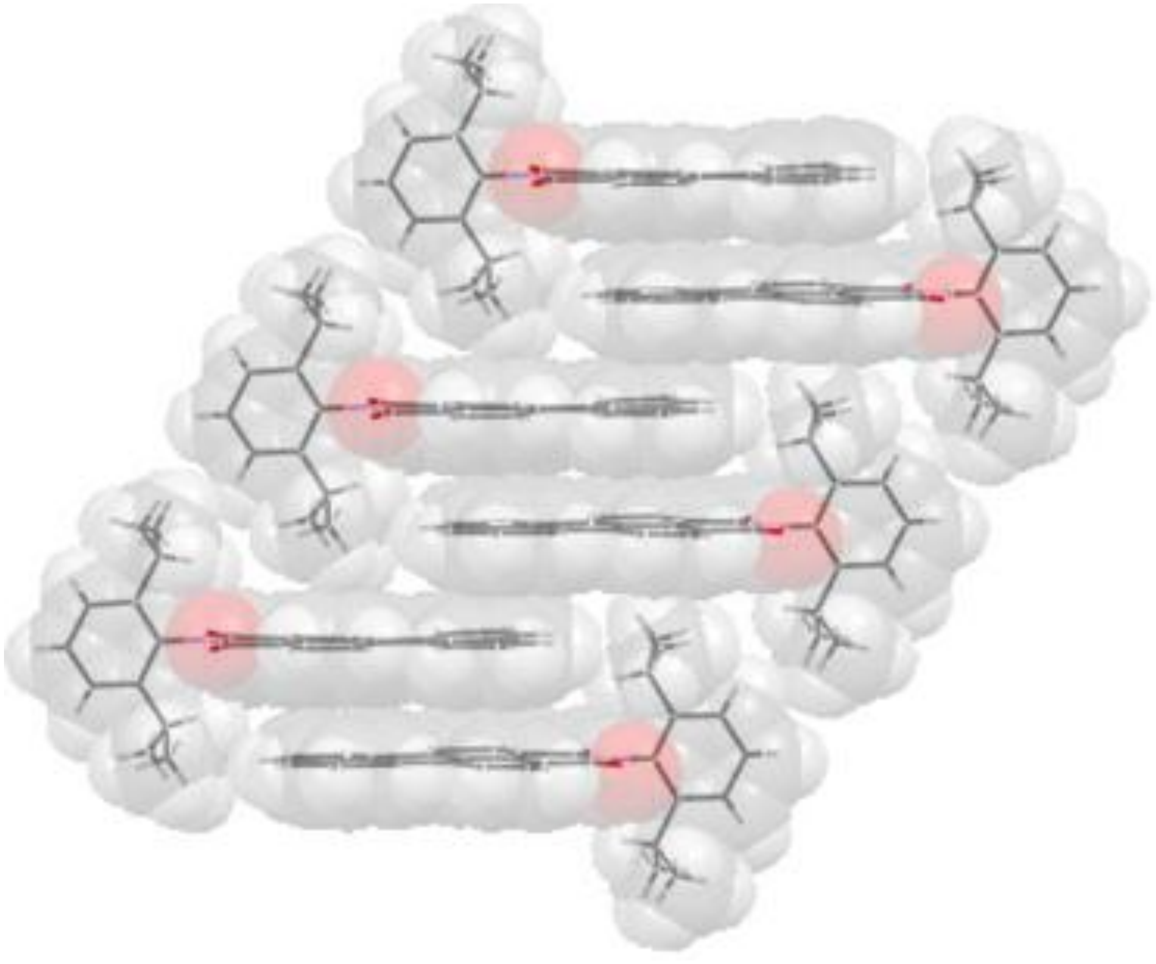

Figure 3.9 *Shows crystal packing in the model derivative* ***PI****.*

3.2.2 Photophysical studies of the dyad NP and the model derivative PI

By virtue of perpendicular arrangement of the two constituent chromophoric planes of naphthalenimide (**NI**) and perylenimide (**PI**) units, negligible orbital overlap effects are evident in the dyad **NP** in solution. The UV-Vis absorption spectrum of the dyad **NP** in organic solvents such as toluene, acetonitrile etc. can be described as the sum of the UV-Vis absorption spectra of the constituent chromophores (Refer chapter 2)[182]. Identity of the individual chromphoric units, **NI** and **PI**, in the covalently linked dyad **NP** in solution is confirmed using cyclic voltammetry, steady-state and time-resolved fluorescence measurements(Refer chapter 2)[182]. Upon photoexcitatation at 345 nm, we observed highly efficient energy transfer (90%) from **NI** to **PI** unit in solution due to adequate spectral overlap between the **NI** emission and **PI** absorption and favourable parallel dipole orientation at short separation of 1.49 Å. Upon photoexcitation of naphthalenimide unit, a marginal loss of photons (ca. 10%) in the dyad **NP** in solution could be attributed to thermodynamically favourable (ΔG = -0.17 eV) electron transfer process from singlet excited state of naphthalenimide unit to perylenimide unit.

Figure 3.10A shows the absorption spectrum of the model derivative **PI** in toluene and the diffuse reflectance spectrum measured in its crystalline state. Whereas the model derivative **PI** exhibited characteristic absorption of monomeric perylenimide moiety centered around 480 and 507 nm in toluene, crystalline form of **PI** exhibited strong bands centered at 428, 538 and 577 nm, similar to the UV- Vis spectrum of self-assembled twisted tetrachloroperylendiimide aggregates (Table 3.1)[185]. UV-Vis spectrum of the model derivative **PI** in thin film state exhibited peaks centered at 481, 516 and 551 nm. Fluorescence measurement of **PI** in toluene exhibited bands centered around 530, 569 and 618 nm having a quantum yield of 0.86 consistent to that of monomeric perylenimide moiety (Figure 3.10B). Crystalline **PI** exhibited a broad band centered at 660 nm having a quantum yield of 0.11. Model derivative **PI** in the thin film state exhibited a strong broad band at 681 nm, in addition to the monomer-like emission at 531 nm with an overall quantum yield of 0.09. Observation of emission bands in the model derivative **PI** centered at 531 and 681 nm corresponding to perylenimide unit in the monomeric and aggregate state, respectively, indicates the possibility of heterogeneity in the thin film in constrast to the model derivative **PI** in the crystalline state.

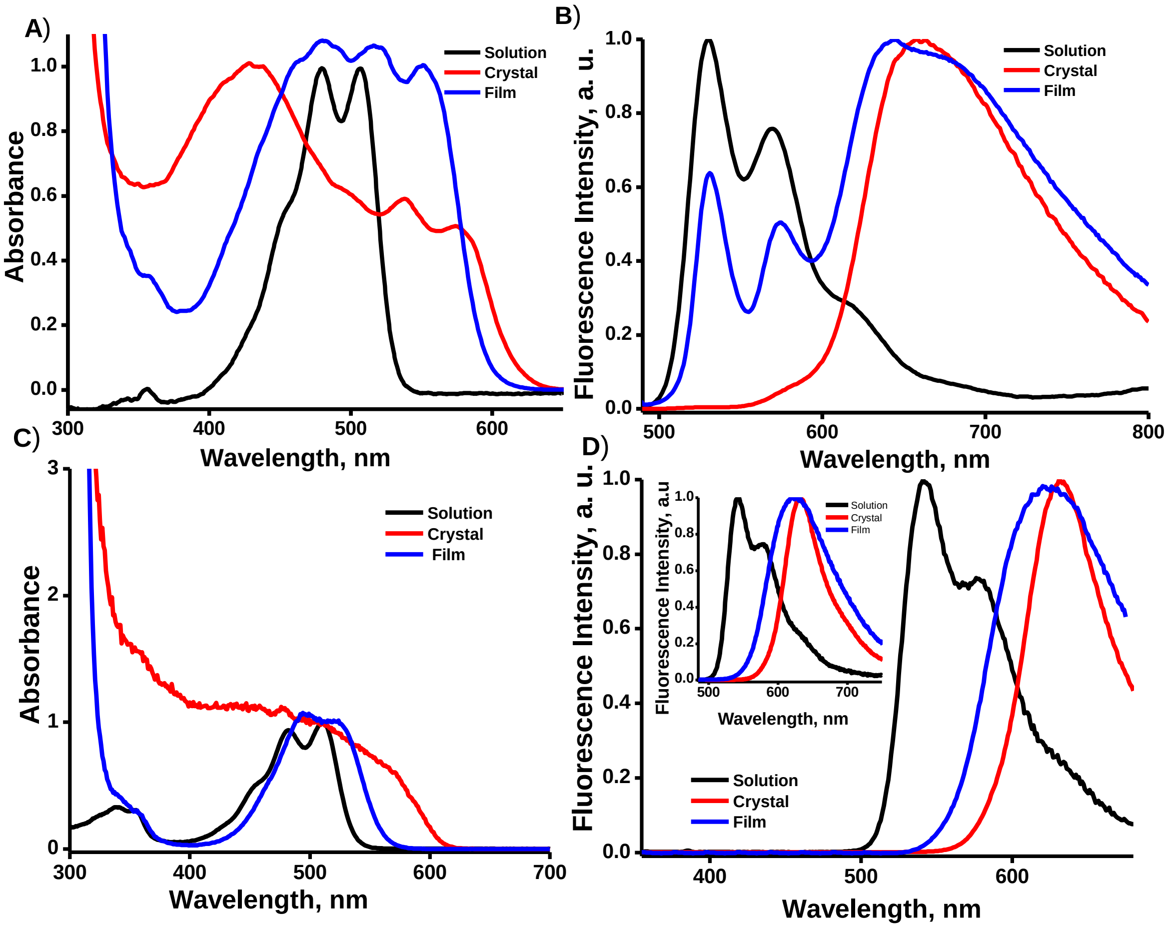

Figure 3.10 *A) Absorption spectra of model derivative* ***PI*** *in toluene (black), diffuse reflectance absorption spectrum in crystalline state (red), and in film state (blue), B) fluorescence emission spectra of model derivative* ***PI*** *in toluene (black), crystalline state (red) and in film state (blue) when excited at 475 nm; C) Absorption spectra of dyad* ***NP*** *in toluene (black), diffuse reflectance absorption spectrum in thin film (blue) and in crystalline state (red), D) fluorescence emission spectra of the dyad* ***NP*** *when excited at 345 nm and inset of D) shows the corresponding emission spectra when excited at 475 nm in toluene solution (black), crystalline (red) and in film state (blue).*

3.2.2 Photophysical studies of the dyad NP and the model derivative PI

UV -Vis absorption spectrum of the dyad **NP** in toluene exhibits individual characteristic bands corresponding to naphthalenimide (λ_{ab} = 338 nm) and perylenimide (λ_{ab} = 482 nm) moieties (Figure 3.10C). We observed a significant red shift (485 cm^{-1}) corresponding to the perylenimide unit in the UV-Vis spectrum when compared to the dyad **NP** in solution indicating the presence of aggregation in the thin film of the dyad **NP**. However, we observed a broad diffuse reflectance absorption spectrum corresponding to the crystalline **NP**, consistent with the reported literature[186]. Steady-state fluorescence measurements of the dyad **NP** in solution when excited both at 345 and 475 nm are shown in Figure 3.10D. Upon direct excitation of perylenimide at 475 nm, we obtained a vibronically resolved emission spectrum corresponding to perylenimide chromophore at 541 nm and a shoulder-like band at 577 nm with a quantum yield of 0.81 ± 0.002 (inset of Figure 3.10D). The observed perylenimide emission while exciting the naphthalenimide unit in dyad **NP** in solution could be attributed to excitonic coupling (V_{DA} = 3.5 cm^{-1}, Refer Figure 2.23, Chapter 2) arising from favourable orientation of transition dipole densities of the naphthalenimide and perylenimide units where V_{DA} is the Coulombic coupling between the donor and acceptor obtained using transition density cube analysis which is described in chapter 2 [182]. Under similar conditions, the dyad **NP** in thin film exhibited a broad band centred on 620 nm corresponding to **PI** unit (Φ_F = 0.19 ± 0.002). While the dyad **NP** in the crystalline state exhibited a narrow emission centred around 631 nm (Φ_F = 0.5 ± 0.04). We observed similar properties in the emission spectra of the dyad **NP** when excited at 345 nm that corresponds to the naphthalenimide unit (Figure 3.10D). The excitation spectrum of the model derivative **PI** and the dyad **NP** in solution, crystalline state and thin film collected at respective emission maxima (Table 3.1) resembles with the corresponding absorption spectrum (Figure 3.11A, B).

The dyad **NP** in thin film and the crystalline state could undergo both intermolecular and intramolecular energy transfer due to the presence of an array of

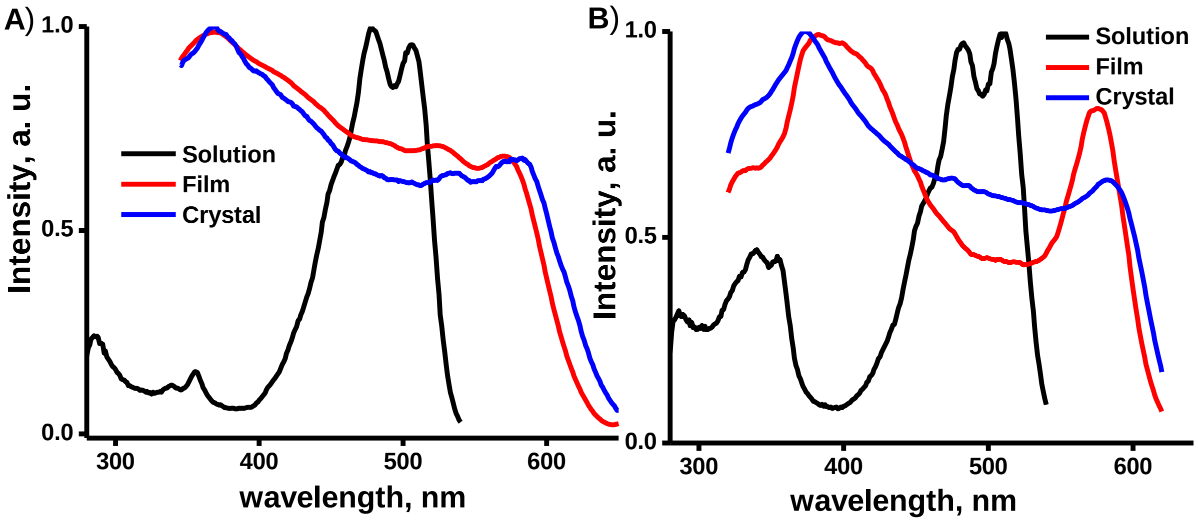

Figure 3.11 *Shows A) the excitation spectra of* ***PI*** *in solution (toluene) monitored at 550 nm, thin film and crystalline state monitored at 670 nm; B) the excitation spectra of* ***NP*** *in solution (toluene), thin film and crystalline state monitored at 550 nm (for solution) and 630 nm (for film and crystalline state).*

donor-acceptor pairs. A narrow emission from the dyad **NP** in the crystalline state arises from a combination of direct excitation at perylenimide (λ_{ex} = 475 nm) unit and through excitation energy transfer upon excitation of naphthalenimide (λ_{ex} = 345 nm) unit. Observed spectral narrowing of the dyad **NP** in the crystalline state (FWHM = 65 nm) when compared to the thin film (FWHM = 115 nm) could be attributed to the significant reabsorption of the photons due to high optical density present in the crystalline form when compared to the thin film. A remarkable red shift (2636 cm^{-1}) in the fluorescence spectrum of the dyad **NP** in solid state when compared to solution makes this dyad red fluorescent in the crystalline state while exhibiting yellow-orange emission in solution. We observed decrease in fluorescence intensity (ca. 15%) of the dyad **NP** in the crystalline state at elevated temperature (100 °C) which is regained when cooled to room temperature repeatedly over several cycles by the dry process (Figure 3.12). Observed decrease in the fluorescence intensity (ca. 15%) of the dyad **NP** at elevated temperature (100 °C) could be attributed to thermally enhanced rate of non-radiative decay. While the recovery of fluorescence intensity of the dyad **NP** at ambient temperature indicates structural stability of the dyad **NP** over thermal fluctuations up to 100 °C.

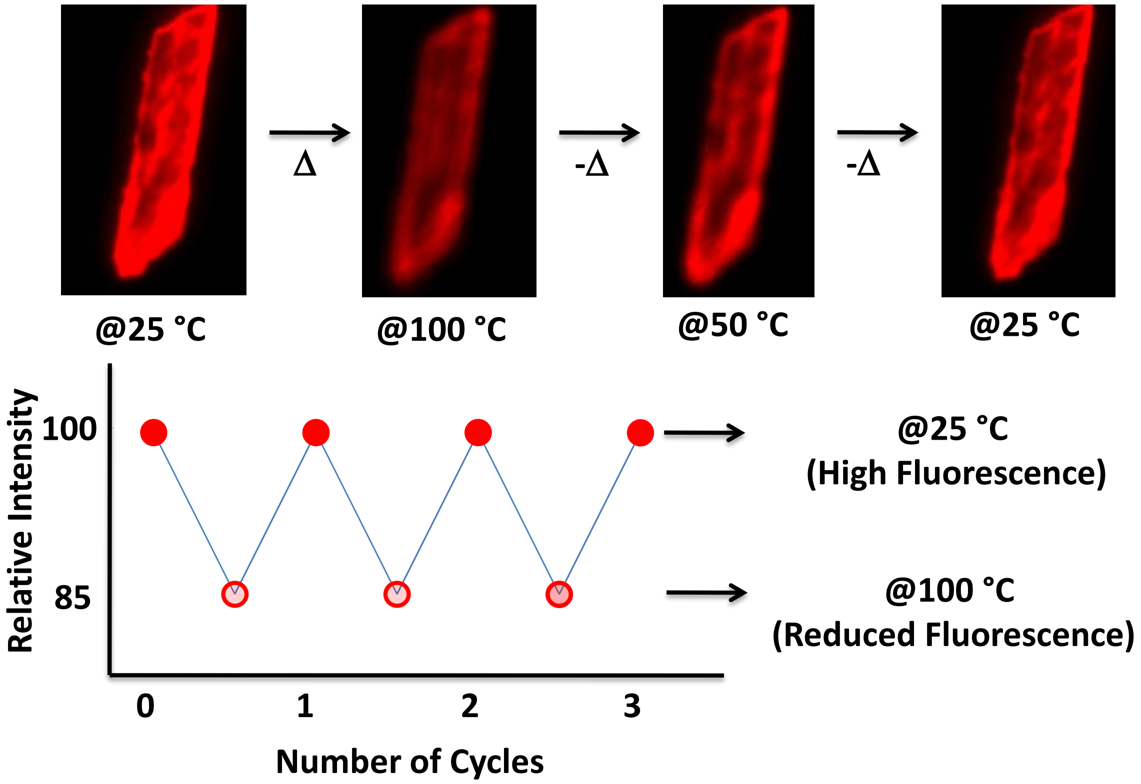

Figure 3.12 *Shows the fluorescence microscopic image of the dyad* **NP** *at various temperatures (top) and a plot of relative intensity of the solid-state luminescence of the dyad* **NP** *against the number of heat-cooling cycles starting from the fluorescent state.*

Time-resolved emission studies were carried out to further understand the conformation of the dyad **NP** in solution, thin film and crystalline state when excited both at 340 nm (Figure 3.13A) and 439 nm (Figure 3.13B). Upon photoexcitation of the dyad **NP** in solution at 439 nm when monitored at 550 nm we observed a mono-exponential decay having a lifetime of 3.6 ns corresponding to perylenimide chromophore. The dyad **NP** in the crystalline form exhibited a bi-exponential decay with the lifetimes of 3.56 ns (74%) and 1.61 ns (26%), upon photoexcitation at 439 nm and monitored at 630 nm. While a tri-exponential decay corresponding to the perylenimide moiety in thin film having the lifetime of 6.42 ns (33%), 1.59 ns (36%) and 0.61 ns (31%) clearly indicates the possibility of different

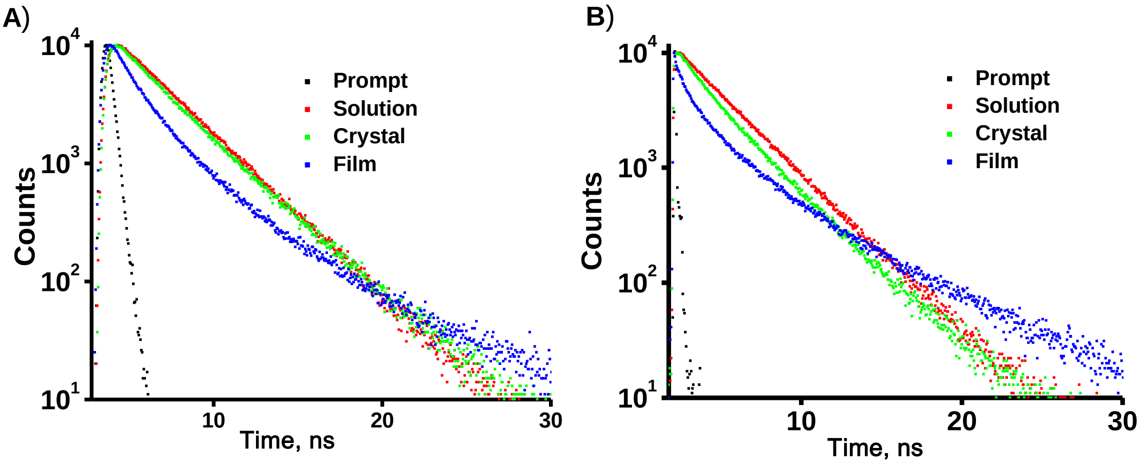

Figure 3.13 *Fluorescence lifetime decay of the dyad* **NP** *A) when excite at 340 nm and (B) when excited at 439 nm in toluene solution (red), crystalline (green) and in film state (blue).*

conformations of the dyad **NP** in thin film. Similar time-resolved fluorescence data were observed for the dyad **NP** in solution, thin film and crystalline state upon excitation at 340 nm. The model derivative **PI** shows a bi-exponential decay in the crystalline state having the lifetimes of 2.64 ns (24%) and 5.0 ns (76%) (Figure 3.14) corresponding to a broad emission centered at 670 nm. In contrast, the derivative **PI** in solution exhibited a mono-exponential decay with a lifetime of 4.9 ns corresponding to monomeric perylenimide unit. While the derivative **PI** in thin film exhibited a bi-exponential decay having a lifetime of 0.45 (42.6%) and 1.53 ns (57.4%), excited at 439 nm and when monitored at 670 nm corresponding to the perylenimide aggregate emission. Similar fluorescence lifetime data were obtained for the derivative **PI** in thin film when monitored at 570 nm corresponding to the monomeric perylenimide unit clearly indicating the co-existence of both monomer and aggregate corresponding to perylenimide unit in the entire emission spectral range of 500-880 nm.

From the quantum yield and fluorescence lifetime of the dyad **NP** and the model derivative **PI**, we have determined the rates of radiative and non-radiative decay pathways in solution, thin film and crystalline state by using the equations 3.1-3.4[29].

3.2.2 Photophysical studies of the dyad NP and the model derivative PI

$$\Phi = \frac{k_r}{k_r + k_{nr}} \tag{3.1}$$

$$\tau = \frac{1}{k_r + k_{nr}} \tag{3.2}$$

$$k_r = \frac{\Phi}{\tau} \tag{3.3}$$

$$k_{nr} = \frac{1}{\tau} - k_r \tag{3.4}$$

In solution, the dyad **NP** exhibited a faster rate of radiative decay ($k_r = 2.32 \times 10^8$ s^{-1}) when compared to the rate of radiative decay in dyad **NP** in thin film ($k_r = 0.37 \times 10^8$ s^{-1}) and crystalline state ($k_r = 1.52 \times 10^8$ s^{-1}). In contrast, rate of non-radiative decay is

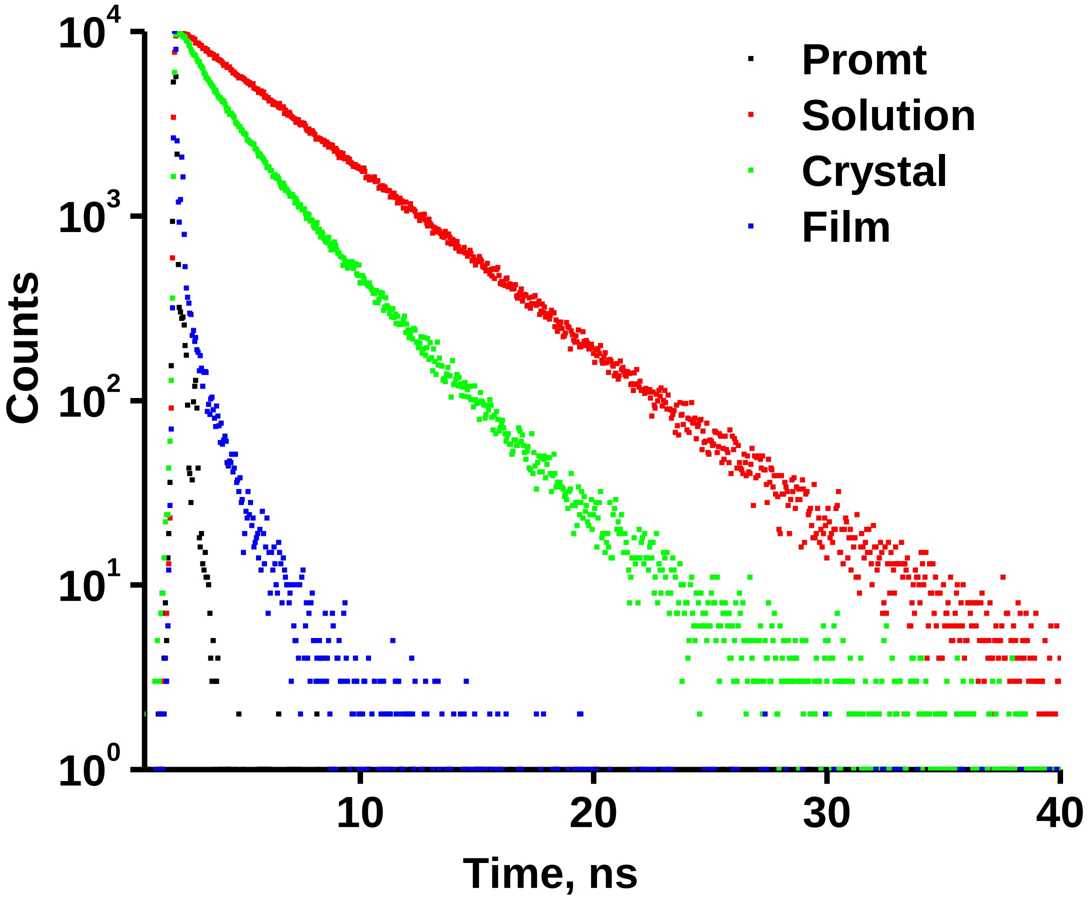

Figure 3.14 *Shows the fluorescence lifetime decays of* ***PI*** *in solution (toluene), film and crystalline state, emission collected at 550 for solution and 670 nm for both crystal and film on excited at 439 nm.*

Table 3.1 *Photophysical properties of conjugate* ***NP*** *and the corresponding model derivative* ***PI*** *in solution (toluene), thin film and crystalline state.*

	PI						**NP**					
	λ_{ab},[a] nm	λ_{em},[b] nm	τ [c] (d), ns	Φ_F[e]	k_r,[f] $[10^8 s^{-1}]$	k_{nr},[g] $[10^8 s^{-1}]$	λ_{ab},[a] nm	λ_{em},[b] Nm	τ [c] (d), ns	Φ_F[e]	k_r,[f] $[10^8 s^{-1}]$	k_{nr},[g] $[10^8 s^{-1}]$
Solution	480, 507	530, 569, 618	4.90	0.86 ± 0.002	1.75	0.29	338, 482, 511	541, 577	3.60	0.81 ± 0.002	2.32	0.54
Film	481, 516, 551	531, 575, 681	0.45 (42.6) 1.53 (57.4)	0.09 ± 0.001	0.67	6.79	496, 524	620	1.59 (36.1) 6.42 (33.0) 0.61 (30.9)	0.19 ± 0.002	0.37	1.59
Crystal	428, 538, 577	660	2.64 (23.7) 5.00 (76.3)	0.11 ± 0.003	0.23	1.91	300-600 (broad)	631	1.61 (26.1) 3.56 (73.9)	0.50 ± 0.001	1.52	1.52

[a]Absorption maxima; [b]Emission maxima (Excitation wavelength, 475 nm); [c]Fluorescence lifetime (Excitation wavelength, 439 nm and emission collected at 550, 670 and 670 nm for **PI** in solution, thin film and crystalline state respectively and 550, 630 and 630 nm for **NP** in solution, thin film and crystalline state respectively); (d) corresponding amplitude; [e]Quantum yield; [f]rate of radiative decay and [g]rate of non-radiative decay.

found to increase in the dyad **NP** in thin film and crystalline state when compared to the solution (Table 3.1). Observed decrease in the rate of radiative decay[30] in the crystalline **NP** corresponding to the perylenimide unit when compared to that insolution could be attributed to weak H-type exciton coupling[185,187] between the perylenimide units[32,101,188]. A moderate reduction in the quantum yield of fluorescence in the crystalline state of dyad **NP** compared to that in the solution could be attributed to the existence of a weak H-type aggregate[41]. Orthogonally oriented sterically bulky obstructs on either side of the perylenimide moiety prevented a strong H-type interactions thereby leading to the strong fluorescence (weak H-type aggregate) in the crystalline state of the dyad **NP**. Moderate fluorescence quantum yield (Φ_F = 0.17) is achieved in a sterically less demanding dicyclohexyl perylenediimide derivative that is assumed to arise from flip-flap arrangement[189]. The model derivative **PI** in toluene exhibited a rate of radiative decay $k_r = 1.75 \times 10^8$ s^{-1}, when compared to the $k_r = 0.67 \times 10^8$ s^{-1} and 0.23×10^8 s^{-1} in the case of derivative **PI** in thin film and crystalline state respectively. A large decrease in the rate of radiative decay (ca. 7-fold) in the derivative **PI** in the crystalline state when compared to the **PI** in solution is clearly indicative of strong H-type aggregate. In contrast, moderate decrease in the rate of radiative decay (ca. 1.5 fold) in the dyad **NP** in the crystalline state vs. the dyad **NP** in solution confirms the formation of weak H-type aggregate in the dyad **NP** in the crystalline state.

We have carried out time-resolved anisotropy measurements to understand the timescale of exciton migration in the crystalline state of dyad **NP** (Figure 3.15). Since fluorescence depolarization through rotational motion is not possible at this time scale in the crystalline state, the observed anisotropy could be attributed to the energy migration[190]. Exciton delocalization can occur due to the very short separation between the chromophoric transition dipoles[191]. Exciton migration within the dyad **NP** in the crystalline aggregated state leads to a loss of the memory of the initial excitation polarization, thereby resulting in equal

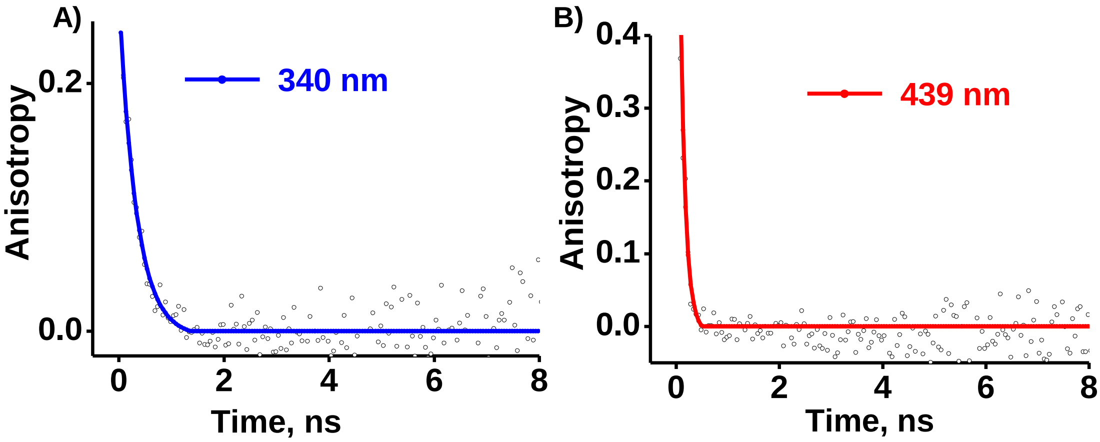

Figure 3.15 *Anisotropy decays of the dyad* **NP** *in the crystalline state A) when excited at 439 nm and B) when excited at 340 nm.*

intensities of the polarized emitted light that is either parallel or perpendicular to the polarization of the excitation source[192]. The dyad **NP** exhibits an initial anisotropy value (r_0) of 0.32 which loses the anisotropy memory with a decay time of 516 ps, upon excitation at 340 nm (**NI** moiety) and monitored at 631 nm (**PI** moiety, Figure 3.15A). Observed slow rate of energy migration (K_{EM} = 1.9 x 10^9 s^{-1}) for the dyad **NP** when compared to single chromophoric systems[69] could be attributed to delayed loss of memory arising from the asymmetry of the dyad **NP**. While excitation at 439 nm (**PI** moiety; Figure 3.15B) of the crystalline dyad **NP** exhibits an initial anisotropy (r_0) of 0.37 having a decay time of 142 ps (K_{EM} = 7.0 x10^9 s^{-1}). However, the fast fluorescence depolarization clearly indicates the rapid interchromophoric migration of the singlet excitons which facilitates the energy transfer to the acceptor perylenimide unit. A slower rate of exciton migration upon excitation of naphthalenimide moiety when compared to perylenimide unit could be attributed to an additional step of exciton migration from naphthalenimide to lower energetic perylenimide unit connected across a single covalent bond[70]. The dyad **NP** in toluene upon drop-casting on HOPG surface exhibited a poor conductivity of 1.8 x 10^{-5} S/cm, obtained using conductive atomic force microscopy (C-AFM; Figure 3.16A). While the drop-casted dyad **NP** exposed to iodine vapor exhibited an order of magnitude increase in conductivity (3.0 x 10^{-4} S/cm, Figure 3.16B)[193].

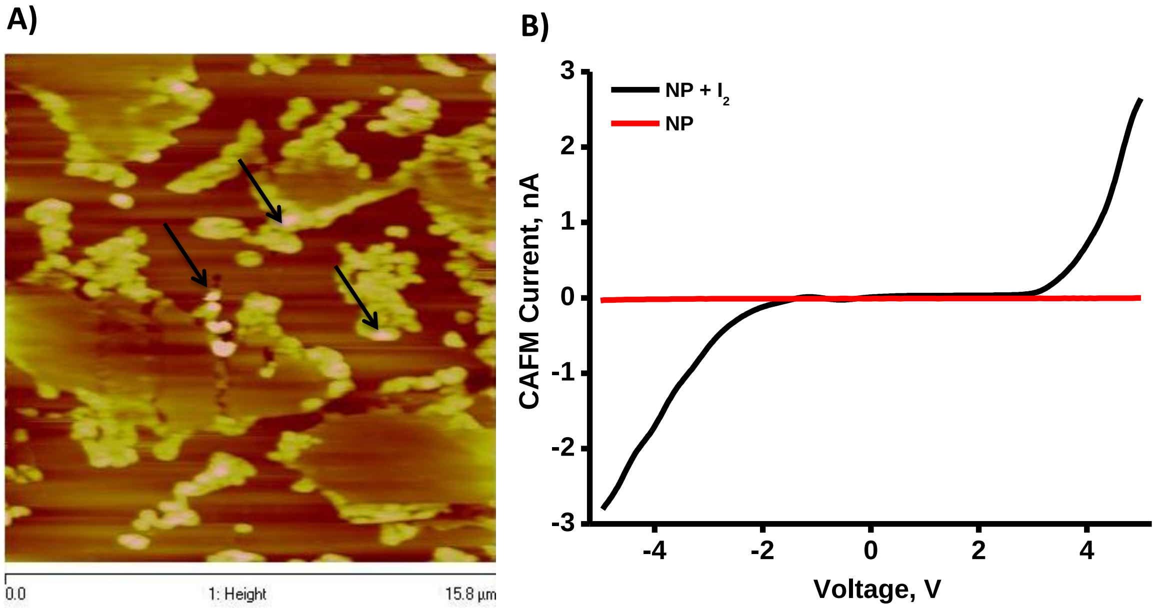

Figure 3.16 *A) AFM height image of the dyad* ***NP*** *drop casted on HOPG; B) C-AFM measurement of the dyad* ***NP*** *drop casted on HOPG in the absence (red) and presence (black) of iodine.*

3.2.3 Tuning the Photophysical Properties of Dyad NP by Incorporating Alkyl Side-Chain Units of Different Length to NI Moiety

In order to tune the solid state photophysical properties of the dyad **NP**, we have synthesized a series of derivatives by carefully modifying the imide substitunet of naphthalenimide unit to butyl **(NP-Bu**), octyl **(NP-Oct**) and hexadecyl **(NP-Hed**) group through the Stille coupling of tributyltin derivative of N-(2,6-diisopropylphenyl)-perylene-3,4-dicarboximide and corresponding bromo naphthalenimide (Scheme 3.1)[142]. The UV-Vis absorption spectra of the **NP** dyads containing different alkyl side-chains in toluene solution exhibit absorption maxima at 340 and 513 nm that correspond to the **NI** and **PI** units respectively (Figure 3.17A). Similar absorption maxima were observed for **NP-Oct** and **NP-Hed** in toluene solution. Upon direct excitation of perylenimide at 475 nm in **NP-Bu**, vibronically resolved emission spectra corresponding to the perylenimide chromophore with emission maximum of 540 nm and shoulder band at 575 nm ($\Phi_F = 0.82 \pm 0.001$, Figure 3.17B) were observed. Similar emission spectra obtained for **NP-Oct** ($\Phi_F = 0.80 \pm 0.00$) and **NP-Hed** ($\Phi_F = 0.80 \pm 0.00$, Figure 3.17B) upon photoexcitation at 475 nm. Upon photo-excitation at 345 nm, a highly efficient energy transfer from **NI** to **PI** unit was observed in **NP-Bu, NP-Oct** and **NP-Hed** due to adequate spectral overlap between the **NI** emission and **PI** absorption, along with favourable parallel dipole orientation between **NI** and **PI** units at a short separation of 1.49 Å, consistent with dyad **NP** (Figure 3.17B).

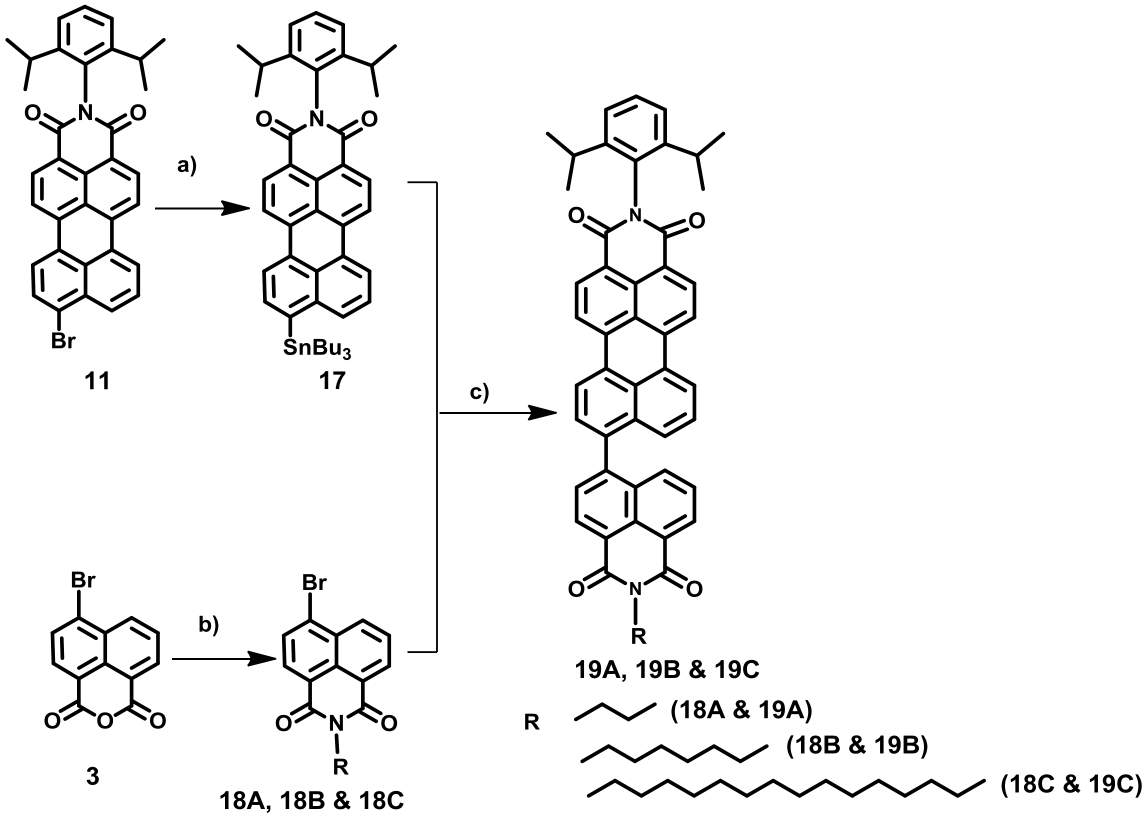

a) Hexabutylditin/Pd(PPh$_3$)$_4$/toluene/reflux; b) alkylamine/acetic acid/reflux;
c) Pd(PPh$_3$)$_4$/DMF/120 °C.

Scheme 3.1 *Synthesis of NP derivatives with different alkyl chain units (**NP-Bu, NP-Oct** and **NP-Hed**).*

3.2.3 Tuning the Photophysical Properties of Dyad NP by Incorporating Alkyl Side-Chain Units of Different Length to NI Moiety

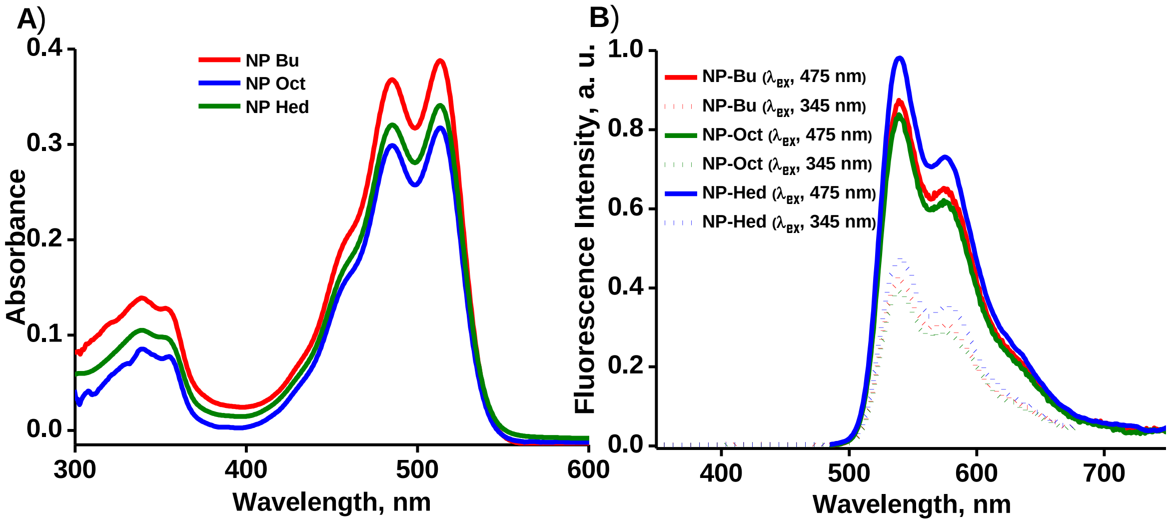

Figure 3.17 *Shows the A) UV-Vis absorption and B) fluorescence emission spectra when excited at 475 nm (solid line) and 345 nm (dotted line) of* ***NP-Bu****,* ***NP-Oct*** *and* ***NP-Hed*** *in toluene.*

We have crystallized all the three derivatives **NP-Bu**, **NP-Oct** and **NP-Hed** by slow diffusion of ethanol into chloroform solution. All the three derivatives exhibit triclinic unit cell with space group $P\bar{1}$ and near-orthogonal arrangement of **NI** and **PI** units similar to the dyad **NP** (Figure 3.18). From the carefull analysis of the crystal structure data**,** we found that the interplanar distance between the two nearest perylenimide units was 3.6 Å **NP-Bu** and it reduced to 3.4 Å in **NP-Oct** and 3.5 Å in **NP-Hed** (Figure 3.19A-C). But going from **NP-Bu** to **NP-Oct** and **NP-Hed**, the transverse slip increased from 3.2 to 3.7 Å. Also a weak perylenimide-perylenimide (**PI-PI**) close packing was observed at a distance of 7 Å in all the three derivatives similar to dyad **NP** (Figure 3.8A). In addition to **PI-PI** close packing, **NP-Bu** exhibits an efficient π-π interaction between the adjacent **NI** units at 3.7 Å (Figure 3.20A). This drives the formation of the ordered crystalline structure of the dyad **NP** despite the inefficient π-π overlap between the perylenimide units. The **NI-NI** close packing distance reduces to 3.4 Å both in the case of **NP-Oct** and **NP-Hed** (Figure 3.20B, C)**.** Thus the association of naphthalenimide units drives the formation of the crystalline structure, preventing the self-aggregation of perylenimide units even in the presence of longer alkyl side chains, as seen in the case of **NP-Hed**.

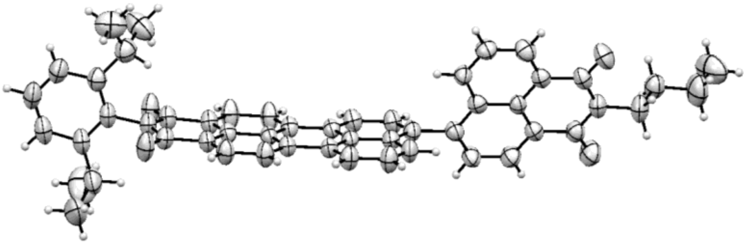

NP-Bu

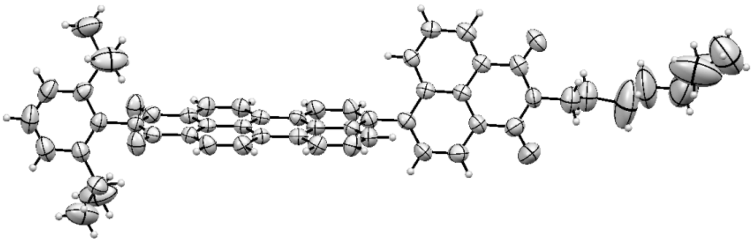

NP-Oct

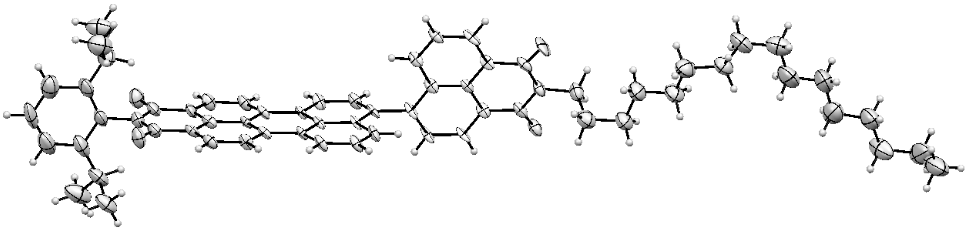

NP-Hed

Figure 3.18 *Shows the crystal structures of the three NP-alkyl chain derivatives,* ***NP-Bu****,* ***NP-Oct*** *and* ***NP-Hed****.*

We observed a broad diffuse reflectance absorption spectra (320-600 nm) for **NP- Bu**, **NP-Oct** and **NP-Hed** in the crystalline state (Figure 3.21A), consistent with the reported literature[186]. A considerable blue-shift in the absorption maxima was observed as the alkyl-chain length increased from butyl to octyl and hexadecyl. In the crystalline state, the dyad **NP-Bu** exhibited a broad emission centered around 640 nm with a shoulder at 535 nm upon excitation at 475 nm (Figure 3.21B). Similar fluorescence properties were observed in the emission spectrum of the dyad **NP-Bu**

3.2.3 Tuning the Photophysical Properties of Dyad NP by Incorporating Alkyl Side-Chain Units of Different Length to NI Moiety

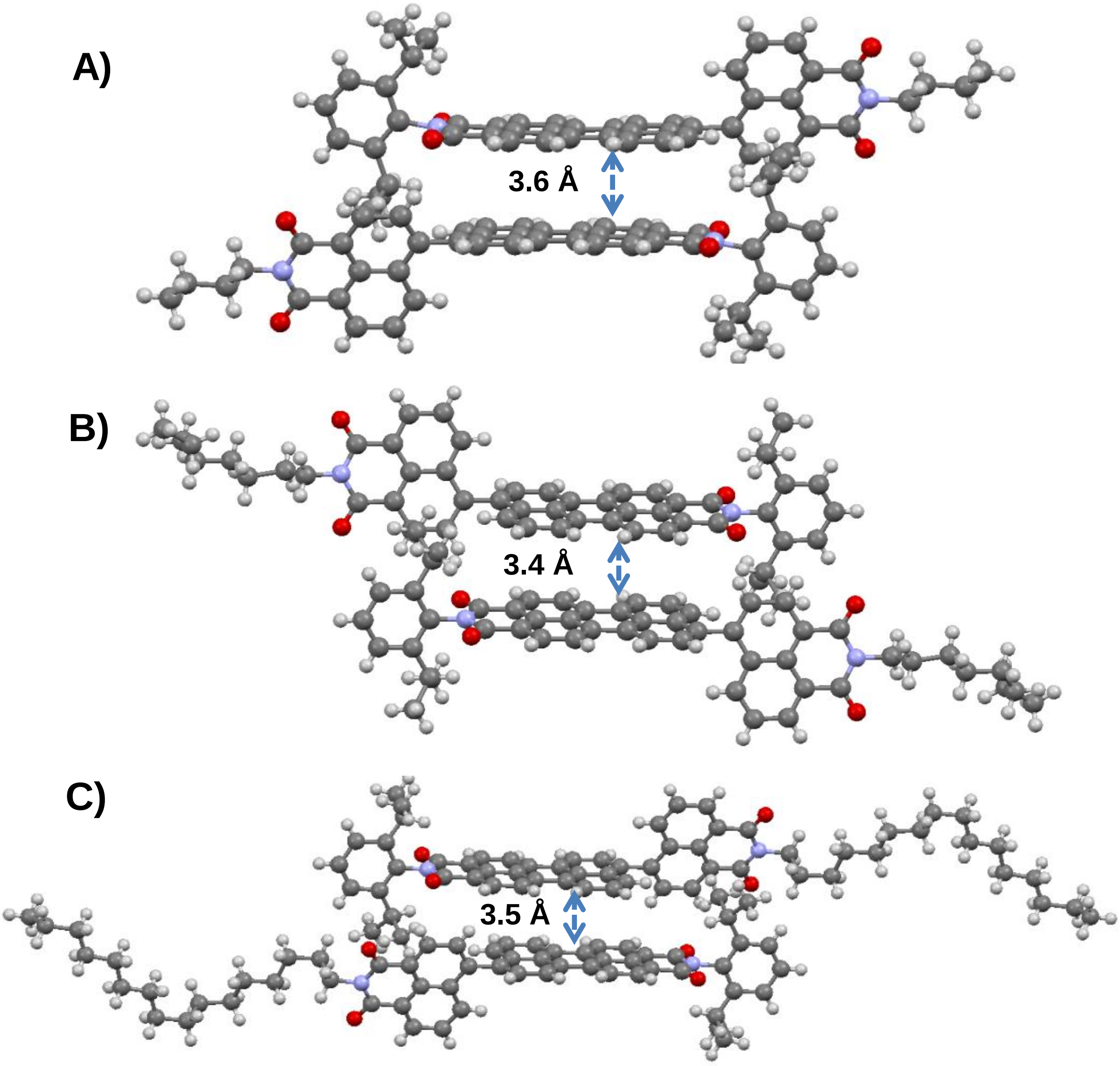

Figure 3.19 *Shows perylenimide-perylenimide close packing observed in the crystal lattice of the dyad A)* ***NP-Bu****, B)* ***NP-Oct*** *and C)* ***NP-Hed****.*

when excited the naphthalenimide unit at 345 nm. This indicates the possibility of an efficient photoinduced energy transfer occurring from **NI** to **PI** in the crystalline state. The dyad **NP-Bu** exhibits a red shifted emission maximum (640 nm) in comparison to **NP-Oct** (617 nm) and **NP-Hed** (589 nm) (Table 3.2)**.** Similarly **NP-Bu** shows a rather higher solid state fluorescence quantum yield (Φ_F = 0.47 ∓ 0.5) in comparison to **NP-Oct** (Φ_F = 0.18 ∓ 0.5) and **NP-Hed** (Φ_F = 0.24 ∓ 0.5) (Table 3.2). This could be attributed to the increased H-type coupling in **NP-Oct** and **NP-Hed** in comparison to **NP-Bu**.

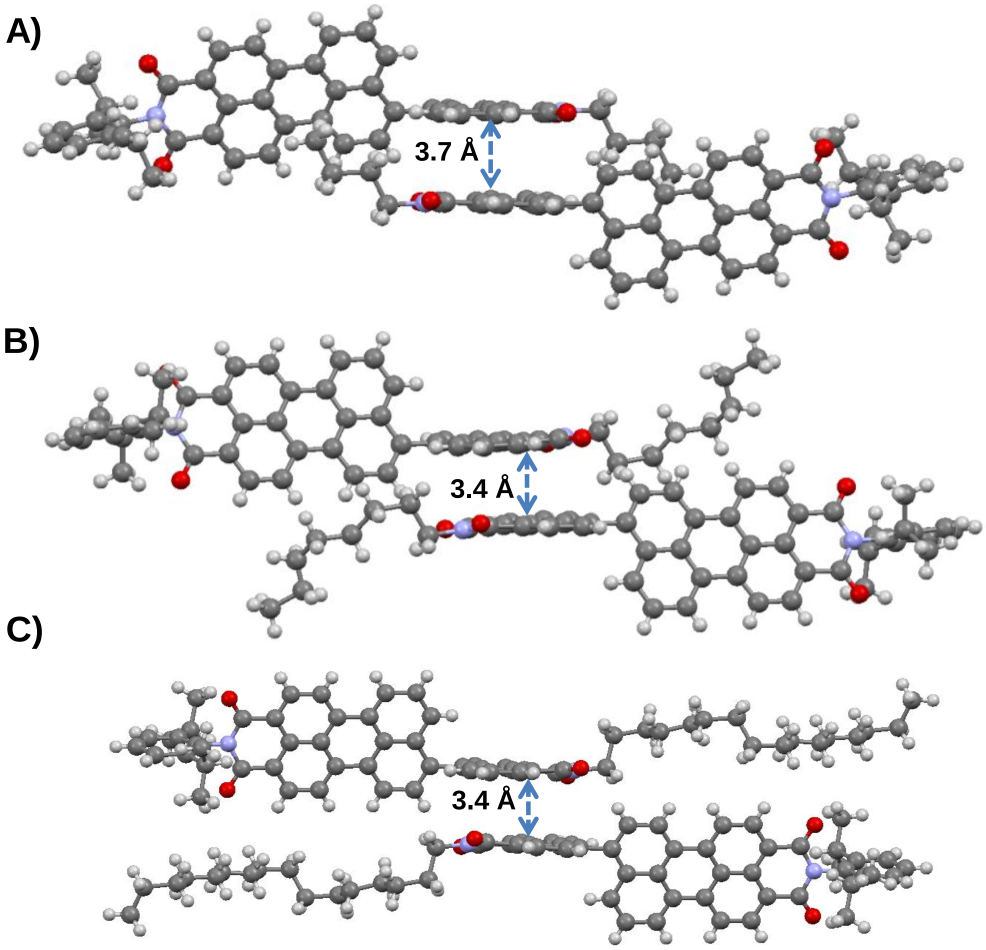

Figure 3.20 *Shows naphthalenimide-naphthalenimide close packing observed in the crystal lattice of the dyad A)* ***NP-Bu****, B)* ***NP-Oct*** *and C)* ***NP-Hed****.*

The fluoresecence lifetime decay analysis of **NP-Bu** in toluene solution exhibits a mono-exponential decay having a lifetime of 3.54 ns comparable to dyad **NP** in solution on excited at 439 nm (Figure 3.22A). Similarly **NP-Oct** and **NP-Hed** in solution state exhibits fluoresecence lifetime decay of 3.54 and 3.49 ns respectively when excited at 439 nm (Figure 3.22A, Table 3.2). The fluoresecence lifetime decay analysis of **NP-Bu** in the crystalline state shows bi-exponential decay with the lifetimes of 2.87 ns (61%) and 6.23 ns (39%), upon photoexcitation at 439 nm (Figure 3.22B, Table 3.2). Similarly **NP-Oct** in the crystalline state exhibits a reduced fluorescence lifetime decay value of 1.99 (47%) 5.81 (53%) in comparison to **NP-Bu**. But **NP-Hed** shows a dramtic decrease in the lifetime deacay with a value of 1.32 (49%) and 3.36 (41%). To further understand the aggregation properties we have

3.2.3 Tuning the Photophysical Properties of Dyad NP by Incorporating Alkyl Side-Chain Units of Different Length to NI Moiety

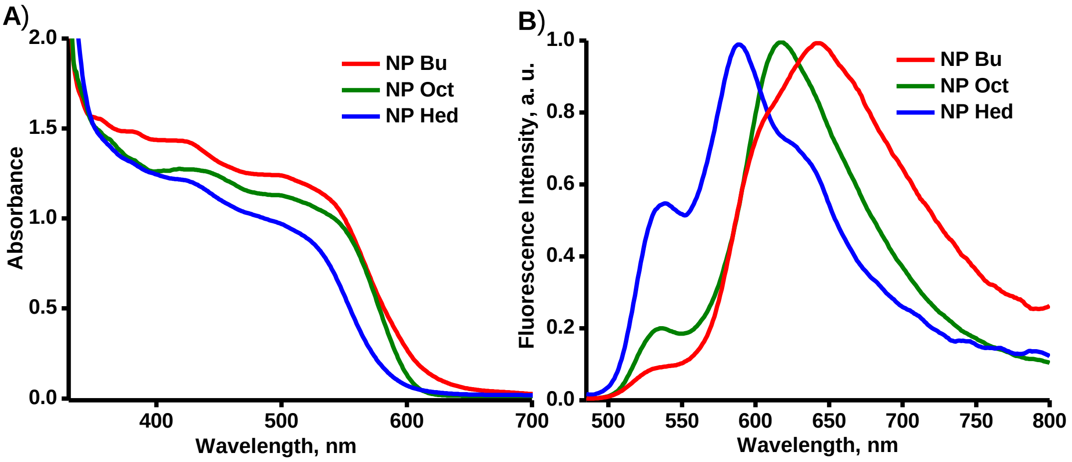

Figure 3.21 *A) Diffuse reflectance absorption and B) fluorescence* emission (λ_{ex}; 475 nm) *spectra of* ***NP-Bu, NP-Oct*** *and* ***NP-Hed*** *in the crystalline state.*

calculated the rate of radiative and non-radiative decay of **NP-Bu**, **NP-Oct and NP-Hed** in the solution as well as crystalline state from fluorescence quantum yield and lifetime by using Eq. 3.1 - 3.4 (Table 3.2). The **NP-Bu** in the crystalline state exhibits a moderately reduced rate of radiative decay (0.97×10^{8} s^{-1}) in comparison to the solution (2.32×10^{8} s^{-1}) attributes to weak H-type aggregates (Table 3.2)[41]. Similarly **NP-Bu** in the crystalline state exhibits an increase in the rate of non-radiative decay (1.01×10^{8} s^{-1}) in comparison to solution (0.51×10^{8} s^{-1}). But in the case of **NP-Oct** we observed a significant reduction in the rate of radiative decay (0.37×10^{8} s^{-1}) in comparison to the solution (2.26×10^{8} s^{-1}) and a significant increase in the rate of non-radiative decay in the crystalline state (1.67×10^{8} s^{-1}) in comparison to the solution (0.56×10^{8} s^{-1}) attributes moderately strong H-type aggregates. The **NP-Hed** exhibits similar trend in the rate of radiative decay like **NP-Bu** but significant increase in the rate of non-radiative decay (2.71×10^{8} s^{-1}) in the crystalline state in comparison to the solution (0.49×10^{8} s^{-1}) attributes to the presence of moderately strong H-type aggregates (Table 3.2). The optical microscopic images of the **NP**-alky dyads in the crystalline state indicate that the colour change occurs from red-orange to yellowish-orange on going from **NP-Bu** to **NP-Oct** and **NP-Hed** (Figure 3.23A-C) consistent

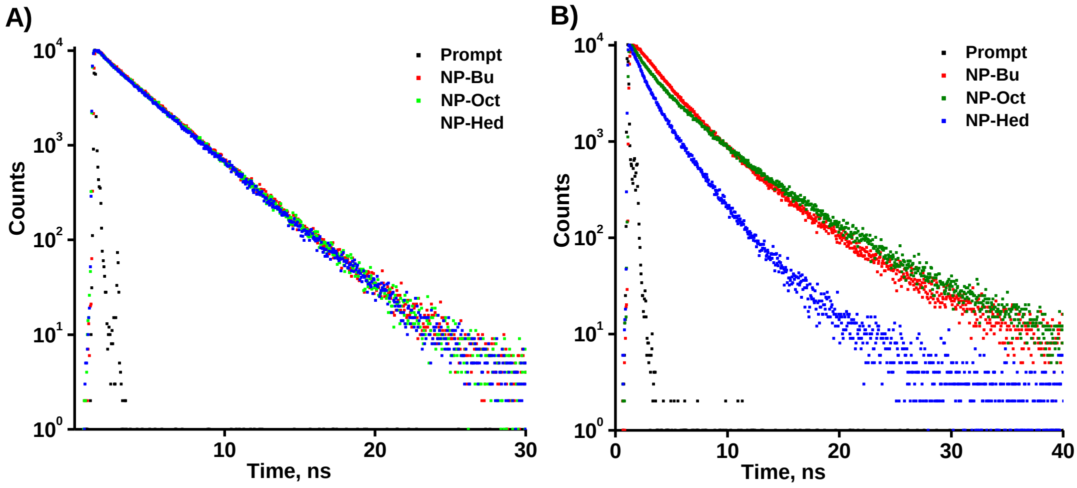

Figure 3.22 *Fluorescence lifetime decay of the dyad* **NP-Bu, NP-Oct** *and* **NP-Hed** *A) in the solution and B) in the crystalline state when excited at 439 nm.*

Table 3.2 *Photophysiscal properties of* **NP-Bu, NP-Oct** *and* **NP-Hed** *in the solution and crystalline state.*

	Solution					**Crystal**				
	λ_{em},[a] nm	ϕ_F[b]	τ[c] (d), ns	k_r,[e] [10^8 s^{-1}]	k_{nr},[f] [10^8 s^{-1}]	λ_{em},[a] nm	ϕ_F[b]	τ[c] (d), ns	k_r,[e] [10^8 s^{-1}]	k_{nr},[f] [10^8 s^{-1}]
NP-Bu	540	0.82 ± 0.001	3.54	2.32	0.51	644	0.47 ± 0.04	2.87 (61) 6.23 (39)	0.97	1.01
NP-Oct	539	0.80 ± 0.001	3.54	2.26	0.56	617	0.18 ± 0.04	1.99 (47) 5.81 (53)	0.37	1.67
NP-Hed	539	0.83 ± 0.001	3.49	2.38	0.49	589	0.24 ± 0.04	1.32 (49) 3.36 (41)	0.86	2.71

[b]Emission maxima (Excitation wavelength, 475 nm); [b]Quantum yield; [c]Fluorescence lifetime (Excitation wavelength, 439 nm and emission collected at 550 for **NP-Bu, NP-Oct** and **NP-Hed** in solution and 644 nm for **NP-Bu**, 617 nm for **NP-Oct** and 589 nm for **NP-Hed** in the crystalline state respectively); (d) corresponding amplitude; [e]rate of non-radiative decay and [f]rate of non-radiative decay.

with the slight blue shift observed in the solid-state diffuse reflectance absorption spectra. The confocal microscopic imaging of the crystalline samples of **NP-Bu, NP-Oct** and **NP-Hed** on exciting at 488 nm confirms the presence of strong red-orange fluorescence observed in the crystalline state (Figure 3.23D-F).

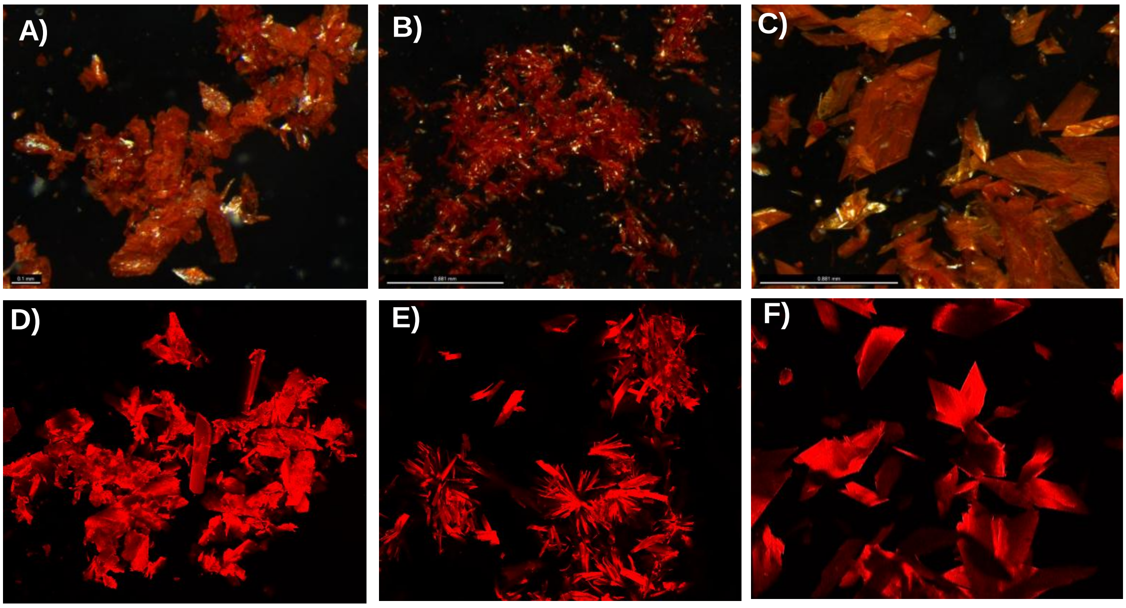

Figure 3.23 *Optical microscopic images of the crystalline samples of A)* ***NP-Bu****, B)* ***NP-Oct*** *and C)* ***NP-Hed***; Confocal microscopic image of the crystalline samples of *D)* ***NP-Bu****, E)* ***NP-Oct*** *and F)* ***NP-Hed*** *(Excitation wavelength, 488 nm and emission wavelength monitored at 550 – 650 nm).*

3.3 Conclusions

As a consequence of the distinct close-packing of the dyad **NP** in the solid state, we observed a strong fluorescence emission in the red region (λ_{max} = 631 nm) having a quantum yield of 0.5 ± 0.04 when excited at 475 nm corresponding to the perylenimide unit. Upon excitation at 345 nm, we observed fluorescence properties corresponding to the weak H-type aggregate of perylenimide unit through energy transfer from the singlet excited state of the naphthalenimide to the perylenimide unit in the crystalline **NP** followed by perylenimide-perylenimide exciton interactions. Since Förster type mechanism can also operate at much larger separation (non-nearest neighbour) between the naphthalenimide (donor) and the perylenimide (acceptor), interference between short and long distance energy transfer may occur that can lead to coherence. Efficient energy transfer in the crystalline **NP** arise from i) efficient overlap between the emission spectrum of naphthalenimide and absorption spectrum of perylenimide units (Figure 3.24A); ii)

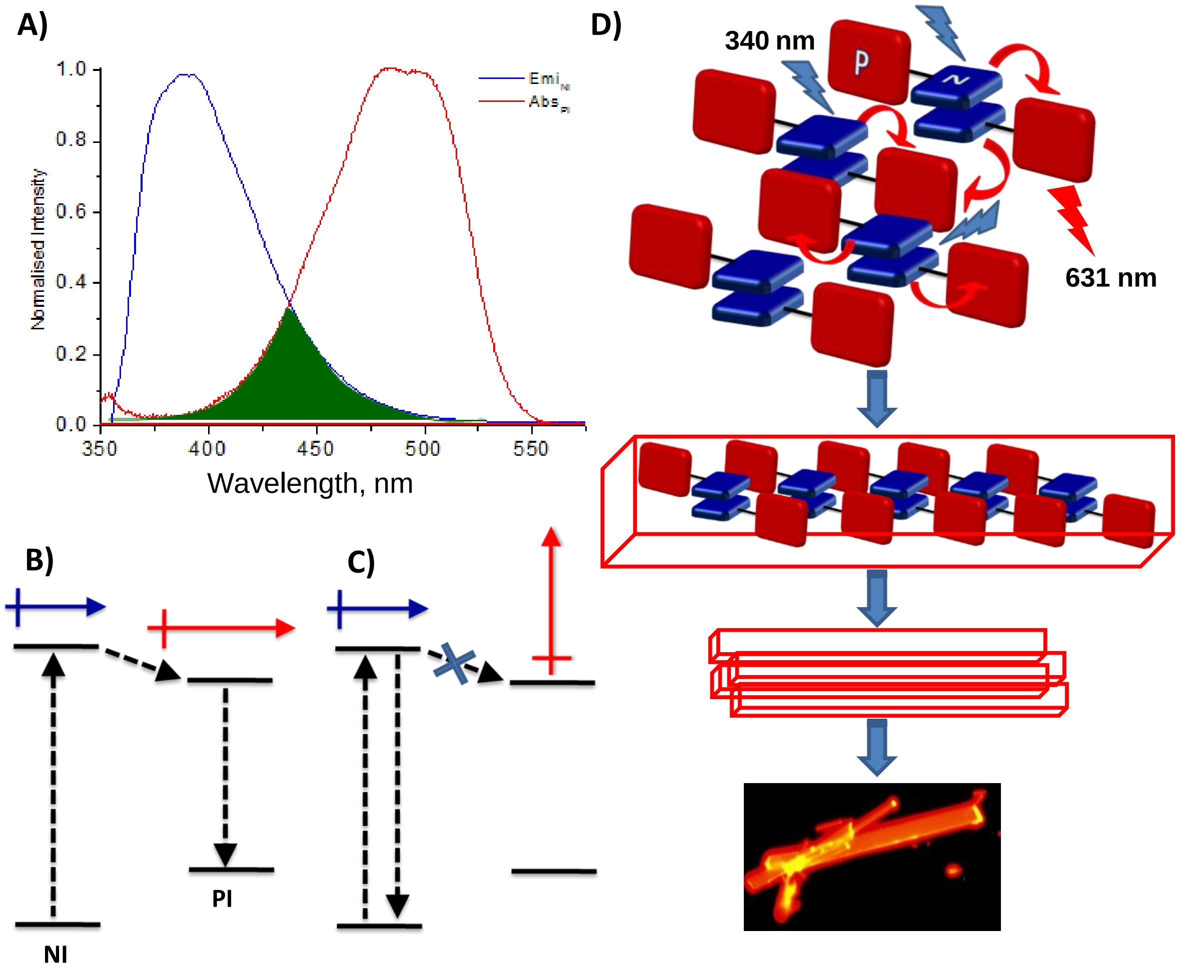

Figure 3.24 *Shows A) spectral overlap between the emission spectrum of the* ***NI*** *(blue) and the absorption spectrum of the* ***PI*** *(Red); Jablonski diagram indicating the B) allowed energy transfer in parallel dipoles and C) forbidden energy transfer in crossed dipoles: D) schematic illustration of energy transfer in the crystal leading to the wave-guided red luminescence (fluorescence microscopic image).*

favorable parallel transition dipole-transition dipole orientation (Figure 3.24B) that includes nearest and non-nearest neighbor[194] interactions in the periodic arrangement of the naphthalenimide and perylenimide units and iii) weak H-type exciton interactions between two perylenimide units. Efficient excitation energy transfer and/or exciton interactions between the nearest neighboring units would be forbidden in the case of cross dipole orientation[170,171] (Figure 3.24C) which is demonstrated to be the ideal arrangement of the transition dipoles in the absence of energy transfer. Interestingly, the dyad **NP** forms plate-like transparent crystals having the edges strongly emissive than the bulk of the crystal, indicating a self-wave-guided[195,196] structure of the crystalline **NP** (Figure 3.24D). Favourable thermal stability, close packing and photophysical properties in the solid-state make this material promising for organic light emitting diode[197,198] and dual excitation based lasing[199,200] applications. By carefully modifying the alkyl side-chains of dyad **NP** from butyl to octyl and hexadecyl, the color of the crystals could be tuned from red-orange to yellowish-orange by decreasing the interplanar distance between the **PI** units. We also tune the emission maxima of the NP dyad by modifying the alky chain from butyl (**NP-Bu**, λ_{em}; 644 nm) to hexadecyl group (**NP-Hed**, λ_{em}; 589 nm). The increased association between **NI-NI** units on going from **NP-Bu** to **NP-Oct** and **NP-Hed** facilitates the crystallisation of the dyad even in the presence of a long alky chain unit like the hexadecyl group. Also the decrease in solid state fluorescence quantum yield on going from **NP-Bu** ($\Phi_F = 0.47 \mp 0.04$) to **NP-Oct** ($\Phi_F = 0.18 \mp 0.04$) and **NP-Hed** ($\Phi_F = 0.24 \mp 0.04$) will be a detrimental effect in the case of long alkyl chain linked **NP** dyad for using various fluorescence based photonic applications.

3.4 Experimental Section

3.4.1 Synthesis Details

Synthetic details of model derivative **PI** and the dyad **NP** were described in chapter 1.

3.4.1.1 Preparation of N-(2,6-diisopropylphenyl)-9-(tributylstannyl))perylene-3,4-dicarboximide (17)

A solution of 9-Bromo-N-(2,6-diisopropylphenyl)-perylene-3,4-dicarboximide **(11)** (0.834 g, 1.49 mmol), hexabutylditin (1.74 g, 2.99 mmol) and $Pd(PPh_3)_4$ (5.16 mg, 0.3%) in 40 ml toluene was refluxed for 4 days. The solvent was then removed under reduced pressure and the residue was purified by column chromatography (silica gel, chloroform : petroleum ether 1 : 3) to give the product **17** (0.804 g, 70%) as a red solid. m. p. 164 °C; ^{1}H NMR (500 MHz, $CDCl_3$) δ ppm 8.71 – 8.69 (m, 2H), 8.55 – 8.50 (m, 3H), 8.44 (d, J = 7.5 Hz, 1H), 7.91 – 7.86 (m, 2H), 7.71 (t, J = 8Hz, 1H), 7.51 (t, J = 7.5 Hz, 1H), 7.37(d, J = 8.0 Hz, 2H), 2.81 – 2.77 (m, 2H), 1.65 – 1.58 (m, 6H), 1.41 – 1.38 (m, 6H), 1.32 – 1.29 (m, 6H), 1.21 (d, J = 7.5Hz, 12H), 0.96 - 0.92 (m, 9H) ; ^{13}C NMR (125 MHz, $CDCl_3$) δ ppm 164.04, 149.70, 145.77, 140.10, 138.07, 137.72, 136.32, 133.41, 132.07, 131.15, 131.13, 130.54, 129.85, 128.17, 126.98, 126.80, 124.02, 124.00, 123.71, 122.75, 120.84, 120. 77, 120.06, 119.93, 77.29, 77.03, 76.78, 29.20, 29.15, 27.37, 24.03, 13.69, 10.98; IR (KBr): 2956, 2926, 1701, 1662, 1589, 1458, 1355, 1292, 1244, 1195, 1178, 1138, 1033, 927, 894, 813, 750 cm^{-1}; Anal. Calcd. for $C_{46}H_{53}NO_2Sn$: C, 71.69; H, 6.93; N, 1.82%. Found: C, 72.07; H, 7.05; N, 1.31%.

3.4.1.2 Preparation of 4-Bromo-N-butyl-naphthalene-1,8-dicarboximide (18A)

To a solution of 4-bromo-1,8-naphthalic anhydride (**3**) (1.00 g, 3.60 mmol) in 30 ml acetic acid, butan-1-amine (1.31 g, 18.00 mmol) was added. This reaction mixture was heated at 119°C for 12 h followed by cooled to room temperature. It was then poured to water, filtered and the precipitate was washed with water and dried. The crude product was then purified by column chromatography (silica gel, EtOAc : petroleum ether 1 : 1) to afford compound **18A** (0.71 g, 60%) as a white solid. m. p. 98 °C; ^{1}H NMR (500 MHz, $CDCl_3$) δ: 8.56 (d, J = 7.50 Hz, 1H), 8.46 (d, J = 8.50 Hz, 1H), 8.31 (d, J = 8.00 Hz, 1H), 7.94 (d, J = 8.00 Hz, 1H), 7.75 (t, J = 8.00 Hz, 1H), 4.09 (t, J = 7.50 Hz, 2H), 1.67 – 1.61 (m, 2H), 1.39 – 1.35 (m, 2H), 0.90 (t, J = 7.50 Hz, 3H); ^{13}C NMR (125 MHz, $CDCl_3$) δ: 162.57, 162.54, 132.13, 130.94, 130.14, 130.04, 129.56, 129.12, 127.94, 127.02, 122.12, 121.26, 39.35, 29.14, 19.34, 12.81; IR (KBr): 2953, 2868, 1696, 1662, 1589, 1570, 1504, 1460, 1346, 1265, 1228, 1074, 941, 854, 781, 746 cm^{-1}; Anal. Calcd. for $C_{16}H_{14}BrNO_2$: C, 57.85; H, 4.25; N, 4.22%. Found: C, 57.51; H, 3.96; N, 3.98%.

3.4.1.3 Preparation of 4-Bromo-N-octyl-naphthalene-1,8-dicarboximide (18B)

To a solution of 4-bromo-1,8-naphthalic anhydride (**3**) (1.00 g, 3.60 mmol) in 30 ml acetic acid octan-1-amine (2.32 g, 18.00 mmol) was added. This reaction mixture was heated at 119°C for 12 h followed by cooled to room temperature. It was then poured to water, filtered and the precipitate was washed with water and dried. The crude product was then purified by column chromatography (silica gel, EtOAc : petroleum ether 1 : 1) to afford compound **18B** (0.84 g, 60%) as a white solid. m. p. 82°C; ^{1}H NMR (500 MHz, $CDCl_3$) δ: : 8.56 (d, J = 8.00 Hz, 1H), 8.48 (d, J = 8.50 Hz, 1H), 8.33 (d, J = 8.00 Hz, 1H), 7.96 (d, J = 7.50 Hz, 1H), 7.77 (t, J = 8.00 Hz, 1H), 4.08 (t, J = 7.50 Hz, 2H), 1.66 – 1.63 (m, 2H), 1.36 – 1.33 (m, 2H), 1.23 – 1.18 (m, 8H), 0.79 (t, J = 7.50 Hz, 3H); ^{13}C NMR (125 MHz, $CDCl_3$) δ: 163.60, 163.58, 133.18, 131.99, 131.18, 131.08, 130.63, 129.02, 128.06, 123.02, 122.34, 40.65, 31.82, 29.33, 29.21, 28.10, 27.14, 22.64, 14.08; IR (KBr): 2920, 2850, 1701, 1649, 1591, 1458, 1355, 1228, 1049, 785 cm^{-1}; Anal. Calcd. for $C_{20}H_{22}BrNO_2$: C, 61.86; H, 5.71; N, 3.61%. Found: C, 61.51; H, 5.46; N, 3.38%.

3.4.1.4 Preparation of 4-Bromo-N-hexadecyl-naphthalene-1,8-dicarboximide (18C)

To a solution of 4-bromo-1,8-naphthalic anhydride (**3**) (1.00 g, 3.60 mmol) in 100 ml acetic acid hexadecan-1-amine (4.34 g, 18.00 mmol) was added. This reaction mixture was heated at 119°C for 12 h followed by cooled to room temperature. It was then poured to water, filtered and the precipitate was washed with water and dried. The crude product was then purified by column chromatography (silica gel, EtOAc : petroleum ether 4 : 1) to afford compound **18C** (1.08 g, 60%) as a white solid. m. p. 74°C; ^{1}H NMR (500 MHz, $CDCl_3$) δ: 8.68 (d, J = 7.00 Hz, 1H), 8.57 (d, J = 8.50 Hz, 1H), 8.44 (d, J = 7.50 Hz, 1H), 8.06 (d, J = 8.00 Hz, 1H), 7.87 (t, J = 7.00 Hz, 1H), 4.19 (t, J = 8.00 Hz, 2H), 1.78 – 1.72 (m, 2H), 1.47 – 1.45 (m, 2H), 1.43 – 1.41 (m, 2H), 1.31 – 1.27

(m, 22H,) 0.91 (t, J = 7.00 Hz, 3H); ^{13}C NMR (125 MHz, $CDCl_3$) δ: 163.62, 163.60, 133.19, 132.00, 131.20, 131.09, 130.65, 130.16, 129.03, 128.07, 123.21, 122.35, 40.65, 31.92, 29.64, 29.63, 29.61, 29.55, 29.37, 29.35, 28.10, 27.14, 22.69, 14,12; IR (KBr): 2920, 2850, 1703, 1660, 1591, 1465, 1352, 1352, 1230, 1082, 777 cm^{-1}; Anal. Calcd. for $C_{28}H_{38}BrNO_2$: C, 67.19; H, 7.65; N, 2.80%. Found: C, 67.45; H, 7.45; N, 2.51%.

3.4.1.5 Preparation of 9-(4-(N-butyl)naphthalene-1,8-dicarboximide)yl)-N-(2,6-diisopropylphenyl)-perylene-3,4-dicarboximide (19A)

A solution of N-(2,6-diisopropylphenyl)-9-(tributylstannyl))perylene-3,4-dicarboximide **(17)** (0.686 g, 0.89 mmol), 4-Bromo-N-butyl-naphthalene-1,8-dicarboximide **(18A)** (0.37 g, 1.11 mmol) and $Pd(PPh_3)_4$ (10.28 mg, 0.0089 mmol) in 50 ml DMF was heated at 120 °C for 2 days. The solvent was removed under reduced pressure and the residue was purified by column chromatography (silica gel, EtOAc:petroleum ether 1:2) to afford compound **19A** (0.32 g, 50%) as a red-orange solid. m. p. > 300°C; ^{1}H NMR (500 MHz, $CDCl_3$,) δ: 8.69 (d, J = 7.50 Hz, 1H), 8.67 – 8.64 (m, 2H), 8.60 – 8.56 (m, 2H), 8.51 (d, J = 8.00 Hz, 1H), 8.47 (d, J = 8.00 Hz, 2H), 7.82 – 7.77 (m, 2H), 7.61 (d, J = 7.50 Hz, 1H), 7.57 (t, J = 8.00 Hz, 1H), 7.46 – 7.43 (m, 2H), 7.35 (d, J = 8.50 Hz, 1H), 7.28 (d, J = 8.00 Hz, 2H), 4.19 (t, J = 8.00 Hz, 2H), 2.72 – 2.70 (m, 2H), 1.74 – 1.68 (m, 2H), 1.46 – 1.41 (m, 2H), 1.13 – 1.11 (m, 12H), 0.95 (t, J = 7.50 Hz, 2H) ; ^{13}C NMR (125 MHz, $CDCl_3$) δ: 163.14, 162.99, 162.93, 144.73, 144.70, 143.17, 138.21, 136.30, 136.03, 132.42, 131.43, 131.16, 131.13, 130.47, 130.10, 129.94, 129.69, 129.53, 128.99, 128.70 128.49, 128.13, 127.91, 127.50, 127.26, 126.63, 126.27, 125.99, 125.99, 123.10, 123.03, 122.14, 121.86, 120.49, 120.36, 119.75, 119.62, 39.37, 29.26, 28.15, 23.02, 23.00, 19.41, 12.86; IR (KBr): 2960, 2868, 1701, 1660, 1587, 1577, 1355, 1238, 1151, 1058 cm^{-1}; Anal. Calcd. for $C_{50}H_{40}N_2O_4$: C, 81.94; H, 5.50; N, 3.82%. Found: C, 81.55; H, 5.27; N, 3.56%.

3.4.1.6 Preparation of 9-(4-(N-octyl)naphthalene-1,8-dicarboximide)yl)-N-(2,6-diisopropylphenyl)-perylene-3,4-dicarboximide (19B)

A solution of N-(2,6-diisopropylphenyl)-9-(tributylstannyl))perylene-3,4-dicarboximide **(17)** (0.686 g, 0.89 mmol), 4-Bromo-N-octyl-naphthalene-1,8-dicarboximide **(18B)** (0.43 g, 1.12 mmol) and $Pd(PPh_3)_4$ (10.28 mg, 0.0089 mmol) in 50 ml DMF was heated at 120 °C for 2 days. The solvent was removed under reduced pressure and the residue was purified by column chromatography (silica gel, EtOAc : petroleum ether 1 : 1) to afford compound **19B** (0.35 g, 50%) as a yellow-orange solid. m. p. 293 °C; ^{1}H NMR (500 MHz, $CDCl_3$,) δ: δ: 8.69 (d, J = 7.50 Hz, 1H), 8.67 – 8.63 (m, 2H), 8.59 – 8.56 (m, 2H), 8.51 (d, J = 8.00 Hz, 1H), 8.46 (d, J = 8.00 Hz, 2H), 7.82 – 7.77 (m, 2H), 7.61 (d, J = 8.00 Hz, 1H), 7.57 (t, J = 8.00 Hz, 1H), 7.46 – 7.40 (m, 2H), 7.36 (d, J = 8.50 Hz, 1H), 7.28 (d, J = 8.00 Hz, 2H), 4.17 (t, J = 7.50 Hz, 2H), 2.73 – 2.68 (m, 2H), 1.75 – 1.69 (m, 2H), 1.41 – 1.39 (m, 2H), 1.34 – 1.31 (m, 2H), 1.27 – 1.24 (m, 6H), 1.13 – 1.11 (m, 12H), 0.82 (t, J = 7.00 Hz, 3H) ; ^{13}C NMR (125 MHz, $CDCl_3$) δ: 164.16, 164.01, 163.97, 145.78, 145.72, 144.19, 139.25, 137.34, 137.07, 133.44, 132.46, 132.20, 132.17, 131.50, 131.12, 130.95, 130.73, 130.55, 130.00, 129.72 129.53, 129.17, 128.94, 128.52, 128.28, 127.66, 127.30, 127.01, 124.14 124.07, 123.18, 123.15, 122.89, 121.49, 120.77, 120.65, 40.67, 31.86, 29.40, 29.27, 29.18, 28.21, 27.21, 24.05, 24.03, 22.67, 14.12; IR (KBr): 2958, 2860, 1701, 1660, 1585, 1458, 1355, 1242, 1155, 756 cm^{-1}; Anal. Calcd. for $C_{54}H_{48}N_2O_4$: C, 82.21; H, 6.13; N, 3.55%. Found: C, 81.95; H, 5.87; N, 3.16%.

3.4.1.7 Preparation of 9-(4-(N-hexadecyl)naphthalene-1,8-dicarboximide)yl)-N-(2,6-diisopropylphenyl)-perylene-3,4-dicarboximide (19C)

A solution of N-(2,6-diisopropylphenyl)-9-(tributylstannyl))perylene-3,4-dicarboximide **(4)** (0.686 g, 0.89 mmol), 4-Bromo-N-butyl-naphthalene-1,8-dicarboximide **(18C)** (0.55 g, 1.12 mmol) and $Pd(PPh_3)_4$ (10.28 mg, 0.0089 mmol) in 50 ml DMF was heated at 120 °C for 2 days. The solvent was removed under reduced pressure and the residue was purified by column chromatography (silica gel, EtOAc : petroleum ether 1 : 1) to afford compound **19C** (0.40 g, 50%) as a yellow-orange solid. m. p. 244 °C; ^{1}H NMR (500 MHz, $CDCl_3$,) δ: 8.69 (d, J = 7.50 Hz, 1H), 8.65 – 8.62 (m, 2H), 8.58 - 8.54 (m, 2H), 8.49 (d, J = 8.00 Hz, 1H), 8.44 (d, J = 8.00 Hz, 2H), 7.81 – 7.76 (m, 2H), 7.61 (d, J = 7.50 Hz, 1H), 7.56 (t, J = 7.50 Hz, 1H), 7.44 – 7.39 (m, 2H), 7.35 (d, J = 8.50 Hz, 1H), 7.27 (d, J = 8.00 Hz, 2H), 4.17 (t, J = 7.50 , 1H), 2.74 – 2.68 (m, 2H), 1.73 – 1.53 (m, 2H), 1.39 – 1.37 (m, 2H), 1.33 – 1.30 (m, 2H), 1.22 – 1.18 (m, 22H), 1.13 – 1.11 (m, 12H), 0.80 (t, J = 7 Hz; 3H); ^{13}C NMR (125 MHz, $CDCl_3$) δ: 163.11, 162.95, 162.91, 144.73, 144.70, 144.15, 138.21, 136.28, 136.01, 132.42, 131.40, 131.14, 131.11, 130.45, 130.10, 129.94, 129.68, 129.52, 128.98, 128.68 128.49, 128.13, 127.90, 127.50, 127.26, 126.62, 126.26, 125.98 123.09, 123.03, 122.14, 121.88, 120.49, 120.37, 119.74, 119.61, 39.63, 30.91, 28.69, 28.67, 28.67, 28.65, 28.62, 28.58, 28.41, 28.35, 28.16, 27.19, 26.18, 23.02, 23.00, 21.67, 13.10; IR (KBr): 2924, 2852, 1701, 1662, 1587, 1460, 1355, 1240, 756 cm^{-1}; Anal. Calcd. for $C_{60}H_{62}N_2O_4$: C, 82.63; H, 7.16; N, 3.11%. Found: C, 82.25; H, 6.87; N, 2.86%.

3.4.2 Photophysical Measurements

Absorption and emission spectra were recorded on Shimadzu UV-3600 UV-VIS-NIR and Horiba Jobin Yvon Fluorolog spectrometers respectively. Solid state quantum yield of crystalline **NP** and the model derivative **PI** was obtained using an integrating sphere and calculated by Horiba Jobin Yvon quantum yield and colour calculator software using tris(8-hydroxyquinolinato)aluminium (Alq3) as standard and is determined to be 0.36 ± 0.04 (Reported quantum yield Φ = 0.40)[201]. Fluorescence quantum yield measurements of the dyad **NP**, model derivative **PI** and Alq3 were carried out on polycrystalline material. Fluorescence lifetime and anisotropy measurements were carried out in an IBH picosecond single photon counting system. The fluorescence decay profiles were de-convoluted using IBH data station software version 2.1, and fitted with exponential decay, minimizing the χ^2 values of the fit to 1 ± 0.05. Fluorescence anisotropy decay profiles are corrected for G-factor and r_0 is obtained from a mono-exponential fit of the anisotropy decay. All spectroscopic experiments were performed using standard quartz cuvettes of path length 1 cm and using dried and distilled solvents. Fluorescent microscopic images of crystalline **NP** is obtained on a Leica DM 500P optical microscope and the excitation wavelength is 337 nm. Fluorescence microscopic images were analysed using ImageJ software to quantify the fluorescence intensity. Confocal microscopic images of crystalline samples of **NP-Bu**, **NP-Oct** and **NP-Hed** are obtained on a Leica SP5 upright confocal microscope with an excitation wavelength of 488 nm and the emission monitored at 550 – 650 nm wavelength range.

3.4.3 X-ray Crystallography

Red, single crystals of **PI**, conjugate **NP**, **NP-Bu**, **NP-Oct** and **NP-Hed** were obtained by slow diffusion of ethanol into a chloroform solution of the sample. A high quality crystal specimen of approximately $0.25 \times 0.05 \times 0.05$ mm^3 was selected for the X-ray diffraction experiment. Single crystals were mounted using oil (Infineum V8512) on a glass fiber. All measurements were made on a CCD area detector with graphite monochromated CuKα radiation. The data was collected using Bruker APEXII detector and processed using APEX2 from Bruker. All structures were solved by direct methods and expanded using Fourier techniques. The non-hydrogen atoms were refined anisotropically. Hydrogen atoms were included in idealized positions, but not refined. Their positions were constrained relative to their parent atom using the appropriate HFIX command in SHELXL-97. Crystallographic data collected for **PI, NP-Bu**, **NP-Oct** and **NP-Hed** are presented in the Table 3.3-3.6. Crystallographic data of **NP** already described in chapter 2 (Refer Chapter 2, Table 2.1).

Table 3.3 *Crystal data and structure refinement for conjugate* ***PI.***

	PI
Empirical formula:	$C_{34}H_{27}NO_2$
Formula weight:	481.58 g/mo
Temperature:	99.83 K
a:	14.5939 Å
b:	8.3677 Å
c:	40.026 Å
α (alpha):	90 °
β (beta):	98.027 °
γ (gamma):	90 °
Volume:	4839.98 $Å^3$
Crystal system:	Monoclinic
Space group:	$P2_1n$
Calculated density:	1.242 g/cm^3
Z:	2
Reflections collected:	8082
R(F):	0.0975
$R_w(F^2)$:	0.2614
Goodness of fit on F^2:	1.127

3.4.3 X-ray Crystallography

Table 3.4 *Crystal data and structure refinement for conjugate* ***NP-Bu.***

	Conjugate **NP-Bu**
Empirical formula:	$C_{50}H_{40}N_2O_4$
Formula weight:	732.84 g/mole
Temperature:	296 (2) K
a:	9.147 Å
b:	14.683 Å
c:	15.290 Å
α (alpha):	70.99 °
β (beta):	77.37 °
γ (gamma):	84.34 °
Volume:	1893.71 Å^3
Crystal system:	Triclinic
Space group:	$P\bar{1}$
Calculated density:	1.285 g/cm^3
Z:	2
Reflections collected:	27994
R(F):	0.0605
$R_w(F^2)$:	0.1709
Goodness of fit on F^2:	1.044

Table 3.5 *Crystal data and structure refinement for conjugate* ***NP-Oct.***

	Conjugate **NP-Oct**
Empirical formula:	$C_{54}H_{48}N_2O_4$
Formula weight:	788.94 g/mole
Temperature:	296 (2) K
a:	9.168 Å
b:	12.843 Å
c:	18.329 Å
α (alpha):	84.99 °
β (beta):	88.53 °
γ (gamma):	79.49 °
Volume:	2113.6(2) $Å^3$
Crystal system:	Triclinic
Space group:	$P\bar{1}$
Calculated density:	1.240 g/cm^3
Z:	2
Reflections collected:	30662
R(F):	0.0679
$R_w(F^2)$:	0.1980
Goodness of fit on F^2:	1.007

3.4.3 X-ray Crystallography

Table 3.6 *Crystal data and structure refinement for conjugate* ***NP-Hed****.*

	Conjugate **NP-Hed**
Empirical formula:	$C_{62}H_{64}N_2O_4$
Formula weight:	901.15 g/mole
Temperature:	125 (2) K
a:	9.151 Å
b:	13.891 Å
c:	19.660 Å
α (alpha):	84.33 °
β (beta):	87.82 °
γ (gamma):	79.49 °
Volume:	2434.5 (2) $Å^3$
Crystal system:	Triclinic
Space group:	$P\bar{1}$
Calculated density:	1.229 g/cm^3
Z:	2
Reflections collected:	28490
R(F):	0.1446
$R_w(F^2)$:	0.3531
Goodness of fit on F^2:	1.056

3.4.4 Conductive Atomic Force Microscopy (C-AFM)

AFM instrument was operated in C-AFM mode and conductive probe was employed to get the I-V curve. The sensor signal was the electric current between the tip and the sample for an applied DC bias voltage. A silicon probe coated with PtIr/Cr having the radius less than 50 nm and a spring constant of 0.2 N/m was used in the experiment. Material was drop-casted from toluene solution to a thickness of 50-80 nm on HOPG surface. Conductance was measured on the surface at different positions before and after exposing to iodine vapors by applying the bias voltage of -10 to 10 V. The value of conductivity was calculated using the equation[202],

$$\sigma = d \,/\, (A_t R)\ S/cm \tag{3.5}$$

where σ is the conductivity of the material, d is the film thickness, A_t is the area of contact between the tip and the surface which can be calculated from the formula area equals to πr^2 in which r is contact radius of the tip (~30-50 nm) and R is the resistance of the sample which can be obtained from the inverse slope of the I-V plot.

Chapter 4

Photoinduced Electron Transfer Assisted by Vesicular Scaffold Containing Near-Orthogonal Dyad

4.1 Introduction

Excitation energy and electron transfer processes in crowded environments are vital for natural[70,203-205]/artificial[4-6] photosynthesis and photonic applications[9,11-13,206]. Such processes in isolated donor–acceptor (D–A) systems still possess immense interest[207]. Non-covalent D–A pairs that exhibit efficient light harvesting and favorable excited-state properties in the condensed media such as amorphous, thin film[208], vesicle[67,209-211], gel[68,69,212,213], liquid crystal[214] and crystalline[215] state received recent attention. Despite being efficient in light-harvesting and colour-tunable properties[68,69,212,216], the major limitations in D–A co-assemblies is the control[99] of i) stoichiometry, ii) distance and iii) orientation between the donor and the acceptor units. Excitation energy transfer in self-assembled covalent D–A dyads that includes amorphous[36], thin film[77,217], crystal[36,218,219] and liquid crystalline state[220] received less attention. The dearth of literature reports in light harvesting self-assembled covalent D–A dyads could be due to the strong propensity of the aromatic surface[221] to self-assemble[222,223] and subsequent exciton interactions[28,224,225]/electron transfer[8,37,72,226] that could alter the excited state properties. By virtue of curvature properties[96], vesicular scaffolds[227,228] could be superior for light harvesting processes similar to the chromatophoric vesicular assembly in the natural photosynthetic unit[39]. A single molecular D–A dyad that can assemble to form vesicles/gel and retain favourable excited state properties could be a potential

Publication based on this work has been reported in *Energy Environ. Sci.* **7**, 1661-1669 (2014) scaffold for light harvesting applications. Concurrently, Wasielewski and co-workers have pioneered covalent D–A pairs that can undergo photoinduced electron transfer in aggregates extending the lifetime of charge-separated intermediates[8,93,229]. However, combination of light harvesting and charge separation in self-assembled architectures received limited attention[37,89]. We demonstrate that vesicular scaffold of a covalent D–A antenna can efficiently harvest light and can undergo photoinduced energy followed by electron transfer in the presence of an electron donor.

The efficient excitation energy transfer in near-orthogonal naphthalimide (donor)–perylenimide (acceptor) dyad **NP(OH)** in solution and crystalline state described in chapter 1 and 2 (Figure 4.1)[182,219]. A subtle modification of the dyad using (***R***/***S***)-α,β-dihydroxypropyl side-chain imparted optimal amphiphilicity to

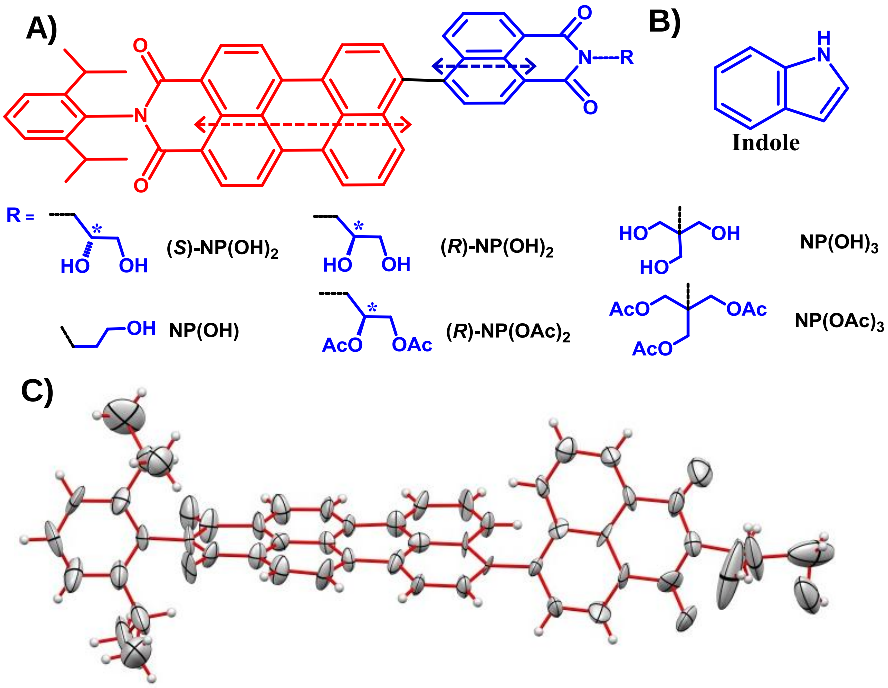

Figure 4.1 *Chemical structure of the molecules under investigation and the crystal structure of the dyad (**R**)-**NP(OH)**₂. Molecular structure of A) the dyads **NP(OH)**, (**R**/**S**)-**NP(OH)**₂, (**R**)-**NP(OAc)**₂, **NP(OH)**₃, **NP(OAc)**₃, arrows indicate the orientation of the transition dipole moment of the naphthalimide (**NI**) and perylenimide (**PI**) units; B) indole (electron donor) and C) single crystal X-ray structure of the dyad (**R**/**S**)-**NP(OH)**₂.*

promote the formation of a (***R***/***S***)-**NP(OH)$_2$** based vesicular gel in 1 : 2 dichloromethane (DCM) : hexane mixture that allowed us to investigate the photoinduced processes of covalent D–A pair in the gel state. To the best of our knowledge, this is the first report of a covalent D–A vesicle/gel that possesses efficient 'Forster-type' light harvesting properties resulting in orange–red fluorescence (λ_{em} = 584 nm) and high-fluorescence quantum yield (Φ_F = 54%). The vesicular gel of **(*R*/*S*)-NP(OH)$_2$** exhibits stability in the presence of an electron donor (indole) making the dyad–donor co-gel, a potential candidate for combining efficient light harvesting and charge separation properties.

4.2 Results and Discussions

The dyads (***R***/***S***)-**NP(OH)$_2$** were synthesised through Stille coupling between tributyltin derivative of perylenimide and 4-bromo-N-(***R***/***S***)-2,3-dihydroxypropyl naphthalimide (Scheme 4.1)[182,230]. Monohydroxy **NP(OH)**[182,230], trihydroxy **NP(OH)$_3$** and protected analogues (***R***)-**NP(OAc)$_2$** and **NP(OAc)$_3$** of the dyad, having different degrees of amphiphilicity, were also synthesised (Scheme 4.1–4.2). UV–Vis absorbance of dyad (***R***)-**NP(OH)$_2$** (Figure 4.2A) in DCM could be described as sum of the absorbance of naphthalimide (**NI**) centred at 340 nm and perylenimide (**PI**) centred at 480 nm indicating that (***R***)-**NP(OH)$_2$** behaves as individual chromophores though connected by a covalent bond (Figure 4.3)[182]. X-ray structure (Figure 4.1C), cyclic voltammetry and photophysical studies of the dyad (***R***)-**NP(OH)$_2$** and structurally analogous **NP(OH**) indicated near-orthogonal arrangement and negligible orbital interactions between constituent naphthalimide and perylenimide units. Absence of circular dichroism (CD) signal (Figure 4.2B) corresponding to **NI/PI** units indicates the presence of equal amounts of mutually enantiomeric atropisomers[231,232] of the (***R***/***S***)-**NP(OH)$_2$** in DCM (Figure 4.4A, B), consistent with both the axially chiral forms (1 : 1) in the unit cell. Upon direct excitation of the PI unit at 475 nm, (***R***)-**NP(OH)$_2$** in DCM exhibited fluorescence emission (Φ_F = 0.75 ±

4.2 Results and Discussions

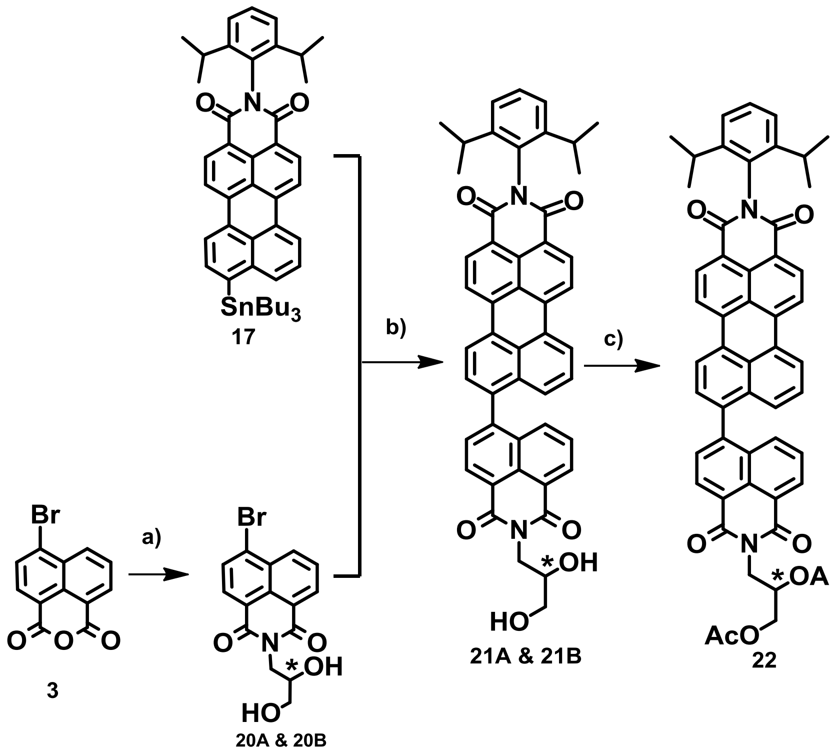

a) (*R*)/(*S*)-3-aminopropane-1,2-diol/H_2O/70 °C; b) $Pd(PPh_3)_4$/DMF/90 °C; c) acetic anhydride/pyridine/RT.

Scheme 4.1 *Shows the synthesis of* ***(R/S)-NP(OH)$_2$*** *and the protected analogue* ***(R)-NP(OAc)$_2$***.

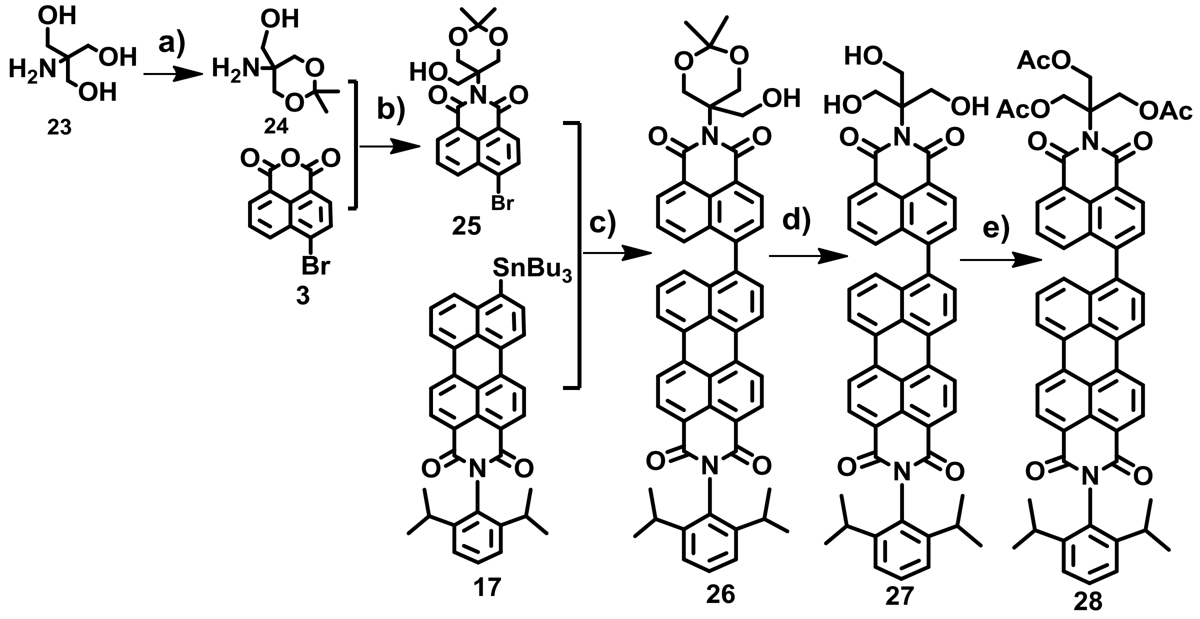

a) Dimethoxy propane/DMF/PTSA; b) pyridine/$Zn(OAc)_2.2H_2O$/reflux; c) $Pd(PPh_3)_4$/DMF/90 °C; d) MeOH/DCM/1N HCl; e) acetic anhydride/pyridine.

Scheme 4.2 *Shows the synthesis of* ***NP(OH)$_3$*** *and the protected analogue* ***NP(OAc)$_3$***.

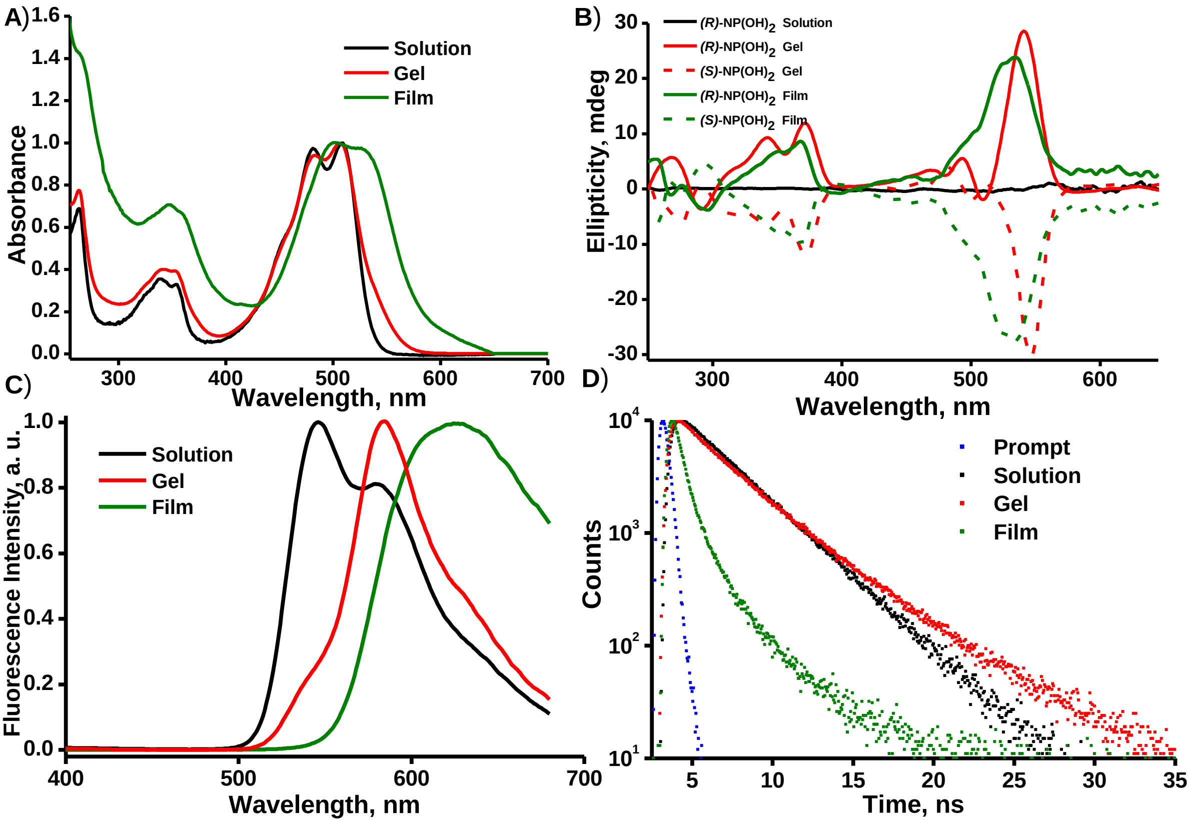

Figure 4.2 *Light harvesting and chiroptical properties of dyad* **NP(OH)$_2$** *in solution, gel and film state. A) UV–Vis absorption spectra; B) CD spectra; C) fluorescence spectra ex = 345 nm) and D) time-resolved fluorescence decay of (**R**)-**NP(OH)$_2$** in DCM [black], (**R**)-**NP(OH)$_2$** gel in* DCM : hexane *(1 : 2) mixture [red], (**R**)-**NP(OH)$_2$** thin film [green] and prompt [blue] when excited at 340 nm and emission collected at 550 nm (solution) and 580 nm (gel and film). (**S**)-**NP(OH)$_2$** gel [dashed red] and thin film [dashed green] only for CD spectra.*

0.04) centred at 546 nm having a shoulder at 580 nm corresponding to the **PI** unit (Figure 4.5A). Upon excitation at 345 nm, efficient energy transfer[233] from singlet excited state of **NI** to **PI** unit of (***R***)-**NP(OH)$_2$** in DCM resulted in the **PI** emission centred at 546 nm (Figure 4.2C). Time-resolved fluorescence of (***R***)-**NP(OH)$_2$** in DCM exhibited mono-exponential decay having a lifetime of 3.7 ns, when excited at 340 nm (Figure 4.2D) and 439 nm (Figure 4.5B). Increasing volume fraction of hexane in a solution of (***R***)-**NP(OH)$_2$** in DCM showed a blue-shift of 5 nm and a systematic decrease in the UV–Vis absorbance centred at 513 nm with the formation of a band

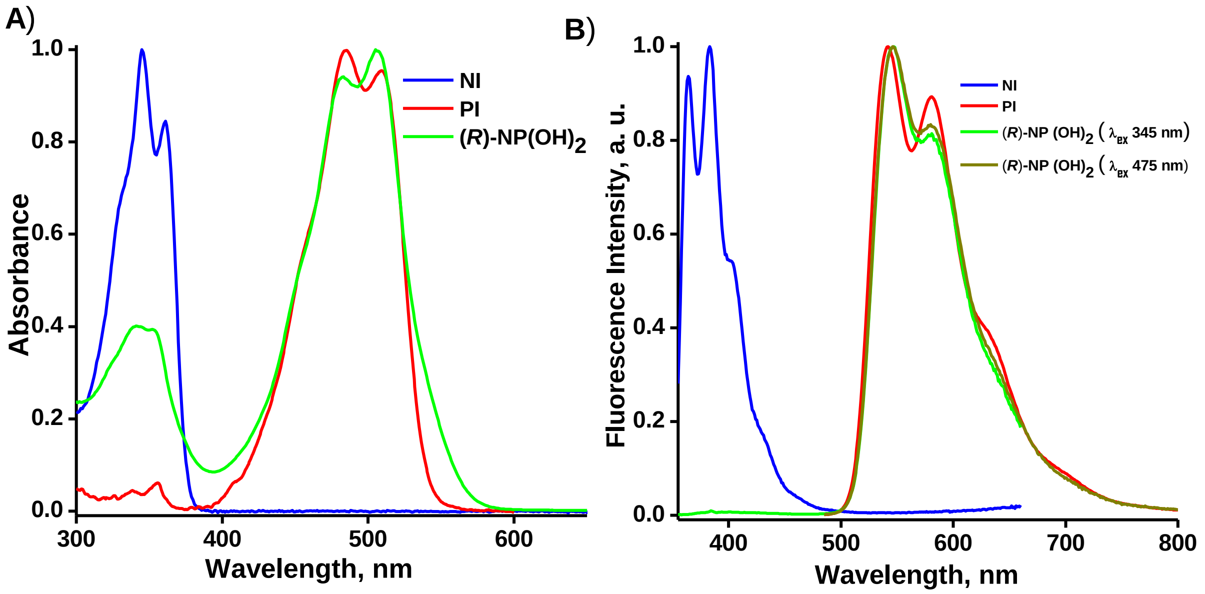

Figure 4.3 *Absorption and fluorescence emission properties. A) Absorption spectra of* ***NI*** *(blue),* ***PI*** *(red) and* ***(R)-NP(OH)₂*** *(green) in DCM and B) Fluorescence emission spectra of* ***NI*** *(blue; λ_{ex}: 345 nm),* ***PI*** *(red; λ_{ex}: 475 nm) and* ***(R)-NP(OH)₂*** *(green; λ_{ex}: 345 nm and dark yellow; λ_{ex}: 475 nm) in DCM.*

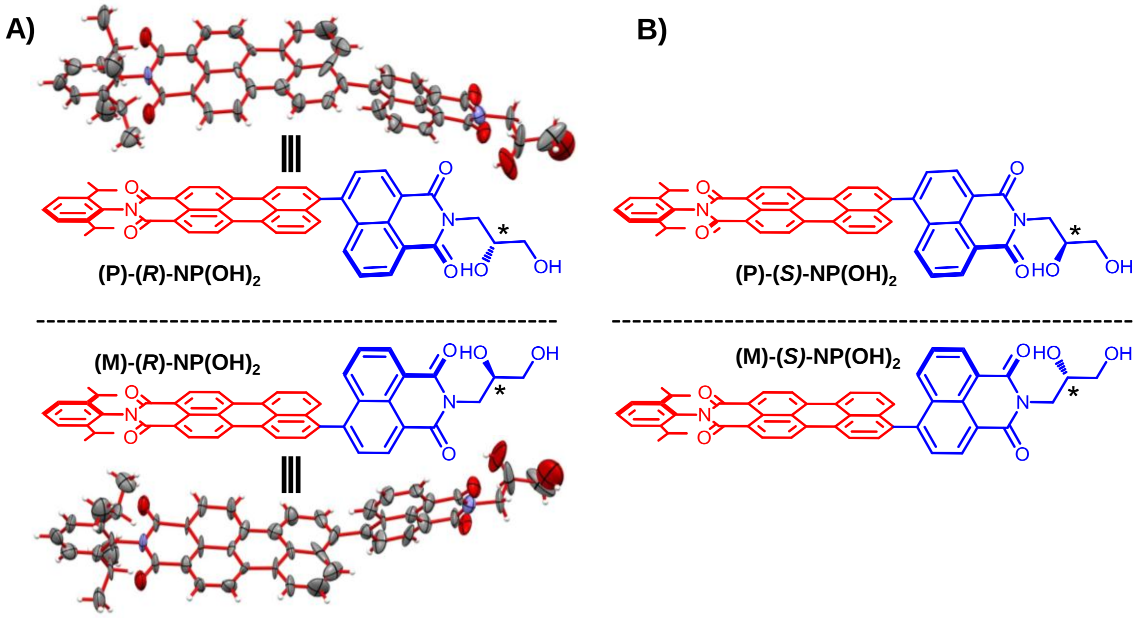

Figure 4.4 *Chemical structure of two optical isomers of* ***(P/M)-NP(OH)₂****. The molecular structure of the P and M stereoisomers of A)* ***(R)-NP(OH)₂****, X-ray crystal structure of the P and M stereoisomers of* ***(R)-NP(OH)₂*** *are also shown and B)* ***(S)-NP(OH)₂****.*

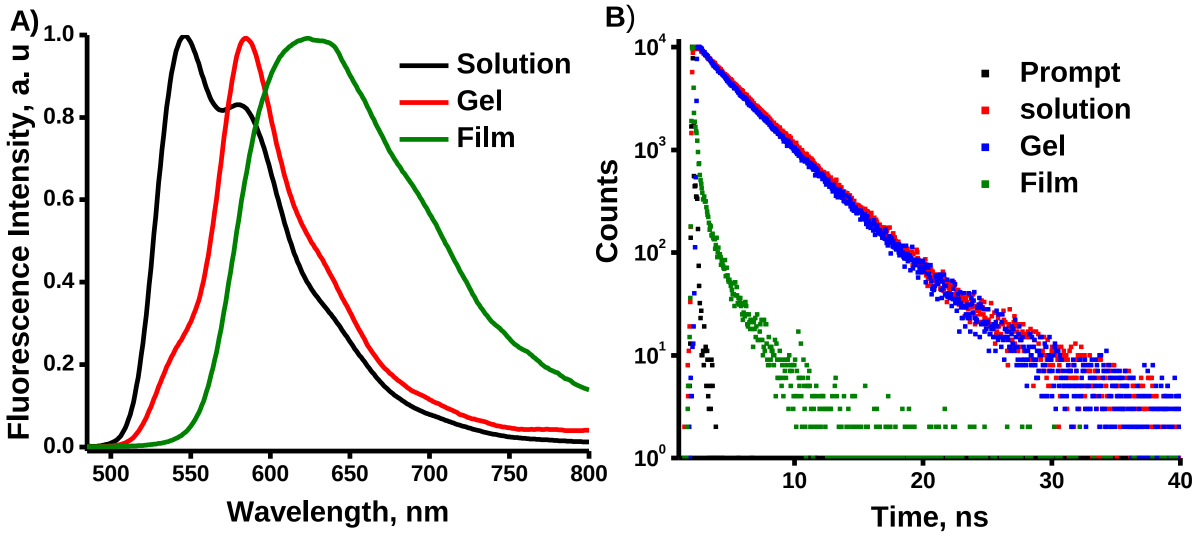

Figure 4.5 A) *Fluorescence emission spectra of* ***(R)-NP(OH)***$_2$ *in solution, gel and film. Fluorescence emission spectra of* ***(R)-NP(OH)***$_2$ *in DCM [black],* ***(R)-NP(OH)***$_2$ *gel in DCM : hexane (1 : 2) mixture [red],* ***(R)-NP(OH)***$_2$ *thin film [green] when excited at 475 nm; B) Fluorescence decay profile of* ***(R)-NP(OH)***$_2$ *in solution (8 μM), gel (1 mM) and film (1 mM). Time-resolved fluorescence decay of* ***(R)-NP(OH)***$_2$ *in B) DCM solution (red), gel (blue) and thin film (green) when excited at 439 nm and monitored at 550 nm (solution) and 580 nm (gel and film).*

around 560 nm (Figure 4.6A). Upon excitation at 345 nm, observed significant quenching and blue-shift in the **PI** emission of (*R*)-**NP(OH)**$_2$ at lower DCM : hexane ratio could be attributed to H-type perylenimide aggregates in (*R*)-**NP(OH)**$_2$. Orthogonally arranged steric groups such as (i) diisopropylphenyl and (ii) **NI** units on either side could prevent stronger association of **PI** units in (*R*)-**NP(OH)**$_2$.

^{1}HNMR titration of (*R*)-**NP(OH)**$_2$ in CD_2Cl_2 with increase in volume fraction of hexane (0–67%) shows significant upfield shift and broadening in the protons corresponding to the **NI** and **PI** units (Figure 4.7) which indicates hydrophobic interactions between aromatic units that results in the self-assembly of (*R*)-**NP(OH)**$_2$ in DCM : hexane mixture. A critical (*R*)-**NP(OH)**$_2$ concentration of 1 mM in DCM : hexane (1 : 2) mixture offered a stable red transparent gel. The d-spacing at 3.7 Å in the (*R*)-**NP(OH)**$_2$ xerogel is indicative of the interplanar distance between two adjacent **PI** units through π–π interactions, as evident from powder X-ray diffraction (PXRD; Figure 4.8). The broad PXRD peaks clearly show less ordered intermolecular close packing arrangement in the gel compared to the sharp peaks observed in the non-gelated powdered (***R***)-**NP(OH)$_2$** solid[234]. Infrared absorption spectra exhibited red-shifted broad peaks at 3432 cm^{-1} (sol-gel) and 3446 cm^{-1} (xerogel) when compared to the sharp peak at 3545 cm^{-1} in the non-gelated solid (***R***)-**NP(OH)$_2$** suggesting intermolecular hydrogen-bonding interactions (Figure 4.9). Similar

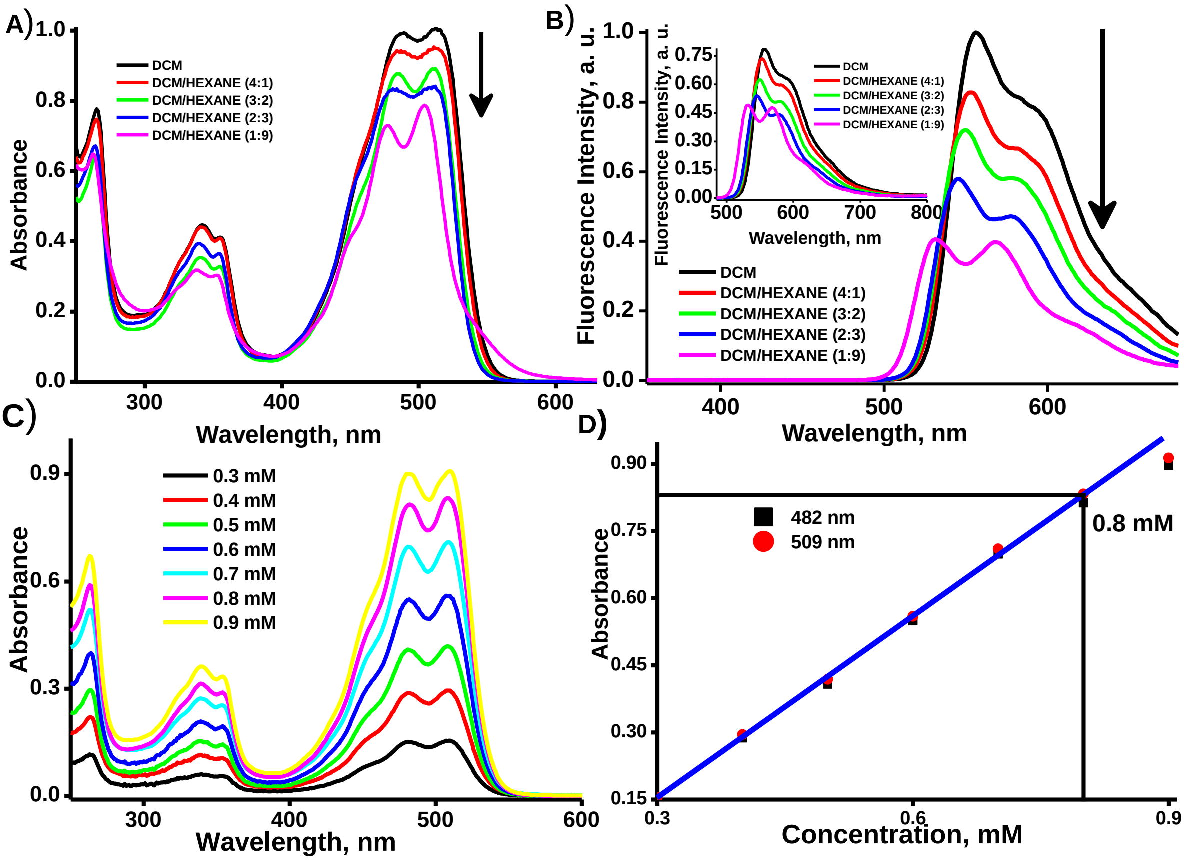

Figure 4.6 *Aggregation dependent changes in absorption and fluorescence spectra. A) Absorption spectra of* ***(R)-NP(OH)$_2$*** *(8 μM) in DCM with increasing concentration of hexane and B) Fluorescence emission spectra* ***(R)-NP(OH)$_2$*** *in DCM with increasing concentration of hexane (λ_{ex}: 345 nm); inset shows the corresponding emission spectra (λ_{ex}: 475 nm); C) concentration dependent absorption spectra of* ***(R)-NP(OH)$_2$*** *in DCM and D) variation of absorbance at the two λ_{max} (482 and 509 nm) with concentration of* ***(R)-NP(OH)$_2$*** *in DCM.*

results were obtained for the (*S*)-**NP(OH)$_2$** isomer of the dyad. However, **NP(OH)**, **NP(OH)$_3$**, **NP(OAc)$_2$** and **NP(OAc)$_3$** could not gelate under similar conditions implying the role of amphiphilicity and/or chirality imparted by the hydroxypropyl side-chain in (***R***/*S*)-**NP(OH)$_2$** on the formation of the gel. Moreover, (***R***/*S*)-**NP(OH)$_2$** in DCM showed negligible self-aggregation even upto 0.8 mM (***R***/*S*)-**NP(OH)$_2$** as understood from UV–Vis absorbance data (Figure 4.6C, D) indicating the role of DCM : hexane mixture in the formation of dyad based vesicular gel.

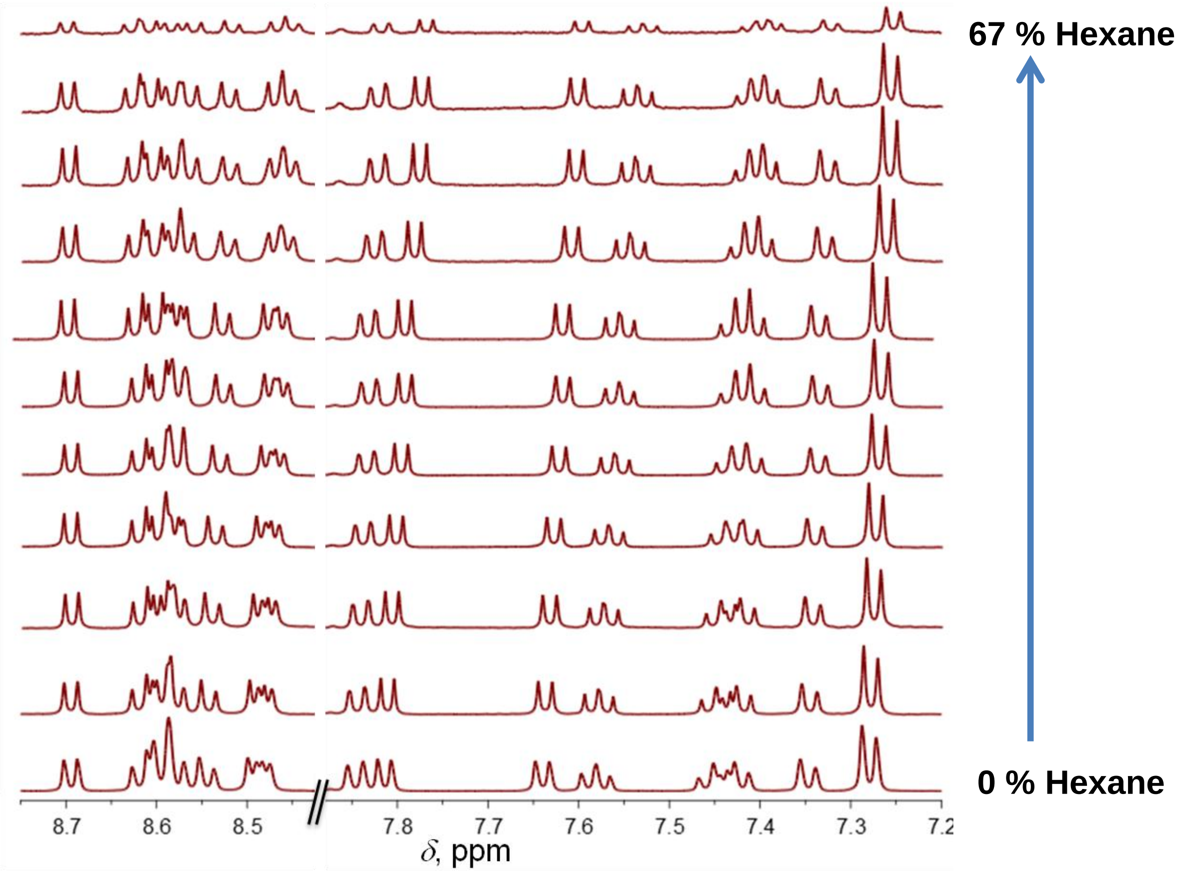

Figure 4.7 *^{1}HNMR investigation of intermolecular aggregation. ^{1}HNMR titration of 13.3 mM* ***(R)-NP(OH)$_2$*** *in CD_2Cl_2 with increasing concentration of hexane.*

Dynamic light scattering (DLS) experiments suggest the formation of spherical particles having an average hydrodynamic diameter of 65 nm and a polydispersity index of 0.17 at 0.01 mM freshly prepared (***R***)-**NP(OH)$_2$** in DCM :

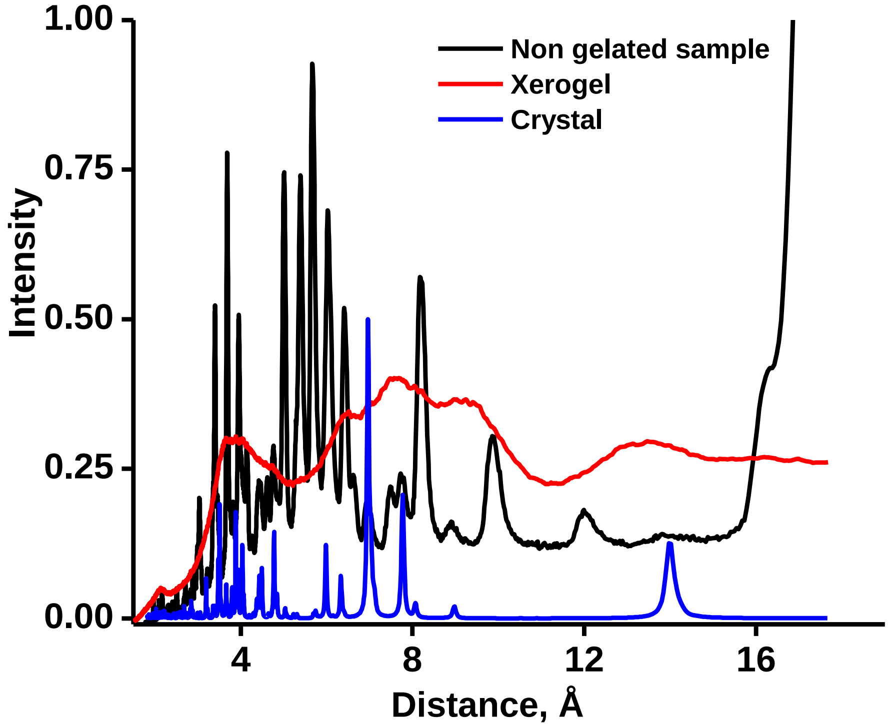

Figure 4.8 *X-ray powder diffracton. Powder X-ray diffraction patterns of* ***(R)-NP(OH)₂*** *non-gelated (black), xerogel (red) and crystalline sample (blue).*

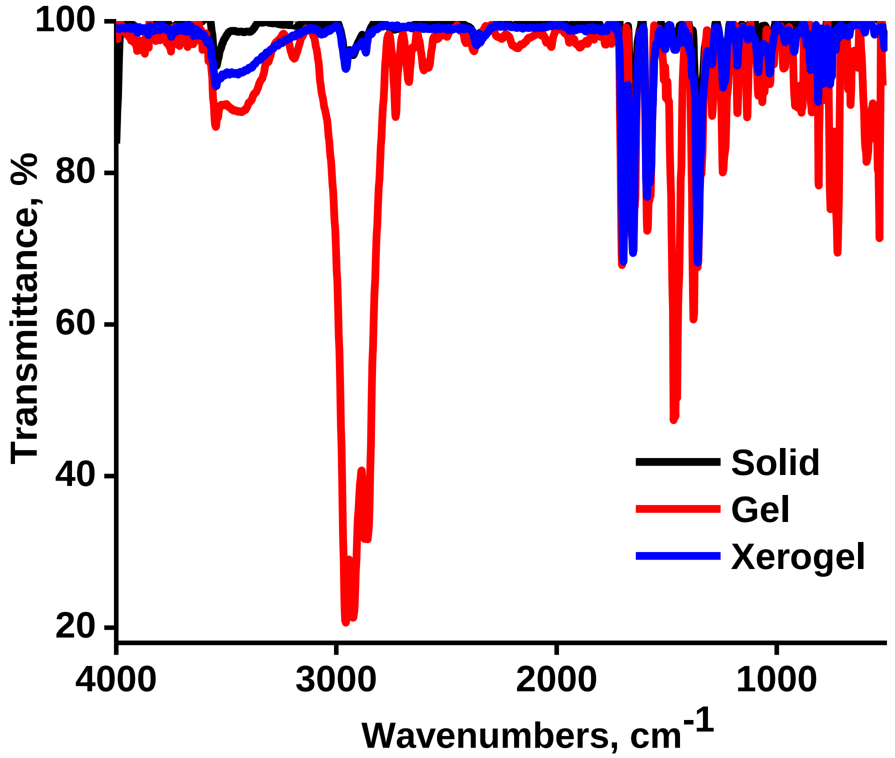

Figure 4.9 *FTIR characterisation. Infrared absorption spectra of* ***(R)-NP(OH)₂*** *in non gelated (black), gel (red) and xerogel sample (blue).*

hexane (1 : 2) solution (Figure 4.10A; Figure 4.11A). With increase in concentration of (***R***)-**NP(OH)$_2$** (0.01–0.25 mM), a progressive increase in the average diameter of the particles ranging from 65–190 nm indicates the concentration-dependent size distribution of the spherical aggregates (Figure 4.10A–E). With the progress of time (~15 min), we observed an initial (***R***)-**NP(OH)$_2$** concentration-dependent increase in the diameter (Figure 4.11B). This reveals aggregation of smaller particles leading to formation of gel at the critical concentration of 1 mM (***R***)-**NP(OH)$_2$**. Initial rate

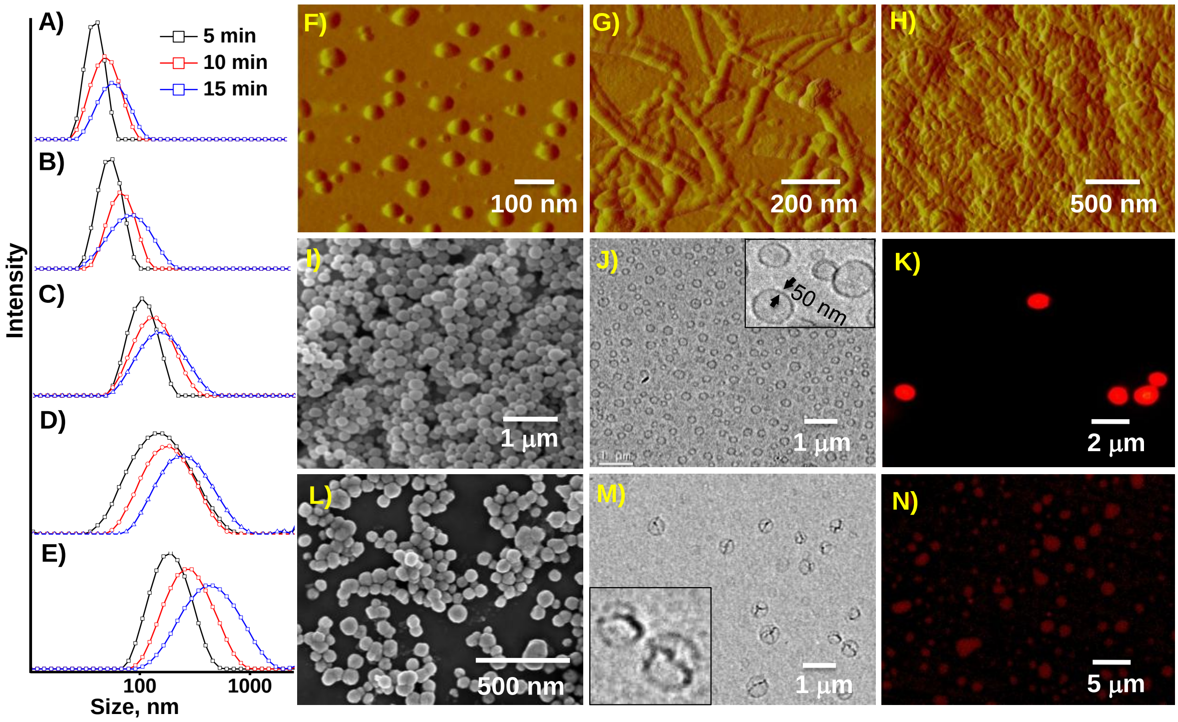

Figure 4.10 *Dynamic light scattering (DLS) and microscopic investigation of vesicular scaffold. Time-dependent size distribution of spherical aggregates at A) 0.01; B) 0.02; C) 0.05; D) 0.1 and E) 0.25 mM (**R**)-**NP(OH)$_2$** in DCM : hexane (1 : 2) determined by DLS measurements; Tapping mode AFM images of (**R**)-**NP(OH)$_2$** at F) 0.05; G) 0.1 and H) 0.5 mM (Amplitude image Z Scale = 12.9 (F), 45.8 (G) and 103.1 (H) mV respectively); SEM images of 0.1 mM (**R**)-**NP(OH)$_2$** in the I) absence and L) presence of indole (1 mM); and HR-TEM images of 0.25 mM (**R**)-**NP(OH)$_2$** in the J) absence and M) presence of indole (2.5 mM); OM images (λ_{ex} = 365 nm) of 0.25 mM (**R**)-**NP(OH)$_2$** in the K) absence and N) presence of indole (2.5 mM) in DCM : hexane (1 : 2) mixture.*

kinetic analysis of the increase in particle size offered first-order rate constant k = 0.03 min^{-1} with respect to the dyad for 0.01 mM (*R*)-**NP(OH)$_2$** (Figure 4.12). At 0.25 mM (*R*)-**NP(OH)$_2$**, we observed a first-order rate constant k = 0.09 min^{-1} implying that rate of particle size growth enhances with increase in initial concentration of (*R*)-**NP(OH)$_2$**.

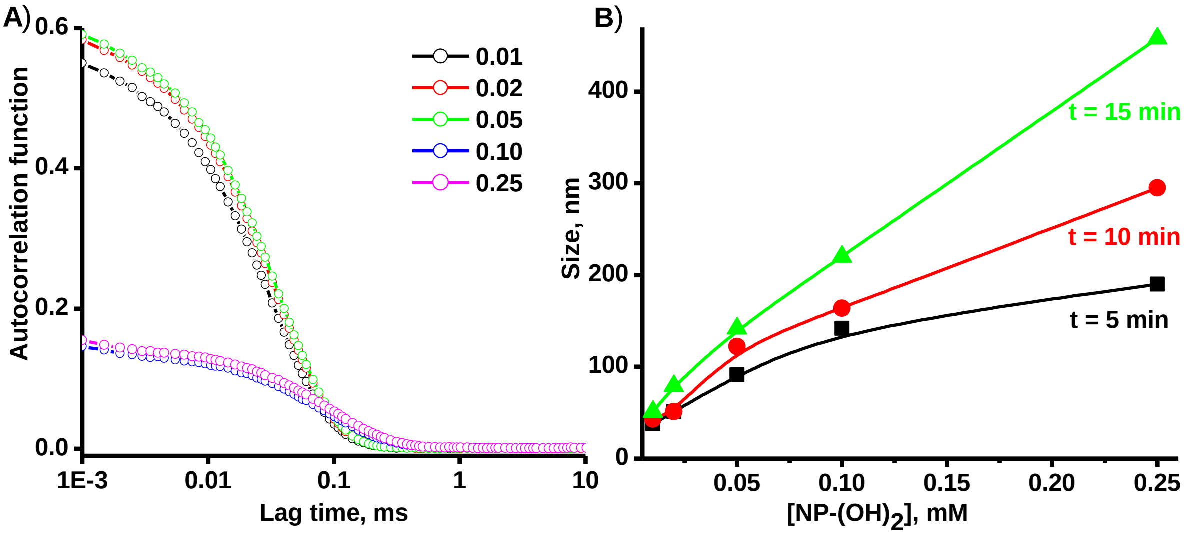

Figure 4.11 *Concentration and time dependent dynamic light scattering. A) Autocorrelation function of* ***(R)-NP(OH)$_2$*** *spherical assemblies in DCM : hexane (1 : 2) mixture with increasing concentration of* ***(R)-NP(OH)$_2$*** *(0.01–0.25 mM) and B) variation of the hydrodynamic diameter of* ***(R)-NP(OH)$_2$*** *spherical assemblies in DCM : hexane (1 : 2) mixture with increase in time (5–15 min) and concentration of* ***(R)-NP(OH)$_2$*** *(0.01–0.25 mM) determined using dynamic light scattering (DLS) measurement.*

Atomic force microscopy (AFM) images at different initial concentrations of (*R*)-**NP(OH)$_2$** were recorded. At 0.05 mM (*R*)-**NP(OH)$_2$**, we observed a distribution of spherical particles having an average diameter of 60 nm (Figure 4.13A), consistent with DLS data (Figure 4.10F). As the initial concentration of (*R*)-**NP(OH)$_2$** increased to 0.1 mM, we observed coalescence of spherical particles to form a linear (Figure 4.10G) assembly that gels at a higher concentration (Figure 4.10H). Scanning electron microscopy (SEM) image of 0.1 mM (*R*)-**NP(OH)$_2$** confirms the formation of regular spherical particles having an average diameter of 160 nm (Figure 4.10I; Figure 4.13B). As the concentration increases from 0.01 mM to 0.5 mM (*R*)-**NP(OH)₂**, SEM showed fusion of spherical particles leading to the formation of a coalesced assembly of spherical aggregates, consistent with AFM data (Figure 4.14A-F). The transmission electron microscopy (TEM) image of 0.25 mM (*R*)-**NP(OH)₂** exhibited an average diameter of 260 nm of spherical particles (Figure 4.10J; Figure 4.13C). The observed contrast between the periphery (ca. 50 nm thickness) and the inner part indicate the vesicular nature of the spherical particles. Under similar conditions, bright fluorescent red spheres having an average diameter of 650 nm were visible in the optical microscope (OM) when excited at 365 nm (Figure 4.10K).

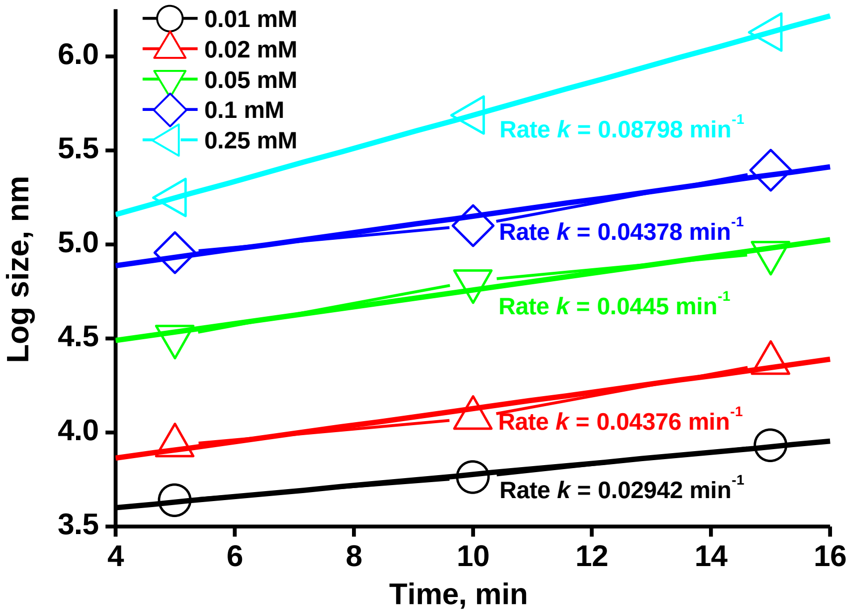

Figure 4.12 *Initial rate kinetic analysis. Plot of log[size (nm)] vs. time (min) for initial rate kinetic analysis on the formation of spherical particles at different initial concentrations of* ***(R)-NP(OH)₂*** *(0.01–0.25 mM) in DCM : hexane (1 : 2) mixture.*

UV–Vis absorption spectrum of (*R*)-**NP(OH)₂** gel exhibited absorbance at 341 nm (**NI**) and 505 nm (**PI**) having a shoulder at 550 nm (Figure 4.2A) corresponding to weak **PI** aggregates. (*R*)-**NP(OH)₂** thin film exhibited significantly red-shifted (~21 nm) absorbance at 530 nm (**PI**) indicating the presence of strong **PI** aggregates.

4.2 Results and Discussions

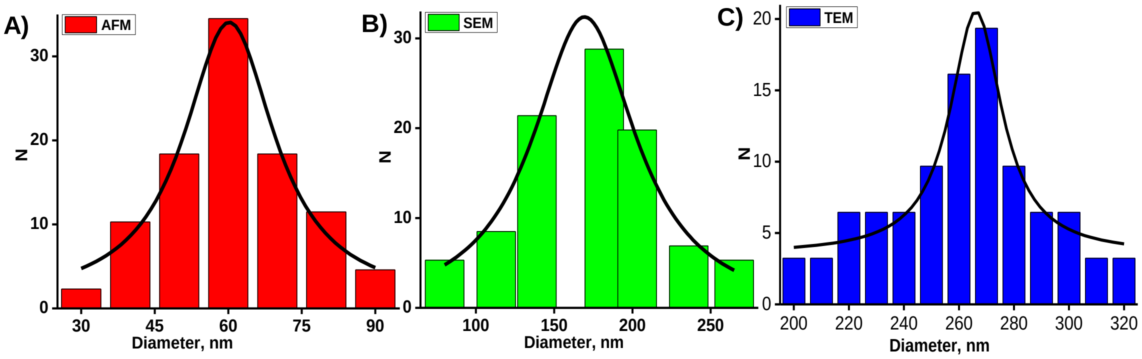

Figure 4.13 *Particle size distribution of vesicular* **(R)-NP(OH)$_2$** *by AFM, SEM and TEM analysis. Histogram of the size distribution of* **(R)-NP(OH)$_2$** *spherical assemblies in DCM : hexane (1 : 2) mixture counted for 500 individual particles obtained from A) AFM ($c = 50 \times 10^{-6}$ M); B) SEM ($c = 10 \times 10^{-5}$ M) and C) TEM images ($c = 25 \times 10^{-5}$ M) at different places of the sample.*

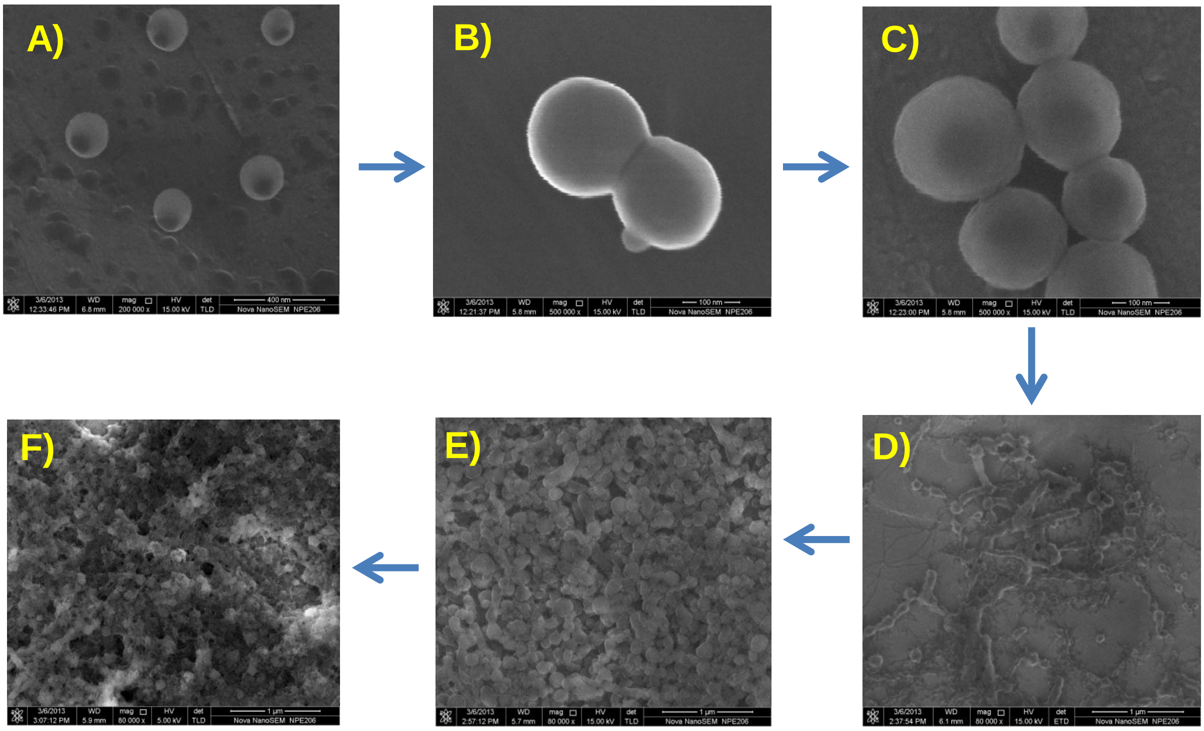

Figure 4.14 *SEM imaging of evolution of the gel from vesicle. Concentration dependent SEM images of* **(R)-NP(OH)$_2$** *spherical assemblies in DCM : hexane (1 : 2) mixture at A) 0.01 mM; B) 0.02 mM; C) 0.05 mM; D) 0.1 mM; E) 0.25 mM and F) 0.5 mM of* **(R)-NP(OH)$_2$**.

(***R***)-**NP(OH)$_2$** gel exhibited strong positively induced CD signals at 370 nm and 545 nm corresponding to **NI** and **PI** units due to the presence of chiral (*R*)-2,3-dihydroxypropyl unit at the **NI** moiety, similar to (***R***)-**NP(OH)$_2$** thin film (Figure 4.2B). Negatively induced CD signals were obtained for **(*S*)**-**NP(OH)$_2$** gel and thin film corresponding to **NI** and **PI** units due to the presence of (*S*)-2,3-dihydroxypropyl unit at the **NI** moiety. A strong red-orange fluorescence (Φ_F = 0.54 ± 0.02; λ_{em} = 584 nm) is exhibited by (***R***)-**NP(OH)$_2$** gel, when excited both at 345 nm and 475 nm (Figure 4.2C; Figure 4.5A). Observed spectral narrowing (fwhm = 60 nm) in the emission of (***R***)-**NP(OH)$_2$** gel compared to thin film (fwhm = 130 nm) could be attributed to the re-absorption of photons due to high optical density in the gel state. Upon excitation both at 345 nm and 475 nm, thin film of (***R***)-**NP(OH)$_2$** exhibited a significantly red-shifted (λ_{em} = 625 nm) weak broad fluorescence corresponding to **PI** (Φ_F = 0.05 ± 0.002) consistent with the UV–Vis absorption data.

Picosecond time-resolved fluorescence of (***R***)-**NP(OH)$_2$** gel (Figure 4.2D) exhibited bi- exponential decay having lifetimes of 2.9 ns (53%) and 4.7 ns (47%), upon excitation at 340 nm. Similar lifetimes were observed on exciting the perylenimide unit at 439 nm (Figure 4.5B). Relatively minor component could be attributed to the slower decay of excimeric **PI** in the dyad (***R***)-**NP(OH)$_2$** gel, while the short-lived component could be attributed to the monomeric **PI**. (***R***)-**NP(OH)$_2$** in DCM exhibited a moderately faster rate of radiative decay (k_r = 1.9 × 10^8 s^{-1}) compared to gel (k_r = 1.4 × 10^8 s^{-1}) which indicates that the **PI** units undergo very weak H-type exciton interactions in the (***R***)-**NP(OH)$_2$** gel, consistent with high-fluorescence quantum yield. (***R***)-**NP(OH)$_2$** thin film showed tri-exponential decay having lifetimes of 3.9 ns (11%), 1.2 ns (34%) and 0.3 ns (55%) upon excitation at 439 nm (Figure 4.5B) consistent with the recently reported literature[235]. Tri-exponential and faster radiative decay (k_r = 0.37 × 10^8 s^{-1}) of (***R***)-**NP(OH)$_2$** thin film compared to solution indicates diverse close packing arrangements of **PI** aggregates that possess strong H-type exciton interactions resulting in low Φ_F in thin film[219].

4.2 Results and Discussions

Time-resolved fluorescence anisotropy of the dyad (*R*)-**NP(OH)₂** gel exhibits an initial anisotropy value of 0.17 that loses the anisotropy memory when monitored at 580 nm (**PI** moiety) with a decay time of 201 ps, upon excitation at 439 nm (**PI** unit; Figure 4.15). Ultrafast energy/exciton migration[236,237] at short separation between the chromophoric transition dipoles predominate over slower fluorescence depolarization through rotational motion at this time-scale in the gel leading to fluorescence anisotropy[190,191]. A relatively slower rate of energy migration (K_{EM} = 4.97 × 10^9 s^{-1}; λ_{ex} = 439 nm) for (*R*)-**NP(OH)₂** gel compared to chromophoric gel assemblies[69] could be attributed to the delayed memory loss arising from the asymmetry of bichromophoric (*R*)-**NP(OH)₂**.

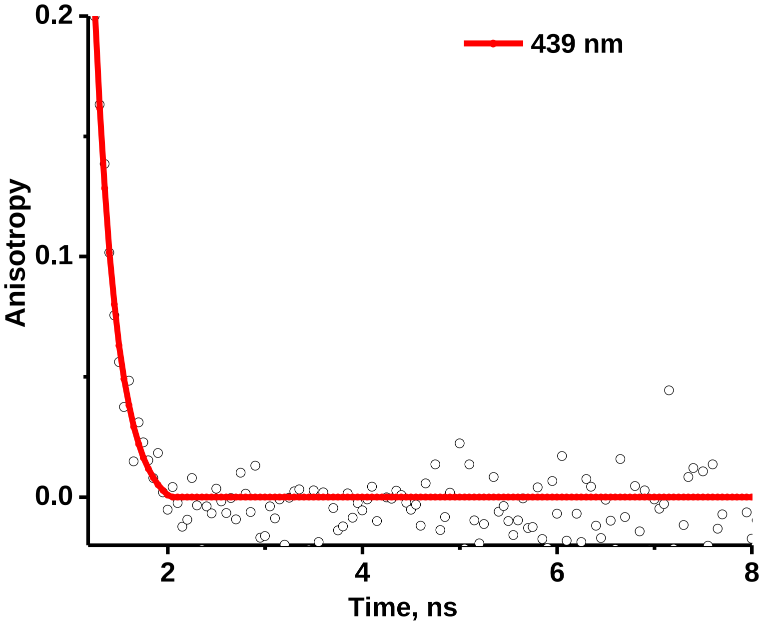

Figure 4.15 *Fluorescent anisotropy of vesicular* ***(R)-NP(OH)₂*** *gel. Time-resolved fluorescence anisotropy decay of* ***(R)-NP(OH)₂*** *gel when excited at 439 nm and monitored at 580 nm. Concentration of* ***(R)-NP(OH)₂*** *in gel state is 1 mM (critical gelator concentration).*

Temperature-dependent UV–Vis absorbance of (*R*)-**NP(OH)₂** gel exhibited a hypochromism at 550 nm and a concomitant increase in the absorbance at 505 nm (Figure 4.16A) which indicates the dissociation of exciton interactions between the **PI** units at elevated temperature resulting in the destabilisation of gel (T_m = 35 °C). With

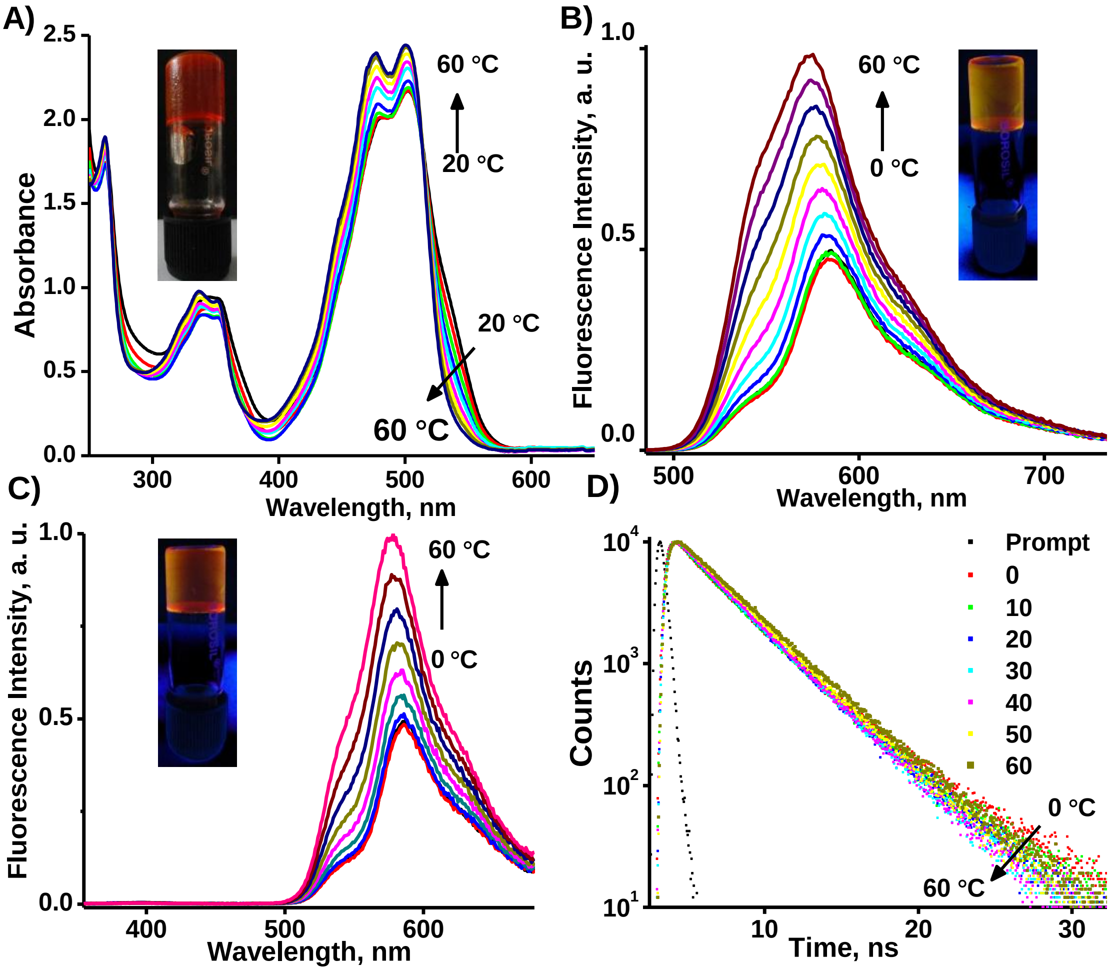

Figure 4.16 *Thermodynamic stability of vesicular* ***(R)-NP(OH)$_2$*** *gel. Temperature dependent A) UV–Vis; B) fluorescence spectra when excited at 475 nm radiation; C) fluorescence spectra when excited at 345 nm and D) time-resolved fluorescence decay upon excitation at 340 nm and monitored at 580 nm. Arrows indicate the increase in temperature from 0–60 °C. Inset shows the photographic image of* ***(R)-NP(OH)$_2$*** *gel in DCM : hexane (1 : 2) mixture under A) visible light; B) long-wavelength UV radiation and C) short–wavelength UV radiation. Concentration of* ***(R)-NP(OH)$_2$*** *in gel state is 1 mM (critical gelator concentration).*

increase in temperature (20–60 °C), (***R***/***S***)-**NP(OH)$_2$** gel shows a gradual decrease in the intensity of CD signal at 370 nm and 545 nm (Figure 4.17). Disappearance of the **NI** and **PI** CD signals at elevated temperature indicates destabilisation of the gel through thermal unstacking of **NI** and **PI** units. Upon excitation at 345 nm and 475 nm, we observed recovery in the fluorescence quantum yield of (*R*)-**NP(OH)**$_2$ (Φ_F = 0.65 ± 0.03) at 60 °C (Figure 4.16B, C) corresponding to the monomeric (*R*)-**NP(OH)**$_2$. Temperature-dependent time-resolved fluorescence decay of an (*R*)-**NP(OH)**$_2$ gel corresponding to **PI** unit, upon excitation at 340 nm exhibited a transformation of bi-exponential decay at 20 °C to mono-exponential decay at 60 °C (τ = 3.8 ns). Mono-exponential decay of (*R*)-**NP(OH)**$_2$ gel at elevated temperature is consistent with the formation of monomeric (*R*)-**NP(OH)**$_2$ and the disappearance of self-assembled structure (Figure 4.16D).

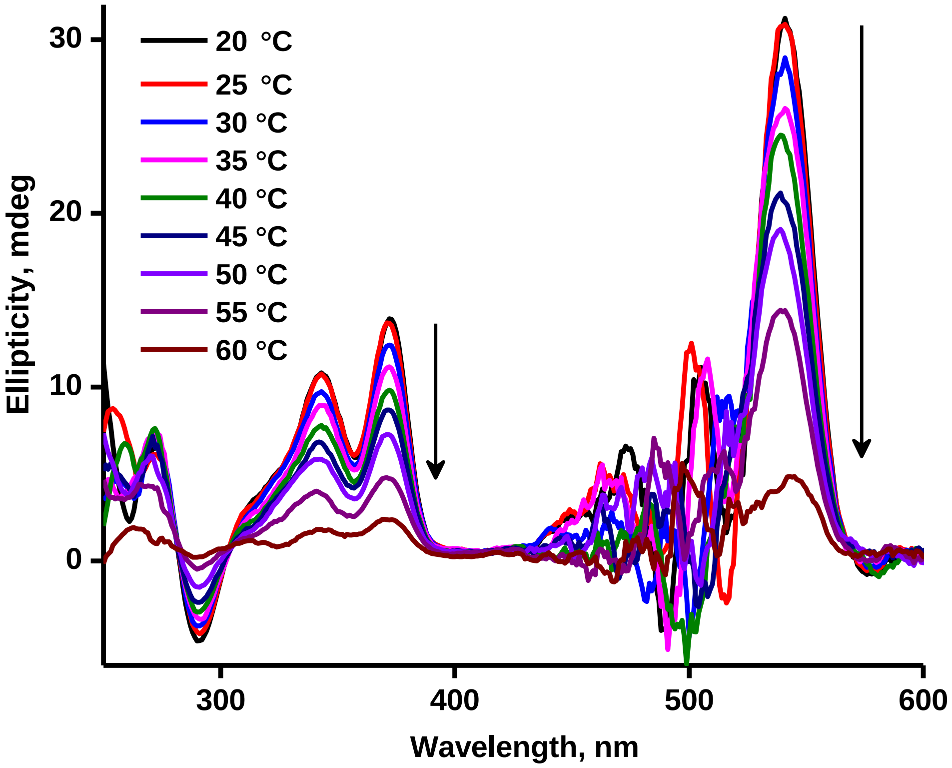

Figure 4.17 *Temperature dependent chiroptical spectra of* ***(R)-NP(OH)***$_2$ *gel. Temperature-dependent circular dichroism spectra of representative* ***(R)-NP(OH)***$_2$ *gel in DCM : hexane (1 : 2). Concentration of* ***(R)-NP(OH)***$_2$ *in gel state is 1 mM (critical gelator concentration).*

Amphiphilic (*R*)-**NP(OH)**$_2$ in DCM : hexane mixture at a low concentration forms individual multi-lamellar vesicles that can transform into bigger vesicles with the progression of time. At higher concentrations (above the critical gelator concentration) the individual bilayer vesicles undergo fusion and forms extended superstructured gel. Kinetically stable gel thus formed slowly transforms, through gliding[238] of the dyad, to thermodynamically stable crystal (Table 4.1) over a period of 48 hours (Figure 4.18). Metastability of (***R***)-**NP(OH)$_2$** containing vesicular gel (Table 4.2) encouraged us to investigate the photoinduced processes in the presence of indole (electron donor). (***R***)-**NP(OH)$_2$** gel retained the stability even at 100 : 1 indole : (***R***)-**NP(OH)$_2$** ratio. SEM image of 0.1 mM (***R***)-**NP(OH)$_2$** in the presence of 1 mM indole exhibited spheroidal particles having an average diameter of 160 nm (Figure 4.10L). Observed surface roughness in the spheroidal particles could arise from the adsorption of indole molecules on (***R***)-**NP(OH)$_2$** vesicular surface. TEM image of 0.25 mM (***R***)-**NP(OH)$_2$** in the presence of 2.5 mM indole exhibits spheroidal particles having an average diameter of 400 nm (Figure 4.10M). An additional contrast on the vesicular surface, apart from the rim of the spheroidal particles of (***R***)-**NP(OH)$_2$** xerogel, confirms the integrity of vesicles having indole molecules adsorbed on the surface. Optical microscopy image (Figure 4.10N) of (***R***)-**NP(OH)$_2$** vesicles containing indole showed a significant fluorescence quenching indicating the possibility of photoinduced electron transfer process from indole to singlet excited states of the chromophoric units.

With increase in indole concentration, (***R***)-**NP(OH)$_2$** gel shows up to 4-fold decrease in the fluorescence quantum yield and significant decrease in the fluorescence lifetime ($\tau = 0.6$ ns), upon excitation both at 345 nm and 475 nm (Figure 4.19A-D). Stern-Volmer analysis[82] of the steady-state and time-resolved fluorescence data (Refer Experimental Section 4.4.13) of (***R***)-**NP(OH)$_2$** gel with increase in concentration of indole offered similar bimolecular quenching rate constant $k_q = 7.2 \times 10^9$ M^{-1}s^{-1} (Figure 4.20A-D) indicating dynamic quenching of singlet excited state of perylenimide (^{1}**PI***) (Refer Experimental Section 4.4.14). Observed bimolecular quenching rate constant in the case of **(*R*)-NP(OH)$_2$** : indole co-gel is lower than the upper bound of diffusional bimolecular quenching constant, $k_q = 1 \times 10^{10}$ M^{-1}s^{-1} confirming the dynamic nature of photoinduced electron transfer.

Table 4.1 *Crystal data and structure refinement for the dyad* ***(R)-NP(OH)*₂**.

Empirical fomula	$C_{49}H_{38}O_6N_2$	
Fomula weight	750.81	
Temperature	296(2) K	
Wavelength	0.71073 Å	
Crystal system	Triclinic	
Space group	$P\bar{1}$	
Unit cell dimensions	a = 8.947 Å	$\alpha = 75.26^{o}$
	b = 14.538 Å	$\beta = 78.85^{o}$
	c = 14.887 Å	$\gamma = 82.01^{o}$
Volume	1829.1 Å^3	
Z, Calculated density	2, 1.363 Mg/m^3	
Absorption coefficient	0.090 mm^{-1}	
F(000)	788	
Crystal size	0.20 x 0.15 x 0.10 mm^3	
Theta range for data collection	1.43 to 25.00^{o}	
Index ranges	-10<=h<=10, -17<=k<=17, -17<=l<=17	
Reflections collected	23878	
Independent Reflections	6369 [R(int) = 0.0966]	
Absorption correction	Semi-empirical from equivalents	
Refinement method	Full-matrix least-squares on F^2	
Data / restraints / parameters	6369 / 5 / 509	
Goodness-of-fit on F^2	1.521	
Final R indices [I>2sigma(I)]	R1 = 0.1541, wR2 = 0.4212	
R indices (all data)	R1 = 0.2678, wR2 = 0.5014	
Extinction coefficient	0.007(5)	

We observed a similar bimolecular quenching rate constant for the photoinduced electron transfer from indole to the singlet excited state of perylenimide in **(*R*)-NP(OH)₂** solution ($k_q = 6.2 \times 10^9$ M^{-1}s^{-1}, Figure 4.21) when compared to the co-gel, consistent with D–A pair reported[239,240]. UV-Vis absorption spectra of the dyad

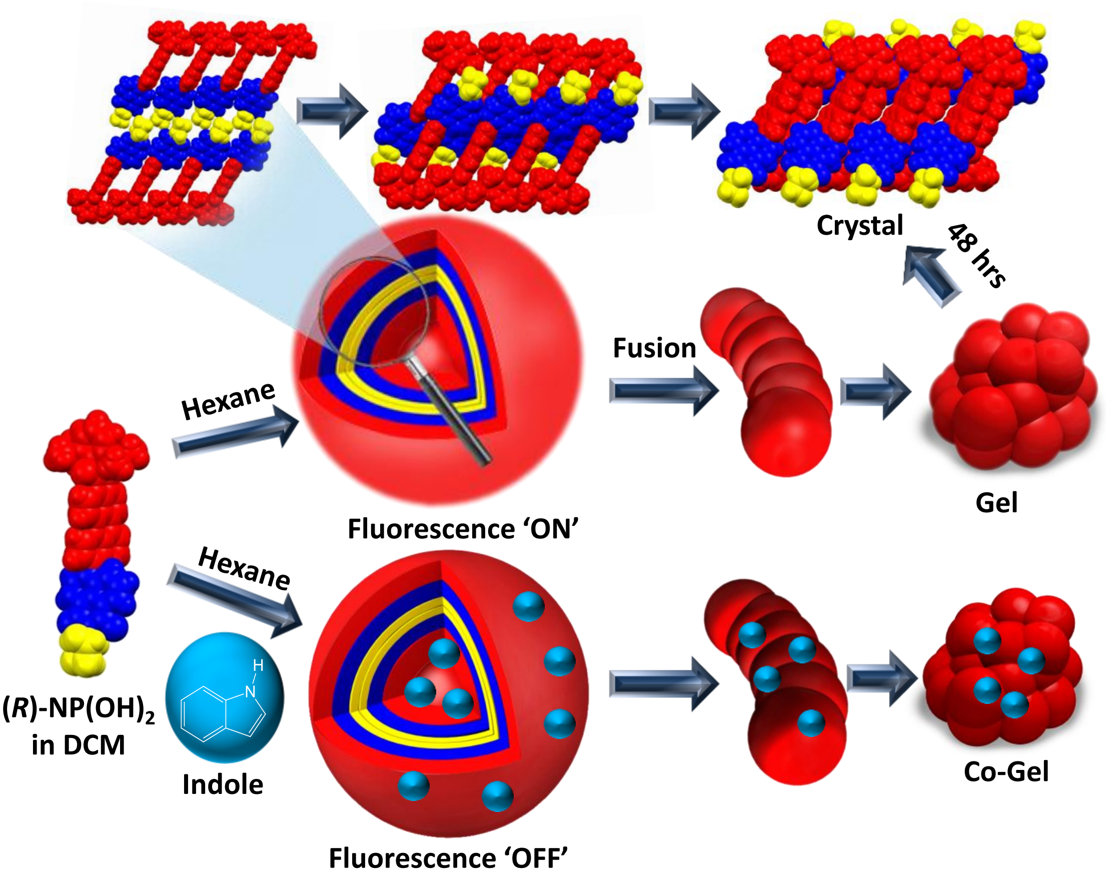

Figure 4.18 *Mechanism for molecule-bilayer-vesicle-gel-crystal transition. Schematic representation of self-assembly of* ***(R)-NP(OH)₂*** *in DCM : hexane (1 : 2) mixture in the absence and presence of indole.*

Table 4.2 *Gel stability of vesicular* ***(R)-NP(OH)₂*** *in the presence and absence of indole. Critical gelator concentration* [a]*(CGC) of* ***(R)-NP(OH)₂*** *in DCM : hexane (1:2) in the absence and presence of indole.*

Gel Sample	CGC (mg/mL)
NP(OH)₂	0.75
NP(OH)₂ + Indole (1 : 6.7)	0.75
NP(OH)₂ + Indole (1 : 13.3)	0.75
NP(OH)₂ + Indole (1 : 26.6)	0.75
NP(OH)₂ + Indole (1 : 66.6)	0.75
NP(OH)₂ + Indole (1 : 100)	0.75

[a]CGC is the minimum concentration of the gelator required for the formation of a stable gel at room temperature.

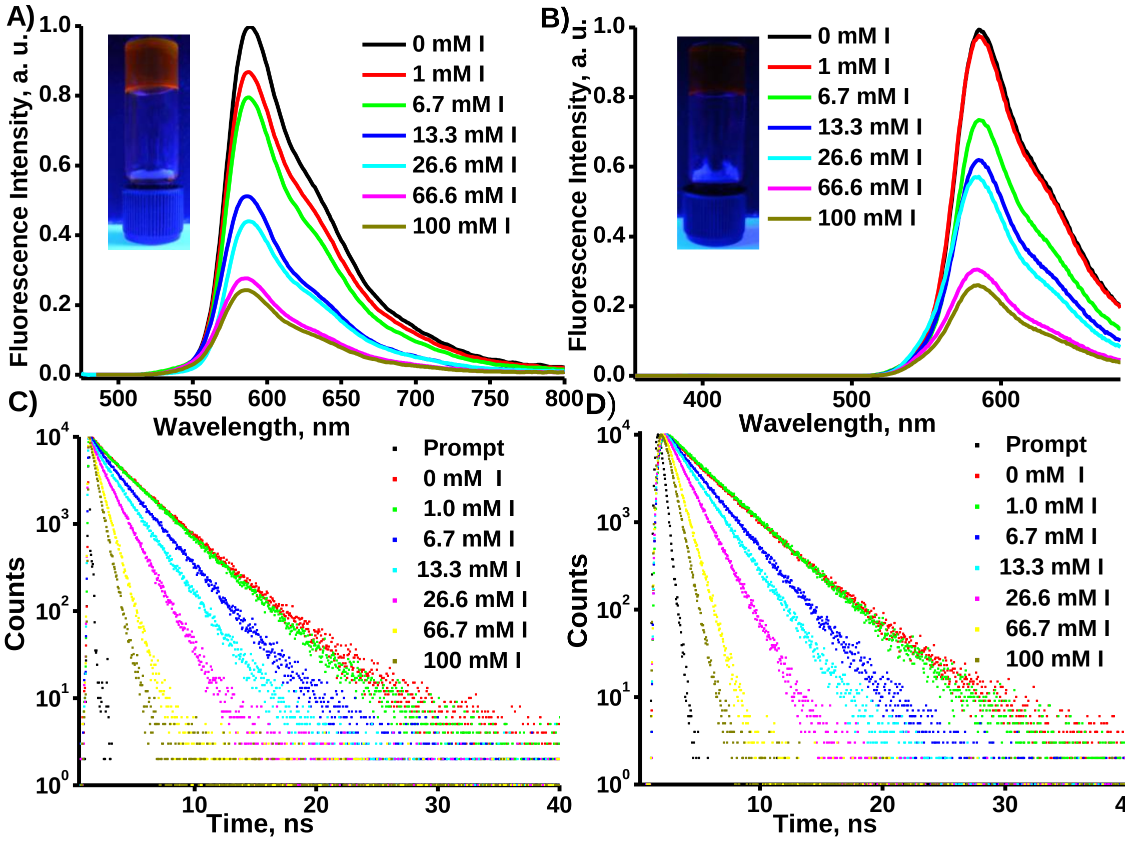

Figure 4.19 *Steady-state and time-resolved fluorescence quenching of vesicular* ***(R)-NP(OH)$_2$*** *gel in the presence of indole* ***(I)****. Indole concentration dependent emission spectra of* ***(R)-NP(OH)$_2$*** *gel when excited at A) 475 nm; B) 345 nm; indole concentration dependent time-resolved fluorescence decay of* ***(R)-NP(OH)$_2$*** *gel when excited at C) 439 nm and D) 340 nm (emission monitored at 580 nm). Insets show the photographic image of* ***(R)-NP(OH)$_2$*** *+* ***I*** *co-gel in DCM : hexane (1 : 2) mixture under A) long–wavelength UV radiation and B) short–wavelength UV radiation. Concentration of* ***(R)-NP(OH)$_2$*** *in gel state is 1 mM (critical gelator concentration).*

(*R*)-NP(OH)$_2$ in DCM exhibited negligible change before and after the addition of indole (1000 equivalents) ruling out the possibility of ground state complexation between indole and the constituents of the dyad (Figure 4.21A). Rehm–Weller analysis[79] shows favourable change in free energy for photoinduced electron transfer from the singlet excited state of **NI** to **PI** (–0.17 eV) in the dyad **NP(OH)** (Refer Chapter 2)[182]. Photoinduced electron transfer from indole to the singlet excited state of **NI** (–1.19 eV) and **PI** (–0.48 eV) units (Refer Experimental Section 4.4.14) are thermodynamically feasible.

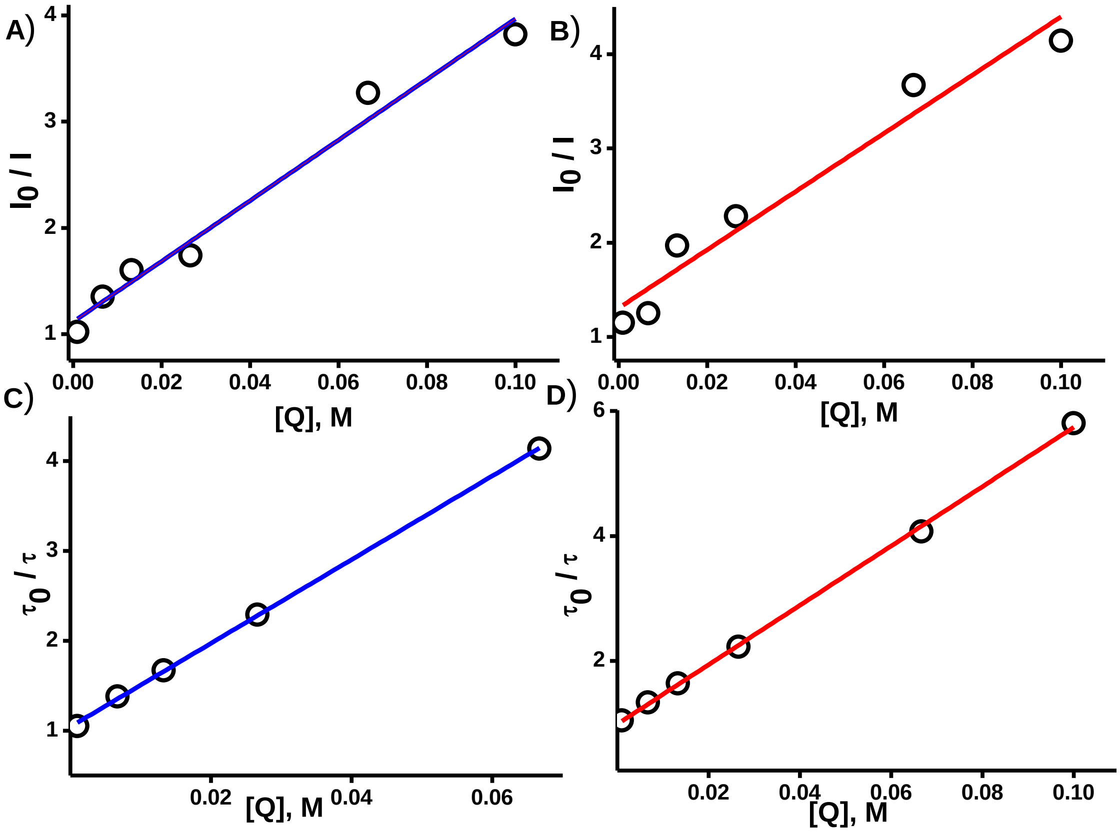

Figure 4.20 *Stern-Volmer plots. Steady-state (when excited at A) 345 nm and B) 475 nm); and time-resolved (when excited at C) 340 nm and D) 439 nm (emission monitored at 580 nm))-based Stern–Volmer plot of* ***(R)-NP(OH)₂*** *gel with increase in concentration of indole. Concentration of* ***(R)-NP(OH)₂*** *in gel state is 1 mM (critical gelator concentration). In the case of 340 nm excitation the lifetime corresponding to 0.1 M concentration is omitted since measured lifetime is shorter than the resolution of the excitation source.*

To characterize the transient intermediates generated upon photoexcitation of **(*R*)-NP(OH)₂** : indole solution and co-gel, we have carried out femtosecond transient absorption measurements and analysed the three dimensional ΔA *versus* time and wavelength spectral data using singular value decomposition (SVD). Femtosecond transient absorption (FTA) spectra of 0.75 mM **(*R*)-NP(OH)₂** solution exhibited a bleach centered at 570 nm and a mono-exponential decay corresponding to singlet

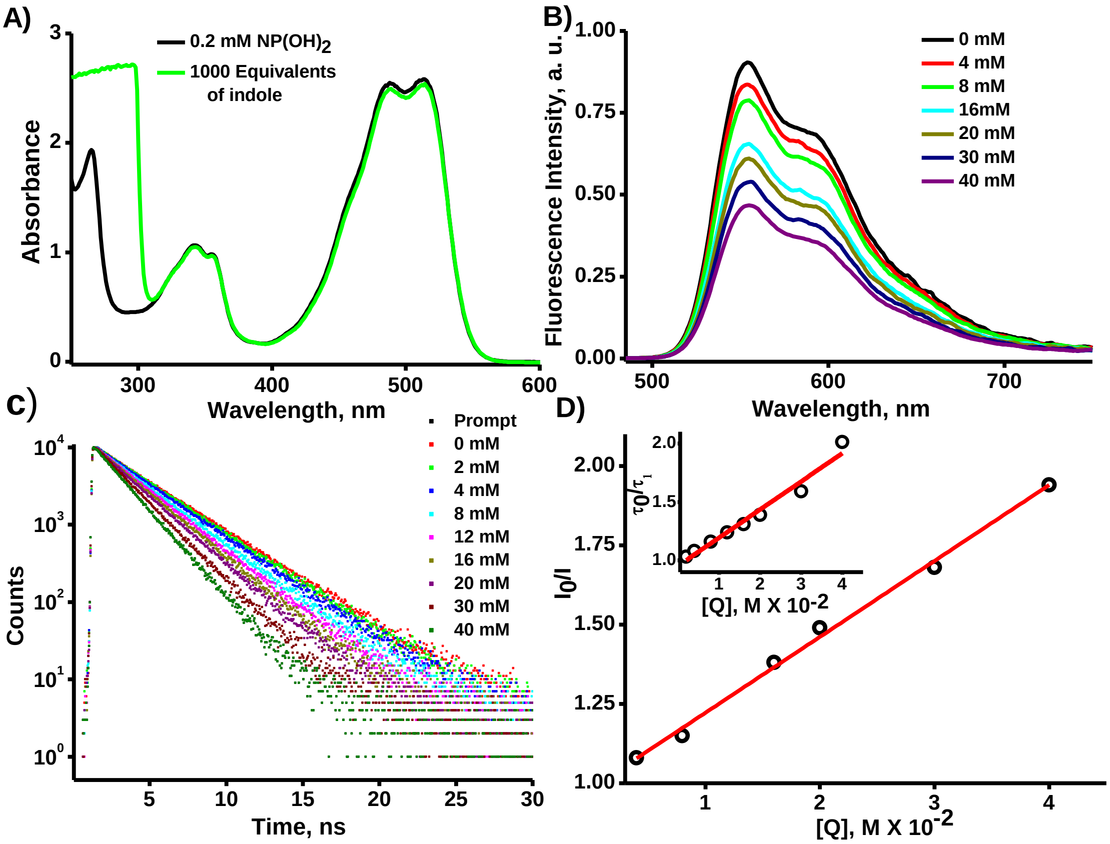

Figure 4.21 *A) Absorption spectra of 0.2 mM* ***(R)-NP(OH)**$_2$* *solution in the absence and presence of 1000 equivalents of indole* ***(I)****; B) indole concentration dependent emission spectra of* ***(R)-NP(OH)**$_2$* *solution when excited at 475 nm; C) indole concentration dependent time-resolved fluorescence decay of* ***(R)-NP(OH)**$_2$* *solution when excited at 475 nm (emission monitored at 580 nm); steady-state when excited at D) 475 nm, inset of D) shows time-resolved (when excited at 439 nm and monitored at 580 nm)-based Stern–Volmer plot of* ***(R)-NP(OH)**$_2$* *solution with increase in concentration of indole. Concentration of* ***(R)-NP(OH)**$_2$* *in solution is 8 μM for steady-state and time-solved fluorescence measurements.*

excited state of perylenimide (^{1}**PI***) at 615 nm having a lifetime of 3.1 ns, upon excitation at 390 nm (Figure 4.22A, D). Marginal decrease in the fluorescence quantum yield of **(*R*)-NP(OH)**$_2$ (Φ_F = 0.75 ± 0.04) corresponding to **PI** unit when compared to the model perylenimide PI derivative (Φ_F = 0.81 ± 0.03) indicates the possibility of photoinduced electron transfer from the singlet excited state of **NI** to **PI** ($\Delta G_{\text{charge separation}} = -0.17$ eV) having an estimated rate of $k_{\text{charge separation}} = 2.29 \times 10^{12}$ s^{-1}[182].

Upon photoexcitation, charge transfer intermediates in the dyad **(*R*)-NP(OH)$_2$** solution were not observed suggesting the fact that rate of charge recombination (<110 fs) is much faster than the rate of charge separation, consistent with similar reported dyads[229]. In the presence of lower concentration of indole, dyad **(*R*)-NP(OH)$_2$** : indole (1 : 10) solution exhibited a mono-exponential decay at 617 nm corresponding to ^{1}**PI*** having a lifetime of 2.9 ns, similar to the lifetime of ^{1}**PI*** in the dyad **(*R*)-NP(OH)$_2$** solution (Figure 4.22B, E)[241]. The lack of formation of charge transfer intermediates in dyad **(*R*)-NP(OH)$_2$** : indole (1 : 10) solution is consistent with insignificant fluorescence quenching corresponding to dyad **(*R*)-NP(OH)$_2$** under similar conditions indicating the absence of photoinduced electron transfer from indole to ^{1}**PI***/^{1}**NI***. At a higher concentrations of indole, dyad **(*R*)-NP(OH)$_2$** : indole (1 : 500 and 1 : 1000) solution showed a bleach around 570 nm and two absorption bands centered around 598 nm and 619 nm, upon photoexcitation (Figure 4.23B, Figure 4.22C, F). SVD analysis followed by global fitting offered a lifetime of 6-6.5 ps at 598 nm corresponding to the radical anion of perylenimide (**PI**$^{\bullet-}$)[93,144] and 0.5-0.64 ns at 619 nm corresponding to the singlet excited state of perylenimide (^{1}**PI***, inset of Figure 4.23B, Table 4.3). The formation of charge transfer intermediate **PI**$^{\bullet-}$ in the dyad **(*R*)-NP(OH)$_2$** at higher concentrations of indole (1 : 500 and 1 : 1000) solution signifies the occurrence of diffusion-controlled photoinduced charge separation[242] that is consistent with the quenching of fluorescence of the dyad **(*R*)-NP(OH)$_2$** (Figure 4.21B, D). Greater dependence on the distribution of charged intermediates with increase in concentration of the electron donor indole indicates that the rate of charge separation dominates over rate of charge recombination ($k_{cs} > k_{cr}$)[243].

Nanosecond transient absorption spectroscopic measurements of dyad **(*R*)-NP(OH)$_2$** : indole (1:500 and 1:1000) in DCM failed to detect the presence of charged intermediates, upon excitation at 355 nm and 532 nm. Lack of transient intermediates in the nanosecond transient absorption measurements of the dyad

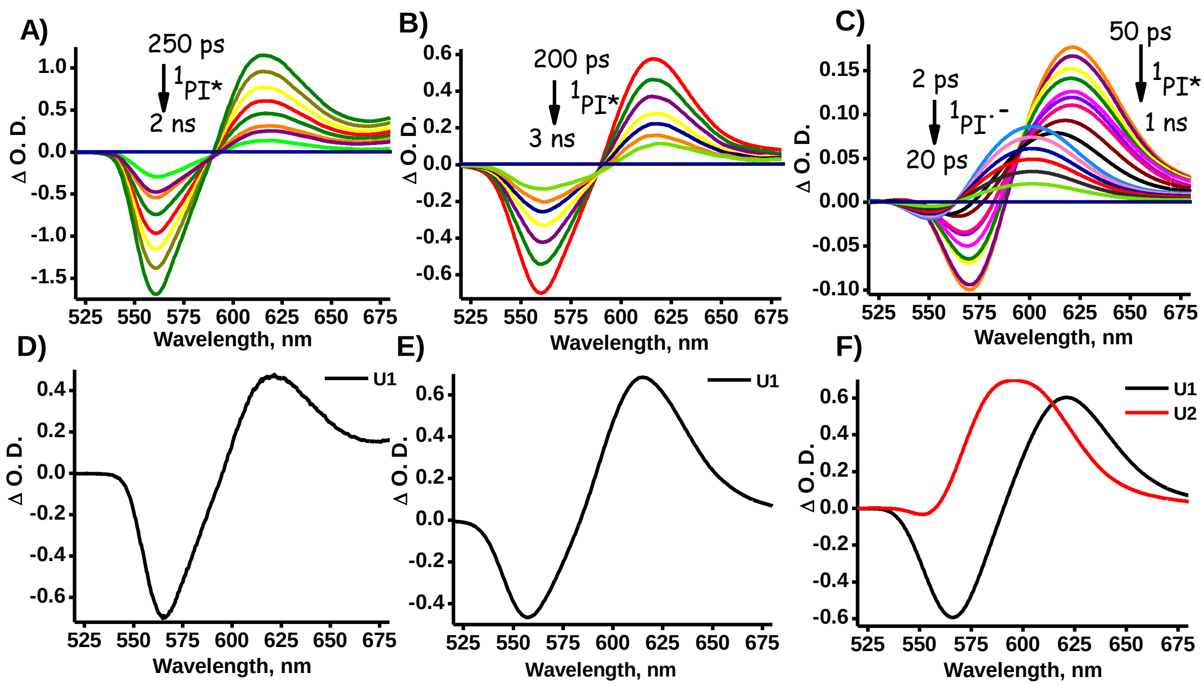

Figure 4.22 *Femtosecond-transient absorption spectra of* **(R)-NP(OH)₂** *A) solution (0.75 mM);* **(R)-NP(OH)₂** *solution (0.75 mM) : Indole B) 1 : 10; C) 1 : 500 and right singular vectors obtained from SVD analysis of* **(R)-NP(OH)₂** *D) solution (0.75 mM);* **(R)-NP(OH)₂** *solution (0.75 mM) : Indole E) 1 : 10 and F) 1 : 500 respectively when excited at 390 nm.*

Table 4.3 *Shows the rate of fluorescence decay (k_F) and rate of charge recombination (k_{cr}) in the dyad* **(R)-NP(OH)₂** *under different conditions upon photoexcitation.*

Context	τ_F (ns)[a]	k_F ($\times 10^8$ s^{-1})	k_q[M][b] ($\times 10^8$ s^{-1})	$\tau_{1_{PI^*}}$ (ns)[c]	τ_{cr}[d]	k_{cr} (s^{-1})
NP(OH)₂ solution	3.7	$k_{F1} = 2.7$	-	3.0	≤ 110 fs	$k_{cr1} \leq 9.0 \times 10^{12}$
NP(OH)₂ : indole (1:1000) solution	3.3	$k_{F2} = 3.0$	0.5	0.5	6.5 ps	$k_{cr2} = 1.5 \times 10^{11}$
NP(OH)₂ : indole (1:500) solution	3.5	$k_{F2'} = 2.8$	0.25	0.64	6.0 ps	$k_{cr2'} = 1.7 \times 10^{11}$
NP(OH)₂ : indole (1:10) solution	3.7	$k_{F2''} = 2.7$	0.005	2.9	≤ 110 fs	$k_{cr2''} \leq 9.0 \times 10^{12}$
NP(OH)₂ gel	3.8	$k_{F3} = 2.6$	-	2.9	≤ 110 fs	$k_{cr3} \leq 9.0 \times 10^{12}$
NP(OH)₂ : indole (1:10) co-gel	2.4	$k_{F4} = 4.2$	0.7	3.0	2.1 ps 1.4 ns	$k_{cr4} = 4.8 \times 10^{11}$ $k_{cr4'} = 7.4 \times 10^8$

[a] obtained from TCSPC measurements when excited at 340 nm using 8 μM **(*R*)-NP(OH)₂** [b] [M] stands for the molar concentration of indole [c] obtained from FTA measurements using 0.75 mM **(*R*)-NP(OH)₂** [d] excited at 390 nm

(*R*)-NP(OH)$_2$: indole could be attributed to ultrafast charge recombination occurring faster than the time-resolution of the instrument (≥ 10 ns). The observed short lifetime (*ca.* 6 ps) of the radical anion of perylenimide (**PI**$^{\bullet -}$) from FTA measurements is consistent with the short-lived coumarin-amine based solvent separated radical ion pair (SSRIP) formed through diffusion controlled intermolecular photoinduced electron transfer as reported earlier[244]. Self-assembled vesicular architecture in the dyad **(*R*)-NP(OH)**$_2$ gel exhibits a similar monoexponential decay of ^{1}**PI*** (τ = 2.9 ns; Figure 4.23A and the inset of 4.23A for singular vector) at 620 nm upon photoexcitation. In contrast to an extension in the photoinduced charge separation lifetimes of an assembled guanine-perylenediimide G-quadruplex structure[229] and melamine-perylenimide based foldamer[93] reported by Wasielewski and co-workers, absence of charge transfer intermediates in the dyad **(*R*)-NP(OH)**$_2$ gel could be attributed to ultrafast charge recombination of **PI**$^{\bullet -}$ and **NI**$^{\bullet +}$ in <110 fs.

SVD analysis followed by global fitting of FTA spectra of dyad **(*R*)-NP(OH)**$_2$: indole (1 : 10) co-gel (Figure 4.23C) yielded three principal components of the spectra as illustrated in Figure 4.23D. The three principal components obtained from SVD could be assigned as the following: i) radical anion of perylenimide (**PI**$^{\bullet -}$)[93,144] and/or radical cation of indole (**I**$^{\bullet +}$) centered at 597 nm having a lifetime of 2.1 ps,[245,246] ii) singlet excited state of perylenimide (^{1}**PI***)[241,247] featured at 620 nm with a lifetime of 3.0 ns and iii) radical anion of π-π stacked perylenimide (π-π **PI**$^{\bullet -}$) at 640 nm having a lifetime of 1.4 ns[93]. We observed a time-dependent shift in the peak corresponding to the decay of **PI**$^{\bullet -}$ indicating the evolution of radical anion of larger π-π stacks of perylenimide (Figure 4.23C)[93,248]. An increase in the survival time of **PI**$^{\bullet -}$ in dyad **(*R*)-NP(OH)**$_2$: indole co-gel indicates sequential electron transfer from singlet excited state of naphthalimide (^{1}**NI***) to **PI** followed by an electron transfer from indole to **NI**$^{\bullet +}$, upon excitation of **NI** unit. Alternatively, ^{1}**PI*** formed *via* energy transfer from ^{1}**NI*** can abstract an electron from indole leading to

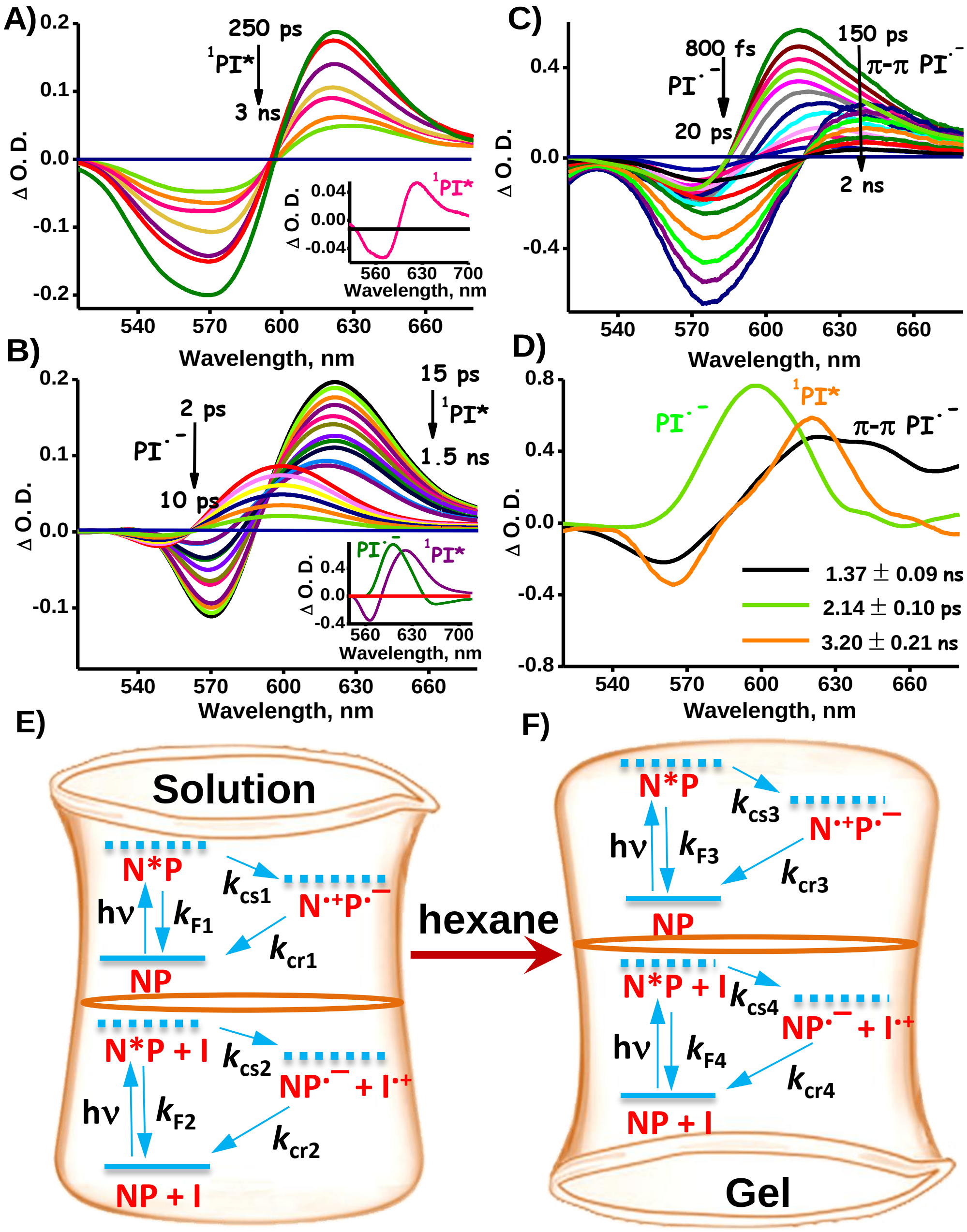

Figure 4.23 *Ultrafast kinetics and Jablonski diagram showing reduced rate of charge recombination in* ***(R)-NP(OH)$_2$*** *: indole co-gel. Femtosecond transient absorption (ΔOD) spectra of A)* ***(R)-NP(OH)$_2$*** *gel, inset shows the principal component of the spectra obtained from SVD; B)* ***(R)-NP(OH)$_2$*** *solution in presence of 1000 equivalents of indole in DCM, inset of B) shows the prinicipal components of the spectra obtained from SVD; C)* ***(R)-NP(OH)$_2$*** *: indole co-gel excited at 390 nm; D) principal components of the spectra shown in C) from SVD; Jablonski diagram of the* ***(R)-NP(OH)$_2$*** *in the absence and presence of indole (**I**) in E) solution and F) gel.*

the formation of $\mathbf{PI^{\bullet-}}$ and radical cation of indole. Lifetime of $\mathbf{PI^{\bullet-}}$ is found to be comparable in the dyad **(*R*)-NP(OH)$_2$** : indole (1 : 10) co-gel and in the dyad **(*R*)-NP(OH)$_2$** : indole (1:1000) solution indicating photoinduced charge separation followed by fast charge recombination (*ca*. 2-6 ps). Meanwhile, the longer survival time of the charge transfer intermediate arising from π-π $\mathbf{PI^{\bullet-}}$ (*ca*. 1.4 ns) in the dyad **(*R*)-NP(OH)$_2$** : indole (1:10) co-gel, which is absent in the dyad **(*R*)-NP(OH)$_2$** : indole (1:1000) solution, could be attributed to the favourable supramolecular arrangement of the donor-acceptor systems for efficient charge separation followed by slow charge recombination. A remarkable increase in survival time of π-π $\mathbf{PI^{\bullet-}}$ in **(*R*)-NP(OH)$_2$** gel (Figure 4.23C, F) *vs*. solution (Figure 4.23E) in the presence of indole could be attributed to the decrease in the rate of diffusion of transient intermediates in highly viscous medium (gel) resulting in slower rate of charge recombination (k_{cr4}) compared to the solution (k_{cr2}), as reported in the self-assembled systems[87,226].

The Jablonski diagram in Figure 4.23E, F demonstrates competitive deactivation pathways of the singlet excited state *via* fluorescence and electron transfer states of the dyad **(*R*)-NP(OH)$_2$** upon photoexcitation under different conditions. Analysis of time-resolved fluorescence and femtosecond transient spectroscopic data revealed that $k_{cs1,3} <<< k_{cr1,3}$, respectively and hence intrinsic fluorescence decay predominates over charge separation in **(*R*)-NP(OH)$_2$** solution/gel. At a lower concentration of indole, **(*R*)-NP(OH)$_2$** in DCM exhibited negligible decrease in the fluorescence quantum yield indicating the lack of forward electron transfer from indole to $\mathbf{^1PI^*/^1NI^*}$ through bimolecular process ($k_q[M] << k_F$; Table 4.3). At higher concentrations of indole, rate of bimolecular quenching is comparable to the rate of fluorescence ($k_q[M] \approx k_F$; Table 4.3) resulting in efficient photoinduced electron transfer from indole to $\mathbf{^1PI^*/^1NI^*}$. Meanwhile, in the case of **(*R*)-NP(OH)$_2$** : indole co-gel (1:10), rate of bimolecular quenching could compete with the intrinsic decay of the singlet excited state thereby resulting in efficient photoinduced charge separation ($k_q[M] \approx k_F$; Table 4.3) followed by slow charge recombination (k_{cr} << k_{cs}; Table 4.3). A significant decrease in the rate of charge recombination could be a consequence of the extended charge delocalisation through supramolecular π-π stacked arrangement of perylenimide units in **(*R*)-NP(OH)$_2$** : indole co-gel.

4.3 Conclusions

In summary, the amphiphilic nature offered by the chiral side-chain (lyophobic) and orthogonal naphthalimide-perylenimide unit (lyophilic) in (***R***/***S***)-**NP(OH)$_2$** in DCM forces the molecules to form bilayer vesicle with an increase in volume fraction of hexane. We observed growth of the vesicles followed by fusion to form superstructured gel with an increase in concentration of the dyad (***R***/***S***)-**NP(OH)$_2$** and progress of time. The metastable nature of gel forces the dyad (***R***/***S***)-**NP(OH)$_2$** to undergo gliding, resulting in thermodynamically stable crystal. Highly efficient energy transfer from naphthalimide to perylenimide unit upon excitation at 345 nm and direct excitation of perylenimide unit (λ_{ex} = 475 nm) in the vesicular gel makes this dyad (***R***/***S***)-**NP(OH)$_2$** an excellent light-harvesting assembly. Upon photoexcitation, a remarkable decrease in the rate of charge recombination of transient intermediates in (***R***/***S***)-**NP(OH)$_2$** gel in the presence of an electron-donor when compared to (***R***/***S***)-**NP(OH)$_2$** : indole solution, is observed. Enhanced survival time of the radical intermediates in the **(*R*/*S*)-NP(OH)$_2$** : indole co-gel is an effect of favourable supramolecular arrangement that stabilises the radical anion of perylenimide in π-π stacked self-assembled structure of (***R***/***S***)-**NP(OH)$_2$**, a feature that is inaccessible in non-assembled D-A systems based photoinduced charge separation. Sequential photoinduced energy/electron transfer processes followed by delayed charge-recombination in solution processable self-assembled donor-acceptor arrays are essential for the fabrication of photovoltaic devices and artificial photosynthesis.

4.4 Experimental Section

4.4.1 Materials and Methods

All chemicals were obtained from Sigma Aldrich and used as received without further purification. All reactions were carried out in glassware oven-dried prior to use and wherever necessary, were performed under dry nitrogen in dried, anhydrous solvents using standard gastight syringes, cannulae, and septa. Solvents were dried and distilled by using standard procedures. TLC analyses were performed on precoated aluminum plates of silica gel 60 F254 plates (0.25 mm, Merck) and developed TLC plates were visualized under short- and long-wavelength UV lamps. Flash column chromatography was performed using silica gel of 200-400 mesh employing a solvent polarity correlated with the TLC mobility observed for the substance of interest. Yields refer to chromatographically and spectroscopically homogenous substances.

Melting points were obtained using a capillary melting point apparatus and are uncorrected. IR spectra were recorded on a Shimadzu IRPrestige-21 FT-IR spectrometer as neat thin films between NaCl plates in the case of liquids and as KBr pellets in the case of solids. ^{1}H and ^{13}C NMR spectra were measured on a 500 MHz Bruker advanced DPX spectrometer. Internal standard used for ^{1}H and ^{13}C NMR is 1,1,1,1-tetramethyl silane (TMS). All CHN analyses were carried out on an Elementar vario MICRO cube Elemental Analyzer. All values recorded in elemental analyses are given in percentages. Photophysical measurements of **(*R*/S)-NP(OH)$_2$** gel in DCM : hexane (1 : 2) mixture were carried out in a cuvette of 1 mm path length unless otherwise mentioned. Absorption and emission spectra were recorded on Shimadzu UV-3600 UV-VIS-NIR and Horiba Jobin Yvon Fluorolog spectrometers respectively. The solid-state fluorescence quantum yield of **(*R*)-NP(OH)$_2$** in the gel as well as in the thin film state was obtained using an integrating sphere and calculated by Horiba Jobin Yvon quantum yield colour calculator software using tris(8-

hydroxyquinolinato)aluminium (Alq_3) as standard and is determined to be 0.36 ± 0.04 (Reported quantum yield $\Phi = 0.40$)[201]. Circular dichroism spectra was recorded on Jasco J-815 spectrometer. Fluorescence lifetime and anisotropy measurements were carried out in an IBH picosecond time correlated single photon counting (TCSPC) system. Pulse duration (<1 ns and <100 ps) of the excitation peak wavelengths (340 nm and 439 nm) was used as excitation source respectively. Multicomponent decay profile of the dyad **(*R*)-NP(OH)$_2$** gel resulted in lifetime data that are lower than the pulse duration of the excitation peak wavelength of 340 nm and hence the decay alone is presented in the manuscript (Figure 4.2D). The fluorescence decay profiles were de-convoluted using IBH data station software version 2.1, and fitted with exponential decay, minimising the χ^2 values of the fit to 1 ± 0.05. Fluorescence anisotropy decay profiles are corrected for G-factor and r_0 is obtained from a mono-exponential fit of the anisotropy decay. All spectroscopic experiments were performed by using standard quartz cuvettes of path length 1 cm for solution and 1 mm for the gel state in dried and distilled solvents.

4.4.2 Preparation of Gel, Thin Film and Solution Samples

1 mM **(*R*/*S*)-NP(OH)$_2$** was dissolved in DCM : hexane (1 : 2) mixture and refrigerated at 0-5 °C for 5-10 minutes. Stability of the gel at ambient temperature was confirmed through the failure of the content to flow on an inverted cuvette. Concentration of **(*R*/*S*)-NP(OH)$_2$** in gel state, used for photophysical measurements, is 1 mM (critical gelator concentration) unless otherwise mentioned. The thin film sample was prepared by drop-casting a 1 mM **(*R*/*S*)-NP(OH)$_2$** solution in DCM on a fresh clean glass slide and allowed to evaporate the solvent atmospherically in a dust free chamber. 8 μM solution of **(*R*/*S*)-NP(OH)$_2$** in DCM is used for solution based photophysical measurements unless otherwise mentioned.

4.4.3 Gelation Studies

Gelation studies were carried out in glass vials of 1 cm diameter. A weighed amount of compound was added to 1 mL of DCM and slowly added to 2 mL of hexane with gentle heating in a water bath. Cooling of the vial in an ice bath provided stable transparent gel. Gel formation was confirmed by the failure of the content to flow on inverting the glass vial. The critical gelator concentration (CGC) is determined from the minimum amount of gelator required for the formation of a stable gel at room temperature.

4.4.4 X-ray crystallography

Red, single crystals of the dyad **(*R*)-NP(OH)$_2$**, which exhibited block morphology, was grown from 1 mM gel sample of **(*R*)-NP(OH)$_2$** in DCM : hexane (1:2). A high-quality specimen of approximately 0.20 × 0.15 × 0.10 mm^3 was selected for the X-ray diffraction experiment. Crystallographic data collected are presented in the supporting information. Single crystals were mounted using oil (Infineum V8512) on a glass fibre. All measurements were made on a CCD area detector with graphite monochromated Mo Kα radiation. The data was collected using Bruker APEXII detector and processed using APEX2 from Bruker. All structures were solved by direct methods and expanded using Fourier techniques. The non-hydrogen atoms were refined anisotropically. Hydrogen atoms were included in idealized positions, but not refined. Their positions were constrained relative to their parent atom using the appropriate HFIX command in SHELXL-97.

4.4.5 Femtosecond Pump-Probe Transient Absorption Technique

Spectra-physics Tsunami Oscillator (80 MHz, 780 nm) was used as seed for a Spectra-Physics Spitfire Regenerative amplifier (1 KHz, 4 mJ). A fraction of the amplified output was used to generate 390 nm pump pulse. Residual 780 nm pulse was sent through a delay line inside an ExciPro pump-probe spectrometer from CDP systems. A rotating CaF$_2$ plate (2 mm thickness) was used to generate continuum of white light from the delayed 780 nm pulses. The continuum of white light was split into two and the streams were used as probe and reference pulses. Transient absorption spectra were recorded using a dual Diode array detector with a 200 nm detection window. Sample solutions were prepared in a rotating sample cell with 400 µm path length. IRF was determined by solvent (10% Benzene in Methanol) two photon absorption and was found to be approximately 130 fs at about 530 nm. Energy per pulse incident on the sample is attenuated employing 80% neutral density filter when required.

The monomeric dyad **(*R*)-NP(OH)**$_2$ solution (0.75 mM; dichloromethane) in the absence and presence of indole was excited with 390 nm, 1000 nJ, ~100 fs pulses, allowing the selective excitation of naphthalimide unit. At lower concentrations of the dyad **(*R*)-NP(OH)**$_2$ solution (8 µM) we could not obtain femtosecond transient absorption data having satisfactory signal/noise ratio and hence we increased the concentration of the dyad **(*R*)-NP(OH)**$_2$ solution (0.75 mM) for FTA measurements. We observed monomeric behavior of the dyad **(*R*)-NP(OH)**$_2$ in dichloromethane with increase in concentration of **(*R*)-NP(OH)**$_2$ upto 0.8 mM (Figure 4.6C, D). Vesicular assembly of the dyad **(*R*)-NP(OH)**$_2$ gel in the absence and presence of indole was excited with 390 nm, 200 nJ, ~100 fs pulses, to moderate singlet-singlet annihilation that occurs in multi-chromophoric assemblies[249]. Dyad **(*R*)-NP(OH)**$_2$ gel and dyad **(*R*)-NP(OH)**$_2$: indole co-gel in the rotating sample cell is mechanically stable throughout the duration of the laser excitation. Kinetic components observed at 597 nm ($\mathbf{PI}^{\bullet-}$), 620 nm ($^{1}\mathbf{PI}^{*}$) and 640 (π-π stacked $\mathbf{PI}^{\bullet-}$) nm are laser intensity independent, ruling out the assignment these kinetic components to singlet–singlet annihilation[93]. Singular value decomposition (SVD) of ΔA versus time and wavelength based three-dimensional map of dyad **(*R*)-NP(OH)**$_2$: indole co-gel obtained from femtosecond transient absorption (FTA) measurements is demonstrated in Figure 4.23. SVD can estimate the number of independent components contributing to the observed spectral data obtained from the FTA spectral signals. For SVD, the FTA spectra of **(*R*)-NP(OH)**$_2$ containing samples recorded from 520 nm to 680 nm at a timescale of 3.5 ns were constructed into a matrix in the Origin graphics software program (Version 8.5; MicroCal, Inc., Northampton, MA) and subjected to SVD using MATLAB (Version 8.0; The Mathworks, Inc., Natick, MA). The dyad **(*R*)-NP(OH)$_2$** solution, dyad **(*R*)-NP(OH)$_2$** + indole (1 : 10) solution and dyad **(*R*)-NP(OH)$_2$** gel offered one significant left and right singular vector while the dyad **(*R*)-NP(OH)$_2$** : indole co-gel offered three significant left singular vectors with significant autocorrelation coefficients. Singular vector observed for the former three cases could be attributed to the **^{1}PI*** centered around 620 nm. While in dyad **(*R*)-NP(OH)$_2$** : indole co-gel, the three singular vectors yielded corresponds to **PI$^{\cdot-}$** (597 nm)[250], **^{1}PI*** (620 nm)[241,251] and π-π stacked **PI$^{\cdot-}$** (640 nm)[93] respectively. Dyad **(*R*)-NP(OH)$_2$** : indole (1:500 and 1:1000) solution offered two singular vectors corresponding to **PI$^{\cdot-}$** (598 nm)[250] and **^{1}PI*** (619 nm)[241,251] respectively. Global analysis of the FTA spectra of **(*R*)-NP(OH)$_2$** + indole co-gel/solution were carried out using Glotaran (version 1.2)[252].

4.4.6 Nanosecond Transient Absorption Technique/Laser flash photolysis

Laser flash photolysis experiments of the argon purged solutions were carried out in an Applied Photophysics Model LKS-60 laser kinetic spectrometer using the second and third harmonic (355 nm and 532 nm, pulse duration ≈10 ns) of a Quanta Ray INDI-40-10 series pulsed Nd:YAG laser. Triplet states of the **NI**, **PI** and **(*R*)-NP(OH)$_2$** in toluene were confirmed using the measurement of oxygen purged solutions through nanosecond flash photolysis studies.

4.4.7 Atomic Force Microscopy (AFM)

Atomic Force Microscopy images were recorded under ambient conditions using multimode scanning probe microscope (Nanoscope V) digital instruments operating in the tapping mode regime. Micro-fabricated silicon cantilever tips (MPP-11100-10) with a resonance frequency of 279–379 KHz and a spring constant of 20–80 Nm^{-1}

were used. The scan rate varied from 0.5 Hz to 1.5 Hz. AFM section analysis were done offline. Samples for the imaging were prepared by drop casting dichloromethane (DCM) : hexane (1 : 2) solution of **(*R*)-NP(OH)$_2$** on freshly cleaved mica at the required concentrations at ambient conditions. Blank experiments were conducted with solvent alone evaporated on mica to exclude any artefacts. The average diameter of the spherical particles of **(*R*)-NP(OH)$_2$** was estimated from the Lorentzian fit of the histogram of the size distribution curves after correcting for the tip-broadening effect.

4.4.8 Transmission Electron Microscopy (TEM)

TEM measurements were carried out using JEOL JEM1011 with an accelerating voltage of 100 kV and the samples were prepared by drop casting DCM : hexane solution of **(*R*)-NP(OH)$_2$** onto a carbon-coated copper grid at the required concentrations at ambient conditions and allowing the excess solvent to evaporate atmospherically. TEM images were obtained without staining. The average diameter of the particles was determined from fitted histograms of the size distribution curve.

4.4.9 Scanning Electron Microscopy (SEM)

For SEM measurements, the **(*R*)-NP(OH)$_2$** in 1 : 2 DCM : hexane mixture were drop casted and air dried on the flat surface of cylindrical copper stubs and subjected to thin gold coating using JOEL JFC-1100 fine coater. The probing side was inserted into JEOL JSM-5600 LV scanning electron microscope for obtaining the images. The average diameter of the particles was determined from fitted histograms of the size distribution curve.

4.4.10 Dynamic Light Scattering (DLS)

Dynamic light scattering (DLS) of **(*R*)-NP(OH)$_2$** was carried out on a Nano Zeta Sizer, Malvern instruments. The particles were prepared in DCM : hexane solution at the required concentrations at ambient condition.

4.4.11 Optical Microscopy

Fluorescent microspheres of **(*R*)-NP(OH)$_2$** were observed on a glass slide by using optical microscope (Leica-DMRX Optical Microscope) under the illumination of UV light (365 nm).

4.4.12 X-ray Diffraction (XRD)

X-ray diffractograms of the xerogel of **(*R*)-NP(OH)$_2$** prepared from 1 : 2 DCM : hexane solution were recorded on a Philips Diffractometer using Ni filtered Cu Kα radiation.

4.4.13 Determination of Bimolecular Quenching Rate Constant

Biomolecular rate constant (k_q) was estimated from the Stern–Volmer rate constant (K_{sv}) obtained by ploting (τ_0/τ) or (I_0/I) along the Y-axis (where τ_0 and τ are the fluorescence lifetimes of **(*R*)-NP(OH)$_2$** and I_0 and I are the corresponding fluorescence intensities at the emission maxima in the absence and the presence of the quencher (indole) respectively) and the quencher concentration along the X-axis. The slope of the plot offered K_{sv}. Biomolecular rate constant (k_q) was obtained from the following equation (Eq. 4.1)

$$k_q = \frac{K_{SV}}{\tau_0} \tag{4.1}$$

4.4.14 Rehm–Weller Analysis

The oxidation potential of indole is found to be 1.1 V[253] and the reduction potentials of **NI** and **PI** are -1.364 and -0.982 V respectively against Saturated Calomel Electrode (SCE). The singlet excited state energies of the acceptor ($E_{0,0}$) values of **NI** and **PI** are found to be 3.65 and 2.56 eV respectively. The change in free energy for the electron transfer (ΔG_{et}) processes were calculated using Rehm–Weller equation, neglecting the Coloumbic interactions to ΔG_{et}.

4.4.15 Synthesis

The dyad **NP(OH)** molecule was synthesised according to the procedure reported in chapter 2[182].

4.4.15.1 Preparation of 4-Bromo-N-((*R*)-2,3-dihydroxypropyl)-naphthalene-1,8-dicarboximide (20A)

To a solution of 4-bromo-1,8-naphthalic anhydride **(3)** (1.00 g, 3.60 mmol) in 100 ml water (*R*)-3-aminopropane-1,2-diol (1.64 g, 18.00 mmol) was added. This reaction mixture was heated at 70°C for 5 h following which it was filtered and the precipitate was washed with water and dried. The crude product was then purified by column chromatography (silica gel, EtOAc : petroleum ether 1 : 1) to afford compound **20A** (1.13 g, 90%) as a white solid. m. p. 176°C; ^{1}H NMR (500 MHz, $CDCl_3$) δ: 8.71 (d, J = 7.15 Hz, 1H), 8.64 (d, J = 8.45 Hz, 1H), 8.46 (d, J = 7.85 Hz, 1H), 8.09 (d, J = 7.85 Hz, 1H), 7.90 (t, J = 8.15 Hz, 1H), 4.50 – 4.46 (m, 1H), 4.42 – 4.38 (m, 1H), 4.15 – 4.11(m, 1H), 3.72 – 3.64 (m, 2H), 2.13 (s, 2H); ^{13}C NMR (125 MHz, $CDCl_3$) δ: 164.90, 133.96, 132.70, 131.85, 131.30, 131.11, 130.71, 129.05, 128.25, 122.52, 121.62, 70.62, 63.75, 42.79; IR (KBr): 3525, 3379, 3319, 2953, 2873, 1701, 1666, 1587, 1568, 1500, 1458, 1433, 1377, 1336, 1232, 1209, 1101, 1056, 1037, 869, 842, 781, 752 cm^{-1}; Anal. Calcd. for $C_{15}H_{12}BrNO_4$: C, 51.45; H, 3.45; N, 4.00%. Found: C, 51.51; H, 3.36; N, 3.60%.

4.4.15.2 Preparation of 4-Bromo-N-((S)-2,3-dihydroxypropyl)-naphthalene-1,8-dicarboximide (20B)

To a solution of 4-bromo-1,8-naphthalic anhydride **(3)** (1.00 g, 3.60 mmol) in 100 ml water (S)-3-aminopropane-1,2-diol (1.64 g, 18.00 mmol) was added. This reaction mixture was heated at 70°C for 5 h following which it was filtered and the precipitate was washed with water and dried. The crude product was then purified by column chromatography (silica gel, EtOAc : petroleum ether 1 : 1) to afford compound **20B** (1.13 g, 90%) as a white solid. m. p. 176°C; ^{1}H NMR (500 MHz,

$CDCl_3$) δ: 8.60 (d, J = 7.25 Hz, 1H), 8.53 (d, J = 8.15 Hz, 1H), 8.36 (d, J = 7.85 Hz, 1H), 7.99 (d, J = 7.85 Hz, 1H), 7.79 (t, J = 8.15 Hz, 1H), 4.39 – 4.35 (m, 1H), 4.31 – 4.28 (m, 1H), 4.04 – 4.00 (m, 1H), 3.61 – 3.53 (m, 2H), 2.09 (s, 2H); ^{13}C NMR (125 MHz, $CDCl_3$) δ: 164.86, 133.91, 132.66, 131.81, 131.29, 131.05, 130.73, 129.07, 128.23, 122.57, 121.67, 70.68, 63.82, 42.84; IR (KBr): 3527, 3383, 2954, 1701, 1668, 1587, 1570, 1500, 1458, 1433, 1377, 1336, 1234, 1209, 1103, 1056, 1037, 869, 842, 781, 752 cm^{-1}; Anal. Calcd. for $C_{15}H_{12}BrNO_4$: C, 51.45; H, 3.45; N, 4.00%. Found: C, 51.61; H, 3.62; N, 4.25%.

4.4.15.3 Preparation of 9-(4-(N-(*R*)-2,3-dihydroxypropyl) naphthalene-1,8-dicarboximide)yl)-N-(2,6-diisopropylphenyl) -perylene-3,4-dicarboximide (21A)

A solution of N-(2,6-diisopropylphenyl)-9-(tributylstannyl))perylene-3,4-dicarboximide **(17)** (0.686 g, 0.89 mmol), 4-Bromo-N-((*R*)-2,3-dihydroxypropyl)-naphthalene-1,8-dicarboximide **(20A)** (0.61 g, 1.12 mmol) and $Pd(PPh_3)_4$ (10.28 mg, 0.0089 mmol) in 50 ml DMF was heated at 90 °C for 2 days. The solvent was removed under reduced pressure and the residue was purified by column chromatography (silica gel, EtOAc : petroleum ether 1 : 1) to afford compound **21A** (0.46 g, 70%) as a yellow-orange solid. m. p. > 300°C; ^{1}H NMR (500 MHz, $CDCl_3$,) δ: 8.73 (d, J = 7.40 Hz, 1H), 8.67 – 8.63 (m, 3H), 8.57 (d, J = 7.85 Hz, 1H), 8.52 (d, J = 8.15 Hz, 1H), 8.47 (d, J = 8.0 Hz, 2H), 7.87 (d, J = 8.45 Hz, 1H), 7.82 (d, J = 7.40 Hz, 1H), 7.62 – 7.58 (m, 2H), 7.47 – 7.40 (m, 2H), 7.34 (d, J = 8.35 Hz, 1H), 7.28 (d, J = 7.8 Hz, 2H), 4.48 – 4.45 (m, 1H), 4.42 – 4.38 (m, 1H), 4.11 – 4.09 (m, 1H), 3.64 – 3.62 (m, 2H), 2.73 – 2.69 (m, 2H), 2.20 (s, 2H), 1.13 – 1.11 (m, 12H); ^{13}C NMR (125 MHz, $CDCl_3$) δ: 164.43, 164.27, 162.89, 144.71, 144.68, 144.06, 137.82, 136.20, 135.91, 132.37, 132.20, 131.16, 131.11, 130.42, 130.15, 129.92, 129.51, 129.51, 129.16, 128.77 128.49, 128.13, 128.09, 127.75, 127.58, 127.28, 126.71, 126.44, 125.99, 123.10, 123.03, 122.08, 121.45, 121.14, 120.59, 120.44, 119.80, 69.76, 62.76, 41.78, 28.16, 23.01, 23.00; IR (KBr): 3549, 3442, 2958, 2866, 1697, 1654, 1591, 1577, 1359, 1234, 1180, 1083, 1031, 812, 788, 758 cm^{-1}; Anal. Calcd. for $C_{49}H_{38}N_2O_6$: C, 78.38; H, 5.10; N, 3.73%. Found: C, 78.25; H, 5.27; N, 3.06%.

4.4.15.4 Preparation of 9-(4-(N-(S)-2,3-hydroxypropyl) naphthalene-1,8-dicarboximide)yl)-N-(2,6-diisopropylphenyl) -perylene-3,4-dicarboximide (21B)

A solution of N-(2,6-diisopropylphenyl)-9-(tributylstannyl))perylene-3,4-dicarboximide (**17**) (0.686 g, 0.89 mmol), 4-Bromo-N-((*S*)-2,3-dihydroxypropyl)-naphthalene-1,8-dicarboximide **(20B)** (0.61 g, 1.12 mmol) and $Pd(PPh_3)_4$ (10.28 mg, 0.0089 mmol) in 50 ml DMF was heated at 90°C for 2 days. The solvent was removed under reduced pressure and the residue was purified by column chromatography (silica gel, EtOAc : petroleum ether 1 : 1) to afford compound **21B** (0.43 g, 65%) as a red-orange solid. m. p. > 300°C; ^1H NMR (500 MHz, $CDCl_3$) δ: 8.82 (d, J = 7.40 Hz, 1H), 8.76 – 8.72 (m, 3H), 8.66 (d, J = 7.80 Hz, 1H), 8.60 (d, J = 8.15 Hz, 1H), 8.55 (d, J = 8.05 Hz, 2H), 7.97 (d, J = 8.45 Hz, 1H), 7.92 (d, 7.40 Hz, 1H), 7.73 – 7.68 (m, 2H), 7.57 – 7.50 (m, 2H), 7.44 (d, J = 8.35 Hz, 1H), 7.38 (d, J = 7.80 Hz, 2H), 4.58 – 4.54 (m, 1H), 4.50 – 4.47 (m, 1H), 4.22 – 4.18 (m, 1H), 3.77 – 3.70 (m, 2H), 2.84 – 2.79 (m, 2H), 2.36 (s, 2H), 1.23 – 1.21 (m, 12H); ^{13}C NMR (125 MHz, $CDCl_3$) δ: 165.46, 165.26, 163.94, 145.74, 145.71, 145.06, 138.87, 137.25, 136.95, 133.38, 133.22, 132.19, 132.15, 131.44, 131.17, 130.93, 130.52, 130.14, 129.75, 129.54, 129.17, 129.12, 128.81, 128.59, 128.28, 127.74, 127.48, 126.98, 124.16, 124.07, 123.14, 122.47, 122.16, 121.56, 121.40, 120.82, 120.70, 70.75, 63.83, 42.80, 31.60, 29.19, 24.05, 24.03; IR (KBr): 3549, 3442, 2958, 2868, 1697, 1654, 1591, 1506, 1359, 1296, 1242, 1180, 1085, 1031, 921, 844, 812, cm^{-1}; Anal. Calcd. for $C_{49}H_{38}N_2O_6$: C, 78.38; H, 5.10; N, 3.73%. Found: C, 78.51; H, 5.25; N, 3.89%.

4.4.15.5 Preparation of 9-(4-(N-(R)-2,3-diacetoxypropyl) naphthalene-1,8-dicarboximide)yl)-N-(2,6-diisopropylphenyl) -perylene-3,4-dicarboximide (22)

A solution of 9-(4-(N-(*R*)-2,3-dihydroxypropyl)naphthalene-1,8-dicarboximide)yl)-

N-(2,6-diisopropylphenyl)-perylene-3,4-dicarboximide **(21A)** (0.100 g, 0.13 mmol), acetic anhydride (0.136 g, 1.3 mmol) in 5 ml pyridine were stirred at room temperature for 12 h. The solvent was removed under reduced pressure and the residue was purified by column chromatography (silica gel, EtOAc : petroleum ether 1 : 2) to afford compound **22** (0.11 g, 95%) as a yellow-orange solid. m. p. > 300°C; ^{1}H NMR (500 MHz, $CDCl_3$) δ: 8.69 (d, J = 7.40 Hz, 1H), 8.66 – 8.63 (m, 2H), 8.59 – 8.56 (m, 2H), 8.51 (d, J = 8.15 Hz, 1H), 8.46 (d, J = 7.95 Hz, 2H), 7.84 – 7.82 (m, 1H), 7.78 (d, J = 7.40 Hz, 1H), 7.61 (d, J = 7.65 Hz, 1H), 7.57 (d, J = 7.8 Hz, 1H), 7.48 – 7.36 (m, 3H), 7.28 (d, J = 7.8 Hz, 2H), 5.53 – 5.51 (m, 1H), 4.62 – 4.59 (m, 1H), 4.38 – 4.34 (m, 2H), 4.26 – 4.23 (m, 1H), 2.73 – 2.69 (m, 2H), 2.06 (s, 3H), 1.97 (s, 3H), 1.13 – 1.11 (m, 12H); ^{13}C NMR (125 MHz, $CDCl_3$) δ : 170.71, 164.28, 164.12, 163.94, 145.75, 145.72, 144.66, 139.09, 137.30, 137.02, 133.42, 132.87, 132.19, 132.15, 131.81, 131.23, 130.96, 130.55, 130.07, 129.73, 129.52, 129.14, 129.00, 128.64, 128.28, 127.71, 127.36, 127.02, 124.15, 124.06, 123.16, 122.66, 122.37, 121.55, 121.40, 120.79, 120.66, 69.83, 63.74, 40.65, 29.18, 24.05, 24.03, 20.98, 20.83; IR (KBr): 2958, 2960, 2868, 1743, 1701, 1622, 1587, 1357, 1238, 1045, 812, 788, 758 cm^{-1}; Anal. Calcd. for $C_{53}H_{42}N_2O_8$: C, 76.24; H, 5.07; N, 3.36%. Found: C, 76.35; H, 5.27; N, 3.06%.

4.4.15.6 Preparation of (5-amino-2,2-dimethyl-1,3-dioxan-5-yl) methanol (24)

A solution of 2-Amino-2-hydroxymethyl-propane-1,3-diol **(9)** (5.00 g, 0.032 mmol) and p-toluene sulfonic acid (0.0297 g, 0.0016 mmol) in 50 ml DMF were stirred overnight. To this 0.4 ml triethyl amine (TEA) was added and solvent evaporated under reduced pressure. The residue is then precipitated by methanol and filtered. To the filterate 2.5 ml TEA added again filtered . The filtrate is then concentrated and purified by column chromatography (silica gel, EtOAc : methanol 9 : 1) to afford compound **24** (2.56 g, 50%) as a white solid. m. p. 32°C; ^{1}H NMR (500 MHz, $CDCl_3$) δ: 3.80 (d, J = 11.5 Hz, 2H), 3.58 (d, J = 11.5 Hz, 2H), 3.52 (s, 2H), 1.45 (s, 3H), 1.42 (s, 3H); ^{13}C NMR (125 MHz, $CDCl_3$) δ: 98. 52, 66.71, 64.30, 50.67, 25.20, 21.87; IR (KBr):

3323, 3269, 2954, 2864, 1612, 1479, 1458, 1369, 1294, 1247, 1199, 1155, 1101, 1051, 1004, 933, 827 cm^{-1}; Anal. Calcd. for $C_7H_{15}NO_3$: C, 52.16; H, 9.38; N, 8.69%. Found: C, 52.51; H, 9.56; N, 8.90%.

4.4.15.7 Preparation of 4-Bromo-N-(5(2-hydroxymethyl 2,2-dimethyl-1,3-dioxan)-naphthalene-1,8-dicarboximide (25)

To a solution of 4-bromo-1,8-naphthalic anhydride **(3)** (2.00 g, 7.20 mmol), (5-amino-2,2-dimethyl-1,3-dioxan-5-yl) methanol **(24)** (1.74 g, 10.83 mmol), zinc acetate (0.946 g, 4.32 mmol) in 10 ml pyridine was added. This reaction mixture was refluxed overnight. The solvent was removed under reduced pressure and the residue purified by column chromatography (silica gel, EtOAc : petroleum ether 1 : 1) to afford compound **25** (0.605 g, 20%) as a white solid. m. p. 186°C; ^{1}H NMR (500 MHz, $CDCl_3$) δ: 8.45 – 8.43 (m, 2H), 8.22 (d, J = 7.85 Hz, 1H), 7.93 (d, J = 7.85 Hz, 1H), 7.75 (t, J = 7.90 Hz, 1H), 4.41 (d, J = 12.85, 2H), 4.30 (d, J = 12.85, 2H), 4.23 (s, 2H), 1.30 (s, 3H), 1.24 (s, 3H); ^{13}C NMR (125 MHz, $CDCl_3$) δ: 166.14, 166.09, 133.06, 131.81, 131.15, 131.03, 130.29, 130.02, 128.65, 128.19, 124.39, 123.49, 99.84, 68.01, 64.45, 62.86, 23.49, 23.30; IR (KBr): 3437, 2947, 2899, 1705, 1660, 1579, 1346, 1232, 1074, 1035, 840, 781 cm^{-1}; Anal. Calcd. for $C_{19}H_{18}BrNO_5$: C, 54.30; H, 4.32; N, 3.33%. Found: C, 54.61; H, 4.36; N, 3.60%.

4.4.15.8 Preparation of 9-(4-(N-(5(2-hydroxymethyl 2,2-dimethyl-1,3-dioxan)-naphthalene-1,8-dicarboximide)yl)-N-(2,6-diisopropylphenyl)-perylene-3,4-dicarboximide (26)

A solution of N-(2,6-diisopropylphenyl)-9-(tributylstannyl))perylene-3,4-dicarboximide **(17)** (0.686 g, 0.89 mmol), 4-Bromo-N-(5(2-hydroxymethyl 2,2-dimethyl-1,3-dioxan)-naphthalene-1,8-dicarboximide (**25**) (0.61 g, 1.12 mmol) and $Pd(PPh_3)_4$ (10.28 mg, 0.0089 mmol) in 50 ml DMF was heated at 90°C for 2 days. The solvent was removed under reduced pressure and the residue was purified by column chromatography (silica gel, EtOAc : petroleum ether 1 : 1) to afford compound **26** (0.46 g, 70%) as a yellow-orange solid. m. p. > 300°C; ^{1}H NMR (500 MHz, CDCl$_3$) δ: 8.66 – 8.63 (m, 2H), 8.60 (d, J = 7.35 Hz, 1H), 8.56 (d, J = 7.80 Hz, 1H), 8.52 – 8.45 (m, 4H), 7.81 – 7.77 (m, 2H), 7.61 (7.65 Hz, d, 1H), 7.58 – 7.55 (m, 1H), 7.47 – 7.40 (m, 2H), 7.34 (d, J = 8.4, 1H), 7.28 (d, J = 7.75 Hz, 2H), 4.48 (d, J = 12.9 Hz, 2H), 4.37 (d, J = 13.00 Hz, 2H), 4.30 (s, 2H), 2.74 – 2.68 (m, 2H), 1.34 (s, 3H), 1.30 (s, 3H) 1.13 – 1.11 (m, 12H); ^{13}C NMR (125 MHz, CDCl$_3$) δ: 166.74, 166.57, 163.94, 145.73, 145.70, 144.20, 139.00, 133.39, 132.40, 132.19, 132.15, 131.33, 130.95, 130.81, 130.59, 130.54, 130.08, 129.75, 129.53, 129.16, 129.04, 128.86 128.29, 127.70, 127.46, 127.01, 124.40, 124.14, 124.11, 124.07, 123.16, 121.54, 121.41, 120.79, 120.67, 99.92, 68.07, 64.78, 62.97, 29.97, 24.06, 24.04, 23.45, 23.42; IR (KBr): 3498, 2947, 2899, 1705, 1660, 1579, 1346, 1232, 1074, 1035, 840, 781 cm^{-1}; Anal. Calcd. for $C_{53}H_{44}N_2O_7$: C, 77.54; H, 5.40; N, 3.41%. Found: C, 77.25; H, 5.27; N, 3.06%.

4.4.15.9 Preparation of 9-(4-(N-(2(2-hydroxymethyl 1,3-dihydroxypropyl)naphthalene-1,8-dicarboximide)yl)-N-(2,6-diisopropylphenyl)-perylene-3,4-dicarboximide (27)

A solution of 9-(4-(N-(5(2-hydroxymethyl 2,2-dimethyl-1,3-dioxan)-naphthalene-1,8-dicarboximide)yl)-N-(2,6-diisopropylphenyl)-perylene-3,4-dicarboximide **(26)** (0.200 g, 0.24 mmol), 1N HCl (0.24 ml, 0.24 mmol) in 5 ml dichloromethane and 5 ml methanol were stirred at room temperature for 1 hour. The solvent was removed under reduced pressure and the residue was purified by column chromatography (silica gel, EtOAc : petroleum ether 2 : 1) to afford compound **27** (0.17 g, 90%) as a yellow-orange solid. m. p. > 300°C; ; ^{1}H NMR (500 MHz, DMSO-d$_6$, 373 K) δ: 8.89 – 8.76 (m, 4H), 8.63 (t, J = 8.5 Hz, 2H), 8.49 (d, J = 7.5 Hz, 1H), 7.87 – 7.75 (m, 3 H), 7.67 – 7.52 (m, 2H), 7.50 – 7.43 9 (m, 2H), 7.36 (d, J = 7.5 Hz, 2H),7.21 – 7.14 (m, 1H), 5.58 (s, 1H), 4.71 (s, 1H), 4.43 (d, J = 8.5 Hz, 2H), 4.30 (s, 1H), 4.18 (d, J = 11 Hz, 1H), 4.02 (d, 10.5 Hz, 1H), 3.95 (d, 13 Hz, 2H), 2.79 – 2.73 (m, 2H), 1.15 – 1.13 (m, 12H); IR (KBr): 3431, 2960, 2868, 1699, 1654, 1589, 1573, 1357, 1246, 1031, 840, 781 cm^{-1}; Anal. Calcd.

for $C_{50}H_{40}N_2O_7$: C, 76.91; H, 5.16; N, 3.59%. Found: C, 76.25; H, 5.57; N, 3.16%. HRMS–TOF–MS Calcd. for $[M+H]^+$ 781.8697; found 781.2737.

4.4.15.10 Preparation of 9-(4-(N-(2(2-acetoxoxymethyl 1,3-aetoxypropyl)naphthalene-1,8-dicarboximide))-perylene-3,4-dicarboximide (28)

A solution of 9-(4-(N-(2(2-hydroxymethyl 1,3-dihydroxypropyl)naphthalene-1,8-dicarboximide)yl)-N-(2,6-diisopropylphenyl)-perylene-3,4-dicarboximide **(27)** (0.05 g, 0.06 mmol), acetic anhydride (0.98 g, 0.96 mmol in 5 ml pyridine were stirred at room temperature for 12 hours. The solvent was removed under reduced pressure and the residue was purified by column chromatography (silica gel, EtOAc : petroleum ether 1 : 3) to afford compound **28** (0.055 g, 95%) as a yellow-orange solid. m. p. > 300°C; ^{1}H NMR (500 MHz, $CDCl_3$) δ: 8.66 – 8.59 (m, 3H), 8.56 (d, J = 8.00 Hz, 1H), 8.49 – 8.45 (m, 4H), 7.81 – 7.77 (m, 2H), 7.61 – 7.55 (m, 2H), 7.47 – 7.38 (m, 3H), 7.28 (d, J = 8.00 Hz, 2H), 4.98 (s, 6H), 2.72 – 2.70 (m, 2H), 1.97 (s, 9H), 1.13 – 1.11 (m, 12H); ^{13}C NMR (125 MHz, $CDCl_3$) δ: 170.32, 166.02, 165.86, 163.91, 163.89, 145.77, 145.74, 143.99, 139.04, 137.26, 136.98, 133.41, 132.14, 132.10, 131.26, 131.00, 130.83, 130.53, 130.10, 129.79, 129.49, 129.14, 129.07, 128.87 128.33, 128.17, 127.66, 127.44, 127.02, 124.48, 124.15, 124.11, 124.03, 123.12, 121.61, 121.48, 120.79, 120.66, 67.07, 62.66, 29.19, 24.02, 24.00, 20.79; IR (KBr): 2964, 2870, 1747, 1703, 1664, 1587, 1359, 1224, 1043, 1035, 840, 781 cm^{-1}; Anal. Calcd. for $C_{56}H_{46}N_2O_{10}$: C, 74.16; H, 5.16; N, 3.59%. Found: C, 74.25; H, 5.27; N, 3.06%.

Other Publications of the Author

1. Cheriya, R. T.; Joy, J.; Rajagopal, S. K.; Nagarajan, K.; Hariharan, M. DNA-Enforced Conformational Restriction of an Atropisomer. *J. Phys. Chem. C* **116**, 22631-22636 (2012).

2. Khandelwal, H.; Mallia, A. R.; Cheriya, R. T.; Hariharan, M. Effect of Temperature on Symmetry Breaking Excited State Charge Separation: Restoration of Symmetry at Elevated Temperature. *Phys. Chem. Chem. Phys* **14**, 15282-15285 (2012).

3. Joy, J.; Cheriya, R. T.; Nagarajan, K.; Shaji, A.; Hariharan, M. Breakdown of Exciton Splitting through Electron Donor–Acceptor Interaction: A Caveat for the Application of Exciton Chirality Method in Macromolecules. *J. Phys. Chem. C* **117**, 17927-17939 (2013).

Bibliography

1 Jiao, G. S. *et al.* Syntheses, Photophysical Properties, and Application of through-Bond Energy-Transfer Cassettes for Biotechnology. *Chem.-Eur. J.* **12**, 7816-7826 (2006).

2 Wan, C.-W. *et al.* Anthracene–Bodipy Cassettes: Syntheses and Energy Transfer. *Chem. – Eur. J.* **9**, 4430-4441 (2003).

3 Lin, W.; Yuan, L.; Cao, Z.; Feng, Y.; Song, J. Through-Bond Energy Transfer Cassettes with Minimal Spectral Overlap between the Donor Emission and Acceptor Absorption: Coumarin-Rhodamine Dyads with Large Pseudo-Stokes Shifts and Emission Shifts. *Angew. Chem., Int. Ed.* **49**, 375-379 (2010).

4 Tachibana, Y.; Vayssieres, L.; Durrant, J. R. Artificial Photosynthesis for Solar Water-Splitting. *Nat. Photonics* **6**, 511-518 (2012).

5 Gust, D.; Moore, T. A.; Moore, A. L. Solar Fuels Via Artificial Photosynthesis. *Acc. Chem. Res.* **42**, 1890-1898 (2009).

6 Nocera, D. G. The Artificial Leaf. *Acc. Chem. Res.* **45**, 767-776 (2012).

7 Schlichting, P. *et al.* A Bichromophore Based on Perylene and Terrylene for Energy Transfer Studies at the Single-Molecule Level. *Chem.-Eur. J.* **5**, 2388-2395 (1999).

8 Wasielewski, M. R. Self-Assembly Strategies for Integrating Light Harvesting and Charge Separation in Artificial Photosynthetic Systems. *Acc. Chem. Res.* **42**, 1910-1921 (2009).

9 Aida, T.; Meijer, E. W.; Stupp, S. I. Functional Supramolecular Polymers. *Science* **335**, 813-817 (2012).

10 Bakulin, A. A. *et al.* The Role of Driving Energy and Delocalized States for Charge Separation in Organic Semiconductors. *Science* **335**, 1340-1344 (2012).

11 Sun, Y. *et al.* Management of Singlet and Triplet Excitons for Efficient White Organic Light-Emitting Devices. *Nature* **440**, 908-912 (2006).

12 Coropceanu, V. *et al.* Charge Transport in Organic Semiconductors. *Chem. Rev.* **107**, 926-952 (2007).

13 Henson, Z. B.; Mullen, K.; Bazan, G. C. Design Strategies for Organic Semiconductors Beyond the Molecular Formula. *Nat. Chem.* **4**, 699-704 (2012).

14 Kumar, M. *et al.* Naphthalimide Appended Rhodamine Derivative: Through Bond Energy Transfer for Sensing of Hg^{2+} Ions. *Org. Lett.* **13**, 1422-1425 (2011).

15 Jiao, G.-S.; Kim, T. G.; Topp, M. R.; Burgess, K. A Blue-to-Red Energy-Transfer Thymidine Analogue That Functions in DNA. *Org. Lett.* **6**, 1701-1704 (2004).

16 Han, J. Y.; Loudet, A.; Barhoumi, R.; Burghardt, R. C.; Burgess, K. A Ratiometric Ph Reporter for Imaging Protein-Dye Conjugates in Living Cells. *J. Am. Chem. Soc.* **131**, 1642-1643 (2009).

17 Muthiah, C. *et al.* Synthesis and Excited-State Photodynamics of a Chlorin-Bacteriochlorin Dyad-through-Space Versus through-Bond Energy Transfer in Tetrapyrrole Arrays. *Photochem. Photobiol.* **84**, 786-801 (2008).

18 Otsuki, J. *et al.* Through-Bond Excited Energy Transfer Mediated by an Amidinium-Carboxylate Salt Bridge in Zn-Porphyrin Free-Base Porphyrin Dyads. *Chem.-Eur. J.* **14**, 3776-3784 (2008).

19 Förster, T. Energiewanderung Und Fluoreszen. *Naturwissenschaften* **6**, 166-175 (1946).

20 Dexter, D. L. A Theory of Sensitized Luminescence in Solids. *J. Chem. Phys.* **21**, 836-850 (1953).

21 Müllen, K.; Scherf, U. *Organic Light Emitting Devices: Synthesis, Properties and Applications*. (Wiley, 2006).

22 Thomas, S. W.; Joly, G. D.; Swager, T. M. Chemical Sensors Based on Amplifying Fluorescent Conjugated Polymers. *Chem. Rev.* **107**, 1339-1386 (2007).

23 Vuorinen, T. *et al.* Photoinduced Electron Transfer in Langmuir−Blodgett Monolayers of Porphyrin−Fullerene Dyads. *Langmuir* **21**, 5383-5390 (2005).

24 Zaumseil, J.; Sirringhaus, H. Electron and Ambipolar Transport in Organic Field-Effect Transistors. *Chem. Rev.* **107**, 1296-1323 (2007).

25 Dodabalapur, A.; Chandross, E. A.; Berggren, M.; Slusher, R. E. Organic Solid-State Lasers: Past and Future. *Science* **277**, 1787-1788 (1997).

26 Cicoira, F.; Santato, C. Organic Light Emitting Field Effect Transistors: Advances and Perspectives. *Adv. Funct. Mater.* **17**, 3421-3434 (2007).

27 Divya, K. P. *et al.* A Zn2+-Specific Fluorescent Molecular Probe for the Selective Detection of Endogenous Cyanide in Biorelevant Samples. *Chem. Commun.* **46**, 6069-6071 (2010).

28 Shimizu, M.; Hiyama, T. Organic Fluorophores Exhibiting Highly Efficient Photoluminescence in the Solid State. *Chem.-Asian J.* **5**, 1516-1531 (2010).

29 Lakowicz, J. R. *Principles of Fluorescence Spectroscopy*. Third edn, (Springer, 2006).

30 Spano, F. C. The Spectral Signatures of Frenkel Polarons in H- and J-Aggregates. *Acc. Chem. Res.* **43**, 429-439 (2009).

31 Möbius, D. Scheibe Aggregates. *Adv. Mater.* **7**, 437-444 (1995).

32 Würthner, F.; Kaiser, T. E.; Saha-Möller, C. R. J-Aggregates: From Serendipitous Discovery to Supramolecular Engineering of Functional Dye Materials. *Angew. Chem. Int. Ed.* **50**, 3376-3410 (2011).

33 Chen, C.-T. Evolution of Red Organic Light-Emitting Diodes: Materials and Devices. *Chem. Mater.* **16**, 4389-4400 (2004).

34 Kaiser, T. E.; Stepanenko, V.; Würthner, F. Fluorescent J-Aggregates of Core-Substituted Perylene Bisimides: Studies on Structure−Property Relationship, Nucleation−Elongation Mechanism, and Sergeants-and-Soldiers Principle. *J. Am. Chem. Soc.* **131**, 6719-6732 (2009).

35 Saragi, T. P. I.; Spehr, T.; Siebert, A.; Fuhrmann-Lieker, T.; Salbeck, J. Spiro Compounds for Organic Optoelectronics. *Chem. Rev.* **107**, 1011-1065 (2007).

36 Benniston, A. C. *et al.* A Donor−Acceptor Molecular Dyad Showing Multiple Electronic Energy-Transfer Processes in Crystalline and Amorphous States. *J. Am. Chem. Soc.* **130**, 7174-7175 (2008).

37 Rybtchinski, B.; Sinks, L. E.; Wasielewski, M. R. Combining Light-Harvesting and Charge Separation in a Self-Assembled Artificial Photosynthetic System Based on Perylenediimide Chromophores. *J. Am. Chem. Soc.* **126**, 12268-12269 (2004).

38 Wolffs, M.; Hoeben, F. J. M.; Beckers, E. H. A.; Schenning, A. P. H. J.; Meijer, E. W. Sequential Energy and Electron Transfer in Aggregates of Tetrakis[Oligo(P-Phenylene Vinylene)] Porphyrins and C60 in Water. *J. Am. Chem. Soc.* **127**, 13484-13485 (2005).

39 Şener, M. K.; Olsen, J. D.; Hunter, C. N.; Schulten, K. Atomic-Level Structural and Functional Model of a Bacterial Photosynthetic Membrane Vesicle. *Proc. Natl. Acad. Sci. USA* **104**, 15723-15728 (2007).

40 Chandler, D. E.; Hsin, J.; Harrison, C. B.; Gumbart, J.; Schulten, K. Intrinsic Curvature Properties of Photosynthetic Proteins in Chromatophores. *Biophys. J* **95**, 2822-2836 (2008).

41 Wurthner, F. Perylene Bisimide Dyes as Versatile Building Blocks for Functional Supramolecular Architectures. *Chem. Commun.*, 1564-1579 (2004).

42 Hsu, C.-P. The Electronic Couplings in Electron Transfer and Excitation Energy Transfer. *Acc. Chem. Res.* **42**, 509-518 (2009).

43 Scholes, G. D.; Ghiggino, K. P. Electronic Interactions and Interchromophore Excitation Transfer. *J. Phys. Chem* **98**, 4580-4590 (1994).

44 Krueger, B. P.; Scholes, G. D.; Fleming, G. R. Calculation of Couplings and Energy-Transfer Pathways between the Pigments of Lh2 by the Ab Initio Transition Density Cube Method. *J. Phys. Chem. B* **102**, 5378-5386 (1998).

45 Scholes, G. D. Quantum-Coherent Electronic Energy Transfer: Did Nature Think of It First? *J. Phys. Chem. Lett.* **1**, 2-8 (2010).

46 Andrews, D. L.; Curutchet, C.; Scholes, G. D. Resonance Energy Transfer: Beyond the Limits. *Laser Photon. Rev.* **5**, 114-123 (2011).

47 Olaya-Castro, A.; Scholes, G. D. Energy Transfer from Forster-Dexter Theory to Quantum Coherent Light-Harvesting. *Int. Rev. Phys. Chem.* **30**, 49-77 (2011).

48 Curutchet, C.; Mennucci, B.; Scholes, G. D.; Beljonne, D. Does Forster Theory Predict the Rate of Electronic Energy Transfer for a Model Dyad at Low Temperature? *J. Phys. Chem. B* **112**, 3759-3766 (2008).

49 Beljonne, D. *et al.* Interchain Vs. Intrachain Energy Transfer in Acceptor-Capped Conjugated Polymers. *Proc. Natl. Acad. Sci. USA* **99**, 10982-10987 (2002).

50 Hsu, C.-P.; You, Z.-Q.; Chen, H.-C. Characterization of the Short-Range Couplings in Excitation Energy Transfer. *J. Phys. Chem. C* **112**, 1204-1212 (2008).

51 Flamigni, L.; Ventura, B.; You, C.-C.; Hippius, C.; Würthner, F. Photophysical Characterization of a Light-Harvesting Tetra Naphthalene Imide/Perylene Bisimide Array. *J. Phys. Chem. C* **111**, 622-630 (2006).

52 Bandichhor, R. *et al.* Water-Soluble through-Bond Energy Transfer Cassettes for Intracellular Imaging. *J. Am. Chem. Soc.* **128**, 10688-10689 (2006).

53 Jiao, G. S.; Thoresen, L. H.; Burgess, K. Fluorescent, through-Bond Energy Transfer Cassettes for Labeling Multiple Biological Molecules in One Experiment. *J. Am. Chem. Soc.* **125**, 14668-14669 (2003).

54 Wu, L. X.; Loudet, A.; Barhoumi, R.; Burghardt, R. C.; Burgess, K. Fluorescent Cassettes for Monitoring Three-Component Interactions in Vitro and in Living Cells. *J. Am. Chem. Soc.* **131**, 9156-9157 (2009).

55 Kim, T. G. *et al.* Correlations of Structure and Rates of Energy Transfer for through-Bond Energy-Transfer Cassettes. *J. Phys. Chem. A* **110**, 20-27 (2006).

56 Ziessel, R.; Alamiry, M. A. H.; Elliott, K. J.; Harriman, A. Exploring the Limits of Förster Theory for Energy Transfer at a Separation of 20 Å. *Angew. Chem. Int. Ed.* **48**, 2772-2776 (2009).

57 Harriman, A.; Mallon, L.; Ziessel, R. Energy Flow in a Purpose-Built Cascade Molecule Bearing Three Distinct Chromophores Attached to the Terminal Acceptor *Chem.-Eur. J.* **14**, 11461-11473 (2008).

58 Bai, D. *et al.* Tuning the Forster Overlap Integral: Energy Transfer over 20 Angstroms from a Pyrene-Based Donor to Borondipyrromethene (Bodipy). *Phys. Chem. Chem. Phys* **15**, 9854-9861 (2013).

59 Langhals, H.; Esterbauer, A. J.; Walter, A.; Riedle, E.; Pugliesi, I. FoìˆRster Resonant Energy Transfer in Orthogonally Arranged Chromophores. *J. Am. Chem. Soc.* **132**, 16777-16782 (2010).

60 Langhals, H.; Poxleitner, S.; Krotz, O.; Pust, T.; Walter, A. Fret in Orthogonally Arranged Chromophores. *Eur. J. Org. Chem.* **2008**, 4559-4562 (2008).

61 Scholes, G. D.; Fleming, G. R. On the Mechanism of Light Harvesting in Photosynthetic Purple Bacteria: B800 to B850 Energy Transfer. *J. Phys. Chem. B* **104**, 1854-1868 (2000).

62 Rabinowitch, E. Photosynthesis and Energy Transfer. *J. Phys. Chem* **61**, 870-878 (1957).

63 Atsbeha, T. *et al.* Photophysical Characterization of Low-Molecular Weight Organogels for Energy Transfer and Light Harvesting. *J. Mol. Struc.* **993**, 459-463 (2010).

64 Elemans, J. A. A. W.; van Hameren, R.; Nolte, R. J. M.; Rowan, A. E. Molecular Materials by Self-Assembly of Porphyrins, Phthalocyanines, and Perylenes. *Adv. Mater.* **18**, 1251-1266 (2006).

65 Röger, C. *et al.* Efficient Energy Transfer from Peripheral Chromophores to the Self-Assembled Zinc Chlorin Rod Antenna: A Bioinspired Light-Harvesting System to Bridge the "Green Gap". *J. Am. Chem. Soc.* **128**, 6542-6543 (2006).

66 Kelley, R. F.; Goldsmith, R. H.; Wasielewski, M. R. Ultrafast Energy Transfer within Cyclic Self-Assembled Chlorophyll Tetramers. *J. Am. Chem. Soc.* **129**, 6384-6385 (2007).

67 Hoeben, F. J. M. *et al.* Direct Visualization of Efficient Energy Transfer in Single Oligo(P-Phenylene Vinylene) Vesicles. *Angew. Chem. Int. Ed.* **45**, 1232-1236 (2006).

68 Ajayaghosh, A.; George, S. J.; Praveen, V. K. Gelation-Assisted Light Harvesting by Selective Energy Transfer from an Oligo(P-Phenylenevinylene)-Based Self-Assembly to an Organic Dye. *Angew. Chem. Int. Ed.* **42**, 332-335 (2003).

69 Ajayaghosh, A.; Praveen, V. K.; Vijayakumar, C.; George, S. J. Molecular Wire Encapsulated into Π Organogels: Efficient Supramolecular Light-Harvesting Antennae with Color-Tunable Emission. *Angew. Chem. Int. Ed.* **46**, 6260-6265 (2007).

70 Amerongen, H. V.; Valkunas, L.; Grondelle, R. V. *Photosynthetic Excitons*. (World Scientific, 2000).

71 Ward, M. D. Photo-Induced Electron and Energy Transfer in Non-Covalently Bonded Supramolecular Assemblies. *Chem. Soc. Rev.* **26**, 365-375 (1997).

72 Wasielewski, M. R. Photoinduced Electron Transfer in Supramolecular Systems for Artificial Photosynthesis. *Chem. Rev.* **92**, 435-461 (1992).

73 Kodis, G. *et al.* Efficient Energy Transfer and Electron Transfer in an Artificial Photosynthetic Antenna-Reaction Center Complex. *J. Phys. Chem. A* **106**, 2036-2048 (2002).

74 Gust, D.; Moore, T. A.; Moore, A. L. Molecular Mimicry of Photosynthetic Energy and Electron Transfer. *Acc. Chem. Res.* **26**, 198-205 (1993).

75 de Silva, A. P.; Moody, T. S.; Wright, G. D. Fluorescent Pet (Photoinduced Electron Transfer) Sensors as Potent Analytical Tools. *Analyst* **134**, 2385-2393 (2009).

76 Odobel, F.; Le Pleux, L. c.; Pellegrin, Y.; Blart, E. New Photovoltaic Devices Based on the Sensitization of P-Type Semiconductors: Challenges and Opportunities. *Acc. Chem. Res.* **43**, 1063-1071 (2010).

77 Le Pleux, L. *et al.* Synthesis, Photophysical and Photovoltaic Investigations of Acceptor-Functionalized Perylene Monoimide Dyes for Nickel Oxide P-Type Dye-Sensitized Solar Cells. *Energy Environ. Sci.* **4**, 2075-2084 (2011).

78 Peet, J. *et al.* Efficiency Enhancement in Low-Bandgap Polymer Solar Cells by Processing with Alkane Dithiols. *Nat. Mater.* **6**, 497-500 (2007).

79 Rehm, D.; Weller, A. Kinetik Und Mechanismus Der Elektronenübertragung Bei Der Fluoreszenzlöschung in Acetonitril. *Ber. Bunsen-Ges. Phys. Chem.* **73**, 834-839 (1969).

80 Weller, A. Z. Photoinduced Electron Transfer in Solution: Exiplex and Radical Ion-Pair Formation Free Enthalpies and Their Solvent Dependence. *Phys. Chem.* **133**, 93-98 (1982).

81 Kavarnos, G. J.; Turro, N. J. Photosensitization by Reversible Electron Transfer: Theories, Experimental Evidence, and Examples. *Chem. Rev.* **86**, 401-449 (1986).

82 Stern, O.; Volmer, M. Über Die Abklingzeit Der Fluoreszenz. *Physikalische Zeitschrift* **20**, 183-188 (1919).

83 Seidel, C. A. M.; Schulz, A.; Sauer, M. H. M. Nucleobase-Specific Quenching of Fluorescent Dyes. 1. Nucleobase One-Electron Redox Potentials and Their Correlation with Static and Dynamic Quenching Efficiencies. *J. Phys. Chem* **100**, 5541-5553 (1996).

84 Fox, M. A. Photoinduced Electron Transfer. *Photochem. Photobiol.* **52**, 617-627 (1990).

85 Lee, C.-H.; Guo, J.; Chen, L. X.; Mandal, B. K. Novel Zinc Phthalocyanine-Benzoquinone Rigid Dyad and Its Photoinduced Electron Transfer Properties. *J. Org. Chem.* **73**, 8219-8227 (2008).

86 Fukuzumi, S. *et al.* Electron-Transfer State of 9-Mesityl-10-Methylacridinium Ion with a Much Longer Lifetime and Higher Energy Than That of the Natural Photosynthetic Reaction Center. *J. Am. Chem. Soc.* **126**, 1600-1601 (2004).

87 Wasielewski, M. R. Energy, Charge, and Spin Transport in Molecules and Self-Assembled Nanostructures Inspired by Photosynthesis. *J. Org. Chem.* **71**, 5051-5066 (2006).

88 Smitha, M. A.; Prasad, E.; Gopidas, K. R. Photoinduced Electron Transfer in Hydrogen Bonded Donor−Acceptor Systems. Free Energy and Distance Dependence Studies and an Analysis of the Role of Diffusion. *J. Am. Chem. Soc.* **123**, 1159-1165 (2001).

89 Grimm, B. *et al.* Step-by-Step Self-Assembled Hybrids That Feature Control over Energy and Charge Transfer. *Proc. Natl. Acad. Sci. USA* **109**, 15565-15571 (2012).

90 Frischmann, P. D.; Mahata, K.; Wurthner, F. Powering the Future of Molecular Artificial Photosynthesis with Light-Harvesting Metallosupramolecular Dye Assemblies. *Chem. Soc. Rev.* **42**, 1847-1870 (2013).

91 Murphy, C. J. *et al.* Fast Photoinduced Electron Transfer through DNA Intercalation. *Proc. Natl. Acad. Sci. USA* **91**, 5315-5319 (1994).

92 Schenning, A. P. H. J. *et al.* Photoinduced Electron Transfer in Hydrogen-Bonded Oligo(P-Phenylene Vinylene)−Perylene Bisimide Chiral Assemblies. *J. Am. Chem. Soc.* **124**, 10252-10253 (2002).

93 Lefler, K. M.; Co, D. T.; Wasielewski, M. R. Self-Assembly-Induced Ultrafast Photodriven Charge Separation in Perylene-3,4-Dicarboximide-Based Hydrogen-Bonded Foldamers. *J. Phys. Chem. Lett.* **3**, 3798-3805 (2012).

94 Adronov, A.; Frechet, J. M. J. Light-Harvesting Dendrimers. *Chem. Commun.*, 1701-1710 (2000).

95 McDermott, G. *et al.* Crystal Structure of an Integral Membrane Light-Harvesting Complex from Photosynthetic Bacteria. *Nature* **374**, 517-521 (1995).

96 Strümpfer, J.; Şener, M.; Schulten, K. How Quantum Coherence Assists Photosynthetic Light-Harvesting. *J. Phys. Chem. Lett.* **3**, 536-542 (2012).

97 Feiler, L.; Langhals, H.; Polborn, K. Synthesis of Perylene-3,4-Dicarboximides — Novel Highly Photostable Fluorescent Dyes. *Liebigs Ann.* **1995**, 1229-1244 (1995).

98 Langhals, H.; Jaschke, H.; Bastani-Oskoui, H.; Speckbacher, M. Perylene Dyes with High Resistance to Alkali. *Eur. J. Org. Chem.* **2005**, 4313-4321 (2005).

99 Zhang, X.; Chen, Z.; Würthner, F. Morphology Control of Fluorescent Nanoaggregates by Co-Self-Assembly of Wedge- and Dumbbell-Shaped Amphiphilic Perylene Bisimides. *J. Am. Chem. Soc.* **129**, 4886-4887 (2007).

100 Weil, T.; Vosch, T.; Hofkens, J.; Peneva, K.; Müllen, K. The Rylene Colorant Family—Tailored Nanoemitters for Photonics Research and Applications. *Angew. Chem. Int. Ed.* **49**, 9068-9093 (2010).

101 Kaiser, T. E.; Wang, H.; Stepanenko, V.; Würthner, F. Supramolecular Construction of Fluorescent J-Aggregates Based on Hydrogen-Bonded Perylene Dyes. *Angew. Chem. Int. Ed.* **46**, 5541-5544 (2007).

102 You, C.-C.; Hippius, C.; Grüne, M.; Würthner, F. Light-Harvesting Metallosupramolecular Squares Composed of Perylene Bisimide Walls and Fluorescent Antenna Dyes. *Chem.-Eur. J.* **12**, 7510-7519 (2006).

103 Addicott, C.; Oesterling, I.; Yamamoto, T.; Müllen, K.; Stang, P. J. Synthesis of a Bis(Pyridyl)-Substituted Perylene Diimide Ligand and Incorporation into a Supramolecular Rhomboid and Rectangle Via Coordination Driven Self-Assembly. *J. Org. Chem.* **70**, 797-801 (2004).

104 Moore, T. A.; Moore, A. L.; Gust, D. The Design and Synthesis of Artificial Photosynthetic Antennas, Reaction Centres and Membranes. *Phil. Trans. R. Soc. Lond. B* **357**, 1481-1498 (2002).

105 Metivier, R.; Kulzer, F.; Weil, T.; Muellen, K.; Basche, T. Energy Transfer Rates and Pathways of Single Donor Chromophores in a Multichromophoric Dendrimer Built around a Central Acceptor Core. *J. Am. Chem. Soc.* **126**, 14364-14365 (2004).

106 Hinze, G.; Haase, M.; Nolde, F.; Muellen, K.; Basche, T. Time-Resolved Measurements of Intramolecular Energy Transfer in Single Donor/Acceptor Dyads. *J. Phys. Chem. A* **109**, 6725-6729 (2005).

107 Metivier, R.; Nolde, F.; Muellen, K.; Basche, T. Electronic Excitation Energy Transfer between Two Single Molecules Embedded in a Polymer Host. *Phys. Rev. Lett.* **98**, 047802 (2007).

108 Fuckel, B.; Hinze, G.; Nolde, F.; Mullen, K.; Basche, T. Control of the Electronic Energy Transfer Pathway between Two Single Fluorophores by Dual Pulse Excitation. *Phys. Rev. Lett.* **103**, 103003 (2009).

109 Curutchet, C. *et al.* Superexchange-Mediated Electronic Energy Transfer in a Model Dyad. *Phys. Chem. Chem. Phys.* **12** (2010).

110 Maus, M. *et al.* Intramolecular Energy Hopping and Energy Trapping in Polyphenylene Dendrimers with Multiple Peryleneimide Donor Chromophores and a Terryleneimide Acceptor Trap Chromophore. *J. Am. Chem. Soc.* **123**, 7668-7676 (2001).

111 Gronheid, R. *et al.* Intramolecular Förster Energy Transfer in a Dendritic System at the Single Molecule Level. *J. Am. Chem. Soc.* **124**, 2418-2419 (2002).

112 Cotlet, M. *et al.* Intramolecular Directional Forster Resonance Energy Transfer at the Single-Molecule Level in a Dendritic System. *J. Am. Chem. Soc.* **125**, 13609-13617 (2003).

113 Maeda, C. *et al.* Large Porphyrin Squares from the Self-Assembly of Meso-Triazole-Appended L-Shaped Meso–Meso-Linked Znii–Triporphyrins: Synthesis and Efficient Energy Transfer. *Chem. – Eur. J.* **16**, 5052-5061 (2010).

114 Yoon, M.-C. *et al.* A Hexagonal Prismatic Porphyrin Array: Synthesis, Stm Detection, and Efficient Energy Hopping in near-Infrared Region. *J. Phys. Chem. A* **111**, 9233-9239 (2007).

115 Bahng, H. W. *et al.* Ensemble and Single-Molecule Spectroscopic Study on Excitation Energy Transfer Processes in 1,3-Phenylene-Linked Perylenebisimide Oligomers. *J. Phys. Chem. B* **116**, 1244-1255 (2012).

116 Kirmaier, C. *et al.* Excited-State Photodynamics of Perylene−Porphyrin Dyads. 5. Tuning Light-Harvesting Characteristics Via Perylene Substituents, Connection Motif, and Three-Dimensional Architecture. *J. Phys. Chem. B* **114**, 14249-14264 (2010).

117 Muthukumaran, K. *et al.* Synthesis and Excited-State Photodynamics of a Perylene-Monoimide-Oxochlorin Dyad. A Light-Harvesting Array. *J. Phys. Chem. B* **107**, 3431-3442 (2003).

118 Langhals, H.; Saulich, S. Bichromophoric Perylene Derivatives: Energy Transfer from Non-Fluorescent Chromophores. *Chem. – Eur. J.* **8**, 5630-5643 (2002).

119 Hayes, R. T.; Walsh, C. J.; Wasielewski, M. R. Using Three-Pulse Femtosecond Spectroscopy to Probe Ultrafast Triplet Energy Transfer in Zinc Meso-Tetraarylporphyrin−Perylene-3,4-Dicarboximide Dyads. *J. Phys. Chem. A* **108**, 3253-3260 (2004).

120 Gunderson, V. L.; Wilson, T. M.; Wasielewski, M. R. Excitation Energy Transfer Pathways in Asymmetric Covalent Chlorophyll a Tetramers. *J. Phys. Chem. C* **113**, 11936-11942 (2009).

121 Bullock, J. E. *et al.* Photophysics and Redox Properties of Rylene Imide and Diimide Dyes Alkylated Ortho to the Imide Groups. *J. Phys. Chem. B* **114**, 1794-1802 (2010).

122 You, C.-C.; Hippius, C.; Grüne, M.; Würthner, F. Light-Harvesting Metallosupramolecular Squares Composed of Perylene Bisimide Walls and Fluorescent Antenna Dyes. *Chem. – A Eur. J.* **12**, 7510-7519 (2006).

123 Sautter, A. *et al.* Ultrafast Energy-Electron Transfer Cascade in a Multichromophoric Light-Harvesting Molecular Square. *J. Am. Chem. Soc.* **127**, 6719-6729 (2005).

124 Flamigni, L.; Ventura, B.; You, C.-C.; Hippius, C.; Wuerthner, F. Photophysical Characterization of a Light-Harvesting Tetra Naphthalene Imide/Perylene Bisimide Array. *J. Phys. Chem. C* **111**, 622-630 (2007).

125 Ren, X.-F.; Ren, A.-M.; Feng, J.-K.; Zhou, X. Density Functional Theory Study on Photophysical Properties of the Porphyrins Derivatives with through-Bond Energy Transfer Characters. *Org. Electron.* **11**, 979-989 (2010).

126 Yang, J.-S. *et al.* Pentiptycene-Derived Oligo(P-Phenyleneethynylene)S: Conformational Control, Chain-Length Effect, Localization of Excitation, and Intrachain Resonant Energy Transfer. *Angew. Chem., Int. Ed.* **48**, 9936-9939 (2009).

127 Eng, M. P.; Albinsson, B. Non-Exponential Distance Dependence of Bridge-Mediated Electronic Coupling. *Angew. Chem., Int. Ed.* **45**, 5626-5629 (2006).

128 Eng, M. P.; Mårtensson, J.; Albinsson, B. Temperature Dependence of Electronic Coupling through Oligo-P-Phenyleneethynylene Bridges. *Chem.–Eur. J.* **14**, 2819-2826 (2008).

129 Diring, S.; Ziessel, R.; Barigelletti, F.; Barbieri, A.; Ventura, B. A Pre-Organised Truxene Platform for Phosphorescent [Ru(Bpy)2] and [Os(Bpy)2] Metal Centres: A Clear-Cut Switch from Förster- to Dexter-Type Energy-Transfer Mechanism. *Chem.–Eur. J.* **16**, 9226-9236 (2010).

130 Agyin, J. K.; Morrison, H.; Siemiarczuk, A. Antenna-Initiated Photochemistry of Distal Groups in Trifunctional Steroids. Z->E Olefin Photoisomerization Involving Ketone Singlet -> Triplet Switches by through-Bond Energy Transfer. *J. Am. Chem. Soc.* **117**, 3875-3876 (1995).

131 Scholes, G. D. Long-Range Resonance Energy Transfer in Molecular Systems. *Annu. Rev. Phys. Chem.* **54**, 57-87 (2003).

132 Krueger, B. P.; Scholes, G. D.; Fleming, G. R. Calculation of Couplings and Energy-Transfer Pathways between the Pigments of Lh2 by the Ab Initio Transition Density Cube Method. *J. Phys. Chem. B* **102**, 9603-9604 (1998).

133 Hsu, C.-P. Ab Initio Characterization of Electron Transfer Coupling in Photoinduced Systems: Generalized Mulliken−Hush with Configuration-Interaction Singles. *J. Phys. Chem. A* **110**, 13640-13641 (2006).

134 Krueger, B. P. *The Role of Carotenoids in Bacterial Light Harvesting.* Ph.D. Thesis thesis, University of Chicago, (1999).

135 Munoz-Losa, A.; Curutchet, C.; Krueger, B. P.; Hartsell, L. R.; Mennucci, B. Fretting About Fret: Failure of the Ideal Dipole Approximation. *Biophys. J.* **96**, 4779-4788 (2009).

136 Reichardt, C. *Solvents and Solvent Effects in Organic Chemistry*. (VCH, 1988).

137 Margineanu, A. *et al.* Visualization of Membrane Rafts Using a Perylene Monoimide Derivative and Fluorescence Lifetime Imaging. *Biophys. J.* **93**, 2877-2891 (2007).

138 Signore, G.; Nifosi, R.; Albertazzi, L.; Storti, B.; Bizzarri, R. Polarity-Sensitive Coumarins Tailored to Live Cell Imaging. *J. Am. Chem. Soc.* **132**, 1276-1288 (2010).

139 Meca, L.; Eha, D.; Havlas, Z. Racemization Barriers of 1,1′-Binaphthyl and 1,1′-Binaphthalene-2,2′-Diol: A Dft Study. *J. Org. Chem.* **68**, 5677-5680 (2003).

140 Berlman, I. B. *Handbook of Fluorescence Spectra of Aromatic Molecules*. (Academic Press, 1971).

141 McWeeny, R.; Sutcliffe, B. T. *Methods of Molecular Quantum Mechanics*. (Academic Press, 1969).

142 Holtrup, F. O.; Müller, G. R. J.; Uebe, J.; Müllen, K. Benzoylperylenedicarboximides: Functional Dyes with Attractive Optical and Electronic Properties. *Tetrahedron* **53**, 6847-6860 (1997).

143 McAdam, C. J.; Morgan, J. L.; Murray, R. E.; Robinson, B. H.; Simpson, J. Synthesis and Fluorescence Properties of New Enaminenaphthalimides. *Aust. J. Chem.* **57**, 525-530 (2004).

144 Boixel, J. *et al.* Hole-Transfer Dyads and Triads Based on Perylene Monoimide, Quaterthiophene, and Extended Tetrathiafulvalene. *Chem.-Eur. J.* **16**, 9140-9153 (2010).

145 Jung, C. *et al.* Photophysics of New Water-Soluble Terrylenediimide Derivatives and Applications in Biology. *ChemPhysChem* **10**, 180-190 (2009).

146 Gaussian 03 (Gaussian, Inc., Wallingford, CT, 2003).

147 Becke, A. D. Density-Functional Thermochemistry. III. The Role of Exact Exchange. *J. Chem. Phys.* **98**, 5648-5652 (1993).

148 Lee, C.; Yang, W.; Parr, R. G. Development of the Colic-Salvetti Correlation-Energy Formula into a Functional of the Electron Density. *Phys. Rev. B: Condens. Matter* **37**, 785-789 (1988).

149 Miertus, S.; Scrocco, E.; Tomasi, J. Electrostatic Interaction of a Solute with a Continuum. A Direct Utilization of Ab Initio Molecular Potentials for the Prevision of Solvent Effects. *J. Chem. Phys.* **55**, 117-129 (1981).

150 Preat, J.; Jacquemin, D.; Wathelet, V.; Andre, J.-M.; Perpete, E. A. Td-Dft Investigation of the Uv Spectra of Pyranone Derivatives. *J. Phys. Chem. A* **110**, 8144-8150 (2006).

151 Cho, D. W. *et al.* Photoinduced Electron Transfer Processes in 1,8-Naphthalimide-Linker-Phenothiazine Dyads. *J. Phys. Chem. B* **110**, 11062-11068 (2006).

152 Rogers, J. E.; Kelly, L. A. Nucleic Acid Oxidation Mediated by Naphthalene and Benzophenone Imide and Diimide Derivatives: Consequences for DNA Redox Chemistry. *J. Am. Chem. Soc.* **121**, 3854-3861 (1999).

153 Rachford, A. A.; Goeb, S. b.; Castellano, F. N. Accessing the Triplet Excited State in Perylenediimides. *J. Am. Chem. Soc.* **130**, 2766-2767 (2008).

154 Ford, W. E.; Kamat, P. V. Photochemistry of 3,4,9,10-Perylenetetracarboxylic Dianhydride Dyes. 3. Singlet and Triplet Excited-State Properties of the Bis(2,5-Di-Tert-Butylphenyl)Imide Derivative. *J. Phys. Chem.* **91**, 6373-6380 (1987).

155 Veldman, D.; Chopin, S. p. M. A.; Meskers, S. C. J.; Janssen, R. A. J. Enhanced Intersystem Crossing Via a High Energy Charge Transfer State in a Perylenediimide−Perylenemonoimide Dyad. *J. Phys. Chem. A* **112**, 8617-8632 (2008).

156 Sariciftci, N. S.; Smilowitz, L.; Heeger, A. J.; Wudl, F. Photoinduced Electron Transfer from a Conducting Polymer to Buckminsterfullerene. *Science* **258**, 1474-1476 (1992).

157 Marcus, R. A. Electron Transfer Reactions in Chemistry: Theory and Experiment (Nobel Lecture). *Angew. Chem., Int. Ed.* **32**, 1111-1121 (1993).

158 Xu, Q. H.; Moses, D.; Heeger, A. J. Time-Resolved Measurements of Photoinduced Electron Transfer from Polyfluorene to C_{60}. *Phys. Rev. B: Condens. Matter* **67**, 245417- 245421 (2003).

159 Bredas, J. L. Charge-Transfer and Energy-Transfer Processes in π-Conjugated Oligomers and Polymers: A Molecular Picture. *Chem. Rev.* **104**, 4971-5004 (2005).

160 Sackett, D. L.; Wolff, J. Nile Red as a Polarity-Sensitive Fluorescent Probe of Hydrophobic Protein Surfaces. *Anal. Biochem.* **167**, 228-234 (1987).

161 Jisha, V. S.; Arun, K. T.; Hariharan, M.; Ramaiah, D. Site-Selective Interactions: Squaraine Dye−Serum Albumin Complexes with Enhanced Fluorescence and Triplet Yields. *J. Phys. Chem. B* **114**, 5912-5919 (2010).

162 Ramaiah, D. *et al.* Halogenated Squaraine Dyes as Potential Photochemotherapeutic Agents. Synthesis and Study of Photophysical

Properties and Quantum Efficiencies of Singlet Oxygen Generation*. *Photochem. Photobiol.* **65**, 783-790 (1997).

163 Grimme, S. Semiempirical Gga-Type Density Functional Constructed with a Long-Range Dispersion Correction. *J. Comput. Chem.* **27**, 1787-1799 (2006).

164 Desiraju, G. R. *Crystal Engineering: The Design of Organic Solids* (Elsevier, 1989).

165 Forrest, S. R. The Path to Ubiquitous and Low-Cost Organic Electronic Appliances on Plastic. *Nature* **428**, 911-918 (2004).

166 Paulini, R.; Müller, K.; Diederich, F. Orthogonal Multipolar Interactions in Structural Chemistry and Biology. *Angew. Chem. Int. Ed.* **44**, 1788-1805 (2005).

167 Oelkrug, D. *et al.* Tuning of Fluorescence in Films and Nanoparticles of Oligophenylenevinylenes. *J. Phys. Chem. B* **102**, 1902-1907 (1998).

168 An, B.-K.; Kwon, S.-K.; Jung, S.-D.; Park, S. Y. Enhanced Emission and Its Switching in Fluorescent Organic Nanoparticles. *J. Am. Chem. Soc.* **124**, 14410-14415 (2002).

169 An, B.-K.; Gierschner, J.; Park, S. Y. Π-Conjugated Cyanostilbene Derivatives: A Unique Self-Assembly Motif for Molecular Nanostructures with Enhanced Emission and Transport. *Acc. Chem. Res.* **45**, 544-554 (2011).

170 Cornil, J.; dos Santos, D. A.; Crispin, X.; Silbey, R.; Bredas, J. L. Influence of Interchain Interactions on the Absorption and Luminescence of Conjugated Oligomers and Polymers: A Quantum-Chemical Characterization. *J. Am. Chem. Soc.* **120**, 1289-1299 (1998).

171 Siddiqui, S.; Spano, F. C. H- and J-Aggregates of Conjugated Polymers and Oligomers: A Theoretical Investigation. *Chem. Phys. Lett.* **308**, 99-105 (1999).

172 Xie, Z. *et al.* Cross Dipole Stacking in the Crystal of Distyrylbenzene Derivative: The Approach toward High Solid-State Luminescence Efficiency. *J. Am. Chem. Soc.* **127**, 14152-14153 (2005).

173 He, F. *et al.* Oligomeric Phenylenevinylene with Cross Dipole Arrangement and Amorphous Morphology: Enhanced Solid-State Luminescence Efficiency and Electroluminescence Performance. *Adv. Mater.* **17**, 2710-2714 (2005).

174 Kasha, M.; Rawles, H. R.; El-Bayoumi, M. L. The Exciton Model in Molecular Spectroscopy. *Pure Appl. Chem.* **11**, 371 (1965).

175 Graser, F.; Hädicke, E. Kristallstruktur Und Farbe Bei Perylen-3,4:9,10-Bis(Dicarboximid)-Pigmenten. *Liebigs Ann. Chem.* **1980**, 1994-2011 (1980).

176 Graser, F.; Hädike, E. Kristallstruktur Und Farbe Bei Perylen-3,4:9,10-Bis(Dicarboximid)-Pigmenten,2. *Liebigs Ann. Chem.* **1984**, 483-494 (1984).

177 Hadicke, E.; Graser, F. Structures of Eleven Perylene-3,4:9,10-Bis(Dicarboximide) Pigments. *Acta Crystallogr., Sect. C* **42**, 189-195 (1986).

178 Hadicke, E.; Graser, F. Structures of Three Perylene-3,4,9,10-Bis(Dicarboximide) Pigments. *Acta Crystallogr., Sect. C* **42**, 195-198 (1986).

179 Klebe, G.; Graser, F.; Hadicke, E.; Berndt, J. Crystallochromy as a Solid-State Effect: Correlation of Molecular Conformation, Crystal Packing and Colour in Perylene-3,4:9,10-Bis(Dicarboximide) Pigments. *Acta Crystallogr., Sect. B* **45**, 69-77 (1989).

180 Zugenmaier, P.; Duff, J.; Bluhm, T. L. Crystal and Molecular Structures of Six Differently with Halogen Substituted Bis (Benzylimido) Perylene. *Cryst. Res. Technol.* **35**, 1095-1115 (2000).

181 Lin, M.-J.; Jimenez, A. J.; Burschka, C.; Wurthner, F. Bay-Substituted Perylene Bisimide Dye with an Undistorted Planar Scaffold and Outstanding Solid State Fluorescence Properties. *Chem. Commun.* **48**, 12050-12052 (2012).

182 Cheriya, R. T.; Joy, J.; Andrews, A. P.; Shaji, A.; Hariharan, M. Energy Transfer in near-Orthogonally Arranged Chromophores Separated through a Single Bond. *J. Phys. Chem. C* **116**, 12489-12498 (2012).

183 Jang, J. *et al.* High Tg Cyclic Olefin Copolymer Gate Dielectrics for N,N′-Ditridecyl Perylene Diimide Based Field-Effect Transistors: Improving Performance and Stability with Thermal Treatment. *Adv. Funct. Mater.* **20**, 2611-2618 (2010).

184 Gautam, D.; Thomas, S. *The Weak Hydrogen Bond in Structural Chemistry and Biology*. (Oxford University Press, 1999).

185 Cao, X. *et al.* Self-Assembly of Twisted Tetrachloroperylenediimide Chromophores into Two Dimensional Brick-Stone Aggregates: Exciton Dynamics and Photoconductivity. *Chem. Commun.* **48**, 6402-6404 (2012).

186 Kumar, N. S. S.; Varghese, S.; Suresh, C. H.; Rath, N. P.; Das, S. Correlation between Solid-State Photophysical Properties and Molecular Packing in a Series of Indane-1,3-Dione Containing Butadiene Derivatives†. *J. Phys. Chem. C* **113**, 11927-11935 (2009).

187 Cao, X.; Wu, Y.; Fu, H.; Yao, J. Self-Assembly of Perylenediimide Nanobelts and Their Size-Tunable Exciton Dynamic Properties. *J. Phys. Chem. Lett.* **2**, 2163-2167 (2011).

188 Veldman, D. *et al.* Triplet Formation Involving a Polar Transition State in a Well-Defined Intramolecular Perylenediimide Dimeric Aggregate. *J. Phys. Chem. A* **112**, 5846-5857 (2008).

189 Che, Y.; Yang, X.; Balakrishnan, K.; Zuo, J.; Zang, L. Highly Polarized and Self-Waveguided Emission from Single-Crystalline Organic Nanobelts. *Chem. Mater* **21**, 2930-2934 (2009).

190 El-ghayoury, A. *et al.* Supramolecular Hydrogen-Bonded Oligo(P-Phenylene Vinylene) Polymers. *Angew. Chem. Int. Ed.* **40**, 3660-3663 (2001).

191 Sassella, A. *et al.* Optical Properties of Highly Oriented Quaterthiophene Thin Films Grown by Organic Molecular-Beam Deposition. *Phys. Rev. B: Condens. Matter* **62**, 11170-11176 (2000).

192 Herz, L. M. *et al.* Fast Exciton Diffusion in Chiral Stacks of Conjugated P-Phenylene Vinylene Oligomers. *Phys. Rev. B: Condens. Matter* **68**, 045203-045209 (2003).

193 Fenwick, O. *et al.* Thermochemical Nanopatterning of Organic Semiconductors. *Nat. Nanotechnol.* **4**, 664-668 (2009).

194 Gierschner, J. *et al.* Excitonic Versus Electronic Couplings in Molecular Assemblies: The Importance of Non-Nearest Neighbor Interactions. *J. Chem. Phys.* **130**, 044105 (2009).

195 Schneider, D. *et al.* An Ultraviolet Organic Thin-Film Solid-State Laser for Biomarker Applications. *Adv. Mater.* **17**, 31-34 (2005).

196 Chandrasekhar, N.; Chandrasekar, R. Reversibly Shape-Shifting Organic Optical Waveguides: Formation of Organic Nanorings, Nanotubes, and Nanosheets. *Angew. Chem. Int. Ed.* **51**, 3556-3561 (2012).

197 Dadvand, A. *et al.* Maximizing Field-Effect Mobility and Solid-State Luminescence in Organic Semiconductors. *Angew. Chem. Int. Ed.* **51**, 3837-3841 (2012).

198 Bandyopadhyay, A.; Pal, A. J. Tuning of Organic Reversible Switching Via Self-Assembled Supramolecular Structures. *Adv. Mater.* **15**, 1949-1952 (2003).

199 Kozlov, V. G.; Bulovic, V.; Burrows, P. E.; Forrest, S. R. Laser Action in Organic Semiconductor Waveguide and Double-Heterostructure Devices. *Nature* **389**, 362-364 (1997).

200 Kena Cohen, S.; Forrest, S. R. Room-Temperature Polariton Lasing in an Organic Single-Crystal Microcavity. *Nat. Photon.* **4**, 371-375 (2010).

201 Cölle, M.; Gmeiner, J.; Milius, W.; Hillebrecht, H.; Brütting, W. Preparation and Characterization of Blue-Luminescent Tris(8-Hydroxyquinoline)-Aluminum (Alq$_3$). *Adv. Funct. Mater.* **13**, 108-112 (2003).

202 Chang, S.-S.; Wu, C.-G. Effects of Polymerization Media on the Nanoscale Conductivity and Current−Voltage Characteristics of Chemically Synthesized Polyaniline Films. *J. Phys. Chem. B* **109**, 18275-18282 (2005).

203 Engel, G. S. *et al.* Evidence for Wavelike Energy Transfer through Quantum Coherence in Photosynthetic Systems. *Nature* **446**, 782-786 (2007).

204 Ringsmuth, A. K.; Milburn, G. J.; Stace, T. M. Multiscale Photosynthetic and Biomimetic Excitation Energy Transfer. *Nat. Phys.* **8**, 562-567 (2012).

205 Scholes, G. D. Quantum-Coherent Electronic Energy Transfer: Did Nature Think of It First? *J. Phys. Chem. Lett.* **1**, 2-8 (2010).

206 Bakulin, A. A. *et al.* Charge-Transfer State Dynamics Following Hole and Electron Transfer in Organic Photovoltaic Devices. *J. Phys. Chem. Lett.* **4**, 209-215 (2012).

207 El-Khouly, M. E. *et al.* Ultrafast Photoinduced Energy and Electron Transfer in Multi-Modular Donor–Acceptor Conjugates. *Chem.-Eur. J.* **18**, 13844-13853 (2012).

208 Kim, J.; McQuade, D. T.; Rose, A.; Zhu, Z.; Swager, T. M. Directing Energy Transfer within Conjugated Polymer Thin Films. *J. Am. Chem. Soc.* **123**, 11488-11489 (2001).

209 Zhang, X.; Rehm, S.; Safont-Sempere, M. M.; Würthner, F. Vesicular Perylene Dye Nanocapsules as Supramolecular Fluorescent Ph Sensor Systems. *Nat. Chem.* **1**, 623-629 (2009).

210 Sakai, N.; Matile, S. Functional Supramolecules: Vesicles Head in White Direction. *Nat. Chem.* **1**, 599-600 (2009).

211 Tseng, K.-P. *et al.* Spontaneous Generation of Highly Emissive Rgb Organic Nanospheres. *Angew. Chem. Int. Ed.* **50**, 7032-7036 (2011).

212 Vijayakumar, C.; Praveen, V. K.; Ajayaghosh, A. Rgb Emission through Controlled Donor Self-Assembly and Modulation of Excitation Energy Transfer: A Novel Strategy to White-Light-Emitting Organogels. *Adv. Mater.* **21**, 2059-2063 (2009).

213 Sugiyasu, K.; Fujita, N.; Shinkai, S. Visible-Light-Harvesting Organogel Composed of Cholesterol-Based Perylene Derivatives. *Angew. Chem. Int. Ed.* **43**, 1229-1233 (2004).

214 Markovitsi, D. *et al.* Triphenylene Columnar Liquid Crystals: Excited States and Energy Transfer. *J. Phys. Chem* **99**, 1005-1017 (1995).

215 Powell, R. C.; Kepler, R. G. Energy Transfer in Doped Organic Crystals. *Mol. Cryst. Liq. Cryst.* **11**, 349-360 (1970).

216 Giansante, C. *et al.* White-Light-Emitting Self-Assembled Nanofibers and Their Evidence by Microspectroscopy of Individual Objects. *J. Am. Chem. Soc.* **133**, 316-325 (2010).

217 Tian, H. *et al.* Synthesis of Novel Multi-Chromophoric Soluble Perylene Derivatives and Their Photosensitizing Properties with Wide Spectral Response for Sno Nanoporous Electrode. *J. Mater. Chem.* **10**, 2708-2715 (2000).

218 Leroy-Lhez, S. *et al.* Tetrathiafulvalene in a Perylene-3,4:9,10-Bis(Dicarboximide)-Based Dyad: A New Reversible Fluorescence-Redox Dependent Molecular System. *J. Org. Chem.* **70**, 6313-6320 (2005).

219 Cheriya, R. T.; Nagarajan, K.; Hariharan, M. Single-Component Organic Light-Harvesting Red Luminescent Crystal. *J. Phys. Chem. C* **117**, 3240-3248 (2013).

220 Olivier, J.-H.; Barberá, J.; Bahaidarah, E.; Harriman, A.; Ziessel, R. Self-Assembly of Charged Bodipy Dyes to Form Cassettes That Display Intracomplex Electronic Energy Transfer and Accrete into Liquid Crystals. *J. Am. Chem. Soc.* **134**, 6100-6103 (2012).

221 Görl, D.; Zhang, X.; Würthner, F. Molecular Assemblies of Perylene Bisimide Dyes in Water. *Angew. Chem. Int. Ed.* **51**, 6328-6348 (2012).

222 Zhang, Z. *et al.* A Self-Assembly Phase Diagram from Amphiphilic Perylene Diimides. *Chem.–Eur. J.* **18**, 12305-12313 (2012).

223 Foster, J. A. *et al.* Anion-Switchable Supramolecular Gels for Controlling Pharmaceutical Crystal Growth. *Nat Chem.* **2**, 1037-1043 (2010).

224 Kumar, N. S. S.; Varghese, S.; Narayan, G.; Das, S. Hierarchical Self-Assembly of Donor–Acceptor-Substituted Butadiene Amphiphiles into Photoresponsive Vesicles and Gels. *Angew. Chem. Int. Ed.* **45**, 6317-6321 (2006).

225 Yagai, S.; Ishii, M.; Karatsu, T.; Kitamura, A. Gelation-Assisted Control over Excitonic Interaction in Merocyanine Supramolecular Assemblies. *Angew. Chem. Int. Ed.* **46**, 8005-8009 (2007).

226 Yamamoto, Y. *et al.* Photoconductive Coaxial Nanotubes of Molecularly Connected Electron Donor and Acceptor Layers. *Science* **314**, 1761-1764 (2006).

227 Steinberg-Yfrach, G. *et al.* Conversion of Light Energy to Proton Potential in Liposomes by Artificial Photosynthetic Reaction Centres. *Nature* **385**, 239-241 (1997).

228 Hoeben, F. J. M.; Jonkheijm, P.; Meijer, E. W.; Schenning, A. P. H. J. About Supramolecular Assemblies of Π-Conjugated Systems. *Chem. Rev.* **105**, 1491-1546 (2005).

229 Wu, Y.-L.; Brown, K. E.; Wasielewski, M. R. Extending Photoinduced Charge Separation Lifetimes by Using Supramolecular Design: Guanine–Perylenediimide G-Quadruplex. *J. Am. Chem. Soc.* **135**, 13322-13325 (2013).

230 Cheriya, R. T.; Joy, J.; Rajagopal, S. K.; Nagarajan, K.; Hariharan, M. DNA-Enforced Conformational Restriction of an Atropisomer. *J. Phys. Chem. C* **116**, 22631-22636 (2012).

231 Mislow, K. Die Absolute Konfiguration Der Atropisomeren Diaryl-Verbindungen. *Angew. Chem.* **70**, 683-689 (1958).

232 Joy, J.; Cheriya, R. T.; Nagarajan, K.; Shaji, A.; Hariharan, M. Breakdown of Exciton Splitting through Electron Donor–Acceptor Interaction: A Caveat for the Application of Exciton Chirality Method in Macromolecules. *J. Phys. Chem. C* **117**, 17927-17939 (2013).

233 Transition Density Cube Analysis Offered a Strong Coulombic Coupling (V_{ET} = 3.5 cm^{-1}) and a Rate of Energy Transfer k_{ET} = 2.2 x 10^{10} s^{-1} for a Dihedral Angle of 75^{o} and a Separation Distance of 1.49 Å between the two Constituent Chromophoric Units.

234 Ostuni, E.; Kamaras, P.; Weiss, R. G. Novel X-Ray Method for in Situ Determination of Gelator Strand Structure: Polymorphism of Cholesteryl Anthraquinone-2-Carboxylate. *Angew. Chem. Int. Ed.* **35**, 1324-1326 (1996).

235 Eaton, S. W. *et al.* Singlet Exciton Fission in Polycrystalline Thin Films of a Slip-Stacked Perylenediimide. *J. Am. Chem. Soc.* **135**, 14701–14712 (2013).

236 Yang, J.-S. *et al.* Probing the Intrachain and Interchain Effects on the Fluorescence Behavior of Pentiptycene-Derived Oligo(P-Phenyleneethynylene)S. *J. Am. Chem. Soc.* **128**, 14109-14119 (2006).

237 Exciton Migration within the Dyad **(R)-NP(OH)$_2$** in the Aggregated State Leads to a Loss of Memory of the Initial Excitation Polarization, thereby Resulting in Equal Intensities of the Polarized Emitted Light that is either Parallel or Perpendicular to the Polarisation of the Excitation Source; Refer: Herz, L. M. et al. Fast Exciton Diffusion in Chiral Stacks of Conjugated P-Phenylene Vinylene Oligomers. *Phys. Rev. B: Condens. Matter*, **68**, 045203-045209 (2003).

238 Cui, J.; Shen, Z.; Wan, X. Study on the Gel to Crystal Transition of a Novel Sugar-Appended Gelator. *Langmuir* **26**, 97-103 (2009).

239 Galindo, F.; Isabel Burguete, M.; Gavara, R.; Luis, S. V. Fluorescence Quenching in Organogel as a Reaction Medium. *J. Photochem. Photobiol. A: Chem* **178**, 57-61 (2006).

240 Babu, S. S.; Kartha, K. K.; Ajayaghosh, A. Excited State Processes in Linear Π-System-Based Organogels. *J. Phys. Chem. Lett.* **1**, 3413-3424 (2010).

241 Odobel, F. *et al.* Coupled Sensitizer–Catalyst Dyads: Electron-Transfer Reactions in a Perylene–Polyoxometalate Conjugate. *Chem.–Eur. J.* **15**, 3130-3138 (2009).

242 Gould, I. R.; Farid, S. Concentration-Dependent Photoinduced Electron-Transfer Reactions: 1:1 and 1:2 Radical-Ion Complexes. *J. Am. Chem. Soc.* **115**, 4814-4822 (1993).

243 Dorfman, R. C.; Lin, Y.; Fayer, M. D. Experimental Investigation of Donor-Acceptor Electron Transfer and Back Transfer in Solid Solutions. *J. Phys. Chem.* **93**, 6388-6396 (1989).

244 Nad, S.; Pal, H. Electron Transfer from Aromatic Amines to Excited Coumarin Dyes: Fluorescence Quenching and Picosecond Transient Absorption Studies. *J. Phys. Chem. A* **104**, 673-680 (1999).

245 Peon, J.; Hess, G. C.; Pecourt, J.-M. L.; Yuzawa, T.; Kohler, B. Ultrafast Photoionization Dynamics of Indole in Water. *J. Phys. Chem. A* **103**, 2460-2466 (1999).

246 Kao, Y.-T. *et al.* Ultrafast Dynamics of Nonequilibrium Electron Transfer in Photoinduced Redox Cycle: Solvent Mediation and Conformation Flexibility. *J. Phys. Chem. B* **116**, 9130-9140 (2012).

247 Petrella, A.; Cremer, J.; De Cola, L.; Bäuerle, P.; Williams, R. M. Charge Transfer Processes in Conjugated Triarylamine−Oligothiophene−Perylenemonoimide Dendrimers. *J. Phys. Chem. A* **109**, 11687-11695 (2005).

248 Lor, M. *et al.* Direct Proof of Electron Transfer in a Rigid First Generation Triphenyl Amine Core Dendrimer Substituted with a Peryleneimide Acceptor. *Photochem. Photobiol. Sci.* **2**, 501-510 (2003).

249 Larsen, J. *et al.* Energy Transfer within Zn-Porphyrin Dendrimers: Study of the Singlet−Singlet Annihilation Kinetics. *J. Phys. Chem. A* **109**, 10654-10662 (2005).

250 Gosztola, D.; Niemczyk, M. P.; Svec, W.; Lukas, A. S.; Wasielewski, M. R. Excited Doublet States of Electrochemically Generated Aromatic Imide and Diimide Radical Anions. *J. Phys. Chem. A* **104**, 6545-6551 (2000).

251 Bell, T. D. M. *et al.* Electron Transfer at the Single-Molecule Level in a Triphenylamine–Perylene Imide Molecule. *ChemPhysChem* **6**, 942-948 (2005).

252 Snellenburg, J. J.; Laptenok, S. P.; Seger, R.; Mullen, K. M.; van Stokkum, I. H. M. Glotaran: A Java-Based Graphical User Interface for the R Package Timp. *J. Stat. Soft.* **49**, 1–22 (2012).

253 Pérez-Prieto, J. *et al.* Photoreaction between 2-Benzoylthiophene and Phenol or Indole. *J. Org. Chem.* **68**, 5104-5113 (2003).